Swansea University
Prifysgol Abertawe

Cronfa
Setting Research Free

Swansea University E-Theses

Near-field spectroscopy of colloidal quantum dots and vertical cavity surface emitting lasers.

Holton, Mark David

How to cite:

Holton, Mark David (2007) *Near-field spectroscopy of colloidal quantum dots and vertical cavity surface emitting lasers..* thesis, Swansea University.
http://cronfa.swan.ac.uk/Record/cronfa42728

Use policy:

This item is brought to you by Swansea University. Any person downloading material is agreeing to abide by the terms of the repository licence: copies of full text items may be used or reproduced in any format or medium, without prior permission for personal research or study, educational or non-commercial purposes only. The copyright for any work remains with the original author unless otherwise specified. The full-text must not be sold in any format or medium without the formal permission of the copyright holder. Permission for multiple reproductions should be obtained from the original author.

Authors are personally responsible for adhering to copyright and publisher restrictions when uploading content to the repository.

Please link to the metadata record in the Swansea University repository, Cronfa (link given in the citation reference above.)

http://www.swansea.ac.uk/library/researchsupport/ris-support/

Near-field Spectroscopy of Colloidal Quantum Dots and Vertical Cavity Surface Emitting Lasers

Mark David Holton

Submitted to the University of Wales in fulfilment of the requirements for the Degree of

Doctor of Philosophy

Swansea University

2007

ProQuest Number: 10807497

All rights reserved

INFORMATION TO ALL USERS
The quality of this reproduction is dependent upon the quality of the copy submitted.

In the unlikely event that the author did not send a complete manuscript
and there are missing pages, these will be noted. Also, if material had to be removed,
a note will indicate the deletion.

ProQuest 10807497

Published by ProQuest LLC (2018). Copyright of the Dissertation is held by the Author.

All rights reserved.
This work is protected against unauthorized copying under Title 17, United States Code
Microform Edition © ProQuest LLC.

ProQuest LLC.
789 East Eisenhower Parkway
P.O. Box 1346
Ann Arbor, MI 48106 – 1346

UNIVERSITY OF WALES
LIBRARY
SWANSEA

DECLARATION

This work has not previously been accepted in substance for any degree and is not being concurrently submitted in candidature for any degree.

Signed ..... (candidate)

Date 28 NOVEMBER 2007

STATEMENT 1

This thesis is the result of my own investigations, except where otherwise stated. Where correction services have been used, the extent and nature of the correction is clearly marked in a footnote(s).

Other sources are acknowledged by footnotes giving explicit references. A bibliography is appended.

Signed ..... (candidate)

Date 28 NOVEMBER 2007

STATEMENT 2

I hereby give consent for my thesis, if accepted, to be available for photocopying and for inter-library loan, and for the title and summary to be made available to outside organisations.

Signed ..... (candidate)

Date 28 NOVEMBER 2007

Abstract

A scanning near-field optical microscope (SNOM) has been employed for developments and measurements that allow spectroscopic characterisations on the nanoscale. To obtain spectral properties on spatial resolutions beyond the diffraction limit a spectrometer has been integrated into the SNOM system, together with various avalanche photodiode detectors, a cooled charge-coupled device and various filters, suitable to the experiments conducted. The system was optimised such that it allowed subsequent probe-positioning to perform point spectroscopy, using localised stimulation and collection techniques in the near-field. This spectral detection scheme has been applied to two areas of study, laser devices and quantum dot systems.

The simultaneous topographical and optical study of semiconductor lasers, specifically vertical cavity surface emitting lasers (VCSEL), was carried out to spatially and spectrally map individual transverse mode emissions at the aperture surfaces in the near-field. These measurements showed the clear presence of modulation of the intensity of the transverse modes in the form of concentric rings. The effect was attributed to a sub-surface defect within the aperture of the device, clipping the Gaussian emission profile of the fundamental transverse mode. Higher order transverse modes were also found to be affected, revealing a more complex modulation structure due to their non-Gaussian emission. Structural defects, in or at the surface of such devices, have been shown to have significant effects on far-field characteristics. It is therefore important to spatially map the spectral source of such effects to gain insight into their origin.

Spectral SNOM studies on quantum dots were conducted on mixed colour cadmium selenide/zinc sulphide (CdSe/ZnS), and cadmium selenide/hexadecylamine CdSe(HDA) quantum dots. Low concentrations were immobilised within a 2-3 nm thick layer of a PMMA polymer matrix, spin coated onto cleaved mica. Optical stimulation in the near-field revealed simultaneous topographic and optical detection of single and small clusters of quantum dots. Spectroscopic measurements of single and small clusters of quantum dots in the near-field, showed a minimum spectral full width half maximum (FWHM) of ~14-16 nm. Repeated imaging of single quantum dots also showed fluorescence intermittency events on a range of time scales from below the time resolution of the set-up, to over an hour, in addition to fluorescence brightening. Conclusions as to the potential for quantum dots in biological imaging are discussed.

Acknowledgements

I would firstly like to thank Dr Peter Dunstan for his enthusiasm, generous time and support throughout this research. His supervision allowed for a great many discussions and interesting ideas that have now also led onto future work for future students. The work performed by the author for this thesis was only possible with the help and expertise of a number of people including Dr Huw Summers, Dr Daniel Matthews and Prof P Rees, for the preparation of VCSELs, RCLEDs, initial quantum dot samples, and discussions of results, Dr Sally James for help with confocal microscopy, and Dr Anthony Higgins and Samson C.C. Seng for help with the work on polymers. I would also like to thank Prof Helmut Telle for his time and interesting insights. The modifications to the experimental set-up would not have been possible if it were not for the technical skills and knowledge of Julian Kivell, Huw Thomas, Mike Rogers and David Payne. I would also like to thank my friends and colleagues Jess Scully, Neil Joseph, Dr Mathew Ackland, Nela Durisic, Richard Baylis, Omar Al Hartomy, Kelly-Ann Walker, my ever supporting family, and many other friends and colleagues both home and abroad, who have encouraged and supported me throughout the course of this work.

Contents

1.1 Introduction

There is an ever increasing demand for faster and more efficient optical and electro-optical structures and devices. To this end, manufacturers have had to develop innovative and intricate methods to continually reduce the size of components and structures. This includes aspects such as mechanical, optical, and electrical characteristics. As structures are reduced to the size of a few tens of nanometres, quantum mechanical principles play an important role in our understanding and interpretation. Devices built at such scales are capable of tasks that are simply not possible on a larger macroscopic dimension.

Conventional optical imaging techniques are limited by diffraction to several hundred nano-metres. The development of technology at the nano-scale therefore needs to be observed using new and innovative techniques that overcome such barriers. In recent decades, a range of techniques that allow a number of characteristics to be determined from a material or structure have been developed. One of the first most notable techniques was the initial development of scanning tunnelling microscopy (STM) by Binnig and Rohrer while working at IBM in Zurich, Switzerland. This allows for the study of surface atomic structure on conducting samples. STM has led to a host of techniques under the heading scanning probe microscopy (SPM) which can probe and even manipulate the electrical properties of materials and devices. The success of STM was largely due to the development of piezo-drives that allowed the precise, sub-nanometre control of a sharp tip in relation to a surface under study. In the years that followed, further nano-scale techniques such as the atomic force microscope (AFM) were developed (1986) by Binnig, Quate and Gerber. It was in 1984 that Pohl *et al* [1] used a quartz probe, partially coated in metal to confine light and positioned using piezo

materials already developed for the STM, to optically study materials at resolutions beyond the diffraction limit. This technique of using a sub-micron aperture has been fully developed into an instrument known as the scanning near-field optical microscope, or SNOM (sometimes referred to as a near-field scanning optical microscope, or NSOM).

SNOM is an important tool because optical techniques offer a wealth of information about the nature of a sample, such as the transparency, density, absorption, fluorescence, stimulation of charge carriers, and refractive index. The significant difference between SNOM and other analytical tools is its potential to characterise materials at the nano-scale. The power of such a tool can be greatly enhanced by coupling it together with instruments that allow spectroscopic measurements to be carried out. Such a set-up has been implemented and exploited within this thesis, allowing the simultaneous collection of topographical, optical intensity and spectroscopic information from light emitting and fluorescent materials, at resolutions far beyond the diffraction limit [2].

In this thesis, the potential of our set-up has been realised in the study of semiconductor lasers. These are nano-scale structures, thus their optical characteristics can be described by quantum mechanical principles. The development of semiconductor lasers has been ongoing for more than 40 years. The first, constructed in 1962 by Hall, was composed of gallium arsenide and emitted at a wavelength of 850nm, while Holonyak [3] also developed a visible wavelength device in the same year. Since that time, combinations of different materials and construction techniques have resulted in a large variety of semiconductor lasers capable of continuous operation at significantly high powers and modulation frequencies.

One particular type is the vertical cavity surface emitting laser (VCSEL), smaller than the more traditional side emitting semiconductor laser. Typical VCSEL dimensions are of the order of a few microns in height, with the width and length a few tens of microns in size. The exit aperture for the laser light is at the top surface, emitting perpendicular to the plane of growth. VCSELs typically possess optical apertures of a few microns across with the size of its gain cavity the order of the emitted wavelength of light. This allows them to be tuned effectively by varying the temperature. At higher injection currents however, the presence of multiple transverse modes within the gain medium reduce the single mode power capability of the device. Multiple transverse modes have the disadvantage of reducing the decoherence length of transmitted light in fibre-optics thus limiting their usefulness at higher powers in a number of areas such as telecommunications. By spectroscopically studying the emissions directly at the aperture, it is possible to gain vital information relating the far-field emissions to the internal structure of such a device. In this thesis, multimode emissions have been mapped and their spatial location compared to the physical aperture dimensions. Chapter 6 discusses these measurements in full and examines features present in the optical cavity that arise due to the fabrication process [2].

Other technologically important materials are nano-crystals, commonly referred to as quantum dots, possessing a highly ordered internal structure, and only a few nanometres in size. As a result, an excited electron-hole pair may be confined within the structure resulting in interesting features such as very narrow band emission at specific wavelengths dependent on their size as shown by Brus [4]. This can be explained by quantum mechanical arguments resulting in a description of a quantum dot having an atomic like nature, as discussed by Liboff [5]. Clearly their size and optical emissions make them ideal for study with a SNOM/spectrometer set-up. This can reveal their

emission as a function of size, dilution, aggregation and any influences due to an embedding matrix. [6]

Due to the discrete size of quantum dots, spectroscopic studies of fluorescent emissions can reveal characteristics representative of a number of quantum mechanical principles. They are increasingly being used in a variety of scientific areas including the biological field. By coating the outer shell of quantum dots with biologically compatible materials, they can for instance be conjugated to a protein or an antibody and detected once bound to their target cell. Other uses include light emitting diodes combined with quantum dots resulting in devices capable of light emission throughout the visible spectrum. From current literature, the stability of emissions is of great importance to the continued development of quantum dots for technological advances. The study presented in Chapter 7 aims to highlight the benefits of studying such materials in the near-field, allowing the topographical and spectroscopic study of single quantum dots and phenomena associated with their physics.

1.2 Thesis outline

Chapter 2 begins by discussing the theory of SNOM, the principal experimental technique used throughout the research. An overview of the nature of semiconductor quantum dots and their fluorescent response to laser excitation is given in Chapter 3, including a literature review on the study of quantum dots using both standard and spectroscopic SNOM. Further theory is discussed on the subject of semiconductor lasers in Chapter 4. Their mode of operation including the fundamentals of longitudinal modes is briefly covered, focussing more on the transverse modes present within VCSELs. The equipment design and implementation that has been necessary to carry

out the various experiments is discussed in Chapter 5, including the importance of using highly sensitive photon counters to detect the extremely low levels of light. This chapter also highlights the limitations of the experimental setup and CCD detectors used. Detailed diagrams of set-ups and modifications made are also included. Chapter 6 presents the results of experiments involving VCSELs both in the far-field and the near-field, and analyses anomalous behaviour seen in the near-field imaging of the optical aperture of VCSELs. Chapter 7 discusses results of near-field imaging and spectroscopy of single, and clusters of, quantum dots. CdSe/ZnS and CdSe/HDA quantum dots were dissolved in low concentrations together with small amounts of PMMA in toluene, and spin coated on mica. This created the necessary PMMA polymer films, the order of a few nano-metres thick, to immobilise dispersed monolayers of these quantum dots for optical study. Finally, Chapter 8 discusses the overall conclusions of the work contained within the thesis and discusses its implications and future developments.

References

[1] Pohl D.W., Denk W., Lanz M., Appl. Phys. Lett. **44**, 651-653, (1984)

[2] Holton M.D., Rees P., Dunstan P.R., J. Appl. Phys. **101**, 023103 (2007)

[3] Holonyak N. Jr, Bevaqua S.F., Appl. Phys. Lett. **1**, 82-83, (1962)

[4] Brus L.E., J. Chem. Phys. **80** (9), 4403-4409, (1984)

[5] Liboff R.L., Phys. Rev. A. **43**, 11, 5765, (1991)

[6] Gómez D.E., van Embden J., Mulvaney P., Appl. Phys. Lett. **88**, 154106, (2006)

2 Scanning near-field optical microscopy

2.1 Introduction

The desire with all types of microscopy is to obtain the highest possible resolution. Many techniques exist today that allow us to acquire ultra-high resolution images of sub-micron structures. An example being the scanning electron microscope (SEM) which was first conceived by M. Knoll and built by Zworykin *et al.* [1] in 1935. Operating in vacuum, a highly focussed beam of electrons is directed over the surface. Secondary electrons as a result of the energetic collisions are used to create an image of the surface structure with a resolution between 1 and 20 nm. Another example is the transmission electron microscope (TEM) that was built by Ruska (under the supervision of Knoll) in 1933. A TEM, like the SEM, operates in vacuum and produces images of materials by passing an electron beam through the structure which these days can achieve remarkable resolutions of less than 0.2 nm. This does however require the material to be a maximum of a few nanometres thick due to signal attenuation.

Conventional optical microscopes utilise a combination of lenses and mirrors to collect light from the surface of, or through the sample. The best achievable resolution with such an instrument however is diffraction limited to about half the wavelength of the illuminating light.

2.2 Optical limit of resolution

For much of scientific history, studies requiring the use of conventional microscopic equipment were limited in resolution. Ernst Abbe, a 19th century German physicist specified the resolution [2] of a lens, R, as,

$$R = \frac{\lambda}{2NA}, \qquad 2.1$$

with NA the numerical aperture of the lens ($NA = n \cdot \sin(\alpha)$), λ the wavelength of the incident light, n the refractive index of the lens material and α the half acceptance angle of the lens. For instance, the smallest resolvable feature using a lens having an NA of 1.4 can be no less than 200nm in size while illuminating a sample with light of wavelength 550nm.

From equation 2.1 it can be clearly seen that imaging resolution may be improved in a number of ways, including reducing the wavelength of the light used for observation or using a lens with a larger numerical aperture, such as an oil immersion lens. In order to maximise the NA of oil objective lenses however, the small space between the lens and the sample or the sample holder must be filled with a substance of equally high refractive index. This is not a problem for many samples as they can then be mounted on the surface of a thin glass slide while observations with an oil based objective can be carried out from beneath by focussing through to the sample surface.

The study of the limit of resolution of optics was defined by Lord Rayleigh [3] for a circular aperture as,

$$r \geq \frac{1.22\lambda}{2NA}, \qquad 2.2$$

where r is the aperture width and λ is the wavelength of the light used to illuminate the sample. As shown in Figure 2.1, two illuminated objects in close proximity will each generate a diffraction pattern. An imaging process using light is said to be diffraction limited when the first diffraction minimum of one of the objects coincides with the central maximum of diffraction of the adjacent object as shown in Figure 2.1(a).

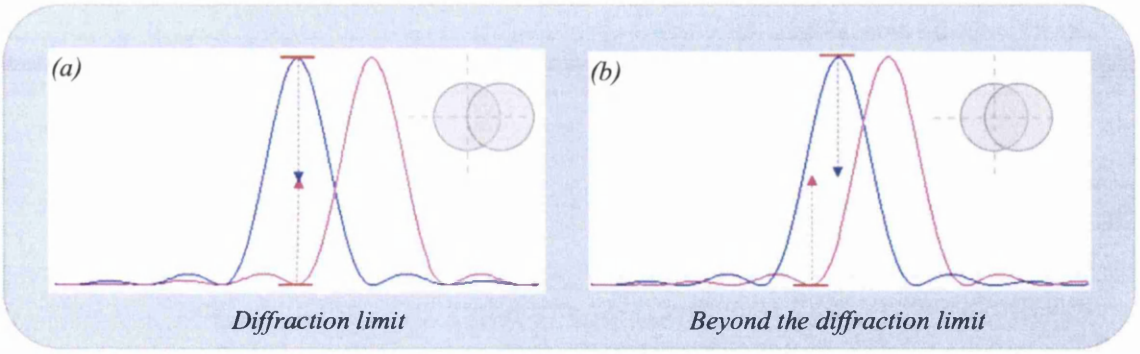

Fig. 2.1 (a) Rayleigh criterion reached at coincidence of the central maximum of diffraction from one object and first minimum of another (b) These points cannot be resolved as they are closer together than that defined by equation 2.2.

Thus, the two point sources of light are just resolvable in Figure 2.1(a) but not in Figure 2.1(b) which are too close together and thus beyond the diffraction limit.

Sir Isaac Newton was the first to point out that too much light was transmitted from the flat edge of a prism to a curved edged prism at the point of contact than would be expected from the touching surface area, as shown in Figure 2.2(a). He carried out an experiment involving the two prisms where one had 3 flat edges, and the other had 2 flat and one curved. He brought the prisms into contact such that the flat and curved edges touched.

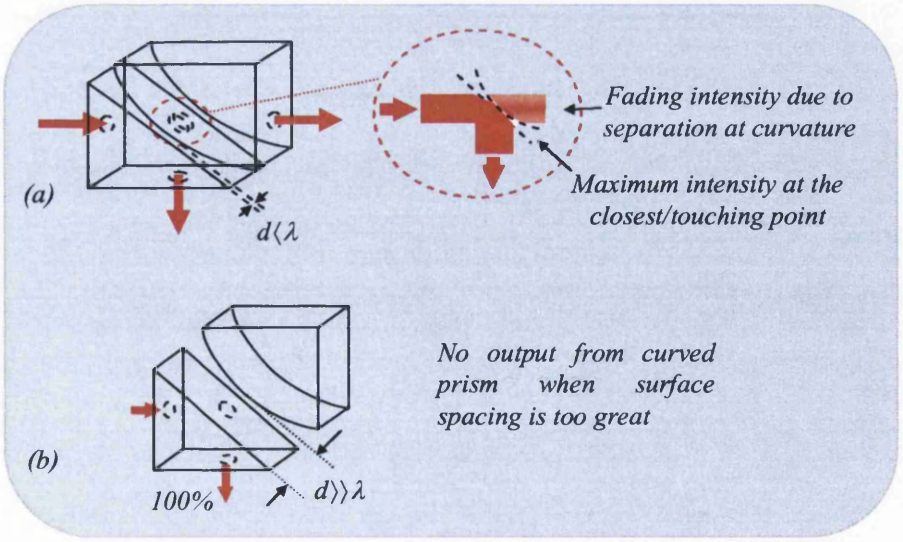

Fig. 2.2(a) Newton's experiment using a curved and a flat prism together resulting in the first recorded observation of evanescent waves being scattered to a nearby medium (b) The flat and curved prism faces are separated such that no energy is scattered into the curved prism.

A beam of light was shone into the first prism such that total internal reflection (TIR) would reflect all light back out of the first. Light was expected only to cross over into the second prism where the two prisms were in intimate contact. He noted however that this was not the case. Instead, a region very close to the point of contact was still in close proximity to the first prism due to the small curvature of the second prism, and thus light was penetrating the second prism from this region, not just from the point of contact. This was explained later to be due to coupling to a non-propagating component existing outside of the prism surface. This non-propagating component is known today as an evanescent field due to its exponential decay with distance from its source. When the two prisms are separated by a distance larger than a few nanometres, the evanescent field has decayed to a point whereby there is no transmitted light, and TIR occurs within the primary, flat faced, prism (Figure 2.2(b)).

2.3 Scanning near-field optical microscopy

In 1928 Synge proposed the initial concept of the scanning near-field optical microscope (SNOM or NSOM) after more than 12 recorded letters of discussion with Albert Einstein [4]. His idea involved shining light onto a screen with a small hole that lies within 10nm of a sample surface. He envisaged moving this screen with the hole in a raster scanning motion, maintaining a distance of a few nanometres from the sample below. He believed correctly that this would allow one to defeat the diffraction limit as defined by the Rayleigh Criterion in equation 2.2, thus gaining optical information of the sample beneath it as shown in Figure 2.3.

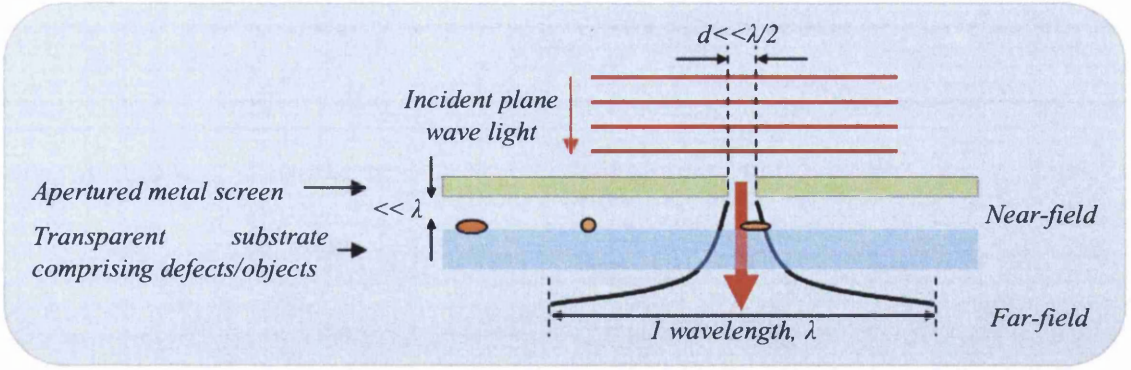

Fig. 2.3 Layout of the experimental method first proposed by Synge in 1928 whereby an incident optical plane wave is confined by a subwavelength aperture. Subwavelength optical resolution information can then be obtained by positioning a transparent sample within the decaying evanescent near-field region.

At the time the technology was not available for Synge to realise his idea, but during these investigations, he theorised a mechanical system consisting of gears to give the small movements required of such a setup. Later Synge suggested the idea of piezoelectric-positioners to provide the nano-scale movements required for such an imaging system [5].

This problem was approached by Bethe in 1944 who calculated the field distribution around a sub-wavelength aperture made through a conducting screen, back illuminated with a plane wave source [6]. Errors in Bethe's expression for the near-field were later corrected in a further publication by Bouwkamp [7]. Together they mathematically showed that it was possible to beat the diffraction limit imposed in the Abbe and Rayleigh equations 2.1-2.2 by applying Maxwell's equations to the boundary conditions at the aperture. It was 2 decades later, in the early 70's, when Ash and Nicholls of University College London conclusively confirmed Synge's ideas experimentally. Together they used 3cm microwave radiation to illuminate a vibrated subwavelength aperture. This vibration was used to modulate the measured signal to aid in the removal of background signals. The experimental setup allowed them to obtain a spatial

resolution of approximately λ/100 at 10 GHz (0.3 mm). Single lines on a test grating close to the aperture with 0.5mm spacing (λ/60) were clearly visible [8].

The field emitted from a conducting nano-sized object might have a well known, uniform, far-field structure. Due to the law of continuity however, the spatial field close to the object must be representative of the surface of the oscillating charge densities inducing it, consisting of both propagating and non-propagating components. Thus, two types of field exist together; a non-propagating field that exists very close to the object, evanescent in nature, and a propagating field that continues on to infinity. By the Rayleigh Criterion however, this far-field component only carries resolution limited information.

The theory of propagating, and non-propagating, evanescent waves at the nano-scale has also been investigated by Wolf and Nieto-Vesperinas [9]. A sub-wavelength structure is one that can be thought of as a sharp discontinuity such that it possesses an infinite spatial Fourier spectrum. It is the lower ranges of frequencies that propagate to a detector in conventional experiments, whereas the higher to infinite range are confined to the surface i.e. the evanescent, non-propagating field components. Equation 2.3, given by Courjon *et al.* [10], describes an evanescent non-propagating field, as

$$U(x,y,z,t) = A(x,y,z)\exp -i(k_x x + k_y y)\exp(-\alpha z)\exp i(\omega t). \qquad 2.3$$

Here A is the amplitude of the field at a point (x,y,z), $exp\ -i(k_x x+k_y y)$ describes the propagation of the field in the plane of the surface at point (x,y), $exp\ i(\omega t)$ describes how the field varies in time, and $exp\ (-az)$ gives the exponential decrease in amplitude of the field with distance from the surface, i.e. evanescent in nature. The evanescent field component is stronger at the surface for larger values of the material dependent constant α.

2.4 Heisenberg Uncertainty Principle and detection of the Near-field

It is possible to introduce Heisenberg's Uncertainty Principle to help determine the limits of resolution. Consider a point $P(x,y,z)$ in a field distribution $U(x,y,z)$ having a propagation vector defined by $k(k_x,k_y,k_z)$ in a medium of refractive index n as shown in Figure 2.4 where $|k| = 2\pi n / \lambda$.

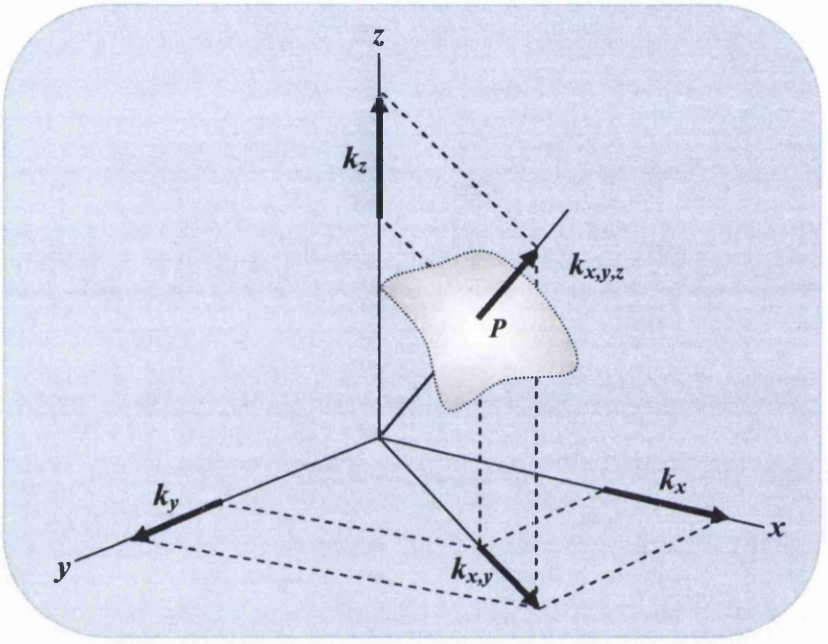

Fig. 2.4 The grey patch represents the minimum field variation at a point P of a propagation vector detectable due to the Heisenberg uncertainty principle [10].

This field varies between two closely separated points; the minimum detectable separation of which defines the maximum achievable resolution.

Ignoring optical limitations due to experimental capabilities, we must define the position uncertainty in point P as $(\Delta x,\Delta y,\Delta z)$ and also, the uncertainty of the propagation vector k as $(\Delta k_x,\Delta k_y,\Delta k_z)$.

Considering just the uncertainty on the x axis, while noting the same can be applied to the y and z, the Heisenberg relation based on light diffraction can, according to Vigoureux and Courjon [11], be presented as,

$$\Delta x \, \Delta k_x \geq 2\pi . \qquad 2.4$$

If the field varies rapidly such that Δx is small, then Δk_x will be large and the light is strongly scattered, i.e. a strongly perturbed field is always strongly scattered and diffracted, as discussed by Born and Wolf [12]. Considering values of k on the x-axis, k_x, where

$$k_x = |k| \sin(\theta), \tag{2.5}$$

such that k_x will always be less than $|k|$ and

$$\Delta k_x = 2k_{xMax} \tag{2.6}$$

is the largest range of variation of the propagation vector in the x direction, such that

$$1/\Delta k_x = 1/2k_x, \tag{2.7}$$

then equation 2.4 can be re-written to define the Abbe limit on the x-axis as [11, 12],

$$\Delta x \geq \lambda / 2n \sin(\theta). \tag{2.8}$$

Refractive index values of 3 are not uncommon thus Δx can be a fraction of λ, however, considering the definition of the magnitude of k_x,

$$|k_x| = \sqrt{|k|^2 - k_z^2 - k_y^2}, \tag{2.9}$$

from the Heisenberg Uncertainty relation equation 2.4, Δx can only take small values if Δk_x takes large values. If either k_y or k_z are imaginary, then from equation 2.9, k_x is not limited to values in the range of $|k|$. Therefore Δx may take on small values allowing sub-wavelength resolution as required. This is the classic case, where the remaining two components are required to be real, satisfying equation 2.3.

The Heisenberg Uncertainty Principle has thus shown that an electromagnetic field does indeed vary with distances far smaller than a single wavelength with one proviso, that two of the axes of propagation are bound to the surface of the object in real space by the third complex component.

2.5 The first scanning near-field optical microscope

Experimental work by Pohl *et al.* [13] published in 1984, utilised piezo-positioning technology as developed by Binnig and Rohrer a few years earlier [14,15]. It was shown that by manufacturing a quartz probe coated in thin layers of various metals to completely confine the light, and then approaching the probe to make contact with a flat surface, resulted in a sub-wavelength aperture where the metal layer had been removed. This was then scanned over a line-patterned semi-opaque sample with a 488 nm light source directed through the quartz probe. A photomultiplier tube was used to detect propagating 488 nm light as it emerged through the patterned sample, with a resolution of around 25 nm ($\lambda/20$). Thus was born the first visible wavelength SNOM.

The principles involved utilise the theories outlined in the preceding sections and rely on the interaction of the near-field components with surfaces. As a result of this interaction, the surface itself will generate both near-field and far-field components. The latter of which can then be detected in a far-field arrangement.

In the two decades that have followed, a variety of experimental techniques such as fluorescent resonant energy transfer by groups such as Müller *et al.* [16], atomic force microscopy (AFM) and Raman spectroscopy merged. Equipment setups such as apertureless SNOM (ASNOM), tip enhanced Raman spectroscopy (TERS), and functionalised SNOM probes can achieve optical resolutions of less than 10 nm. It wasn't until around the early 90's that the SNOM became commercialised and therefore generally accessible in the scientific community. This was due to continued work by several groups including Betzig *et al.* [17,18] who worked on the development of shear-

force feedback mechanisms along with metal coated single-mode optical fibres for use with visible light.

2.6 Typical setup of a shear-force SNOM

The typical setup for a SNOM is shown in Figure 2.5.

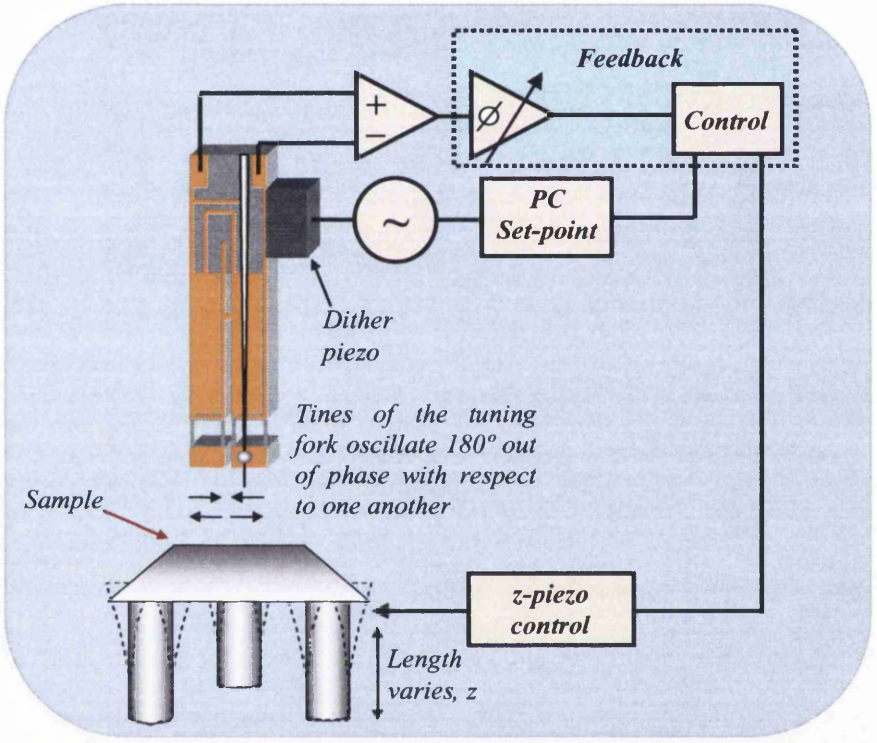

Fig. 2.5 Typical feedback system for maintaining a constant probe-sample distance, achieved through the monitoring of the amplitude of vibration of the tuning fork as a response to the drive frequency.

A metal coated and tapered fibre optic probe with a sub-micron aperture, usually 50-150 nm in diameter, is used to illuminate or collect light from an object in the near-field. This probe is attached to either a tuning fork or a piezo tube-scanner with a sample stage below, that is either scanned using piezo tube-scanners or a fixed stage respectively.

The sample is positioned beneath the probe on the sample stage, which is raised until the surface of the sample is within a few nanometres of the probe. The tuning fork is vibrated by a dither piezo at a set frequency. Shear forces acting on the probe alter the

resonant frequency of the tuning fork to which it is attached. An *ac* electrical signal, generated by the quartz crystal tuning fork in response to the vibrating dither, is fed through an amplifier feedback circuit. This signal is compared to a 'set-point' defined by the operator and an error signal generated to adjust the *z*-piezo to maintain a fixed probe-sample distance through extension or retraction of the sample stage.

Effectively, the system is instructed to maintain a fixed level of damping relative to the free oscillation level that the tuning fork experiences when situated far from the surface. Care however must be taken to not bring the probe too close as damage can rapidly occur as a result; conversely, too little damping results in the probe losing stability of feedback with the surface, resulting in retraction of the probe out of the near-field regime.

2.7 Tuning fork Q-factor

Sweeping the tuning fork through a range of frequencies, including that of its natural resonance, produces a curve as shown in Figure 2.6.

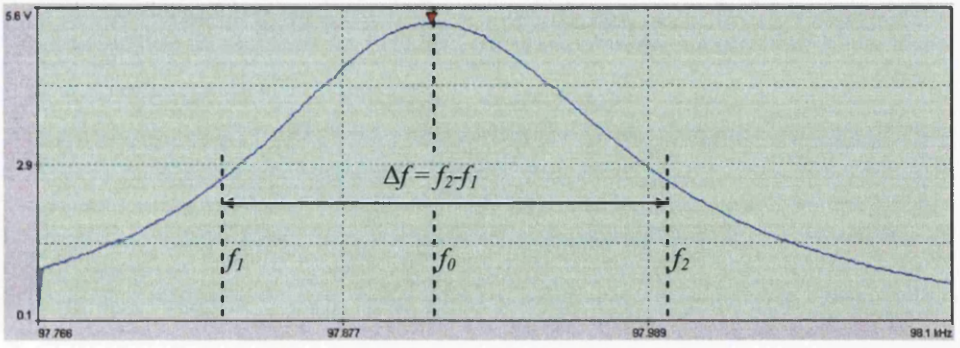

Fig. 2.6 Typical tuning fork response as a function of frequency centred at f_0. The bandwidth of the peak is defined as the full width, at half the peak maximum (FWHM).

The shape of this curve is a function of several aspects of the vibrating system such as the tuning fork, including its dimensions, structural material, and the mass of the

attached SNOM probe. The quality, or Q-factor, is a measure of the sensitivity of change to frequency of the device under test. The higher the Q-factor, the quicker the tuning fork response will drop off for a given set frequency distance from the resonant frequency, f_0. The calculation for Q-factor is defined as,

$$Q = \frac{f_0}{f_2 - f_1}. \qquad 2.10$$

Typical Q-factors for the tuning forks used for this work were of the order of 4500, dropping to ~ 400 with a mounted probe. Q-factors as low as 100 however are still sufficient for use within this experimental setup by careful use of the operating parameters such as scanning speed and feedback controls. Without such considerations, probe to sample contact may occur resulting in damage to the delicate sub-wavelength aperture. As the sample is retracted away from the probe, the shear-force magnitude is lessened and the tuning fork response returns to its predefined oscillation amplitude/phase set-point. Such small changes in sample height are possible by the use of piezo legs mounted beneath the sample that allow it to be moved up to 30 microns or more in the X-Y direction and extend by up to 3 microns in Z. This movement can be considered the fine adjustment for sample manipulation. Larger adjustments are generally achieved by motor driving the entire sample stage including the piezo tube-scanners.

2.8 Characteristics and general manufacture of fibre probes

SNOM is an optical instrument that utilises optical fibres to communicate surface information to a variety of detectors. Single mode optical fibres, after standard manufacture, have a core diameter of about 3-5 μm. This is far greater than the wavelength of visible light. Typically apertures of ~ 100 ± 50 nm are standard for

SNOM probes. To achieve this, single mode fibres are modified by either chemical etching of the end of the probe or by heating while under tension.

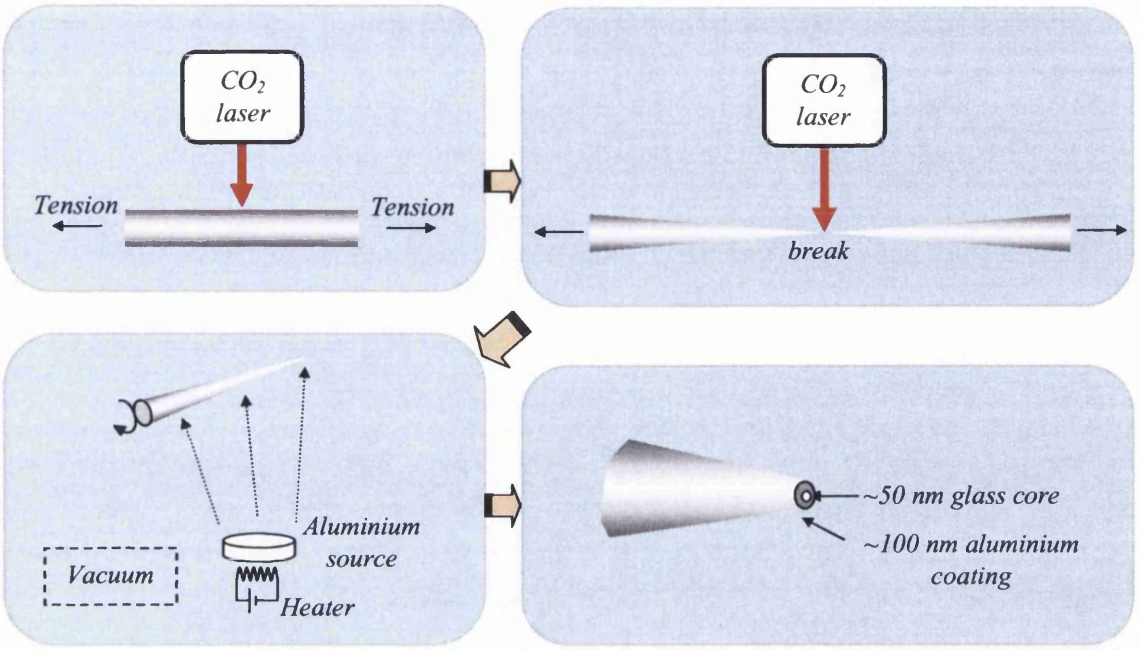

Fig. 2.7 Practical method of manufacture of a fibre-optic probe, by pulling while heating with an intense laser, followed by a final evaporated coating with a suitably opaque coating such as aluminium.

The probes used mainly for the work contained within this thesis were commercially purchased pulled-fibre probes. A glass single mode fibre optic is heated while under controlled tension by a laser to cause it to taper to a point until a break occurs. The tapered probe is then angled and rotated in a vacuum over a pure metal source, typically aluminium or gold, such that all but the very end of the fibre is fully coated with ~100nm thin film. The nano-aperture at the end can be obtained by using focussed ion beam milling which takes planes off the end of the probe until a suitable fibre core diameter of 50-150nm is exposed as shown in Figure 2.7.

Fibre probes are supplied either mounted or un-mounted to a tuning fork/pad assembly as shown in Figure 2.8(a). The Q-factor of a bare tuning fork used on equipment of this type of optical work has a Q-factor of a few thousand, but this value drops to ~ 400 when a fibre probe is attached. A fibre optic probe mounted on a quartz crystal tuning

fork is shown below in Figure 2.8(b). Its position is secured with a small spot of glue so that the metal coated probe barely protrudes from the end of one of the tines.

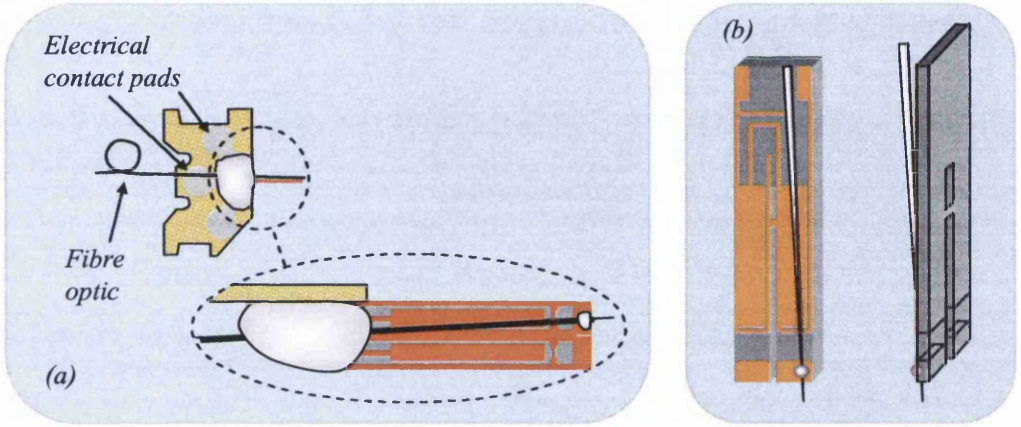

Fig. 2.8 The tuning fork is mounted on a shaped piece of material that can be fitted within the equipment to hold the tip/tuning fork at a specific height/angle above the sample.

2.9 The mechanism of scanning

Figure 2.9 shows a piezoelectric tube-scanner. Such a device can be used for positioning of an electrode with sub-nanometre precision for scanning tunnelling microscopy. The equipment used for the work described in this thesis possessed three such tube scanners that moved in synchrony to position a sample within a few nanometres of a SNOM probe.

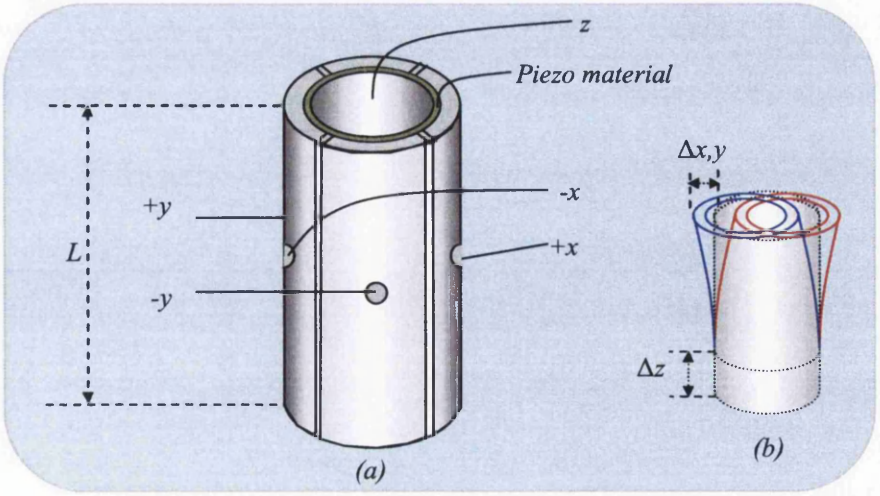

Fig. 2.9 The physical layout of a 'piezo tube scanner' consisting of a cylindrical piece of piezo material, with an inner electrode and 4 electrodes surrounding the outer surface. Placing an electrical field on the sides by assigning opposite potentials for electrode pairs (+x,-x), (+y,-y), allows it to be bent in x and y directions. Applying a potential to all of the outer electrodes relative to the inner electrode causes the tube to extend or contract in length, L.

As illustrated in Figure 2.9(a), by applying a potential to any of the 4 electrodes surrounding the piezo material relative to the inner electrode that lines the entire length of the piezo structure, the tube can be made to bend through extension or contraction; generally opposite potentials are applied to the two sides, $(+x,-x)$, or $(+y,-y)$. Applying the same potential to all 4 electrodes relative to the inner electrode, z, causes the tube to extend or contract in length, L. The overall flexibility is shown in Figure 2.9(b).

The probe is held a few nanometres from the surface of the sample as shown in Figure 2.10.

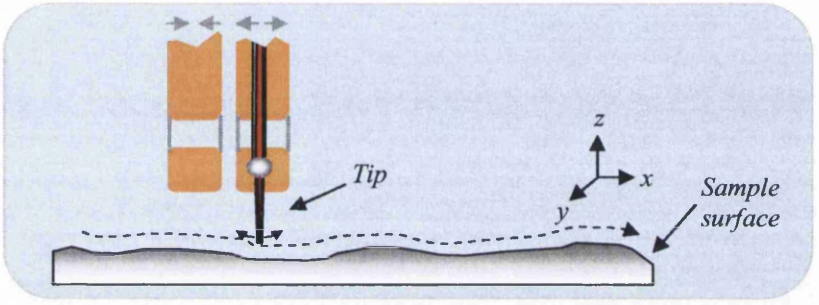

Fig. 2.10 The probe is scanned over the surface while the tuning fork vibrates above. Interactions between the tip and the sample surface dampen the tuning fork response to the dither piezo vibrations resulting in a different electrical response being sent to the feedback electronic circuits.

The feedback circuit monitors the amplitude and phase of the tuning fork in response to the dither drive. The length of the 3 tube-scanner piezos are adjusted simultaneously, maintaining the small but constant probe-sample distance. The length of the piezo tube-scanners are adjusted in conjunction with the potentials applied to the $\pm x$ and $\pm y$ electrodes, used to raster scan the stage beneath the probe.

A complete image is obtained by scanning line by line in a raster-like motion, as shown in Figure 2.11. Such images contain topographic information through conversion of the voltages applied to the 3 piezo tube-scanners required to maintain a set probe-sample distance.

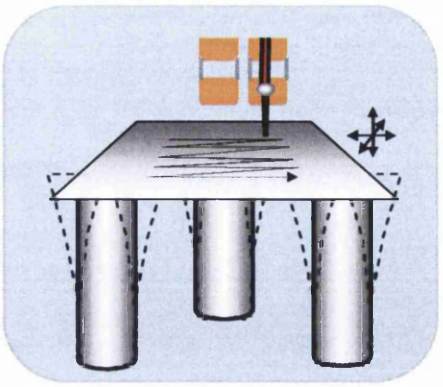

Fig. 2.11 Illustration of the raster scanning method used to gather optical and topographic information from the sample, by simultaneously bending and stretching the 3 piezo tube-scanners.

Under optimum operating conditions, it is possible to achieve very high quality results yielding a wealth of both optical and topographic information.

2.10 The optics of SNOM

When the fibre optic probe is brought in close proximity with the surface it can be used to collect light from an illuminated surface by scattering the evanescent field into the probes' aperture. In much the same way, a light source such as a laser can be coupled into the optical fibre. An evanescent field will thus be present at the aperture, decaying exponentially with increased distance from the fibre probe. As the probe is scanned over the sample surface the evanescent field is scattered to far-field propagating light, as shown in Figure 2.12.

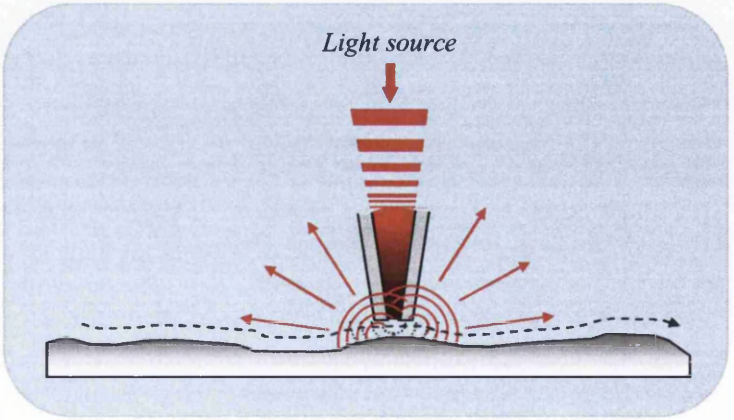

Fig. 2.12 The evanescent field present at the sub-wavelength aperture of the tip is scattered to the far-field due to interactions with the fine structure at the surface of the sample.

There are a number of optical configurations that a SNOM can utilise, with six of the most common illustrated in Figure 2.13. These are mainly a combination of illuminating a sample in the near-field using a fibre optic probe, or from a far-field source. Collection is then either from the far-field, or up the fibre-optic probe. The mode used depends wholly on the aim of the experiment and the nature of the sample. If the sample is opaque then this obviously limits the choice to a geometry utilising reflection, while far-field illumination is not practical for a biological sample containing photosensitive fluorophores that photo-bleach easily.

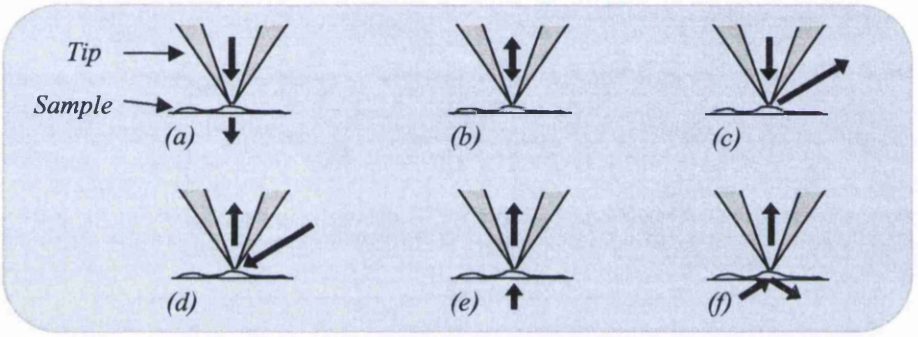

Fig. 2.13 The 6 primary configurations commonly used in SNOM, (a) transmission, (b) illumination, (c) oblique illumination, (d) oblique collection, (e) collection, (f) dark field.

The power of light injected into the fibre optic in configurations Figure 2.13(a-c) is generally of the order of a few mW, resulting in the order of a few hundred nW at the aperture. The reason for the extremely low transmission efficiency, typically 10^{-4}-10^{-7}, is due to the shape of the tapered fibre-optic. This causes back reflections, and heating of the fibre as the light is absorbed by the coating, as discussed by Stahelin *et al.* [19]. It is important to note that at high injection powers, significant damage may result due to a differential thermal expansion between the coating and the fibre. Several hundred degrees Celsius is the typical operating temperature at the end of the SNOM probe, so one must bear in mind the melting point of the coating.

To a first approximation, the aperture is too small for light to exit as a propagating field thus it reflects back up the fibre optic or is absorbed by the metal coating. At the same time it generates an evanescent field, exponentially reducing in magnitude with distance from the aperture. It should be noted that a small amount of propagating light does escape from the probe which can interact with the sample producing a background signal. The intensity of the evanescent field however is far greater than the propagating component of the field, thus light scattered to the far-field from the evanescent region will dominate the detection scheme, provided the aperture dimension remains far below the wavelength of the light source.

2.11 Conclusion

Scanning near-field optical microscopy is a versatile tool that is used to map topographic features and simultaneously obtain optical information far beyond the diffraction limit imposed on conventional microscopic setups. Developments in the field of SNOM have generated a range of ingenious configurations allowing both topographical and optical detection of nano-sized features. Combined with additional spectroscopic equipment, the SNOM is a powerful tool. Its ability to optically stimulate single, localised points, allows longer term studies of samples sensitive to photo-bleaching to be made.

Although no examples have been provided in this chapter, SNOM applications are discussed in some depth within the results sections of the thesis found in Chapters 6 and 7.

References

[1] Zworykin V.K., Hiller J., Snyder R.L., *ASTM Bull.* **117**, 15-23, (1942)

[2] Abbe E., Arch. Mikrosk. Anat. **9**, 413-468, (1873)

[3] Rayleigh, Lord, Phil. Mag. **8,** 261, (1879)

[4] Synge E.H., Phil. Mag. **6**, 356-362, (1928)

[5] Synge E.H., Phil Mag **13**, 297-300, (1932)

[6] Bethe H.A., Phys. Rev. Lett. **66** (7/8), 163, (1944)

[7] Bouwkamp C.J., Philips Res. Rep. **5**, 321, 401, (1950)

[8] Ash E.A. and Nichols G., Nature **237**, 510, (1972)

[9] Wolf E., Nieto-Vesperinas M., J. Opt. Soc. Am. **2**, 886-889, (1985)

[10] Courjon D., Bainier C., Rep. Prog. Phys. **57**, 989-1028, (1994)

[11] Vigourex J.M., Courjon D., Appl. Opt. **31**, 3170-3177, (1992)

[12] Born M., Wolf E., Princ. Of Opt. Oxford Pergamon Press 81-84, (1980)

[13] Pohl D.W., Denk W., Lanz M., Appl. Phys. Lett. **44**, 651-653, (1984)

[14] Binnig G., Rohrer H., Gerber C., Weibel E., Phys. Rev. Lett. **49**, 57, (1982)

[15] Binnig G., Rohrer H., Helv. Phys. Actua, **55**, 726, (1982)

[16] Műller F., Götzinger S., Gaponik N., Weller H., Mlynek J., Benson O., J. Phys. Chem. B **108** (38), 14527-14535, (2004)

[17] Betzig E., Trautman J.K., Harris T.D., Weiner J.S., Kostelak R.L., Science **251**, 1468 (1991)

[18] Betzig E., Trautman J.K., Science **257**, 189 (1992)

[19] Stahelin M., Bopp M.A., Tarrach G., Meixner A.J., Zschokke-Granacher I., Appl. Phys. Lett. **68**, 2603-2605, (1996)

3 Semiconductors and quantum dots

3.1 Introduction

A semiconductor is a solid whose electrical conductivity may be controlled, giving it properties similar to both insulators and conductors. Such control is achieved through electric currents, light and electric fields allowing the construction of a range of electronic devices that can amplify or switch signals, and produce light of a specific intensity and wavelength.

More recently, it has been shown that the properties of semiconductor nano-crystals are such that they exhibit favourable properties for efficient light emission. These properties are based upon quantum confinement and quantum mechanical principles. To fully exploit their development it is important to develop a quantitative understanding of their characteristics.

This chapter introduces some of the background physics that explains observed electrical and optical effects of quantum dots since their conception in the 1980's.

3.2 Bulk semiconductor properties

The conduction and valence bands of a semiconductor material are separated by forbidden energy states as dictated by the periodic crystal structure. The valence band maximum (VBM) is defined as the highest occupied energy level and the conduction band minimum (CBM) is that of the lowest unoccupied energy level. The basic energy band scheme is shown in Figure 3.1. Electrons highest in energy, i.e. at the VBM, are more likely to be excited to energy states at the CBM than those below this level. If an electron is excited to the conduction band, it leaves behind a positive hole, thus forming

an electron-hole pair. The energy band-gap, E_g, is the energy difference between the CBM and the VBM. The electron can then drop from the CBM to the VBM via recombination with a hole, possibly emitting a photon of energy equal to the transition, E_g.

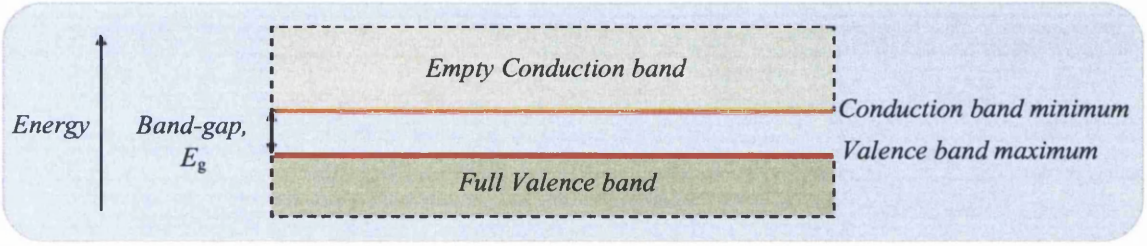

Fig. 3.1 Conduction and valence bands with associated conduction band minimum and valence band maximum. The band-gap is the difference between these two energy states (at T=0 K).

3.2.1 Band-gap transitions of bulk semiconductor materials

Electrons in some semiconductors are excited to the conduction band by a direct process of photon absorption, with no significant change in wavevector k, that specifies the wavenumber and direction of propagation for a wave. This is due to the comparatively small photon momentum, as shown in Figure 3.2(a). The wavevector being the vector representation of the wavelike property of the electron that describes the magnitude and direction of propagation. The electron is promoted to the higher energy state leaving behind a positive charge in the valence band, i.e. the energy of the transition can be stated as,

$$E = \hbar\omega \ . \qquad 3.1$$

However, in some semiconductors, a change in k is required, such that the CBM and the VBM do not fully align, as discussed by Kittel [1]. The electrons and holes can be separated by a larger value of k, shown in Figure 3.2(b).

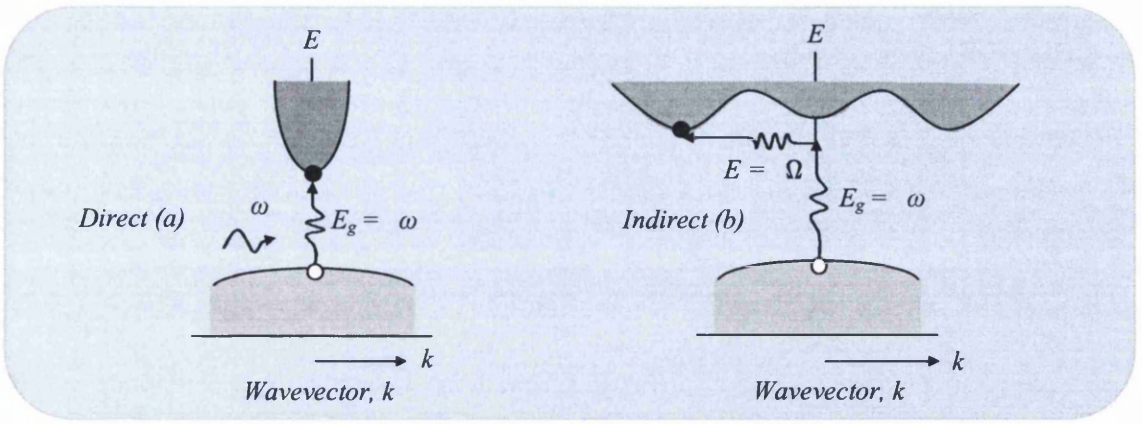

Fig. 3.2 Photon absorption through direct (a) and indirect (b) mechanisms resulting in the promotion of an electron from the VBM to the CBM. The indirect method requires an additional phonon of energy Ω for conservation of k [1].

For such an indirect transition to occur requires an additional phonon of energy $E = \Omega$ such that the total energy is,

$$\hbar\omega = H_g + \hbar\Omega \qquad 3.2$$

The phonon energy required is small, perhaps a few 10's of meV, thus it is possible that the temperature is high enough such that the necessary phonon is already thermally excited within the semiconductor crystal and so the required photon energy for an electron to be excited to the CBM from the VBM is reduced by Ω. An electron excited from the VBM into the conduction band can lose energy to phonons within the crystal lattice hence lowering its energy to, or close to, the CBM.

3.2.2 Excitons within bulk semiconductor materials

Upon excitation of an electron, it is possible that the electron and hole may remain bound as an electron-hole pair, known as an exciton. The electron and hole can be separated by a distance *r*, *of* up to several lattice constants, and their attractive coulomb interaction, *U*(r) is given by,

$$U(r) = -e^2/4\pi\sigma r \qquad 3.3$$

with e the electron charge and ϵ the dielectric constant of the semiconductor material. The exciton can transport energy but not charge within the crystal structure due to its electrical neutrality. Figure 3.3 illustrates exciton absorption for GaAs, demonstrating a peak at lower energy than the band-gap of approximately 1.52 eV.

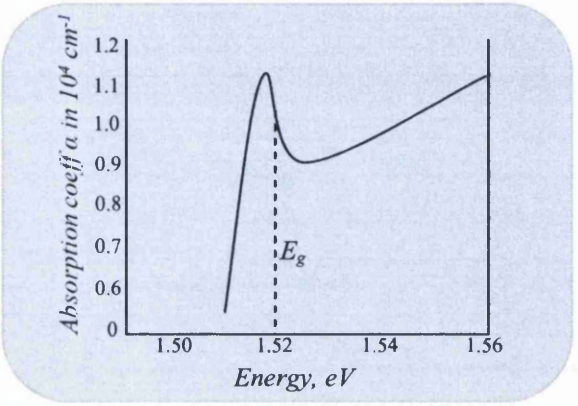

Fig. 3.3 Absorption of GaAs semiconductor material showing excitonic creation below the band-gap energy, E_g at 1.521 eV [1].

The difference between the band-gap energy, E_g, and that required to create an exciton is its binding energy. Multiple exciton energy levels exist below the conduction band as shown in Figure 3.4. The lower the energy level, the more tightly bound the exciton, but this does not generally occur with bulk semiconductors due to lack of confinement, as discussed later in this chapter.

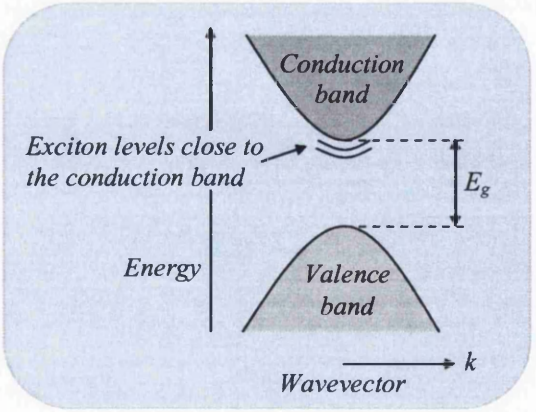

Fig. 3.4 Excitons with energy below the band-gap, E_g, due to their binding energy.

An exciton within a semiconductor periodic structure, separated by a distance r, moving with $\boldsymbol{k}$ is shown in Figure 3.5.

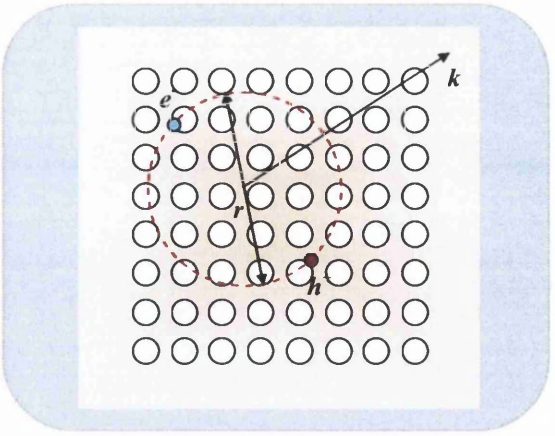

Fig. 3.5 An exciton - bound electron (e^-) and hole (h^+) pair, separated by a distance **r** *moving in periodic semiconductor crystal lattice with wavevector* **k**.

The exciton Bohr radius (EBR), α_B, is defined as the separation r of the electron-hole bound state [2],

$$\alpha_B = \frac{\varepsilon \hbar^2}{\mu_{e,h} e^2}, \qquad 3.4$$

with e the electron charge, $\mu_{e,h}$ the reduced mass of the electron-hole pair, ϵ the dielectric constant of the semiconductor material and , the reduced Planks constant. This is in many ways similar to the Bohr radius of the electron-proton in a ground state hydrogen atom. With such a bound system we can consider the reduced mass $\mu_{e,h}$ of the electron-hole pair. This is given by,

$$\mu_{e,h} = \frac{m_e^* + m_h^*}{m_e^* m_h^*}, \qquad 3.5$$

with m_e^*, m_h^* the effective masses of the electron and hole in the semiconductor respectively.

3.3 Reduced crystal sizes – quantum confinement

Quantum dots, also known as nano-crystals, are considered zero-dimensional particles due to their confinement in 3 dimensions when compared to bulk materials. They are less than 10 nm in diameter and can consist of a few hundred to perhaps a few thousand atoms. Because of this 3 dimensional confinement, the allowed energy states are restricted. Quantum dots have an absorption spectrum extending far into the UV, but emit fluorescence as a function of their size at the energies dictated by the confinement.

3.3.1 Particle in a box

A simplified model approach for calculating the allowed energies for electrons in a quantum dot is to first consider an electron confined within a box having sides of small dimension l_x, l_y, and l_z. The electron of mass m_e may then possess only discrete energies defined by,

$$E_n = \frac{h^2}{8m_e}\left[\left(\frac{n_x}{l_x}\right)^2 + \left(\frac{n_y}{l_y}\right)^2 + \left(\frac{n_z}{l_z}\right)^2\right], \qquad 3.6$$

which can be generalised to,

$$E_n = \frac{h^2}{8ml^2}\sum_{i=1}^{m} n_i^2 . \qquad 3.7$$

Thus, the allowed energies are quantised by n^2 and have a $\frac{1}{l^2}$ dependence, i.e. reducing the size of the box significantly increases the energy of the allowed states.

The density of states, D(E), quantifies how closely packed energy levels are in some physical system. At such extremes of confinement at small dimensions, the density of states reduces, i.e. the energy levels separate far apart, reducing the effective continuous band of bulk material to discrete states. As discussed by Prasad [3], by Pauli's

exclusion principle, these discretely defined energy levels can be occupied by only 2 electrons of opposite spin, and can be expressed as,

$$D(E) \propto \sum_n 2\delta(E - E_n). \qquad 3.8$$

Ideally, the density of states is a series of delta (δ) functions only at discrete energies resulting in sharp emission lines; however these are broadened due to other effects that will be discussed later in this chapter.

3.3.2 Spherical quantum dots

This analogy of confinement in a box can be extended to quantum dots of spherical shape by first defining the wave-function of the state ψ,

$$\psi(r) = R(r)\mathrm{Y}_l^m(\theta,\phi) \qquad 3.9$$

with r the confinement radius, $R(r)$ the solution to spherical Bessel functions of the first kind, and $Y_l^m(\theta,\varphi)$ the spherical harmonics with, θ, ϕ, m and l, two angular coordinates and the magnetic and orbital quantum numbers respectively. Solutions of the radial form of the 1-dimensional Schrödinger equation,

$$\left[-\frac{\hbar^2}{2mr^2}\frac{d}{dr}\left(r^2\frac{d}{dr}\right)+\frac{l(l+1)\hbar^2}{2mr^2}+V(r)\right]R(r) = ER(r) \qquad 3.10$$

with quantum number l, the orbital quantum number, reveal eigen-energies $E(l,n)$, of a particle within a spherical well of radius r, as discussed by Liboff [4], as,

$$E(l,n) = \frac{\hbar^2 z_{ln}^2}{2mr^2}. \qquad 3.11$$

Here z_{ln} is the nth zero of the spherical Bessel function $j_l(z_{ln})$, where $j_l(z_{ln})=0$ is the wave-function as it vanishes at the boundary of the spherically square potential well. The first non-zero solution occurs at $z_{ln} = \pi$. It is clear from Equation 3.11 that energy states again increase as the square of a reduction in radius r, as,

$$E(l,n)=\frac{\hbar^2\pi^2}{2mr^2}. \qquad 3.12$$

We can thus redefine the first energy state transition of the quantum dot for the lowest electron and hole 1s states by accounting for confinement as an adjustment of the bulk crystal energy gap E_g and for the reduced mass, $\mu_{e,h}$ from Equation 3.4 [2],

$$E_{1s1s} = E_g + \frac{\hbar^2\pi^2}{2\mu_{e,h}r^2}. \qquad 3.13$$

3.4 Electron-hole Coulomb interaction in quantum dots

An electron-hole pair confined within a quantum dot will experience a Coulomb interaction (Equation 3.3) as the radius r of the quantum dot is reduced below the exciton Bohr radius, α_B, given in Equation 3.4. This is known as the strong confinement limit, where $r \ll \alpha_B$. As discussed by Prasad [3], Javier *et al.* [5] and Efros and Efros [6], this interaction becomes significant, in contrast to the zero Coulomb energy of a free electron-hole pair within the bulk. Brus [7] accounted for this interaction for a CdSe quantum dot and calculated a further adjustment to the lowest electron and hole 1s energy state transition as a function of quantum dot radius r. This energy is given by,

$$E_{1s1s} = E_g + \underbrace{\frac{\hbar^2\pi^2}{2\mu_{e,h}r^2}}_{Confinement} \underbrace{-1.786\frac{e^2}{\varepsilon r}}_{Coulombic} + Further\ perturbations \qquad 3.14$$

with the 3rd term in Equation 3.14 is the transition energy adjustment due to the effective electron / hole Coulomb interaction.

Typical absorbance and fluorescent emission of CdSe quantum dots as a function of their diameter are shown in Figure 3.6, from reference [5]. Increased confinement of the exciton due to reduced size of the quantum dot further separates the allowed energy states within the quantum dot. An important aspect of the absorption of quantum dots is their long absorption into the UV allowing multiplexed excitation of different quantum dots, as discussed later in Chapter 7.

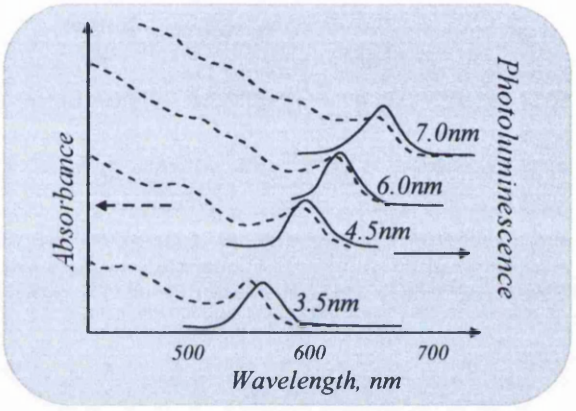

Fig. 3.6 This figure illustrates the increase in emission wavelength, and an increase in the absorption band, as a result of increasing CdSe quantum dot size. (Adapted from Javier et al. [5].)

3.5 Quantum numbers and allowed transitions in CdSe quantum dots

For CdSe quantum dots, a simple two band isotropic effective mass model to approximate the bulk valence and conduction bands shows the first excited state can be expressed as $1S_h1S_e$ where the electron and hole are in the n_e=1 and n_h=1 *S*-like envelope function respectively. Selection rules allow optical transitions coupling electron and hole states having the same quantum numbers as illustrated in Figure 3.7 [2]. This figure illustrates the first few, lowest energy exciton states.

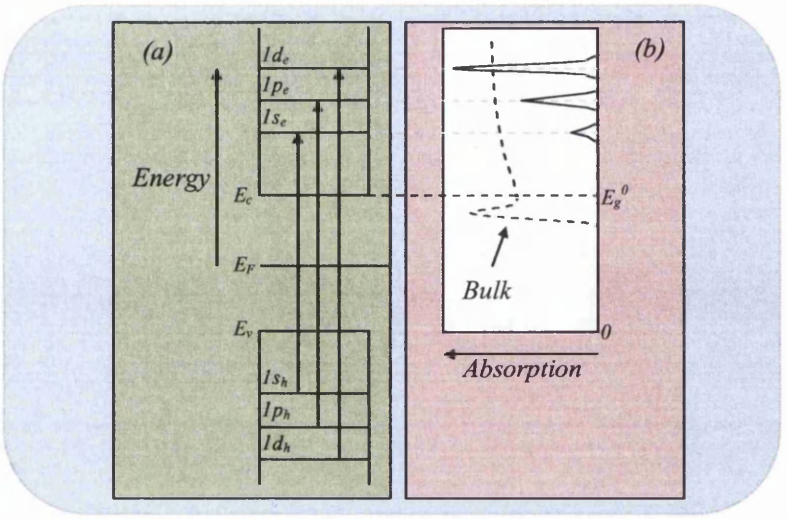

Fig. 3.7 Simplified optical properties of an ideal spherical quantum dot with scalar effective masses of non-interacting electrons and holes for the first few, lowest energy transitions. (a) Illustrates the quantised states inherent for a particle in a spherical box surrounded by an infinite barrier. (b) Represents the resultant optical absorption spectrum reduced from bulk to discrete energy bands. (Adapted from [2].)

This however is not complete as there is further degeneracy due to spin-orbit coupling, thus total unit cell angular momentum $J=l+s$ must be accounted for, where l is the orbital quantum number ($0 \leq l \leq n-1$) and s is the spin quantum number ($\pm\frac{1}{2}$). Within a zinc-blende structure such as CdSe, the valence band arises from p-orbitals. Its 6-fold degeneracy results in a 4-fold degenerate $p_{3/2}$ band and a 2-fold degenerate $p_{1/2}$ band, where J has the value of $3/2$ or $1/2$.

Norris and Bawendi [8] discussed the effects on the allowed quantum dot hole states and determined that the hole is affected by valence band mixing. Only parity and total hole angular momentum F are good quantum numbers to consider for the hole envelope function, where $F=L_h+J$. L_h and J are not conserved, where L_h is the angular momentum of the hole. Holes in quantum dots have contributions from L_h and L_h+2 spherical harmonics, the total of which is denoted as L_F. In addition there are contributions from heavy-hole, light-hole and valence sub-bands, due to degeneracy of the p-type orbitals. The hole envelope function can be labelled as $n_hL_F = 1S_{3/2}$.

Meanwhile, the electron is unaffected by the valence band mixing and so is labelled as $n_eL_e = 1S_{1/2}$. Thus, the first excited pair state is labelled as $1S_{3/2}1S_{1/2}$, often written as $1S_{3/2}1S_e$.

Photo-luminescent excitation (PLE) measurements were carried out at low temperature on various sized CdSe quantum dots by Norris *et al.* [8]. Their experiments noted the range of exciton emission peaks for different excitation energies. The most intense transition, $1S_{3/2}$-$1S_{1/2}$, was observed to be at the lowest energy confirming the above theory. The next most intense transition was $1P_{3/2}$-$1P_e$, although it was noted that the $1S_{1/2}$-$1S_e$ transition was present between these two transition energies at a significantly lower intensity. This implies the $1S_{1/2}$-$1S_e$ transition has a lower probability due to the poor overlap of the mostly *D*-like $1S_{1/2}$ with $1S_e$ orbitals for larger quantum dot sizes. It was found however that with decreasing dot size, the $1S_{1/2}$ orbital became more *S*-like due to mixing with the $2S_{1/2}$ orbital resulting in an increased intensity of the $1S_{1/2}$-$1S_e$ transition.

3.6 Methods of quantum dot manufacture

There are two distinct ways to manufacture quantum dots, the advantages of which depend on their eventual use. The first is by molecular beam epitaxy (MBE) [9,10] where layers of different materials are evaporated onto a substrate and clustering of atoms occurs resulting in nano-dimensional crystalline structures at the surface. The second method is by pyrolysis of organo-metallic reagents that provide the required growth medium in which nano-crystallites may form over a period of time under the correct temperature and pressure conditions.

3.6.1 Molecular beam epitaxy

MBE is a vital tool in the development of nano-scaled materials. It allows one to control the growth of a material with a high level of precision. This is achieved by the use of directional, ultra-low dense beams of atoms (or molecules) directed at a substrate under ultra-high vacuum (UHV) conditions. If the parameters such as temperature, vapour density, and substrate surface are correct, then these atoms will adhere to the surface, forming layers. Given the correct choice of materials, clusters can form atom by atom, commonly known as self-assembled quantum dots. This nano-grouping of atoms has been attributed to an intrinsic elastic strain field which arises due to a lattice mismatch at the substrate surface. For instance, GaAs and InAs are common combinations of semiconductor for self-assembled quantum dots.

This idea of nano-island formation was first proposed in 1938 by Stranski and Krastanow [11] and has been studied intensely for several decades in work involving quantum dots embedded in light emitting diode (LED) structures [12]. For example, island growth of InAs may be carried out on a material such as semi-insulating GaAs substrates by using MBE [13]. The thickness of such clusters can be controlled to sub-nanometre precision. Once the desired cluster dimensions are achieved, the atomic source is removed and replaced with one of a different material thus 'capping' the quantum dots. This capping is important in at least two respects. Firstly it protects the quantum dots from damage through oxidation with the air upon completion of growth and also contamination from impurities. Secondly, it alters the electronic properties of the quantum dot by removing unwanted surface states enhancing the overall optical properties [14].

3.6.2 Solvent synthesis

Murray *et al.* [15] devised a method to manufacture quantum dots in a solution. The benefit of this route of growth is that the quantum dots are near-spherically shaped. The process involves the combining of reagents such as Me_2Cd in Tri-n-octylphosphine (TOP) 25:1ml and 1.0M Trioctylphosphine-selenide (TOPSe) in TOP 10:15ml to 50g of Tri-n-octylphosphine oxide (TOPO) in a reaction flask at 300°C in Argon gas at 1 atmosphere. Maintaining the temperature of the reaction flask at 230-260°C results in colloidal crystalline CdSe nano-crystals. The growth can be monitored by observation of the solution's absorption and emission spectra. Growth can be temporarily paused by dropping the temperature, at which time, size selective samples of the material can be removed from the reaction vessel. The solution containing the quantum dots and other chemical remnants from the growth process are then separated with the aid of a centrifuge. The centrifuge is then repeatedly used to narrow the size range of quantum dots present within the sample until no further sharpening of the optical absorption is observed. The result of this long process is nearly mono-disperse <5% size variation of the nano-crystals. These nano-crystals may then be dispersed in a number of solvents for further study. They are reported by Murray *et al.* [15] to be slightly prolate with an aspect ratio of 1.1-1.3.

This work has been progressed by many groups since the early 1980's by the growth of a shell of differing material surrounding the quantum dot core structure, analogous to 'capping' with self-assembled quantum dots via the MBE growth method. This outer shell is ideally made with a larger band-gap material, thereby enhancing the confinement of the exciton. This is discussed further in Section 3.7.4. A calculation

that gives an estimate of the number of CdSe/ZnS core/shell quantum dots in a known material mass can be found in Appendix 1.

3.7 Structural effects on quantum dots

3.7.1 Surface states

Quantum dots by themselves are not particularly structurally stable as they are likely to either bond with adjacent quantum dots or break down. Another issue is that surface atoms have a crystalline structure different to the central core atoms. This is due to a lack of nearest neighbours with which surface atoms can bond. In the case of CdSe core quantum dots, the surface atoms adjust their position, minimising their energy, with bond lengths being smaller by up to 3.29% compared with the bulk material. This is due to the restructuring of the anions that move out of the surface and cations that move inward towards the core, as calculated by Watari *et al.* [16]. This results in an approximate 4% drop in lattice constant for the surface material. The effect this has on the electronic nature of the quantum dot as a whole is the generation of trap states at energies possibly within the energy gap region defined by the confinement from Equation 3.14. Such surface states provide mechanisms to trap excited carriers allowing non-radiative recombination for further absorbed photons, as discussed by Steigerwald and Brus [17].

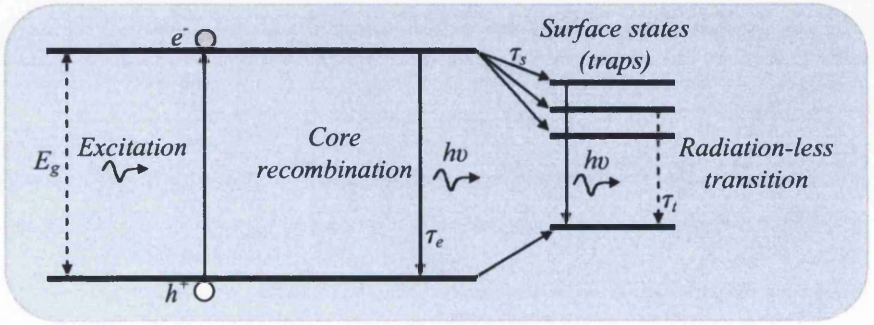

Fig. 3.8 Without a capping layer, surface states originating from free atomic bonds are present within the energy-gap region. (Adapted from [18].)

Figure 3.8 illustrates the excitation of an electron and subsequent recombination. In addition, it shows an alternative recombination route via surface states that trap the electron and/or hole within the band-gap. Recombination can then either be radiative with a lower energy photon or via non-radiative relaxation.

Spanhel *et al.* [18] show how energy states within the band-gap, originating from surface states, efficiently bridge the valence and conduction bands resulting in efficient radiationless relaxation. This mechanism of trapping and radiationless recombination applies equally to both growth types of quantum dots.

3.7.2 Deep traps

Queisser and Haller [19] and Efros and Rosen [20] state impurity atoms can cause structural defects in the crystal lattice. Such distortions can reach several lattice constants in size and generate additional energy states deep within the energy gap defined by Equation 3.14, as with surface states. In the case of an exciton within a colloidal quantum dot, an electron (hole) caught within this trap cannot recombine with the associated hole (electron). Thus, the quantum dot has entered a 'dark-state'. The trapped carrier will eventually non-radiatively recombine. Efros and Rosen [20] give the trap lifetime, τ_{trap} as a function of temperature, T, as,

$$\tau_{trap} = \tau_{ph} \exp\left(\frac{E_{trap}}{kT}\right), \qquad 3.15$$

where τ_{ph} is the phonon scattering time, and E_{trap} the trap potential depth. From Equation 3.15 it can be seen that the lower the temperature, the longer the carrier can remain trapped within the defect potential. The number of deep traps is of course dependent on the purity of both the materials used and the process of manufacturing.

Norris *et al.* [8] state that deep trap emission is dependent on quantum dot size. They found the frequency of deep trap emission negligible in their largest dots of diameter 5.3 nm but found this slowly increases with decreasing size, becoming significant with the smallest size samples having a diameter of 1.2 nm. The reason for this size dependence can be attributed to the defect number to volume ratio. As the size is reduced, there is a greater probability that the exciton will always be close to any trap within the small volume.

3.7.3 Auger processes

As discussed by Javier and Strouse [21], a quantum dot can be in a temporary dark state whereby the electron has been excited and trapped at the surface leaving the core in a positively charged state, unable to recombine. Further photon absorption either excites this initial exciton, or a second exciton forms within the quantum dot. This then leads to one of several possible outcomes. The first being auto-ionisation of the neutral quantum dot due to one of the carriers being ejected by a 3-body Auger process, shown in Figure 3.9(a).

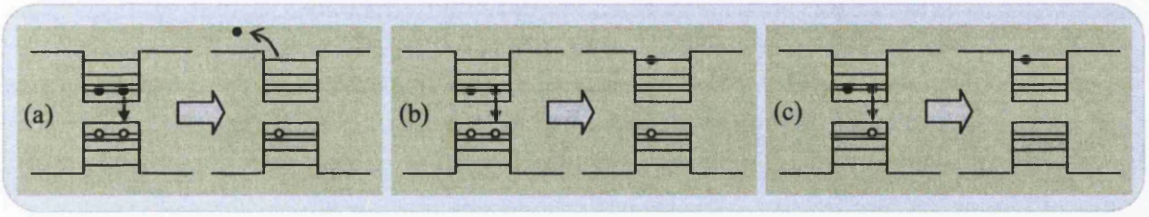

Fig. 3.9 Three types of Auger processes involving bi-excitons whereby one recombines resulting in either (a) autoionisation of a neutral quantum dot, with eventual carrier absorption and recombination, (b) exciton being further excited followed by radiative recombination (Auger relaxation of a biexciton in a neutral dot), and (c) Auger relaxation of an already ionised quantum dot being excited and eventually relaxing but unable to recombine resulting in extinction. (Adapted from Brokmann et al. [22].)

The ionised quantum dot remains in a dark state waiting for a donated carrier from a neighbouring quantum dot or the original ejected carrier to return in order to neutralise it. A second route for non-radiative recombination Figure 3.9(b) is by the energy from

exciton recombination in a biexcitonic state promoting the electron from the other exciton which subsequently relaxes to its previous state. The third Auger process which might occur, shown in Figure 3.9(c), shows an electron in an already ionised state entering an excited state, which can then non-radiatively relax through internal losses (not shown).

From work by Brokmann *et al.* [22], CdSe/ZnS core/shell quantum dots are shown to exhibit single-photon emission due to Auger processes. In their work [22], time gated photon counters were used with pulsed laser excitation having a pulse length of 50 ps, and a pulse repetition period of 100 ns to avoid two-photon emission. The radiative lifetime of a single exciton was determined to be 20 ns. This compares well with previous work by Lounis *et al.* [23] and Klimov *et al.* [24], who also experimentally established a mean lifetime of 22 ±1 ns with little or no coincidences of recombination. This verifies that non-radiative Auger processes are dominant when more than one exciton exists within a CdSe quantum dot.

Auger processes within quantum dots are theoretically discussed in detail by Chepic *et al.* [25]. The processes are described such that a quantum dot, possessing a single delocalised hole or electron, absorbs a photon and relaxes non-radiatively. This process is preferred as it has a substantially shorter lifetime, of the order of 100 ps, compared to the 20 ns radiative recombination rate of the exciton, shown experimentally and theoretically by Achermann *et al.* [26] and Wang *et al.* [27]. Essentially, while a colloidal quantum dot possesses an exciton, further photonic absorption results in non-radiative recombination.

3.7.4 Core/shell necessity

It is common for both self assembled and colloidal quantum dots to be manufactured with a protective shell surrounding the core. Generally, a shell of a semiconductor material possessing a larger band-gap than the core material is used to aid in the exciton confinement.

Protective shells typically a few Angstroms thick, known as capping layers with self assembled quantum dots, also help protect the delicate crystalline structured core from degradation, as discussed by Peng *et al.* [28]. Bowen-Katari *et al.* [29] have shown that the absence of capping layers for CdSe nano-crystals, prepared with a solution of TOPO (tri-n-octylphosphine oxide), results in the TOPO bonding with the cadmium surface atoms. The selenium atoms however are left open to oxidation, causing the degradation of the quantum dot with time.

The passivating shell, if it is crystalline in nature such as ZnS on a CdSe core, requires a close match of the lattice constants of the two materials, else growth of the shell might be impossible. Mismatched lattice constants could also reduce the level of passivation at the core surface resulting in further trap states at the core/shell interface. Sometimes a two shell approach such as CdS in the CdSe/ZnS core/shell system is used, whereby a material possessing a lattice constant between those of the core and outer shell acts as a graded layer. According to constants from the Handbook of Chemistry and Physics [30], CdSe has a lattice constant of 0.605 nm while ZnS is only 0.541 nm. This is quite a large lattice mismatch of 11.2%, but it has been experimentally shown by Hines and Guyot-Sionnest [31], that 2 to 3 monolayers of ZnS around the core material enhances the electron confinement to the core. This greatly improves the efficiency of the

quantum dot by removing dangling bonds present at the core surface that generate surface states. It also reduces the presence of impurities at the core surface that can cause deep traps as discussed in section 3.7.2.

Simulations of electron and hole wave-functions of single CdSe/CdS quantum dots by Peng *et al.* [28] showed that an electron in an excited state is delocalised throughout the core/shell structure while the hole is confined to the core material. It was found that without a protective shell present around the core, there was a greater probability that the electron could become trapped by improperly bound cadmium atoms at the surface. The protective shell does not have to be crystalline in nature. It is possible to passivate the surface structure with amine groups such as Hexadecylamine (HDA) but these don't help improve the confinement of the electron to the shell.

The term quantum yield is essentially the probability of detecting a photon for a given excitation. As shown by Danek *et al.* [32] and Empedocles *et al.* [33], the quantum yield of an ensemble of CdSe quantum dot cores at room temperature can be as low as 10% for uncapped cores compared to as much as 50% when having a protective shell of inorganic material having a wider band-gap.

3.8 Spectral properties of quantum dots

As discussed previously in section 3.3, quantum dots fluoresce at a peak wavelength as a function of their size. As the size of the dot is reduced, electron confinement increases, resulting in larger transition energy for the lowest energy exciton. For colloidal quantum dots, after size filtering processes have been applied, the size distribution of the resulting quantum dot ensemble can be as small as 5%, as shown for

solvent synthesis experiments by Murray *et al.* [15] and Empedocles *et al.* [33]. Size variation contributes to the spectral broadening of an ensemble of dots. A spectral full width at half maximum (FWHM) of 50 nm is typical. This value however, is dependent on the semiconductor material used. Further effects that result in broadening of the emission are due to Stark shift, temperature and environment.

3.8.1 Stark shift

The Stark effect, named after its discoverer Johannes Stark, is due to the splitting and shift of a spectral line emission from an atom or molecule into several components when in the presence of an electric field. This is due to an interaction between the electric field and the charge distribution of an atom or molecule.

The Stark effect when applied at the nano-scale is known as the quantum confined Stark effect (QCSE). The effect of electric fields on excitons in quantum well structures is discussed in detail by Miller *et al.* [34]. They describe how electrons and holes are attracted to opposite sides of the layered structure creating the quantum well, reducing the electron-hole energy giving a Stark shift in the absorption band.

Seufert *et al.* [35] studied single self-assembled CdSe quantum dots with a ZnSe cap using a far-field 488 nm light source. The emitted photoluminescence (PL) was collected with an integration time of 10 seconds per spectrum over the period of an hour. Multiple spectra showed a randomly centred peak of PL emission with time. A strong correlation was found between a reduction of intensity in the peak energy in the spectra with a simultaneous red-shift. This was explained due to the presence of an electric field induced by fluctuating charges in the vicinity of the quantum dot. This

caused a change in the spatial separation between the electron and hole and thus a decrease in energy of the 1st excitation of the quantum dot as discussed by Miller *et al.* [34]. Empedocles and Bawendi [36] show that red-shifts of a few meV from a colloidal quantum dot are possible due to the presence of a single electron within a distance of 10 nm, possibly residing within the surrounding media. Seufert *et al.* [35] also note that excitation densities below 200 Wcm^{-2} produced little or no spectral shift, but as this was increased to 6 $kWcm^{-2}$, spectral shifting also increased up to 3.5 meV. This was explained to be due to carriers predominantly being captured within the self-assembled quantum dot, while at higher power densities, excess carriers become trapped in defect states, in or near the quantum dot, in agreement with Empedocles and Bawendi [36] and Neuhauser *et al.* [37]. This causes alterations in the local electric field resulting in a transient Stark shift of exciton recombination within the self-assembled quantum dot.

3.8.2 Thermal broadening

Spectral broadening for emissions from a quantum well is partly due to thermal broadening and from non-uniformity of the structural interfaces, possibly as a result of impurities. With quantum dots, carriers can only be excited up to one of several discretely defined levels, more than an order of magnitude greater than achievable due to room temperature induced phonons ($kT_{RT} \sim 26$ meV). Thus experiments are often carried out on quantum dots at cryogenic temperatures, < 40 K, minimising thermal broadening of the emission line.

Arzberger and Amann [38] show that spectral emissions from quantum dots at cryogenic temperatures are in fact Lorentzian in shape, however, due to thermal broadening the line shape becomes Gaussian in nature. Such effects can be modelled by

using Voigt functions that are comprised of both Gaussian and Lorentzian functions, making it possible to achieve the correct spectral line shape. Thermal broadening was also observed by Empedocles and Bawendi [39] who conducted experiments on colloidal CdSe quantum dots at a range of temperatures below 40 K. Ultra-low concentrations of these dots were mixed with polymethyl-methacrylate (PMMA) and immobilised in a thin film, spin coated on a crystalline quartz substrate. Using a 514 nm laser at an excitation power of 200 W/cm^2, emission spectra of single dots were recorded with a CCD. 150 successive spectra, each with an integration time of 0.1 second, showed spectral diffusion. This was attributed to changing local electric fields resulting from charges on the surface of the quantum dot i.e. a Stark shift as discussed previously. It was found that the minimum line-width was 0.4 meV. The minimum line-width however was shown to increase to several meV with increased temperature at 40 K, becoming the dominant broadening factor at room temperature, with spectral widths of the order of 50 to 60 meV.

Further room temperature studies have been carried out by Seufert *et al.* [35], Gómez *et al.* [40] and Neuhauser *et al.* [37] highlighting significantly broad spectra from quantum dots compared to cryogenic temperatures [39]. Studies by Gómez *et al.* [40] involved far-field illumination of single CdSe/CdS/ZnS and CdSe/ZnS quantum dots. These were immobilised in a variety of polymers, such as PVP (poly-N-vinylpyrrolidone), PS (polystyrene), PMMA, and PVA (polyvinylalcohol) spin coated onto cover-slips. The quantum dots were imaged and spectrally detected using a laser scanning confocal microscopic setup. The excitation wavelength used was 488 nm and spectra were acquired with an integration time of 3 seconds. Their large data set obtained at room temperature shows spectral line-widths of between 50 and 60 meV at a maximum peak

at 2.019 eV, in good agreement with Empedocles *et al.* [39]. Successive collections showed spectral shifting of up to 3.7 meV for single quantum dots at room temperature. This compares well with work by Seufert *et al.* [35] who detected spectral shifts up to 3.5 meV in experiments conducted at only 2 K. It can thus be seen that temperature has little or no effect on the magnitude of spectral diffusion, which itself is caused due to changes in the electronic configuration of the quantum dot.

3.8.3 Fluorescent intermittency (Blinking)

An important aspect of quantum dots is that of fluorescence intermittency, commonly referred to as blinking. Observations have shown these intermittent processes to be highly complex in nature. A quantum dot can absorb a photon of energy approximately equal to, or greater than that of the first excitation energy transition, as given by Equation 3.14 for CdSe quantum dots. Due to the size of the quantum dot being smaller that the exciton Bohr radius, the generated exciton is tightly confined within the quantum dot. The electron moves close to, or finds itself at the surface of the core material, leaving behind a charged core as discussed by Javier and Strouse [21]. At this point, the electron can decay, radiatively recombine, or remain trapped in a surface state or a deep trap. An electron trapped at a surface site remains in this dark state for an extended time as discussed in section 3.7.2, deep traps states. The duration of the dark state can be of the order of nano-seconds to minutes, or even hours, dependent on the depth of energy of the trap state. Equation 3.15 shows that the duration of a dark state is a function of an inverse exponential of temperature. Thus, at cryogenic temperatures, non-coated quantum dots might spend much of their time in deep traps or surface states. This problem of trap states can be reduced significantly by the use of a passivation layer

as described in section 3.7.4. Thus, dangling bonds are removed from the core surface, maintaining a high purity of material during quantum dot manufacture.

Gómez *et al.* [40], who carried out far-field illumination of single quantum dots embedded in a variety of different polymer materials, found that blinking events due to trapping processes were followed immediately by spectral shifts of up to 3.7 meV at room temperature. Javier and Strouse [21], Shimizu *et al.* [41], Brokmann *et al.* [22], and Klimov [42] show how the energy from further excitations does not contribute to radiative recombination but is redistributed internally by Auger processes. This is because of the significantly shorter, pico-second lifetime of this further excitation compared to the typical lifetime of nano-seconds of a single exciton through radiative recombination. This is discussed in detail in section 3.7.3.

Shimizu *et al.* [41], Isaac *et al.* [43], and Brokmann *et al.* [22] to name but a few, have shown experimentally that the frequency of the occurrence of quantum dot dark states is related to the intensity of absorbed photons, as well as thermal effects. At low intensity, an exciton is formed within the quantum dot and can, assuming conditions are right, radiatively recombine. But, if the exciton absorbs another photon directly or indirectly by a 3-body Auger process such as that shown in Figure 3.9(b), this second photon is lost and the quantum dot can be said to have been in a dark state. Surface states and deep traps aside, a quantum dot is effectively only able to absorb and emit photons at the rate determined by the decay lifetime of the radiative transition, if it is to contribute fluorescence as a function of excitation intensity. Any further absorption will contribute instead to non-radiative decay and thus a reduction in brightness of the dot or the ensemble.

3.9 Conclusion

Quantum dots possess attributes that allow them to be used in a variety of subjects. Their small size and well defined spectral properties, makes them ideal for incorporating into a range of materials and structures. A variety of important properties of quantum dots have been highlighted which illustrate the beauty, and yet, the utter complexity of semiconductor material crystals at such a small scale. Studies have shown how quantum dots are not limited to just semiconductor materials, but may also consist of small numbers of gold atoms for instance. They are not limited to cryogenic experiments, but instead, are perhaps more effective at room temperature due to positive contributions of thermal effects. The main points affecting quantum dot fluorescence at both cryogenic and room temperatures are illustrated in Figure 3.10.

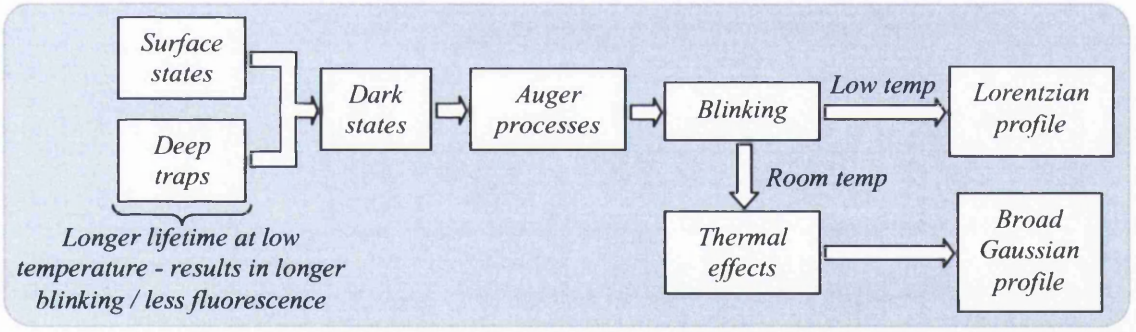

Fig. 3.10 Illustration highlighting the main points that affect quantum dot fluorescent emission at low, and room temperature.

Many potential roles exist for quantum dots such as, improving the output efficiency of light emitting diodes and anti-counterfeiting inks, with recent interest in the development of quantum dot lasers.

Growing scientific practical uses are in the biological tagging of genetic material in lieu of standard organic fluorophores that have a tendency to photo-bleach and also possess a low quantum yield. Fluorescent emissions from organic fluorophores are very broad, typically the order of 80-100 nm, with long emission tails into the red [44], therefore not

many dyes may be used simultaneously within one sample. They also require excitation sources with a wavelength close to that at which they fluoresce, whereas quantum dots have extended absorption bands far into the UV.

As future studies of quantum dots progress, our understanding of their quantum nature grows, opening up avenues of applications and research to which they may be applied.

References

[1] Kittel C., Introduction to solid state physics, 7th Ed. Wiley, (1996)

[2] Gaponenko S.V., Optical properties of semiconductor nanocrystals, Camb', (1998)

[3] Prasad P.N., Nanophotonics. Wiley, (2004)

[4] Liboff R.L., Phys. Rev. A **43**, 115765, (1991)

[5] Javier A., Yun C.S., Sorena J., Strouse G.F., J. Phys. Chem. B **107**, 435-442, (2003)

[6] Efros A.I.L., Efros A.L., Sov. Phys. Semicond. 16, 772, (1982)

[7] Brus L.E., J. Chem. Phys. **80** (9), 4403-4409, (1984)

[8] Norris D.J., Bawendi M.G., Phys. Rev. B **53** (24), (1996)

[9] Shen M.Y., Goto T., Kurtz E., Zhu Z., Yao T., J. Phys. Cond. Matt. **10**, L171-L176, (1998)

[10] Young-Jun Y., In-Taek J., Jong-Chun W., Jhe W., Appl. Phys. Lett. **87**, 143108, (2005)

[11] Stranski I.N., Krastanow L., Akad. Wiss. Wien Kl. Iib **146**, 797, (1938)

[12] Zinoni C., Alloing B., Paranthoen C., Fiore A., Appl. Phys. Lett. **85**, 2178, (2004)

[13] Ledentsov N.N., Springer Tracts in Modern Physics **156** (Berlin), (1999)

[14] Louie S.G., Chelikowsky J.R., Cohen M.L., J. of Vac. Sci. and Tech. **13** (4), 790-797, (1976)

[15] Murray C.B., Norris D.J., Bawendi M.G. J. Am. Chem. Soc. **115**, 8706-8715, (1993)

[16] Watari K., Alves J.L.A., Ferraz A.C., Braz. J. of Phys. **26** (1), (1996)

[17] Steigerwald M.L., Brus L.E., Acc. Chem. Res. **23**, 183-188, (1990)

[18] Spanhel L., Haase M., Weller H., Henglein A., J. Am. Chem. Soc. **109**, 5649-5655, (1987)

[19] Queisser H.J., Haller E.E., Science **281** (5379), 945-950, (1998)

[20] Efros A.L., Rosen M., Phys. Rev. Lett. **78** (6), 1110-1113, (1997)

[21] Javier A., Strouse G.F., Chem. Phys. Lett. **391**, 60-63, (2004)

[22] Brokmann X., Messin G., Desbiolles P., Giacobino E., Dahan M., Hermier J.P., New J. of Phys. **6** (99), (2004)

[23] Lounis B., Bechtel H.A., Gerion D., Alivisatos P., Moerner W.E., Chem. Phys. Lett. **329**, 399, (2000)

[24] Klimov V.I., Mikhailovsky A.A., McBranch D.W., Leatherdale C.A., Bawendi M.G., Science **287** (5455), 1011-1013, (2000)

[25] Chepic D.I., Efros A.L., Ekimov A.I., Vanov M.G., Kharchenko V.A., Kudriavtsev I.A., Yazeva T.V., J. Lumin. **47**, 113, (1990)

[26] Achermann M., Hollingsworth J.A., Klimov V.I., Phys. Rev. B **68**, 245302, (2003)

[27] Wang L.W., Califano M., Zunger A., Franceschetti A., Phys. Rev. Lett. **91**, 056404, (2003)

[28] Peng X., Schlamp M.C., Kadavanich A.V., Alivisatos A.P., J. Am. Chem. Soc. **119**, 7019-7029, (1997)

[29] Bowen-Katara J.E., Colvin V.L., Alivistos A.P., J. Phys. Chem. **98**, 4109-4117, (1994)

[30] Handbook of Chemistry and Physics, 64th Ed. CRC Press. (1983-1984)

[31] Hines M.A., Guyot-Sionnest P., J. Phys. Chem. **100**, 468-471, (1996)

[32] Danek M., Jenson K.F., Murray C.B., Bawendi M.G., Chem. Mater. **8**, 173-180, (1996)

[33] Empedocles S.A., Norris D.J., Bawendi M.G., Phys. Rev. Lett. **77** (18), 3873-3876, (1996)

[34] Miller D.A.B., Chemla D.S., Damen T.C., Gossard A.C., Wiegmann W., Wood T.H., Burrus C.A., Phys. Rev. Lett. **53** (22), (1984)

[35] Seufert J., Weigand R., Bacher G., Kűmmell T., Forchel A., Leonardi K., Hommel D., Appl. Phys. Lett. **76** (14), 1872-1874, (2000)

[36] Empedocles S.A., Bawendi M.G., Science **278**, 2114, (1997)

[37] Neuhauser R.G., Shimizu K.T., Woo W.K., Empedocles S.A., Bawendi M.G., Phys. Rev. Lett. **85** (15), 3301-3304, (2000)

[38] Arzberger M., Amann M.C., Phys. Rev. B **62** (16), 11029-11037, (2000)

[39] Empedocles S.A., Bawendi M.G., J. Phys. Chem. B **103**, 1826-1830, (1999)

[40] Gómez D.E., van Embden J., Mulvaney P., Appl. Phys. Lett. **88**, 154106, (2006)

[41] Shimizu K.T., Neuhauser R.G., Leatherdale C.A., Empedocles S.A., Woo W.K., Bawendi M.G., Phys. Rev. B **63**, 205316, (2001)

[42] Klimov V.I., Los Alamos Science **28**, 214-220, (2003)

[43] Isaac A., von Borczykowski C., Chicos F., Phys. Rev. B **71**, 161302, (2005)

[44] Schwartz A., Wang L., Early E., Gaigalas A., Zhang Y., Marti G.E., Vogt R.F., J. of Res. Of The Nat. Inst. Of Standards And Tech **107**, 83-91 (2002)

4 Theory of semiconductor lasers

4.1 Introduction

The semiconductor laser, first proposed in the late 50's by Nikolay G Basov and Ali Javan, was experimentally realised in 1962 by Robert N Hall with gallium arsenide operating at a wavelength of 850 nm, as shown in Figure 4.1. This success was quickly followed in the same year with a similar device that emitted light in the visible spectrum by Holonyak Jr and Bevaque [1]. These first generation semiconductor lasers were only stable in pulsed operation and while cooled to liquid nitrogen temperatures (77 K) due to the extremely high threshold current required to obtain a lasing condition. In the decades that followed, construction techniques developed using a variety of materials to enable devices to cover the full visible spectral range and beyond, at both low and high emission powers.

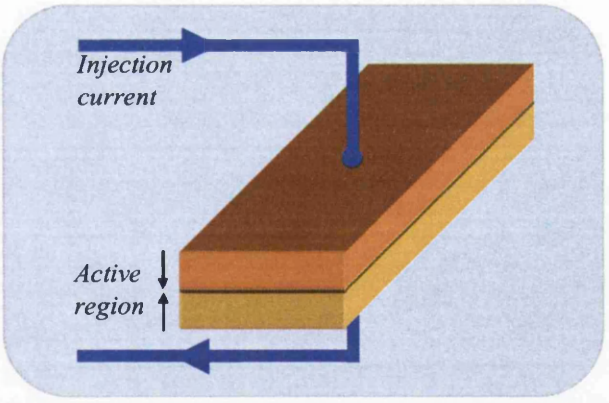

Fig. 4.1 Construction of the basic laser diode used by Hall in 1962.

Today, semiconductor lasers are used in devices ranging from personal CD players to high-tech communications. Common configurations use the edge-emitting Fabry-Perot structure whereby the cavity length is several times the wavelength of the generated light, with the ability to operate in different modes depending on, amongst other things, injection current and temperature of the device.

4.2 The cavity and gain threshold condition

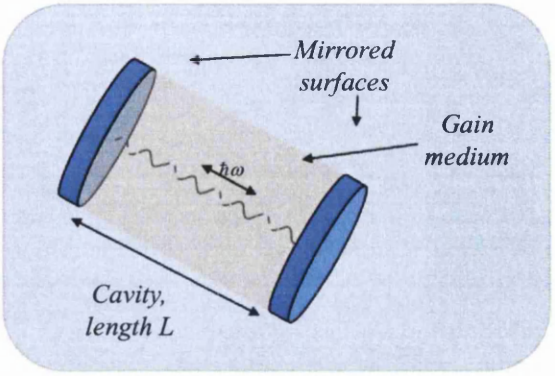

Fig. 4.2 A basic gain cavity setup, with mirrored surfaces at either end for optical confinement.

Figure 4.2 shows the basic concept of an optical cavity, necessary in order to achieve stimulated emission. It consists of two mirrors, with the space between filled with a gain-medium such that with each pass of the cavity, the intensity increases due to stimulated emission, as illustrated schematically in Figure 4.3.

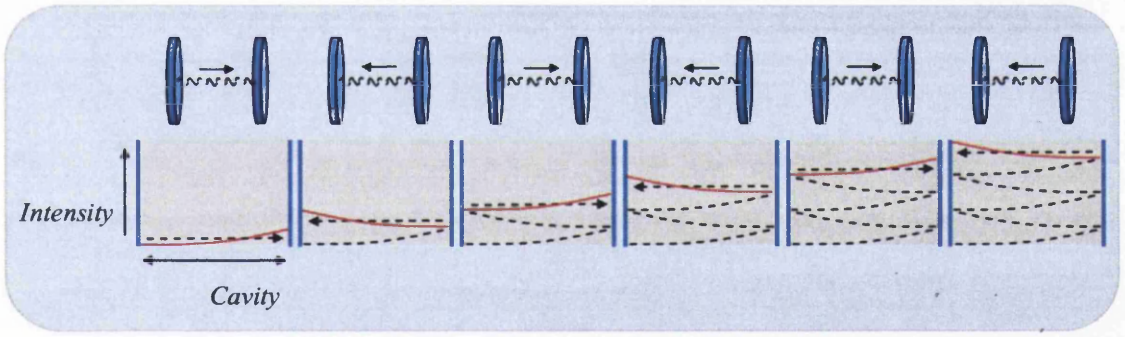

Fig. 4.3 The cavity gain across the length increases the overall intensity within the device.

Losses within the cavity must be considered to determine the optimum operating conditions. There will be losses from defects within the gain medium, and losses at the mirrors which have a typical reflectivity of 30%. This however is sufficient due to the large gain of the cavity.

The overall intensity as a result of a single round trip of the gain cavity, from an initial intensity of I_0 can be given as,

$$Intensity_{roundtrip} = I_0[\exp((g-\alpha)2L_c)]R_1R_2 \quad , \qquad 4.1$$

with α and g the loss and gain per unit length, L_c the gain medium length, and R_1, R_2 the reflectivity of the 2 mirrored surfaces respectively. At the lasing threshold, the cavity gain, g, just compensates for losses within the cavity, α, and reflectance losses at the mirrors.

Within a laser, either light or an electrical current is used to generate photons. With enough stimulation, a population inversion can be generated whereby the majority of electrons are in an excited state. Therefore, there is a high probability that a photon-electron interaction will result in stimulated emission such that an electron will drop down to a lower energy level releasing the energy difference as a photon having the same energy, propagation vector and phase as the stimulating photon. As the photons oscillate back and forth through the gain medium, more electrons are stimulated with each pass to drop from the conduction band back down to the valence band.

4.3 Longitudinal modes

It is important that L_c be equal to an integer number, q, of half wavelengths at the emission wavelength, λ,

$$L_c = q \times \frac{\lambda}{2} \,. \qquad 4.2$$

A large number of longitudinal modes may therefore find resonance in a sizeable Fabry-Perot cavity. For large cavity lengths, temperature becomes an issue, whereby, a small variation in temperature can result in thermal expansion of the device shifting the gain peak off the quantum well emission wavelength. The difference in frequency between successive modes, $\Delta\upsilon$, that may be supported by the cavity is known as the free spectral range (FSR) and is given by,

$$\Delta\upsilon = \frac{c}{2L_c} \,, \qquad 4.3$$

with the speed of light, *c*.

Fine gain control can be achieved by manipulation of the device temperature which causes the cavity length to expand or contract. Temperature control is achieved as a consequence of resistive heating through the injection current. This causes a cavity length change of ~ 0.006 nm mA^{-1}. Temperature control is also possible with the aid of an array of thermocouples resulting in a coarse 0.06 nm K^{-1}, known as a Peltier module. If the cavity temperature is allowed to drift, mode hopping may occur between different allowed modes, invoking undesired modulation of the emission.

4.4 Transverse modes

Laser systems generally operate along a single axis with reflecting surfaces at either end, such that radiation emitted non-axially does not contribute much to the gain of the device. Only photons emitted parallel to the central axis between the mirrors will be reflected back into the gain medium, stimulating excited electrons to return to the ground state emitting further photons. However, as the cavity is 3-dimensional, contributions must be accounted for not only in z but also in x and y dimensions, as discussed by Schawlow and Townes [2]. Siegman [3] describes a Gaussian-spherical wave, $\tilde{u}(x,y,z)$, at a distance z, emerging from a point source at a plane, z_0,

$$\tilde{u}(x,y,z) \equiv \frac{1}{\tilde{q}(z)} \exp\left[-ik\frac{x^2+y^2}{2R(z)} - \frac{x^2+y^2}{w^2(z)}\right], \qquad 4.4$$

where $R(z)$ is the radius of curvature that varies with distance from the source at z_0, $w(z)$ the Gaussian spot-size, x and y represent the transverse plane coordinates from the central optical axis, and $\tilde{q}(z)$ represents the complex radius of curvature where,

$$\frac{1}{\tilde{q}(z)} \equiv \frac{1}{R(z)} - i\frac{\lambda}{\pi w^2(z)}. \qquad 4.5$$

In free space, $\tilde{q}(z)$ follows the propagation law $\tilde{q}(z) \equiv \frac{1}{R(z)} - i\frac{\lambda}{\pi\omega^2(z)}$ with the initial value $\tilde{q}_0 = iz_r$.

Such equations apply to the edge-emitting variety of devices that generally consist of a square cavity.

4.5 Edge emitting Fabry-Perot semiconductor lasers

Semiconductor lasers are essentially formed in much the same way as diodes that utilise *p*-type and *n*-type doped semiconductors to construct a *p-n* homojunction as shown in Figure 4.4. With a forward current applied across the junction, electrons from the *n*-type recombine at the junction with holes in the *p*-type emitting photons, each equal to the energy difference between the conduction band and the valence band (generally the band-edge difference).

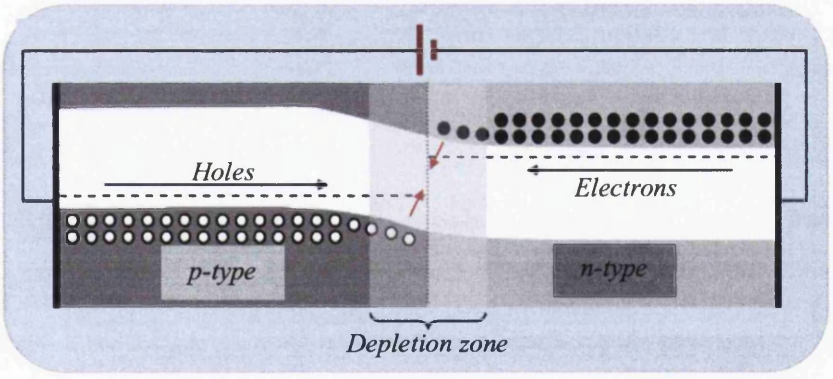

Fig. 4.4 A p-n junction formed allowing the recombination of electrons and holes.

Emitted photons as a result of recombination may be reabsorbed causing the excitation of an electron from the valence band maximum (VBM) to the conduction band

minimum (CBM), or might stimulate an already excited electron to recombine, thus emitting a further photon.

The first semiconductor laser devices were constructed from heavily doped *p-n* junctions. With mirrored surfaces at each end, under forward biased conditions, electrons and holes recombined at the interface resulting in laser action. Very high threshold currents were required however, as majority carriers would drift away from the junction interface making such devices highly inefficient.

A heterojunction is a structure comprised of two dissimilar materials each possessing a different band-gap. Kroemer and Alferov in 1963 independently suggested the idea of a double-heterojunction (DH) to confine electrons and holes closer to the junction to enable a lower threshold current for lasing action. Seven years later Alferov [4] constructed a modified version of the basic *p-n* junction in the form of a DH, as illustrated in Figure 4.5.

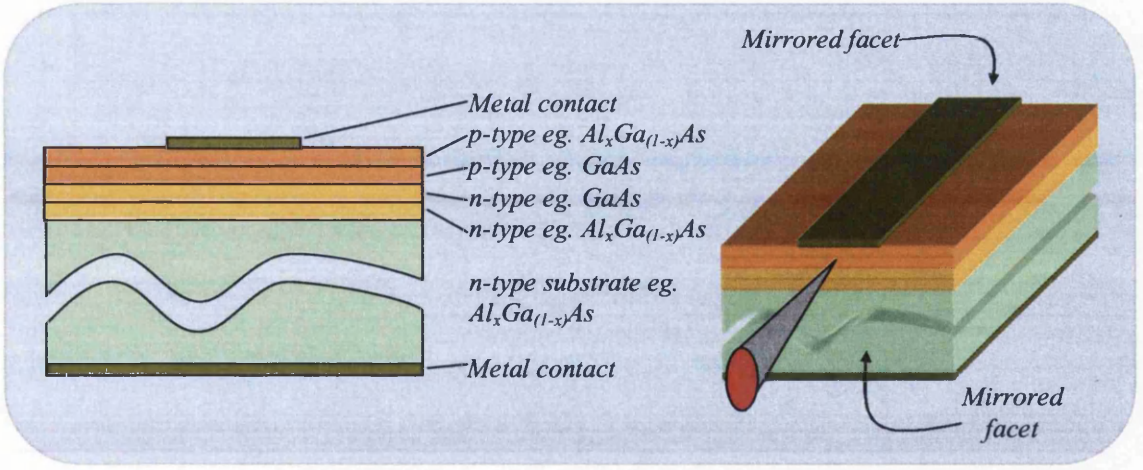

Fig. 4.5 Typical structure of a double-heterojunction laser diode.

In such devices, a lower band-gap material such as *p* and *n* type GaAs, (E_g = 1.424 eV) is sandwiched between two layers of a *p* and *n* type material with a higher band-gap

such as $Al_xGa_{(1-x)}As$ ($E_g < 2.168$ eV), as discussed by Adachi [5]. It's important that these materials have a closely matched lattice constant otherwise a large number of dislocations at the interfaces of the two materials will alter the electrical characteristics of the junction by generating localised states which can trap charge carriers. Too many such interfacial traps will dominate the electrical properties of the interface and degrade the ability of the overall device to function with sufficient efficiency for lasing action.

A Fabry-Perot type structure is used for its mirrored surfaces cut, perpendicular to the active interface of the lasing active medium, to reflect photons back and forth through the gain medium. A typical cavity length for an edge emitting semiconductor laser is of the order of 300 μm. When the single-pass gain between the two mirrors exceeds the losses, a point defined as threshold gain, laser action occurs. A current injection density of the order of 1000 Acm^{-2} is typical for continuous wave (CW) operation of a DH laser.

Figure 4.6 shows the band structure of a DH laser. This arrangement of semiconductor materials allows more charge carriers to be within the active region by confining them within the active region. This creates the necessary population inversion at lower injection currents, the outer layers having a larger band-gap, the electrons there being unable to absorb the generated photons, thus creating a natural confinement.

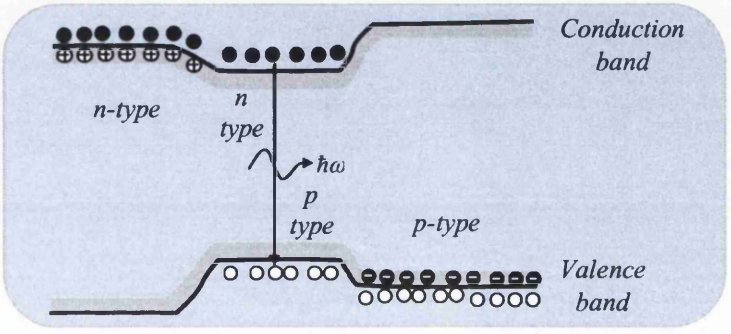

Fig. 4.6 The associated band diagram for the DH laser with the outer larger band-gap present due to the p and n-type AlGaAs material. The lasing region is at the layers of recombination, having a narrower band-gap.

The output of a Fabry-Perot edge emitting laser is a very divergent beam, which is also asymmetric in shape by as much as 10° horizontally and 30° vertically from the optical axis. This can for example cause coupling inefficiencies in optical transport in fibre optics. This has led to a great deal of investigative research into vertical cavity surface emitting lasers (VCSEL) which not only possess a narrower beam divergence, but also one that emerges from the surface of the device, perpendicular to the plane of growth. This has a number of advantages and also disadvantages, which will be discussed.

4.6 Vertical cavity surface emitting lasers

VCSELs function differently to the edge emitting Fabry-Perot variety of semiconductor lasers. Light is instead emitted along the axis of the current injection, rather than perpendicular to it. Varying material types and current confinement methods have been proposed to take advantage of their various properties. Key issues include the ability to operate at high injection currents and higher output power, efficiency, stability of lasing wavelength, frequency switching, and angle dependent intensity. All these factors are important as they determine the usefulness of the device in a range of categories.

Advantages of VCSELs over edge emitting devices include high modulation bandwidths, of the order of 10-15 GHz, single longitudinal mode, and low threshold currents. A circular beam profile enhances coupling efficiency to fibre optics, and due to the structure, more devices can be packed onto a wafer during the manufacturing process. Due to the size of the cavity a number of potential transverse modes can simultaneously exist thus VCSEL devices often exhibit multimode and mode switching behaviour, properties that make them unsuitable for high-speed single-mode telecommunication applications.

For a cavity, as discussed by Siegman [3], the intensity patterns of transverse electromagnetic (TEM) modes can be denoted by TEM_{mn}, where m and n are the vertical orders of the resulting patterns. These are described by a combination of a Gaussian beam profile together with a Hermite polynomial. The field amplitude at a point in Cartesian coordinates (x,y) is determined by equation 4.6 and is illustrated in Figure 4.7 [6],

$$\tilde{u}_{mn}(x,y)=\left[H_m\left(\frac{\sqrt{2}x}{w}\right)\exp\left(\frac{-x^2}{w^2}\right)\right]\left[H_n\left(\frac{\sqrt{2}y}{w}\right)\exp\left(\frac{-y^2}{w^2}\right)\right]. \qquad 4.6$$

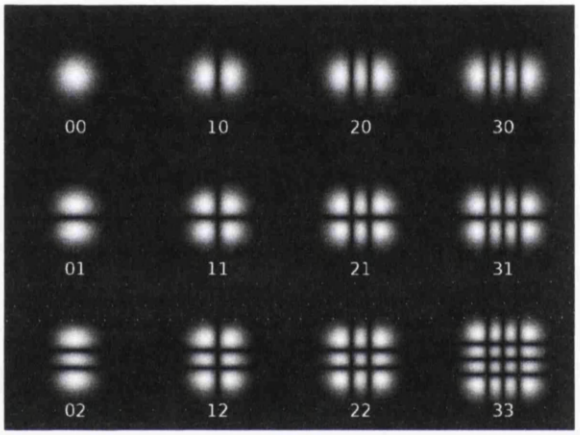

Fig. 4.7 Examples of the first few transverse modes from a cavity with mn=00 to mn=33 [6].

As will be discussed in section 4.7, the number of transverse modes present in the beam profile is the result of a number of factors, including aperture size, and injection current relative to its lasing threshold. Generally, the greater the injection current, the more carriers that will be available within the gain medium capable of supporting a complex interplay between competing transverse modes.

The first vertical cavity surface emitting laser (VCSEL) was built by Melngailis [7] in 1965. Mounted on a copper heat-sink cooled to 10 K, a magnetic field was used to confine the carriers, and functioned in a pulsed mode at 45 A/50 ns to prevent meltdown. VCSELs now capable of functioning in both continuous wave and pulsed

mode are constructed from semiconductor materials whose properties can be tailored to the device-specific operational parameters. With traditional edge-emitting semiconductor lasers the gain region is often several hundred wavelengths long and so a passing photon would interact with many excited electrons with each pass of the cavity. This generates a large number of stimulated photons, and so mirrors having efficiency as little as 30% are sufficient to create enough gain to overcome all losses within the cavity. With the VCSEL gain cavity being typically only one wavelength in length however, there is little gain medium to build sufficient intensity with each pass of the cavity, therefore mirrors of approximately 99.95% are required to minimise losses. Conventional mirrored surfaces are at best 98% reflective and therefore not of sufficient quality. Instead, a new method of reflecting the photons back into the gain region is used in the form of distributed Bragg reflectors (DBR), illustrated in Figure 4.8.

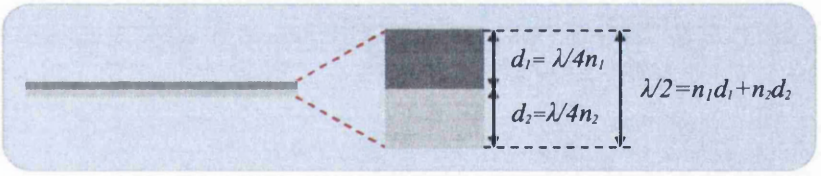

Fig. 4.8 A DBR consisting of two materials of differing refractive index values, having a 1 wavelength return path.

Semiconductors with an energy band-gap larger than the energy of each photon emitted from the active region have a low absorption coefficient, such that placing two dielectric materials with a highly contrasting refractive index next to each other causes some of the photons to be reflected at the discontinuity, forming the DBR. They are a half-wavelength in thickness, accounting for the differing refractive indices of the two materials, and engineered specifically to produce a zero phase shift to maintain coherence of the eventual output of the device. The reflection coefficient for a single

DBR is however low, and so a VCSEL requires as many as 30-40 of these stacked as in Figure 4.9, to obtain the required high reflectivity of 99.95%.

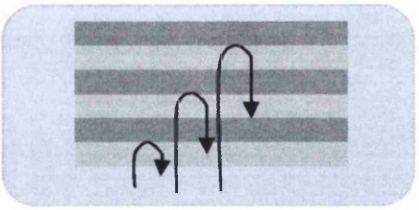

Fig. 4.9 Each DBR reflects, in phase, a small percentage of the incident light.

Stacking so many of these reflectors, each of a critical thickness, is quite an engineering feat as they must each reflect in-phase. Any errors will result in out of phase stimulation of photons thus reducing the coherence of the resulting beam. The reflectivity R, of m periodic DBR pairs is given by [8],

$$\sqrt{R} = \frac{1 - \frac{n_s}{n_0}\left(\frac{n_1}{n_2}\right)^{2m}}{1 + \frac{n_s}{n_0}\left(\frac{n_1}{n_2}\right)^{2m}}, \qquad 4.7$$

where n_0, n_s, n_1 and n_2 are the refractive indices of the surrounding medium, the substrate, and the two alternating materials of the DBR pairs respectively.

Different VCSEL structures have been developed over the years, each having a variety of advantages and disadvantages depending on the type of optical and current confinement. These include aspects such as reliability and necessity of stability, operational wavelength and frequency of modulation. The basic construction is shown in Figure 4.10 whereby an active region for recombination is surrounded by many pairs of reflecting DBRs.

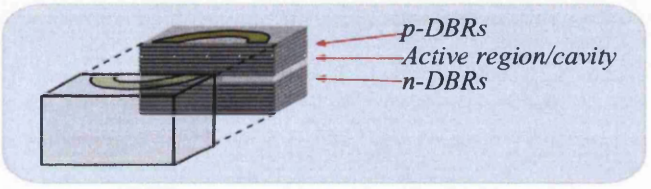

Fig. 4.10 The basic construction of a VCSEL – 2 mirrors, generated from p and n-type DBRs, sandwich an active region where recombination occurs .

Advantages and disadvantages are highlighted for four basic types of VCSEL, shown in Figure 4.11(a-d).

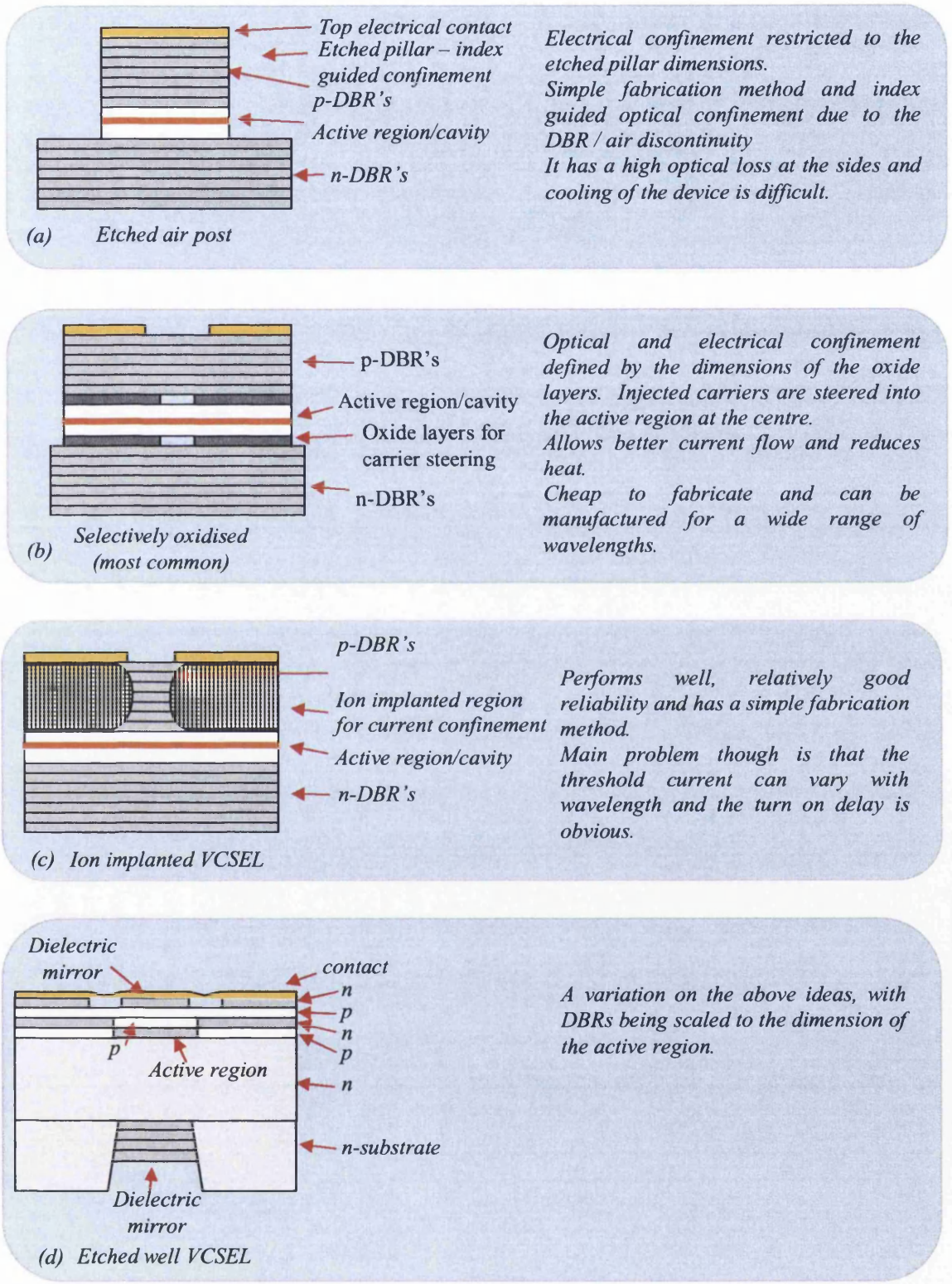

Fig. 4.11 Basic construction of a VCSEL – 2 mirrors generated from multiple p and n-type DBRs, sandwiching an active region where recombination occurs. Four types of construction are shown: (a) etched air post, (b) selectively oxidised, (c) ion implanted, and (d) etched well.

Above lasing threshold, as discussed by Wilk *et al.* [9], the profiles of different optical modes drastically alter the carrier distribution during stimulated emission by a process known as spatial hole burning (SHB). SHB is where the carriers within the active region are depleted such that no further gain action occurs. As a result, the index of refraction of the medium is altered, thus modifying the spatial presence of transverse modes, commonly referred to as mode competition, and prevalent in wide aperture VCSELs. This complex interplay of processes eventually finds an equilibrium that can sustain a fixed modal profile as discussed by Valle *et al.* [10], Goorjian and Ning [11], and Gustavsson *et al.* [12]. Zhang *et al.* [13] theoretically investigated the geometry of the current-intensity and current-spreading in efforts to control the eventual transverse mode structure at the output aperture. It was generally found that a small radius disk-contact or a ring-contact were favourable to the establishment of the fundamental transverse mode. Uchida *et al.* [14] have recently shown that elongating the cavity suppresses higher order transverse modes due to a reduction in the carrier-induced refractive index change in the active layer. Another recent example of continued improvements in VCSEL operation is that by Shi *et al.* [15] in fabricating an 850 nm emitting, circular ringed Zn diffused aperture VCSEL, with ion implantation for current confinement. Such a structure resulted in the ability to drive at higher injection current for higher output power at a single mode in addition to the relatively narrower beam divergence when compared to the Fabry-Perot type construction.

4.7 Mode profiles within a VCSEL aperture

Applications utilising lasers, to first approximations, assume a perfect Gaussian beam profile, corresponding to a theoretical TEM_{00} mode, emerges from a lasing device. However, this is not necessarily true. VCSEL cavities are generally capable of

supporting multiple transverse modes within the single longitudinal mode allowed within the cavity. The number of supported transverse modes increases with higher injection current. The injection current is dependent on the diffusion constant of the material. This quantity is a measure of the rate at which the carriers diffuse through the medium, and can be affected by factors such as the material structure, including impurity content, and temperature. Each transverse mode depletes carriers within the gain region. SHB results as the gain is saturated at the antinodes with the amplification of the device being dominated by the excitation density at these points. This can lead to inhomogeneous gain saturation where the spectral shape of the gain is no longer uniform. It has been theoretically shown that transverse modes compete for the available gain within the device due to SHB. Transverse modes can exist simultaneously or oscillate periodically into existence due to the presence of others, as discussed by Wilk *et al.* [9] and Law and Agrawal [16]. It is known both experimentally and theoretically that the dimensions of the inner and outer diameters of the top contact play an important role in determining the eventual dynamics of the device. A narrow disc-shaped contact results in few or single transverse modes being present, while a wide inner diameter contact results in many transverse modes, all of which must compete for the available gain. In order to sustain a constant set of transverse modes, the number of injected carriers must be equal to, or greater than, those used for stimulated recombination. If the available carrier density falls below the lasing threshold, the end result is a loss of stimulated emission output. This effect can actually be utilised for a mode of operation known as gain-switching whereby the injected carriers are pulsed into the device at a frequency such that for a brief period of time there are enough available carriers to generate stimulated emission, but then the

level quickly falls below the lasing threshold thus switching the device off until the next pulse. The resulting output of the VCSEL is a series of very narrow duration pulses.

The spatial and spectral profiles of VCSELs very much depend not only on the structural properties of the cavity and the active region, but also the size, shape and thickness of the carrier injection contact and the exit aperture. They are also heavily dependent on the frequency and type of modulation of the injection current [10]. This dependence of mode competition and SHB sets VCSELs apart from edge emitting devices which function simply as a result of a range of competing longitudinal modes from the onset of current injection. Reflections by the stacked DBRs and the confinement method help to determine the mode profiles present within the cavity that use up the available gain. As the light exits through the top surface aperture, if the beam profile is of the same order as the size of the aperture diameter, then there is almost certainly going to be diffraction at the edges. The effect this has on the far-field propagation will thus depend on the degree of interaction between the light and the aperture.

4.7.1 Gaussian beam profile

VCSELs with a circular aperture generally emit an electromagnetic beam of coherent light in the form of a Gaussian profile known as the fundamental transverse mode (TEM_{00}). The source field, $\tilde{u}_0(r_0)$, within the aperture can be described as a centred Gaussian plane-wavefunction as discussed by Siegman [3],

$$\tilde{u}_0(r_0) = e^{-r_0^2/w_0^2}, \qquad 4.8$$

where r_0 is the radial distance from the Gaussian centre. The field amplitude of such a Gaussian is illustrated in Figure 4.12. The beam waist radius, w_0, at the source of the plane-wavefront, is defined as being the distance at the $1/e$ points as shown.

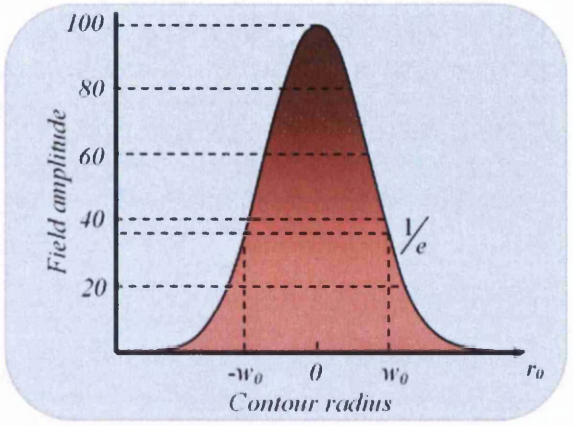

Fig. 4.12 Gaussian illustrating the $1/e$ points that define the beam waist radius, w_0.

4.8 Gaussian beam diffraction with a circular aperture

The operation of a VCSEL is determined by several factors including structural dimensions, temperature, medium, and dimensions of the electrical contacts from which current might flow through to the recombination centre. It is important to emphasize that the top contact is not necessarily the same as the size of the cavity, thus the profile of the Gaussian beam impinging on such a contact will be altered. As discussed by Siegman [3], a circular aperture illuminated with an incident uniform plane wave results in interesting phenomena.

Consider field amplitude at a distance z of a Gaussian function $\tilde{u}_0(r_0)$, clipped by a circular aperture of diameter $2a$, both located at z_0. The resulting diffracted source function, $\tilde{u}(r)$ is the Huygens integral,

$$\tilde{u}(r) = 2\pi i N e^{-i\pi N\left(r/a\right)^2} \int_0^1 \frac{r_0 \tilde{u}_0(r_0) e^{-i\pi N\left(r_0/a\right)^2}}{a} J_0\left(\frac{2\pi N r r_0}{a^2}\right) d\left(\frac{r_0}{a}\right), \qquad 4.9$$

where r is the radial distance from the central optical axis, a is the aperture radius, J_0 a Bessel function of order zero, present due to the circular nature of the aperture, and N the Fresnel number,

$$N \equiv \frac{a^2}{(z - z_0)\lambda} . \qquad 4.10$$

To determine how the far-field (Fraunhofer regime) will behave resulting from the uniformly illuminated circular aperture, i.e. $z >> z_0$ such that $N \rightarrow 0$, one can use $\frac{d}{dz}[zJ_1(z)] = zJ_0(z)$ to solve Huygens integral above giving an equation relating the field intensity to the angular separation from the central axis as [3],

$$\tilde{u}(\theta) \approx 4\pi i N e^{-i\pi N\left(r/a\right)^2} \frac{2J_1(2\pi a\theta/\lambda)}{2\pi a\theta/\lambda}. \qquad 4.11$$

This results in a varying field-amplitude as a function of angular separation from the central axis, shown in Figure 4.13.

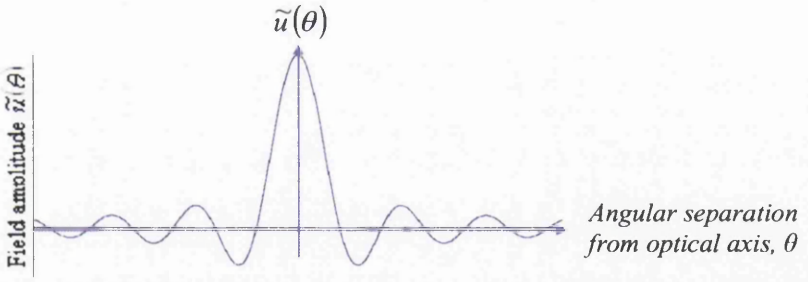

Fig. 4.13 Cross section of the far-field amplitude as a function of angular separation from the optical axis (N→0) as a result of a plane wave-front illuminated circular aperture.

However, in the near-field (Fresnel diffraction) where $N > 1$, the field amplitude pattern consists of a top-hat pattern, highly modulated by a series of concentric circular rings as shown in Figure 4.14.

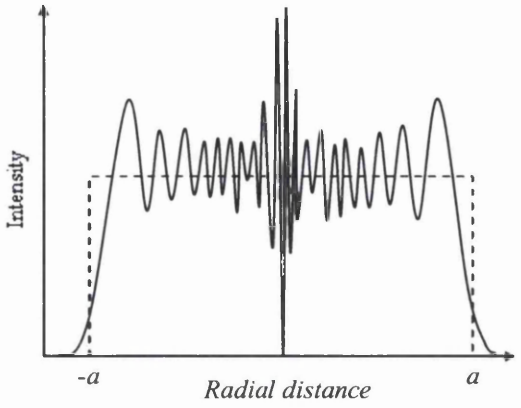

Fig. 4.14 Cross section of the field amplitude as a function of radial distance from the optical axis in the near-field (N > 1) showing the intensity ripples as a result of a circular aperture illuminated with a plane wavefront.

The number of Fresnel ripples present across the entire cross section of the beam is approximately *N*.

Figure 4.15 illustrates a cross-section of a source Gaussian beam $\tilde{u}_0(r_0) = e^{-r_0^2/w_0^2}$, from equation 4.8, passing through a circular aperture of radius *a*, with the edges of the Gaussian being clipped.

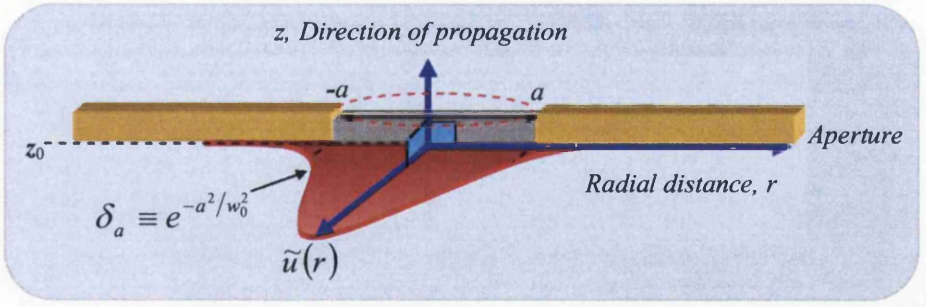

Fig. 4.15 Cross section of a circular aperture, illuminated with a Gaussian plane-wave.

Huygens' integral containing the above Gaussian source field can be expanded into an infinite series of successively higher order Bessel functions, the first 2 leading terms of which are [3],

$$\tilde{u}(rz) \approx \frac{\tilde{q}_0 e^{-i\pi N(r/a)^2}}{\tilde{q}(z)}\left[1 - e^{-i\pi N} e^{-a^2/w_0^2} J_0(2\pi N\, r/a)\right]. \qquad 4.12$$

Using this equation and the substitution $\delta_a \equiv e^{-a^2/w_0^2}$, the intensity of the signal can be expressed as [3],

$$I(r,z) \approx \left[\frac{w_0}{w(z)}\right]^2 \left|1-\delta_a e^{-i\pi N} J_0(2\pi Nr/a)\right|^2. \qquad 4.13$$

The resulting intensity pattern in Figure 4.16 bears a strong resemblance to that for the uniformly illuminated circular aperture in Figure 4.14, while only the incident field amplitude has been switched from a top-hat structure to one of a Gaussian. This does however still show a strong concentric ring modulation when viewed in plan-view.

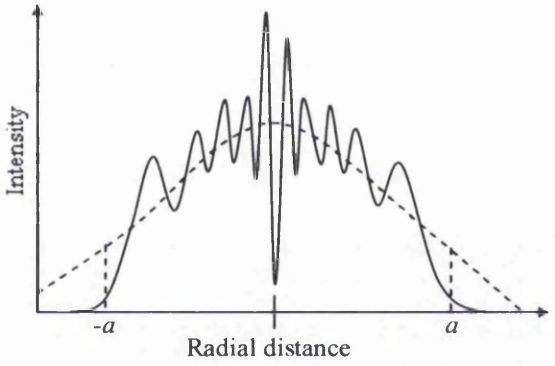

Fig 4.16 Cross section of the field amplitude as a function of radial distance from the optical axis in the near-field (N > 1), showing the modulation ripples as a result of a circular aperture illuminated with a Gaussian wavefront.

The narrower the circular aperture in relation to the width of the Gaussian beam, the lesser the modulation of the central spike on the optical axis. The reason for this can be understood by examining equation 4.13. The δ_a function is a coefficient of the Bessel function. As the value of δ_a reduces below 1, the level of modulation is minimised for the central hole or spike, which arise whether N is even or odd. The effect on the far-field central lobe due to a Gaussian beam truncation is a reduction by,

$$(1-\delta_a)^2. \qquad 4.14$$

The far-field intensity and structure is dependent on modulations in the near-field as a result of diffraction at the aperture boundary of the Gaussian beam. The presence of

higher order modes within the optical cavity will result in a far more complicated modulation profile due to clipping at the aperture.

4.9 Conclusion

This chapter has discussed several principles of two types of semiconductor laser, Fabry-Perot edge emitters and VCSELs. Advantages and disadvantages of each were highlighted and attention was drawn to the vertical cavity surface emitting laser, a device which possesses several features making it desirable in the electronics and telecommunications industry. Due to its design, instabilities in the emission profile can be present, inhibiting their use. Ideally such lasers are operated in a single TEM_{00} (Gaussian) mode, however due to their size and shape; the cavity can simultaneously support several transverse modes. This has the problem of significantly reducing the single mode power in the far-field.

Near-field studies offer the possibility of investigating phenomena such as transverse mode generation and aperture effects in great detail. Important concepts for discussion of results presented in Chapter 6 were introduced in this chapter.

References

[1] Holonyak N. Jr, Bevaqua S.F., Appl. Phys. Lett. **1**, 82-83, (1962)

[2] Schawlow A.L., Townes C.H., Phys. Rev. **112**, 1940 (1958)

[3] Siegman A.E., Lasers, University Science Books, 727-736, (1986)

[4] Alferov Zh.I., Sov. Phys. Semicond. **4m** 1573 (1970)

[5] Adachi S., J. Appl. Phys. **58** (3), R1-R29, (1985)

[6] Poprawe R., Wester R., Institut Lasertechnik, Germany

[7] Melngailis I., Appl. Phys. Lett. **6** (3), 59-60 (1965)

[8] Sale T.E., Vertical cavity surface emitting lasers, Res. Studies Press Ltd, (1995)

[9] Wilk J., Sarzala R.P., Nakwaski W., J. Phys. D **31**, L11, (1998)

[10] Valle A., Rees P., Pesquera L., Shore K.A., J. Opt. Soc. Am. B **16**, 2045, (1999)

[11] Goorjian P.M., Ning C.Z., Opt. Express **5**, 55, (1999)

[12] Gustavsson J.S., Vukušić J.A., Bengtsson J., Larsson A., IEEE J. Quantum Electron. **38**, 203, (2002)

[13] Zhang H., Mrozynski G., Wallrabenstein A., Schrage J., IEEE J.. Quantum Electron. **40**, 18, (2004)

[14] Uchida T., Miyamoto T., Koyama F., Jpn. J. Appl. Phys. **45**, 2550, (2006)

[15] Shi J.W., Jiang C.H., Chen K.M., Yen J.L., Yang Y.J., Appl. Phys. Lett. **87**, 031109, (2005)

[16] Law J.Y., Agrawal G.P., IEEE J. Quantum Elec. **33** (5), 462, (1997)

5 Experimental arrangements

5.1 Introduction

Throughout the experimental work required for this thesis, a variety of equipment configurations were designed and implemented for the first time. The samples studied were either electroluminescent, or fluorescent in nature. Configurations for the scanning near-field optical microscope (SNOM) were optimised for far-field and near-field, using both the reflection and transmission modes of operation. Three of the main configurations used in these studies were 'Transmission', 'Oblique reflection' and 'Collection', as shown in Figure 5.1(a,c,e).

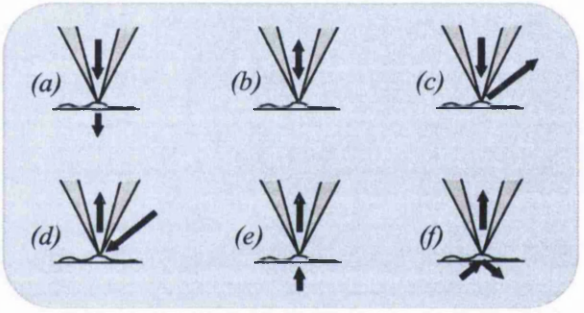

Fig. 5.1 The primary modes of operation of the SNOM: (a) transmission, (b) illumination, (c) oblique reflection, (d) oblique collection, (e) collection, (f) dark-field.

For work involving semiconductor lasers and their optical emissions, the collection mode was used as shown in Figure 5.1(e). Emitted light was collected through a 50-100 nm aperture at the end of a metal-coated fibre optic probe. The study of quantum dots, however, required the use of a laser for optical excitation. The SNOM probe was utilised to stimulate mono-disperse or small clusters of quantum dots in the near-field. The resulting emitted fluorescence was then collected either from the reflection mode, Figure 5.1(c), or via the transmission mode, as shown in Figure 5.1(a).

5.2 Equipment

The range of equipment used throughout this study of light emitting devices consisted of:

- Veeco Aurora-3 Scanning near-field optical microscope (SNOM)
- 2 Avalanche Photodiodes (APD)
- Photomultiplier Tube (PMT)
- Acton SpectraPro 2300i spectrometer with side exit for monochromatic mode
- Princeton Instruments Spec-10 CCD, cooled to -70°C
- Anti-vibration air-table, pressurised to 6-bar with N_2
- 20 mW Argon Ion CW Laser
- 10 mW HeNe CW Laser
- Laser line filters
- Raman edge filters
- Standard optics with antireflection coatings, optimised at approximately 500 nm

The Aurora-3 SNOM has two optical paths that can work simultaneously, unlike its predecessor, the Aurora-2. It is able to collect light via reflection mode, at an angle approximately 45° to the horizontal sample plane, and via transmission through the sample, using a close working distance lens configuration. This transmission path illustrated in Figure 5.2 was the method used for optical stimulation of light sensitive materials such as quantum dots.

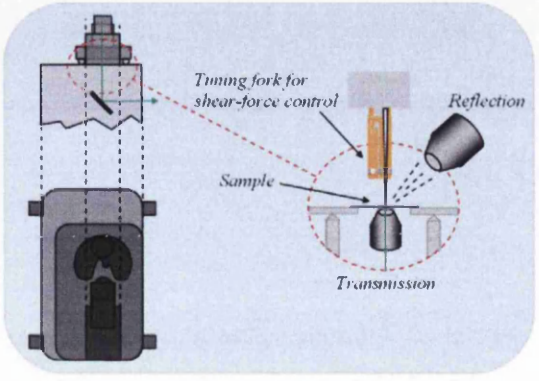

Fig. 5.2 A scanning near-field optical microscope with 2 optical paths. The reflection path is at a distance of approximately 5cm from the aperture, while the transmission collection lens focuses at <1 mm.

Light exiting the side of the SNOM unit is passed to standard optics for focussing and detection. The maximum scan range of this microscope is limited to 30 μm^2 in x-y with a maximum z-range of 5 μm.

APDs are highly sensitive photon counters. 2 models of APDs from the same manufacturer were used, but with different dark count (dc) levels, one of 100 dcs^{-1} and also a less noisy 50 dcs^{-1}. They function by the application of a high reverse bias voltage across a silicon sample which generates a high current gain of the order of 100. An absorbed photon causes a sudden rise in current which, upon detection, generates a TTL pulse at the output of the detector. Once the sudden increase in current is detected, it needs to be stopped and the circuitry reset to await the next photon. This happens on the order of 30-50 ns, followed by a dead-time of 50 ns while the circuitry prepares for the next detection. Overall, the APDs were able to detect photons at a maximum rate of ~10 MHz.

The PMT that was available for use with the work contained within this thesis was a far less sensitive light detector than the APD due to its quality, capable of detecting only moderate-low levels of light at the expense of a decreased signal to noise ratio. Because of this, it was not used in highly sensitive experimental setups.

The spectrometer used was a 2300i Acton model, possessing a motorised triple grating turret with a 30 cm focal length. The three mounted gratings were 300 l/mm, 600 l/mm and 1200 l/mm, with their blaze angles optimised at 500 nm. This is discussed in some detail in Appendix 2. A motorised internal mirror, which reflects light from the centre of the spectral band viewed at the CCD out of a side-exit, was also available. This

narrow bandwidth of light then passes through an adjustable slit that can be used to tune the bandwidth down to sub-nanometre resolutions, making this instrument a versatile monochromator.

The CCD module is a Princeton Instruments Spec-10 cooled to -70 °C with a Peltier stack. The CCD chip is a back illuminated 2048 x 512 CCD pixel detector array. The back of this array has of a few micron thick layer of silicon for absorption within the visible spectrum. The presence of this layer presents a problem when attempting to detect wavelengths longer than ~ 650 nm due to the increasing transparency of the silicon. Reasons for these limitations are discussed in section 5.7 and Appendix 4.

In order for a SNOM probe to function effectively in the near-field, without damage to the aperture, it is necessary to completely isolate the device from vibrations. This is achieved by mounting equipment on an air table, filled with nitrogen to a pressure of 6 bar.

For optical stimulation, a 20 mW argon ion (Ar^+) laser and a 10 mW helium neon (HeNe) laser were available, at wavelengths of 488 nm and 632.8 nm respectively. Generally, the HeNe laser was not utilised for these experiments other than for optical alignment /couplings as it was easier to see and track across the optical table. The Ar^+ laser was the primary laser used due to its higher energy photons. Laser line filters were necessary to remove light at wavelengths other than that of the lasing wavelength from the laser. These are briefly discussed later in this chapter in section 5.3. Raman edge filters were used to remove the laser line from the output of the SNOM, thus allowing only the fluorescence to pass to the detectors.

An enclosure was required that could maximise the use of the optical bench, encompassing all of the optical components including the spectrometer/CCD and associated optics. In this way, other activities within the lab could continue, and also, due to the very low light levels, long collection times would be possible with low level background noise. An enclosure of suitable design, shown in Figure 5.3, was built and used at all times.

Fig. 5.3 The replacement enclosure, designed to make full use of the optical table, with enough room for the spectrometer, CCD and APD detectors.

5.3 Laser line and Raman edge filters

A Raman edge filter, essentially a high pass (wavelength) filter, has a sharp transition width of the order of 2.5 nm. Below its cut-off wavelength it has a x6 optical density. When placed at the output of the SNOM it removes the laser line allowing the measurement of fluorescent intensity from optically active samples.

Gas lasers suffer from the presence of many transitions often appearing at the output of the device. The cavity length of the laser is optimised for only one of these transitions

but the others are still present at the output, though at a significantly lower intensity. For the Ar^+ laser used for stimulation of optically active materials and the subsequent spectroscopic detection, it is important that these lines be removed to keep results clean of noise spikes at the wavelengths shown in Figure 5.4. Several other transitions are also present but the selected few shown were dominant.

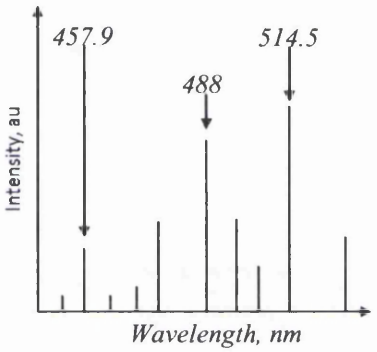

Fig. 5.4 Some of the more prominent transitions within the Argon Ion spectrum, several of which may be used for the lasing wavelength by setting the cavity length for resonance at the appropriate wavelength.

Two examples illustrating the effect the presence of these unwanted lines has on data are shown in Figure 5.5. The Gaussian fluorescent peak at 600 nm is modulated by spikes at wavelengths ranging from 600 nm to above 750 nm.

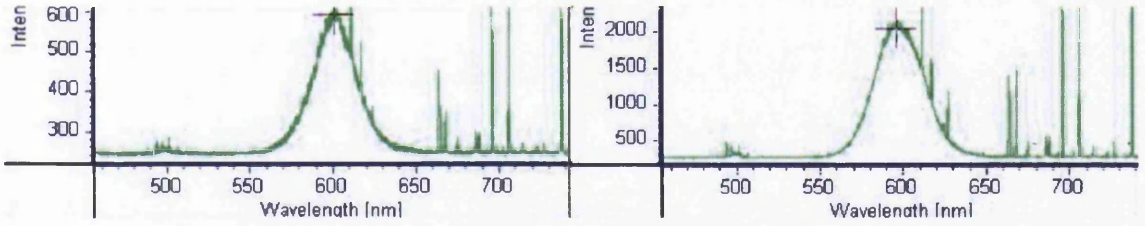

Fig. 5.5 Two near-field collections from a sample containing clusters of fluorescent quantum dots. Argon ion transitions are clearly visible at longer wavelengths.

A simple mount was manufactured at the exit of the laser, to hold a laser line filter – a band-pass notch filter allowing only the 488 nm laser line to pass, as shown in Figure 5.6.

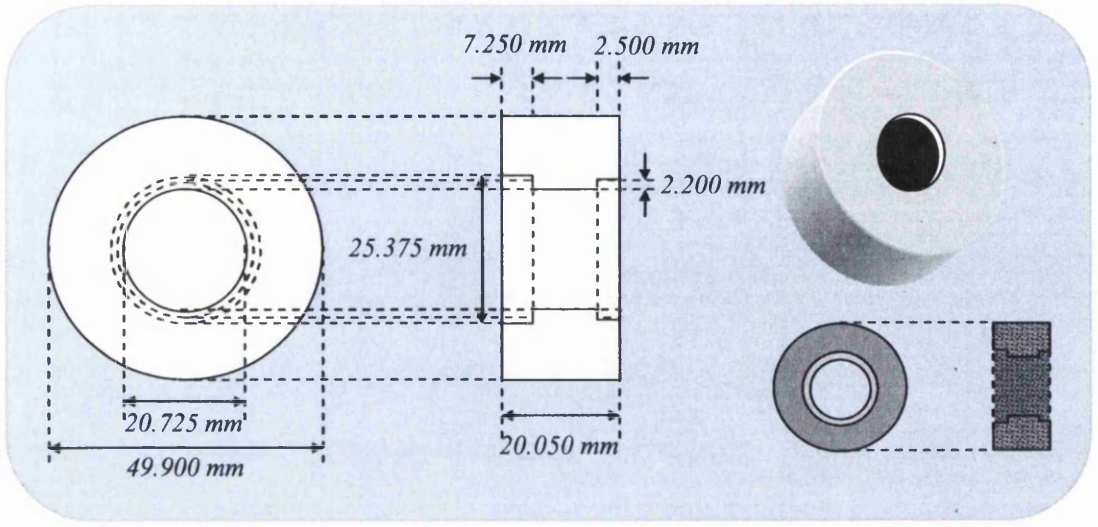

Fig. 5.6 Laser-line mount as a modification to the existing laser guide block.

The final spectroscopic setup consisted of a laser, immediately followed by a laser line filter to remove undesired argon ion atomic transitions, and the Raman edge filter to remove the laser light from the fluorescent signal, as shown in Figure 5.7.

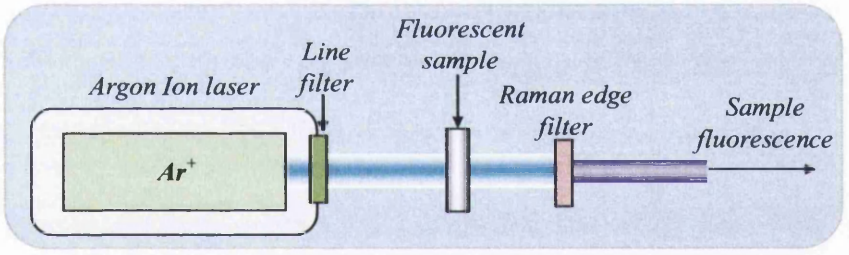

Fig. 5.7 A flow diagram that illustrates the filters used to remove unwanted laser lines before illuminating the sample, and a Raman edge filter to remove the laser line, thus separating out the fluorescence for detection.

5.4 The spectrometer

A 'grating spectrograph', illustrated in Figure 5.8, consists of spherical mirrors to collimate light onto one of 3 gratings, each having typically up to 10^5 lines achieving 3 different resolutions. These have spectral windows of ~ 60 nm, 120 nm and 250 nm respectively. Under optimum conditions, the 1200 l/mm grating was capable of resolving spectral features below 0.1 nm. Light entering the spectrometer through the left input slit is reflected onto one of the 3 gratings. Light incident on the grating lines,

of spacing *d*, is diffracted. The diffracted light is then reflected onto the CCD by a second curved mirror for detection.

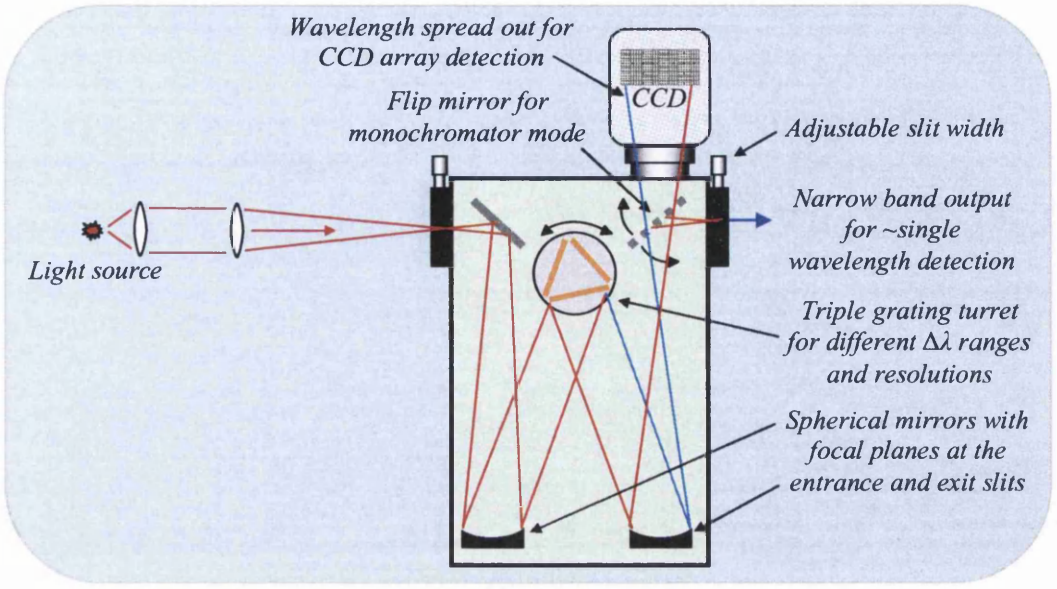

Fig. 5.8 Internal layout of the SpectraPro 2300i with two exit-slits.

An internal flipper mirror in this particular model can be motorised into place reflecting the centre band of wavelengths out of a side exit. The slit on the right side of the spectrometer allows one to set the bandwidth of the exiting light. This allows the spectrometer to function as a monochromator with a variable bandwidth output at the side-exit. The focal length of this spectrometer is 30 cm, as discussed in section 5.2, thus it is important to optimise optics to this specification to maximise the optical resolution for collected spectra.

The gratings and internal mirrors were optimised for maximum efficiency at 500 nm as this was deemed to be the optimum wavelength for most experiments to be carried out. The input shutter had a minimum open/close reaction time of 5 ms, beyond this and it failed to fully open. This obviously set the minimum collection time, but was not deemed to be a problem due to the long duration collection times expected.

Where possible, background subtraction was used to minimise noise within the detected spectra. Also, where a few rows were used for detection within the CCD instead of the total 512, only the illuminated rows were included in the hardware binning prior to passing the data to the computer. This helped minimise noise in the accumulated spectra.

5.5 Configurations used to obtain VCSEL results

Figure 5.9 illustrates the setup used to obtain spectrally filtered images of the spatial variation of transverse modes emitted in the near-field from the aperture of a VCSEL, and also to map to spatial intensity at the aperture of resonant cavity light emitting diodes (RCLED).

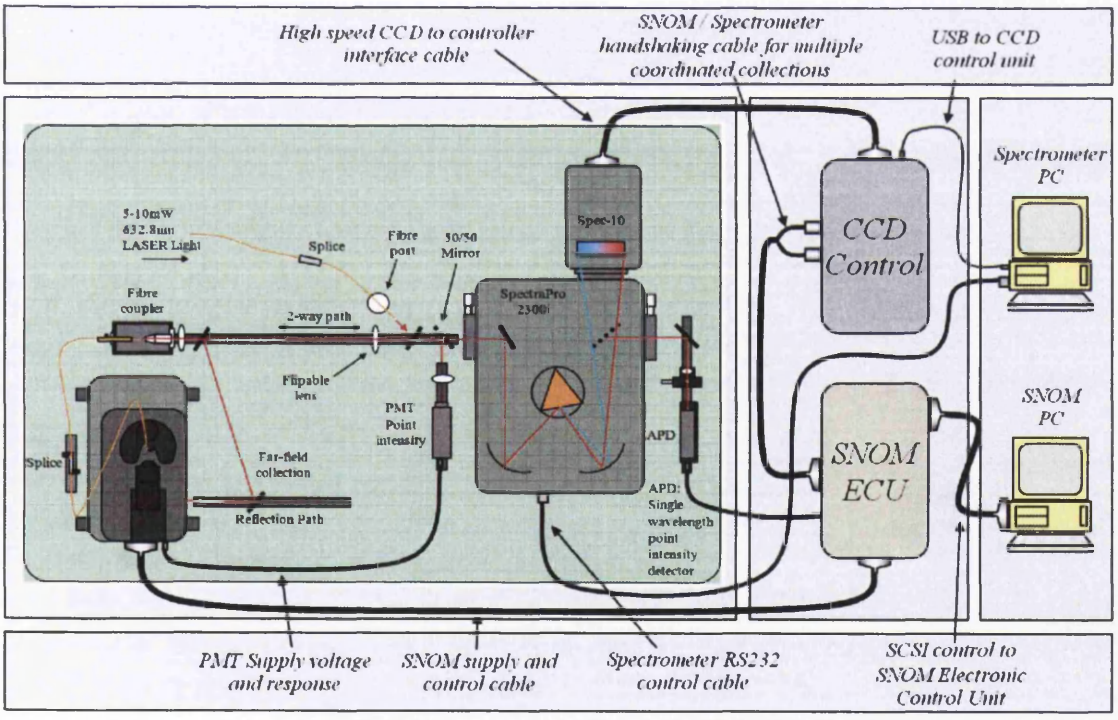

Fig. 5.9 Optical collection mode setup used for the detection of light from RCLEDs and VCSELs for intensity and spectroscopic studies with the aid of APDs and a spectrometer/monochromator.

The setup utilised the majority of the equipment available such as the SNOM, the spectrometer/CCD, PMT, APD, as well as both the Ar^+ and the HeNe lasers. The SNOM was setup for collection mode, as illustrated in Figure 5.1(e).

The SNOM fibre probe was brought to within a few nanometres of the surface within the light emitting aperture of a VCSEL. As shown in Figure 5.9, collected light was passed through the splice, positioned at the left side of the SNOM, into a 2nd fibre optic cable to the fibre-coupler. It was then launched into free space through a lens towards the spectrometer and the PMT. Before the experiment was begun however, the HeNe laser was connected directly to the splice on the left and alignment of the laser onto the PMT and the spectrometer input slit was maximised. The HeNe laser was then directed through a second splice, shown at the top of Figure 5.9, into a 3rd fibre optic that launched the light onto a removable mirror, reflecting it back towards the fibre coupler and down through the splice to the SNOM probe. This allowed the coupling efficiency at the left side splice to be maximised for collected light up the SNOM probe, passing through the fibre coupler, and focussing onto the PMT and spectrometer simultaneously. The flip-able lens was present to aid with the focussing of the diverging HeNe laser light emerging from the fibre optic onto the fibre coupler lens during initial optical alignment. The efficiency of the fibre coupler used in this manner was very low, giving only a small amount of laser light at the SNOM probe aperture, but sufficient for the purpose of maximising the coupling efficiency of the left hand side splice. Once this was achieved, the HeNe laser was switched off and the flip-able lens and mirror situated to its right removed, leaving a collection mode spectroscopic SNOM ready for use. Having this 2-way optical path made the optical setup complicated, but was ultimately necessary.

The mirror in front of the PMT, next to the spectrometer, is a 50/50 mirror such that 50% of collected light enters into the PMT, with the remaining 50% collected by the spectrometer. Light entering the spectrometer could then be detected by the CCD for spectral analysis, or, with the use of a software controllable internal flipper mirror, directed out of a side exit slit to a 2nd APD, as shown in Figure 5.10.

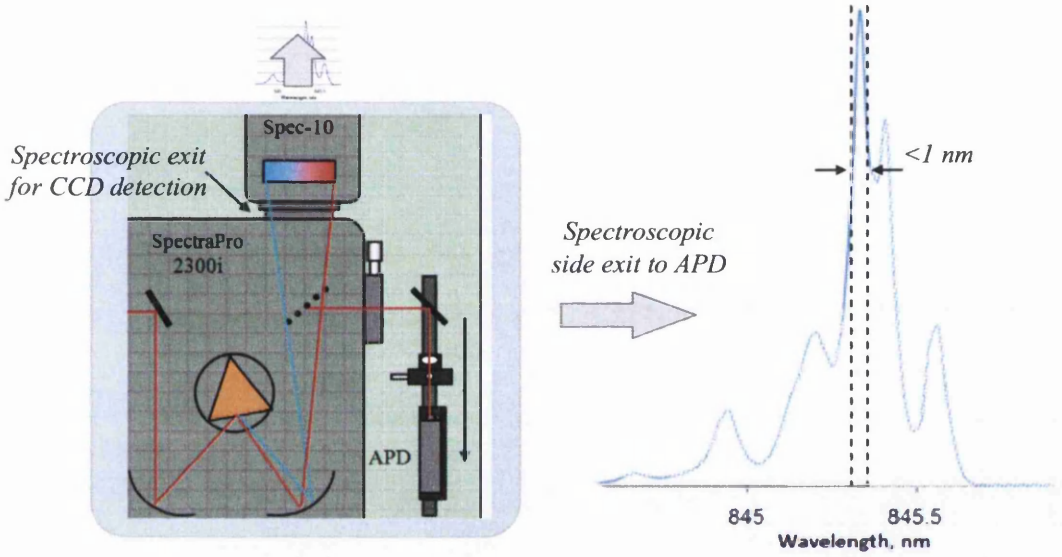

Fig 5.10 Narrow band of wavelengths are passed to the APD for single wavelength detection.

What is defined as being the centre wavelength on a spectral collection on the spectrometer is that which exits the side slit. This side exit has an adjustable slit from 10 μm up to a millimetre or so. At small slit-widths, this slit can be used to control the bandwidth around the centre wavelength that passes through this side exit, from sub-nanometre to several nanometres. For example, single transverse modes emitted from a VCSEL, separated by as little as 0.2 nm can be filtered out and detected using this method. Figure 5.11(a) shows an example of the topography, along with simultaneously collected optical intensity image in Figure 5.11(b), and a spectrally filtered intensity image in Figure 5.11(c), across a VCSEL aperture.

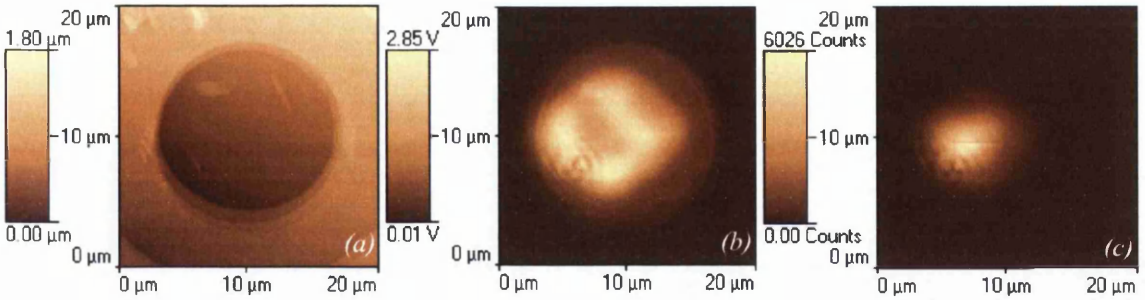

Fig. 5.11 Topographic (a), total intensity (b), and wavelength filtered intensity (c) images are obtained simultaneously using the setup described above.

Figure 5.12 highlights the 3 main optical components used to generate the 3 images shown in Figure 5.11.

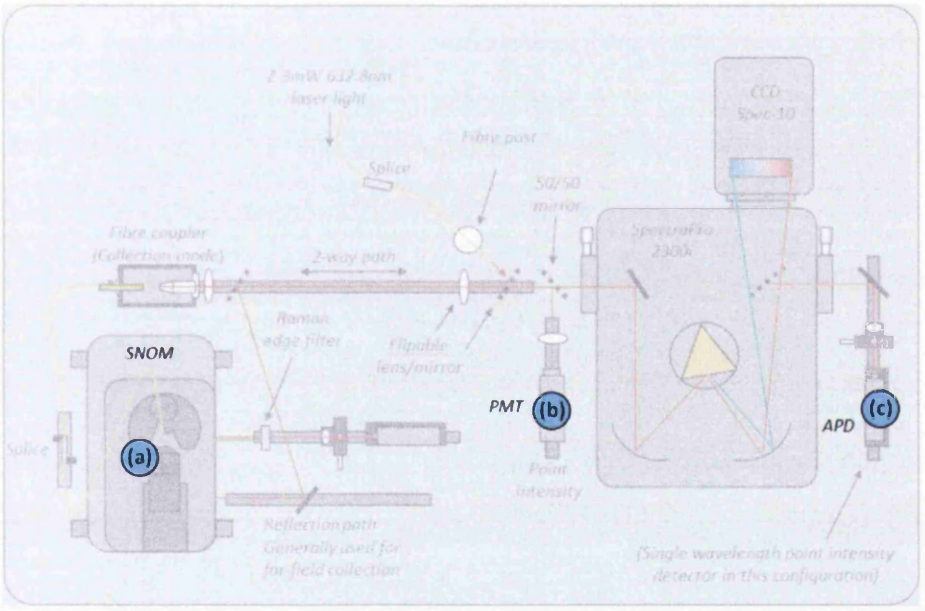

Fig. 5.12 Optical collection mode setup used for the detection of light from VCSELs for intensity and spectroscopic studies with the aid of a SNOM (a), PMT (b) and an APD/monochromator (c).

Figure 5.12(a) is the SNOM that generates the topographic data from variations in the *z*-piezo to maintain a constant tip-sample separation as it scans the probe across the aperture. Figure 5.12(b) and 5.12(c) are the PMT and APD used to record the intensity and spectrally filtered intensity respectively. The collected signal was intense enough to use the PMT in this case, else a second APD would have been utilised at this location.

Hörsch *et al.* [1] used a SNOM to investigate transverse modes of VCSELs, but instead of filtering using a monochromator, spectra were collected with a spectrometer at every point in a 64x64 grid. Images were then produced by post-processing filtering of the spectral data at each grid point. This method has both advantages and disadvantages. The advantage was that the data was collected in one session. The resolutions of the acquired images however were of a lower quality than those shown and discussed in Chapter 6. To improve on this [1], a much longer scan would have been required in addition to the storage and manipulation of a great deal of spectroscopic data. It was for this reason it was decided to use the set-up described in Figure 5.9 to obtain successive images in as short a time as possible thus minimising any thermal variations within the VCSEL with time in any one image.

5.6 Configurations used to obtain spectra and detect fluorescent emissions from single / multiple quantum dots

Preliminary investigations of quantum dot samples involved bottles of bulk solutions containing one or more sizes of quantum dot, resulting in multiple-peak fluorescence. Far-field fluorescent tests were carried out by illuminating the solution directly with the laser as shown in Figure 5.13 allowing immediate determination of spectral output and quality.

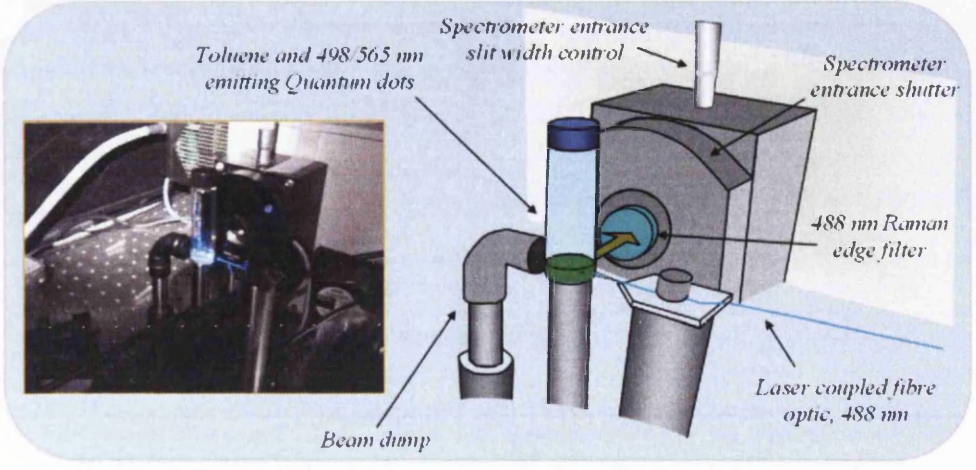

Fig. 5.13 Illumination of quantum dot bottle samples to determine expected spectral output when used in the near-field.

The spectrometer was used to detect the fluorescence from single quantum dot solutions, in addition to a combined solution, shown in Figure 5.14. This spectral data provided important spectroscopic information prior to near-field studies such as peak position, the spectral width and range of the fluorescent emission of the quantum dot ensemble.

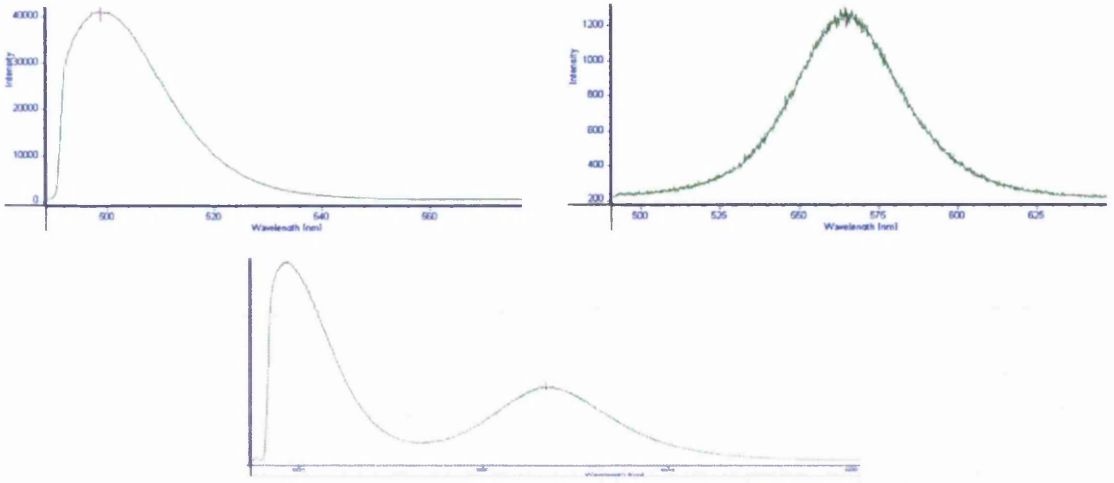

Fig. 5.14 Far-field collections of quantum dot solutions using the above setup.

With regards to experiments involving near-field studies of single quantum dots, the PMT was of insufficient quality to detect the required near single-photon levels. For such a fluorescent response, an APD was used with its approximately efficiency of 0.45 within the visible spectral range. Figure 5.15 illustrates this simplified setup.

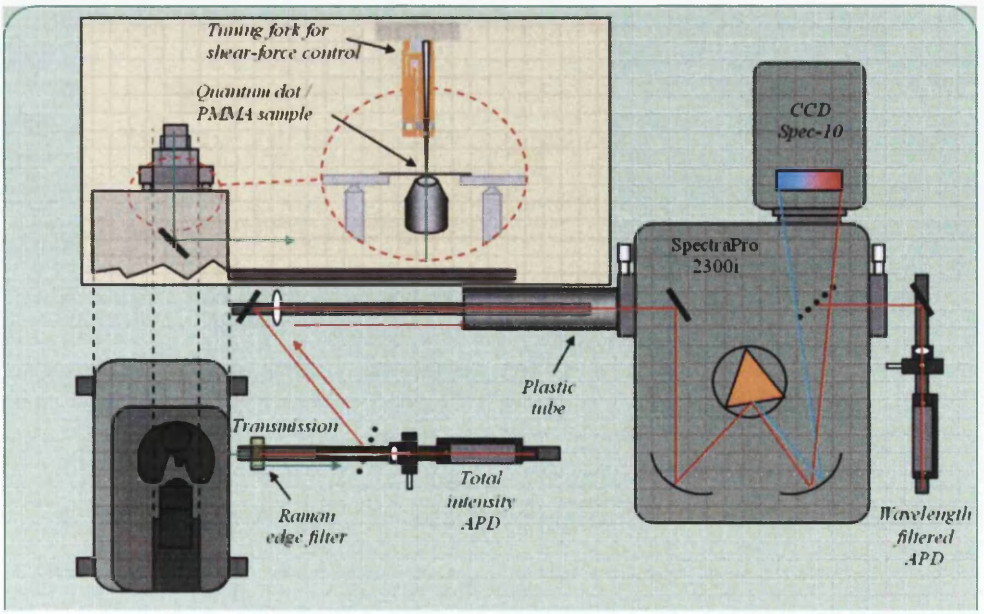

Fig. 5.15 Spectroscopic setup used to detect single quantum dots. APDs are used to detect total intensity and single wavelength emissions via the monochromator.

The SNOM tip illuminating a 50-100 nm wide area was used to stimulate, in the near-field, nanometre thick layers of PMMA embedded with a dilute solution of < 5 nm sized quantum dots. Fluorescence emitted from the quantum dots passed through the mica substrate to the transmission optics. A collimated beam consisting of both laser light and fluorescence passed to the Raman edge filter and was stripped of all but the required fluorescence. The APD labelled 'Total intensity APD' was used to detect ~ 50% of light that passed through the 50/50 mirror, and focussed with an achromatic lens mounted in an *x-y-z* positioner. The remaining 50% fluorescence was focussed down onto the spectrometer entrance slit. The plastic tube, painted internally matt black, was used to dampen any side stray light from fibres within the black box that were directed toward the spectrometer. The spectrometer, as discussed earlier in this chapter, was used in two configurations, primarily for spectral detection and secondly as a monochromator, by passing a narrow spectral band out of the side exit for detection with a second APD. It has been shown by Matsuda *et al.* [2], that using near-field excitation and simultaneous collection with the same SNOM probe is also possible, at least at cryogenic temperatures. Such a setup, however, would have made the system less flexible to other researchers using this equipment, in addition to the difficult task of alignment.

5.7 Optical limitations of setup based upon spectrometer CCD detector etalon effect

For some work during the course of the present study, experiments were carried out at wavelengths ~ 650 nm or more. With results at such wavelengths, where a peak broader than a few nano-metres was detected, severe modulation of the waveform were observed. To investigate this, a white-light source was directed into the spectrometer

and a spectrum collected, as shown in Figure 5.16. A smooth blackbody curve was expected, peaking at ~700 nm, but instead, at wavelengths from ~ 650 nm and to longer wavelengths, strongly modulated spectra were detected as before. A complete image was also collected whereby the horizontal is still representative of wavelength, and height that of the different rows of the CCD.

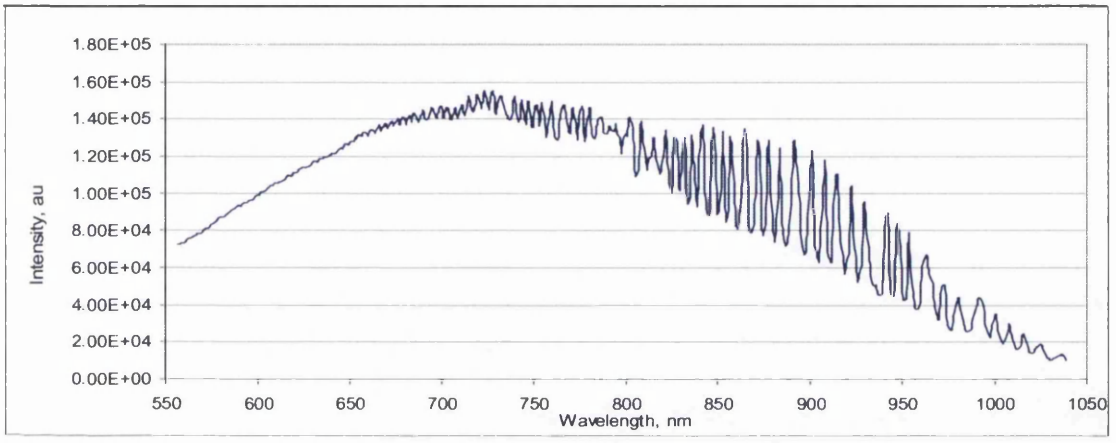

Fig. 5.16 White light data obtained from the spectrometer (one CCD row only) in two collections and 'glued' together using the in-built software to give a broad spectral range.

This is shown in Figure 5.17 for the range 560 nm to 840 nm with an inset highlighting the range 650 nm to 700 nm. It is very clear from this image that the modulation effect varies between successive CCD pixel rows.

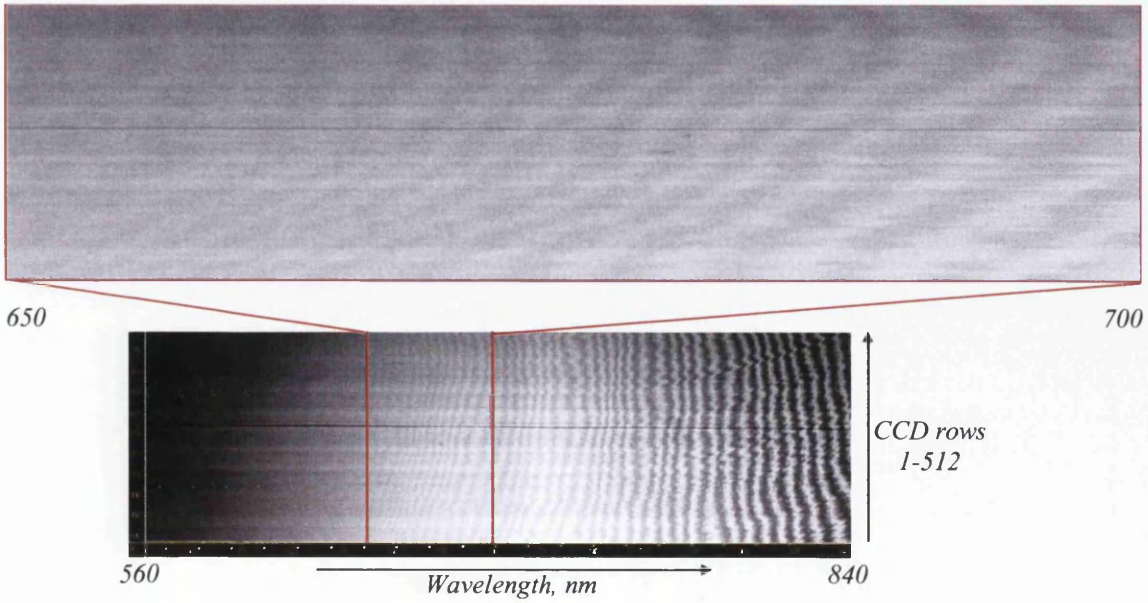

Fig. 5.17 A spectral image of a white-light source showing all the CCD rows in the range 560 nm to 840 nm, with an inset highlighting the range 650 nm to 700 nm.

As an example of some of the work that suffered from this issue, Figure 5.18 represents a far-field spectrum collected from a resonant cavity light emitting diode (RCLED). The peak is asymmetric but no modulations were observed in the spectrum, as discussed by Schubert [3] and Castagna *et al.* [4].

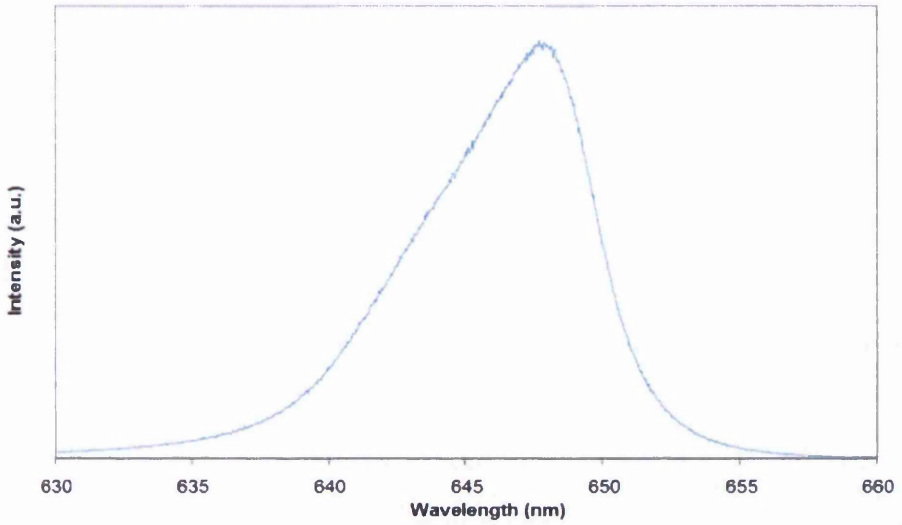

Fig. 5.18 Asymmetric emission spectrum from an RCLED driven at 10 mA, collected in the far-field.

This far-field spectrum established initial spectral parameters before using the SNOM to obtain information from the near-field. Topographical and optical images at the edge of the aperture of the RCLED in Figure 5.19 were collected, and subsequent point spectroscopy was carried out at 2 locations within the aperture marked *A* and *B*, where the intensity of the emitted light was vastly different.

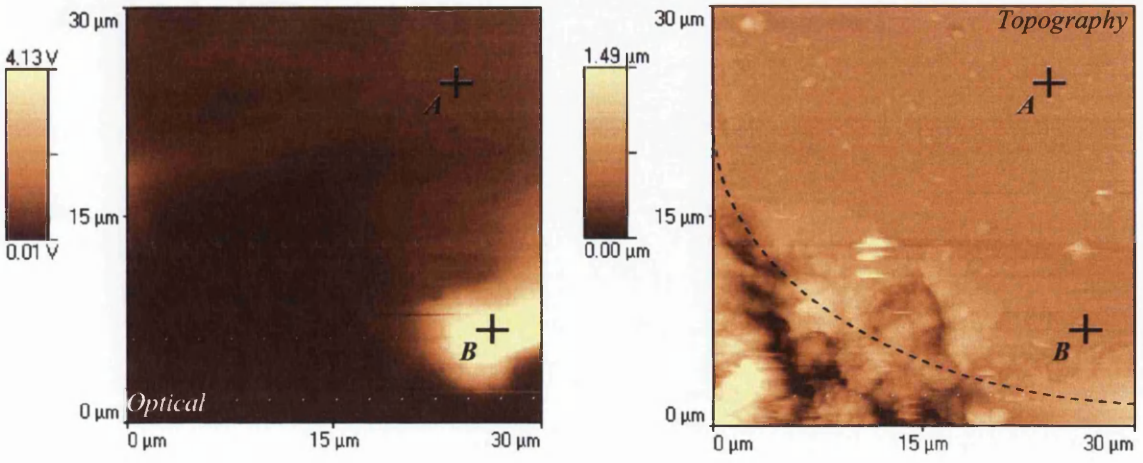

Fig. 5.19 Topographic and intensity images collected in the near-field at the aperture of an RCLED. Point spectroscopy was then carried out at two locations, marked A and B, of differing intensity.

The spectra shown in Figure 5.20 that were collected in the near-field of the RCLED aperture, however, showed strong modulations of an asymmetric peak compared to the far-field spectrum shown in Figure 5.18.

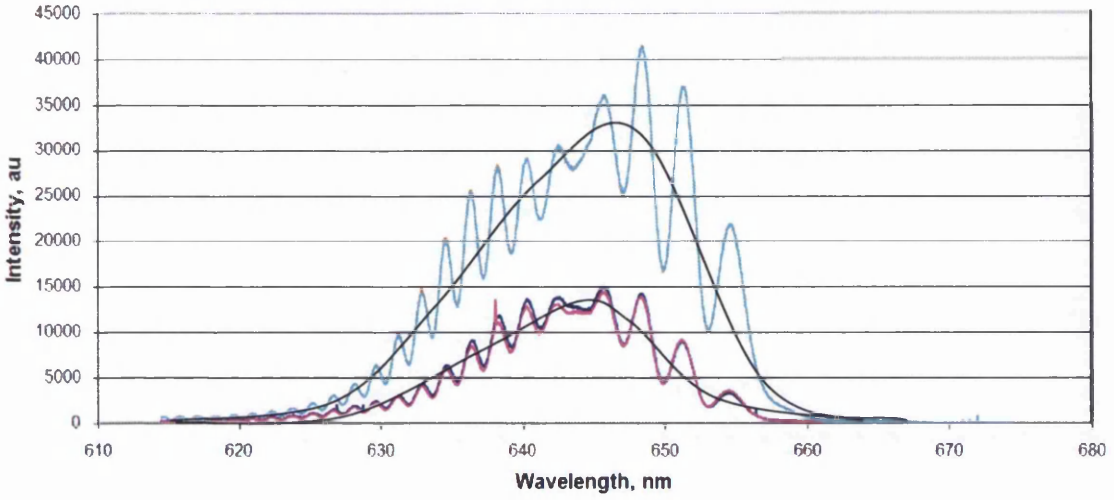

Fig. 5.20 Two repeated collections at 5 and 20 seconds, each at two different locations highlighting the reproducibility of the peaks at specific wavelengths.

The spectral profiles at the two locations marked *A* and *B* in Figure 5.19 were very different as expected, however, the peak positions of the modulations didn't shift in wavelength. Two collections at each location were carried out to show reproducibility. This investigation of RCLEDs in the near-field continued to attempt to explain this behaviour, as the far-field didn't show such modulations. The very presence of the modulations however was unexpected, regardless of their apparently repetitive spectral signature.

It was found that this issue of modulation of spectral data above 600 nm was a known experimental setup issue. The refracted light from the grating that enters the CCD has to pass into a silicon layer, an integral part of the CCD detector. Figure 5.21 shows the relative silicon absorption from the UV, through the visible spectrum and up to 1100 nm.

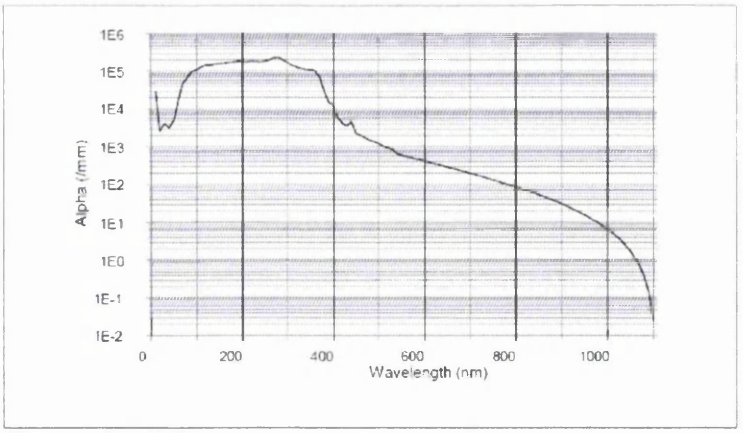

Fig. 5.21 Optical absorption coefficient for silicon as a function of wavelength (Data obtained from Marconi Applied Technologies).

The scale is logarithmic and it is clear that the absorption changes by a factor of 10 between wavelengths ~ 600 nm and ~ 800 nm. This increasing transparency results in an effect known as spectral etaloning. It is also important to note that variations in the thickness of the silicon layer result in an effect known as spatial etaloning. Together, these two factors produce the effects seen in spectral results from the near-field RCLED data and the white light source data.

5.7.1 Spectral etaloning

As illustrated in Figure 5.22, light from the spectrometer grating enters the CCD detector through the back of the CCD with the angle of incidence varying with wavelength and position. The photons enter a layer of silicon with refractive index ~ n = 4 and of thickness ~10 μm as part of the detection process. However, as described in section 5.7, the absorption of silicon is significantly reduced at wavelengths from ~ 650 nm and above such that it becomes transparent. Figure 5.22 illustrates the first few wavelengths of light that strike the silicon on the left side of the CCD. Due to large discontinuities in refractive index between the different layers of the CCD, as the light reflects back and forth, points of constructive and destructive interference form along

the CCD array. These occur where the path length of the incident wavelength within the etalon cavity, formed as a result of the silicon transparency, is an integer multiple of wavelength, $m\lambda$.

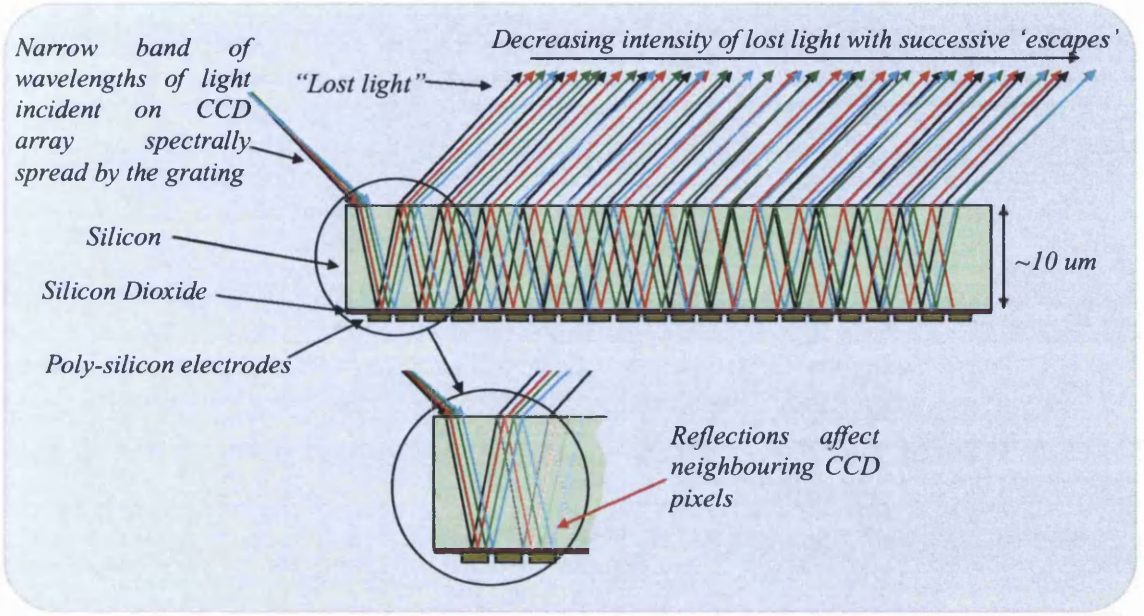

Fig. 5.22 The thin silicon slice (a few μm thick) becomes transparent at wavelengths longer than ~ 650 nm.

Intensity decreases due to losses at the etalon edges, some of which fall on a CCD pixel. Intensities and associated phase of reflections add to the intensity and phase of the wavelength originally intended for a particular CCD pixel upon first entering the silicon layer, as indicated in Figure 5.22 with the red arrow. This constructive and destructive interference modulates the detected spectrum. The fundamentals of etalon theory are addressed in Appendix 3.

5.7.2 Spatial etaloning

This effect causes a variation in the spectral etaloning that occurs due to the silicon layer, as discussed in section 5.7.1. Spatial etaloning arises as a result of monochromatic light falling on the silicon layer which has a varied thickness along its length. This causes a change in the position of the points of constructive and

destructive interference. If the silicon layer were of a completely uniform thickness, then only spectral etaloning would occur due to the increasing transparency of silicon with wavelength.

Back illuminated CCD arrays, as used for the spectroscopy work presented, have anti-reflection coatings to minimise the reflections of light back and forth through the silicon layer at transparent wavelengths. The back illuminated structured CCDs are the preferred type of detector due to their direct absorption, giving superior quantum efficiency compared to the front illuminated variation, in which the light must traverse electrodes, thereby reducing efficiency.

After the realisation of the limitations of the spectrometer at such wavelengths, simulations shown in Appendix 4 were carried out to confirm the origin of these modulations, and to determine the possibility of compensating for these effects during post-processing of collected spectra. The reason for the difference in the spectra from the RCLED obtained from the far-field, Figure 5.18 and near-field, Figure 5.20, became clear. The far-field collections, detected by the spectrometer were not so focussed on the spectrometer input slit and so fell on a broad range of CCD rows. Over several rows, the silicon backing layer thickness varied enough such that the modulations in the asymmetric spectra averaged out to a relatively smooth curve. The near-field collections however were more focussed and fell on only a few CCD rows. Thus, no matter how many rows the collection was averaged over, the few rows that were illuminated from the near-field collection, dominated the resulting spectrum, revealing the modulating nature of the etalon behaviour within the CCDs silicon layer. Had the

near-field collection been defocused to land on all 512 rows, these peaks would also have blended to form a smoothed curve as seen in the far-field in Figure 5.18.

5.8 Conclusion

The final experimental arrangements that were assembled and utilised to obtain the results contained within Chapters 6 and 7, were designed to be extremely flexible. This was important as there were several users of the equipment through the course of this work and it was therefore necessary to minimise changes to the precise alignment of the optical paths once they had been established and optimised. The arrangements described allowed simultaneous spectroscopic and intensity imaging of a range of devices and materials without the necessity of interaction with the optics, once an experiment was in progress.

The experimental arrangements used have paved the way for future experiments such as apertureless SNOM Raman [5,6]. It may also allow for the integration of pulsed lasers and detectors for life-time measurement techniques, as discussed by Cadby *et al.* [7]. The near-field work carried out on quantum dots can be furthered by investigations using FRET as discussed by Sekatskii [8]. This technique, coupled with life-time measurements, could produce significantly enhanced optical and spectroscopic information, possibly at resolutions as far as 10 nm.

Limitations of the spectrometer have been observed such as an etalon effect at near infra-red wavelengths. These have been shown to be fully understood, and discussions have highlighted the possibility of compensating for such effects in future work.

References

[1] Hörsch I., Kusche R., Marti O., Weigl B., Ebeling K.J., J. Appl. Phys. **79**, 3831, (1996)

[2] Matsuda K., Saiki T., Nomura S., Mihara M., Aoyagi Y., Nair S., Takagahara T., Phys. Rev. Lett. **91** (17), 177401.1-177401.4, (2003)

[3] Schubert E.F., Light Emitting Diodes, Cambridge University Press, (2003)

[4] Castagna M.E., Muscará A., Leonardi S., Coffa S., Caristia L., Tringali C., Lorenti S., J. of Luminescence **121**, 187-192, (2006)

[5] Hayazawa N., Saito Y., Kawata S., Appl. Phys. Lett. **85** (25), (2004)

[6] Anderson N, Bouhelier A, Novotny L, J. Of Optics: Pure Appl. Opt. **8**, S227-S233, (2006)

[7] Cadby A.J., Dean R., Elliott C., Jones R.A.L., Fox A.M., Lidzey D.G., Adv. Mat., **19** (1), 107, (2007)

[8] Sekatskii S.K., Phil. Trans. R. Soc. Lond. A **362**, 901-919, (2004)

6 Results of near-field studies of vertical cavity surface emitting lasers

6.1 Introduction

This work was undertaken in order to characterise the optical properties of vertical cavity surface emitting lasers (VCSEL) in the near-field region and to expand the understanding of their spectroscopic properties. To this end it was also essential to obtain some complementary far-field measurements.

This chapter also describes the observations of several VCSELs in both the far-field and the near-field. Samples of VCSELs for study were obtained from Cardiff University (Dr HD Summers) and Thorlabs, in the UK.

The experimental setup shown in Figure 5.9 was used for spectroscopic studies of VCSELs. This comprised of a far-field path for initial measurements on which more in-depth studies were based in the near-field. For this, a SNOM was utilised to collect light emitted from the semiconductor laser directly at the aperture and guided with standard optics to sensitive light sensing and discriminating equipment. APDs, a PMT and a spectrometer were controlled with the aid of two PC's linked together using hand-shaking mechanisms to coordinate intensity and spectroscopy measurements.

6.2 Far-field study of an 800 nm VCSEL

An 800 nm emitting VCSEL sample, manufactured at Cardiff University, with a maximum injection current rated at 50 mA, was placed with its output directed into the reflection path of a SNOM. Spectroscopic properties were obtained via the far-field reflection path as indicated in Figure 5.9.

The VCSEL was driven with a Thorlabs LDC202 Laser Diode Driver unit. This allowed a maximum injection current of 200 mA, far beyond that of the maximum allowed for the VCSEL under test. The VCSEL was driven with an injection current ranging from 22.01 mA to 49.99 mA by manual adjustment in 1 mA steps. At each current step, the VCSEL was given time to settle at the new injection current level for 20 s, at which time a spectrum was collected with an accumulation time of 1 s. A graph of the accumulated spectra is shown in Figure 6.1 (a shift up has been applied to the intensity scale to each spectrum to clearly show the spectra separately).

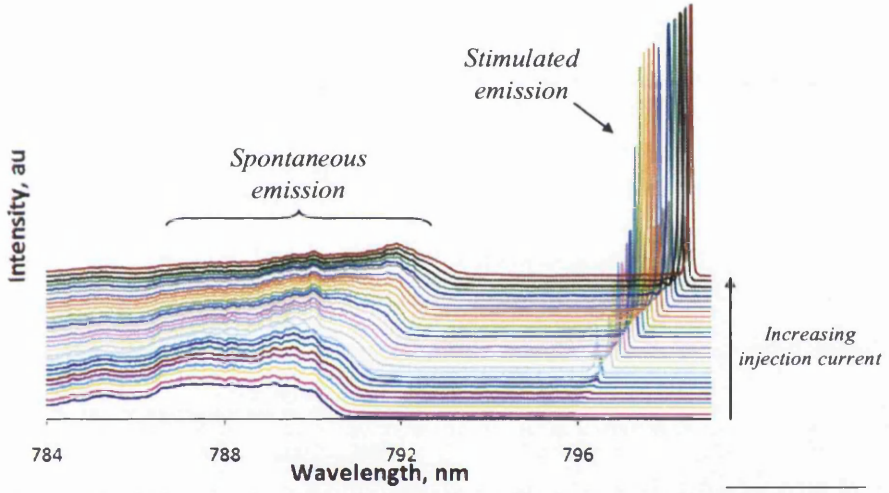

Fig. 6.1 Far-field collection from an ~ 800 nm emitting VCSEL for a range of injection currents. The baseline for each injection current has been raised to separate them for illustrative purposes.

The lasing peaks, beginning around 796 nm, red-shift with increasing injection current. This is due to the cavity resonance shifting as the cavity increases in length with temperature, and the changing refractive index with increasing numbers of available carriers. Effectively, as discussed by Sharma *et al.* [1], the band-gap of the gain medium changes with temperature, resulting in a shift of the gain window of the device.

The lasing threshold for this device is approximately at an injection current of 30 mA with the fundamental transverse mode first appearing at a wavelength of 796.50 nm. The intensity of this lasing peak is however significantly lower compared to that of the

spontaneous emission at 30 mA, but increases steadily with injection current as a response to the increased availability of carriers. This transverse mode eventually reduces with higher injection current due to a significant increase in carriers making possible a second, simultaneous transverse mode that dominates at 38.50 mA. Figure 6.2 shows the second transverse mode emitting at a shorter wavelength than that of the fundamental, at 797.32 nm. The peak shift in wavelength as a function of injection current is very close to being linear, at a reasonable rate of 0.1 nm mA^{-1}. This is attributed to the linear expansion of the optical cavity with steadily increasing temperature due to the lack of any temperature control.

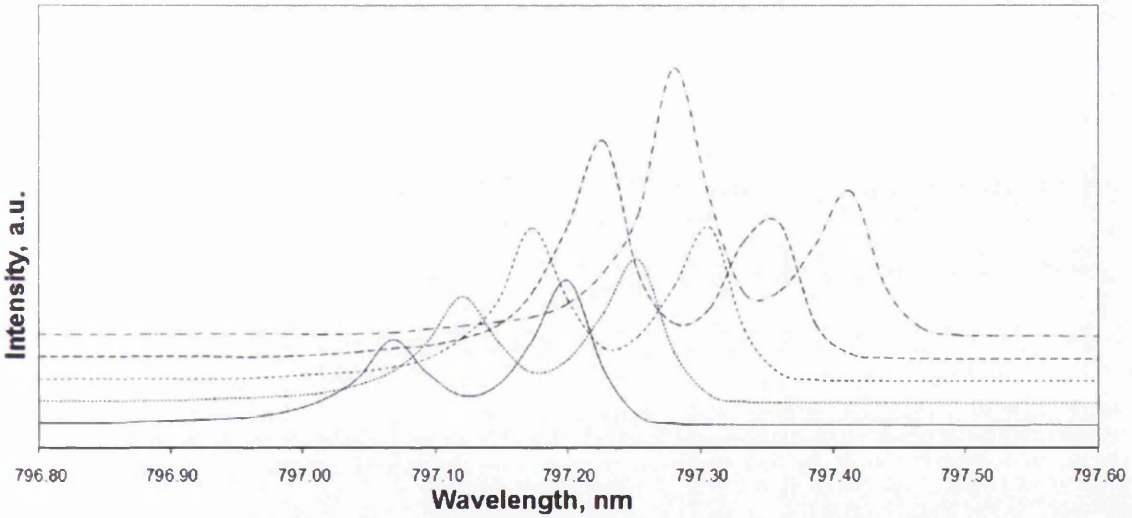

Fig. 6.2 Software zoom of Figure 6.1 above showing the steady switch over of dominance of transverse modes with increasing injection current, from 37.00 mA, to 38.99 mA.

6.3 Spontaneous emission

Below the lasing threshold, spontaneous emission is the primary output from the device. Population inversion has not occurred due to the injection current providing insufficient excited states within the gain medium to compete with cavity losses. From Figure 6.3, 30 mA was found to be the lasing threshold of the device. Below this injection current, the peak was lost into the background spectrum.

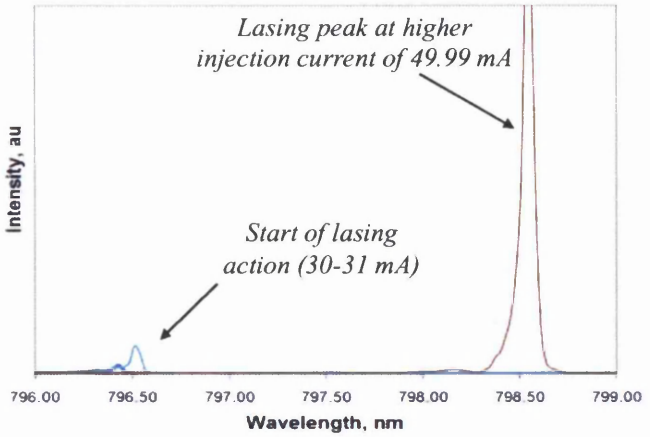

Fig. 6.3 Increasing injection current from 28.99 mA to 49.99 mA, illustrating the injection current at which lasing action begins.

The rise in the integral of the area of spontaneous emission for each current from Figure 6.1 with injection current is apparent up to 30-31 mA as shown in Figure 6.4. At this point the total spontaneous emission intensity begins to decrease as cavity gain results in lasing action dominating the emission, thus reducing the excited states available for spontaneous recombination.

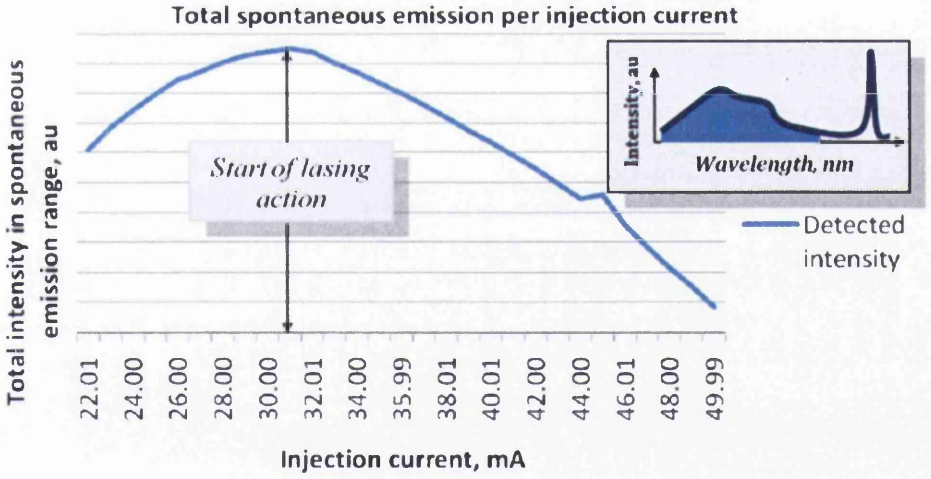

Fig. 6.4 Illustrating the injection current at which lasing action truly begins by monitoring the peak in the integral of spontaneous intensity.

6.4 Initial near-field studies of a second 800 nm VCSEL

A second VCSEL manufactured on the same substrate was electrically connected with a thin gold wire, bonded with silver loaded epoxy via its top ring contact. This was due to

the failing of the first VCSEL tested, most probably due to over-heating during the test results are shown in Figure 6.3.

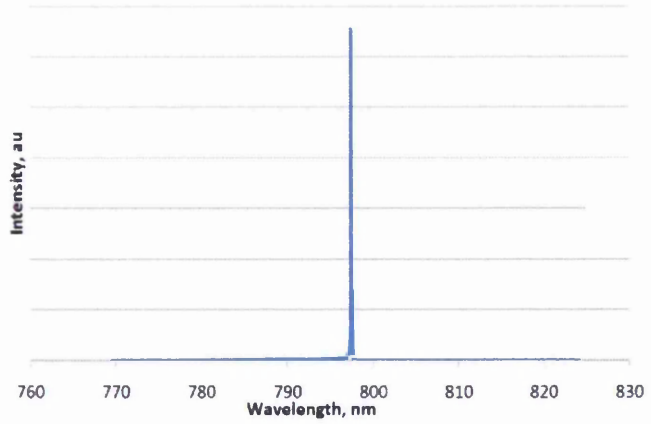

Fig. 6.5 Lasing peak at 797.44 nm for an injection current of 39.49 mA.

The current was set to 39.49 mA that revealed a lasing peak at a longer wavelength of 797.44 nm, as shown in Figure 6.5. The spectrometer was utilised in a monochromatic mode, with its centred wavelength passing collected light to a second APD at a side exit, acting as a narrow bandwidth intensity detector. Photons detected via the APD within this narrow band of wavelengths were signalled as individual pulses to the SNOM ECU as illustrated in Figure 5.9, and used to produce spectrally filtered intensity images. In this way, topographic, intensity, and spectrally filtered images with no spontaneous recombination or other transverse modes being present were obtained simultaneously.

Topographic and optical images of the VCSEL were obtained from around the large ~ 60 μm aperture as shown in Figure 6.6. A complete aperture image was however not possible due to the equipment's 30 μm scan range limit.

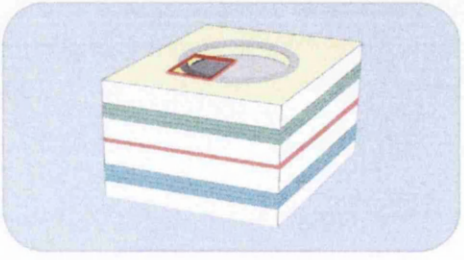

Fig. 6.6 A partial scan was carried out at the surface of the VCSEL of an area close to the aperture edge.

UNIVERSITY OF WALES LIBRARY

Figure 6.7 shows the topographic (a), total intensity (b), and spectrally filtered at 797.44 nm (c) images obtained from the VCSEL using the collection mode of the SNOM.

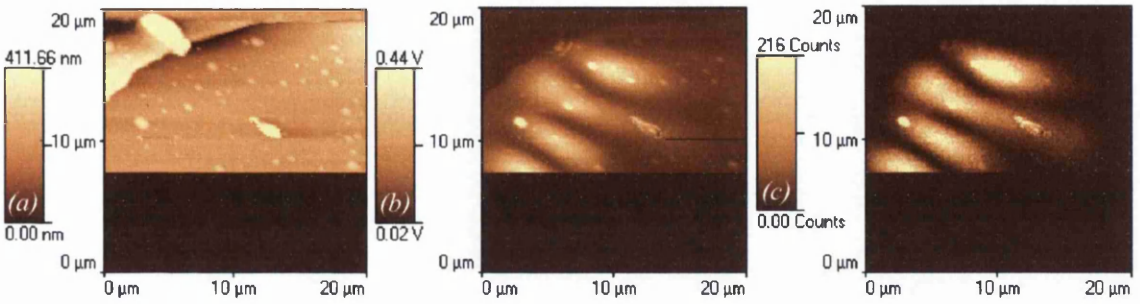

Fig. 6.7 A Partial scan of an area close to the aperture edge showing topographic (a) total intensity (b) and spectrally filtered intensity (c) (at 797.44 nm).

For this lasing VCSEL, the transverse modes within the cavity compete for available carriers resulting in a detectable spatial separation at the aperture, as shown in Figure 6.7. Not all transverse modes are rotationally symmetric due to non-uniformities within the cavity and the aperture, thus modes that appear in only certain regions of the aperture will form. This non-uniformity aspect can be compared to work using a SNOM by Knopp *et al.* [2] who showed intensity and topographic images of ~ 15 µm apertured VCSELs, and Sharma *et al.* [1] who spectroscopically studied a 10 µm apertured selectively oxidised VCSEL. Both groups detected a partially structured, yet non-uniform field intensity at the aperture surface.

Due to the irregularly structured optical response of the VCSEL shown in Figure 6.7, and the size of its aperture being far larger than the scan range of the SNOM, it was decided to study a commercially available VCSEL. This would have the benefit of possessing known parameters, along with a smaller emitting aperture to study.

6.5 Study of an 845 nm commercial VCSEL

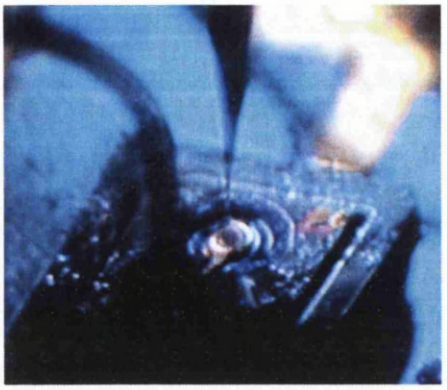

Fig. 6.8 SNOM probe approaching the 13 μm aperture from above, with the top contact wire entering the picture from the left.

The primary study was carried out on a commercially available, oxide confined, 845 nm emitting/1.85 mW VCSEL in a TO-46 package, details of which can be found in Appendix 6. A photo showing the VCSEL with the top contact wire, with an outer-ring diameter of approximately 23 μm and an aperture of ~ 13 μm, is shown in Figure 6.8. Current confinement within the device was achieved with an oxide-confinement configuration as shown in Chapter 4, section 4.6. A simple non-cooled VCSEL mount was devised to secure the position of the VCSEL in its TO-46 package as shown in Figure 6.9. This allowed electrical connections to be made within the tight confines of the SNOM.

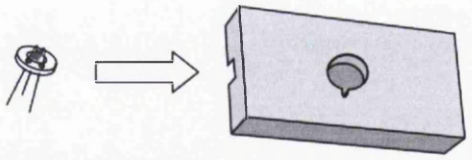

Fig. 6.9 VCSEL Laser in a TO-46 package, and the hard plastic mount to secure its position within the SNOM optics.

As with the previous VCSEL lasers, far-field collections of the device were carried out, initially for a range of currents ranging below the specified typical threshold of 2.2 mA, from 1.00 mA up to 1.55 mA. The spectral data from 1.34 mA to 1.44 mA are

illustrated in Figure 6.10. The lasing threshold can be seen to be approximately 1.40 mA where a peak in intensity rises sharply at a wavelength of ~ 845.40 nm.

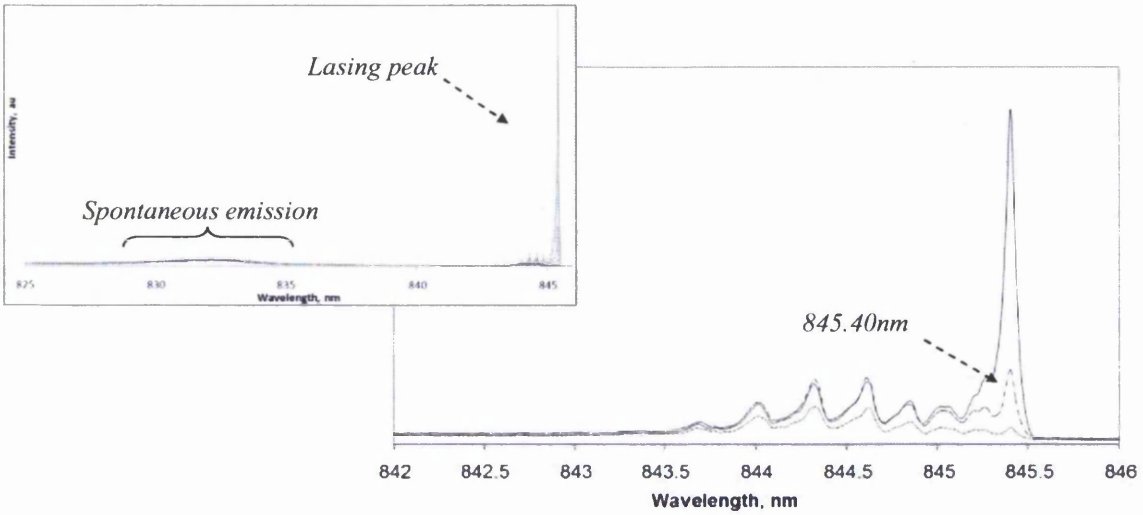

Fig. 6.10 Far-field collection with increasing injection current from 1.34 to 1.44 mA, illustrating the point of lasing of the device at 1.40 mA, resulting in the fundamental mode emission at a wavelength of 845.40 nm. Figure (a) shows the both the spontaneous and stimulated emission, while (b) shows only the stimulated emission spectral range.

Integrating spontaneous emission intensities over the range 825 nm to 840 nm as before, and graphing this against iniection current we find a peak at 1.40 mA in Figure 6.11.

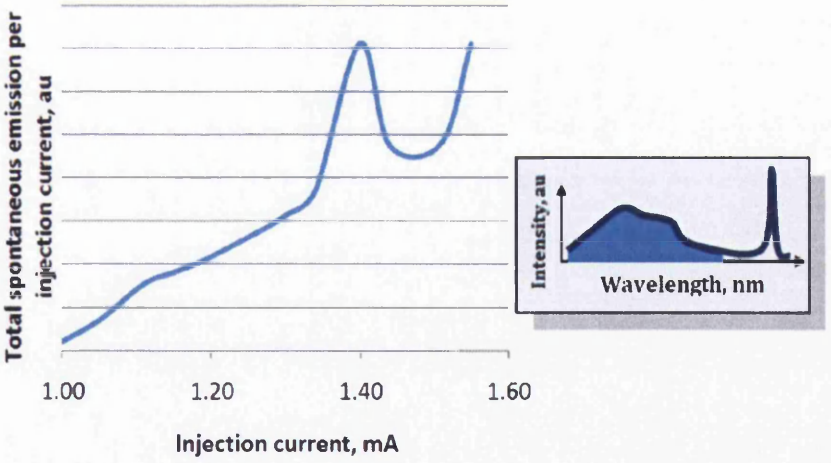

Fig. 6.11 The peak in the integral of spontaneous intensity indicates the probable point of lasing threshold.

The peak occurring in the spontaneous emission at 1.40 mA, as shown for a previous VCSEL device in Figure 6.4, corresponds precisely with the lasing threshold fundamental transverse mode at a wavelength of 845.40 nm, shown in Figure 6.10. The drop off in spontaneous emission intensity is due to the lack of available carriers as

excited electrons are instead stimulated to the ground state more readily at this critical injection current. Once the injection current is increased sufficiently however, the spontaneous emissions rise again. Figures 6.10 and 6.11 have been combined into Figure 6.12 to illustrate the simultaneous nature of spectral events. Figure 6.12(a) shows the normalised data to help visualise the simultaneity of the onset of lasing, while Figure 6.12(b) shows the measured integrated spontaneous and lasing intensity on the same graph. Unfortunately, there are no further data available to determine the spontaneous emission intensity beyond 1.55 mA, but as it is a lasing device it is assumed this intensity curve will quickly drop off for lack of available carriers due to stimulated emission, as was the case for Figure 6.4. It must be noted that the injection current was adjusted manually, and the resultant heating effect of the VCSEL's cavity was allowed to stabilise before subsequent spectra were collected. If insufficient time is given for the device to thermalise, as can be seen in Figure 6.4 and Figure 6.12, there are very likely to be some anomalous peaks in the stimulated or spontaneous emission graphs.

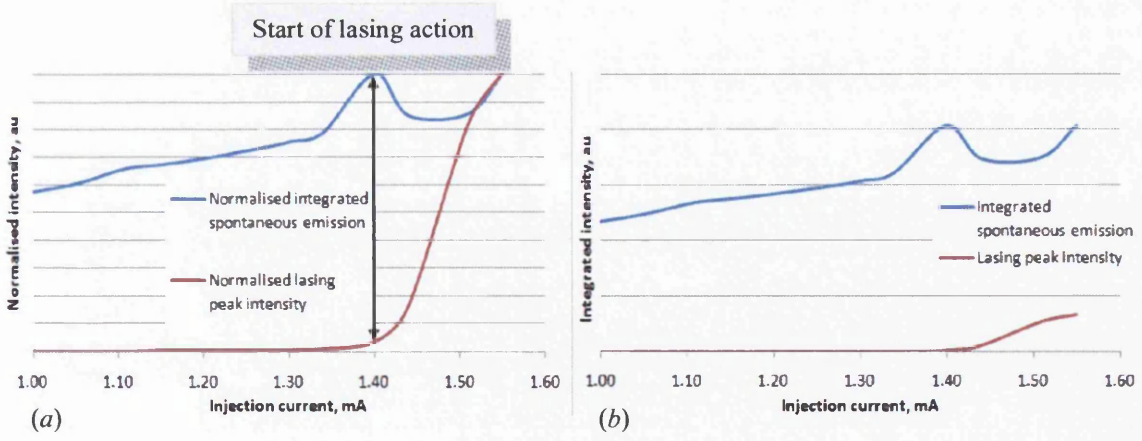

Fig. 6.12 Graph highlighting the point of population inversion where the threshold injection current at a wavelength of 845.40 nm results in a reduction of the carriers available for spontaneous emission. (a) shows the normalised data for the stimulated and spontaneous, while (b) shows the true intensity for each.

6.5.1 Multiple transverse modes

With increasing injection current the gradual development of subsequent transverse modes at ever higher energies occurs, each taking up some of the available gain within the cavity. Figure 6.13 illustrates this, with each transverse mode red-shifting with injection current at a rate of approximately 0.163 nm mA^{-1}. This is half that compared to Lu *et al.* [3] who studied similar aperture sized VCSELs in the near-field using SNOM.

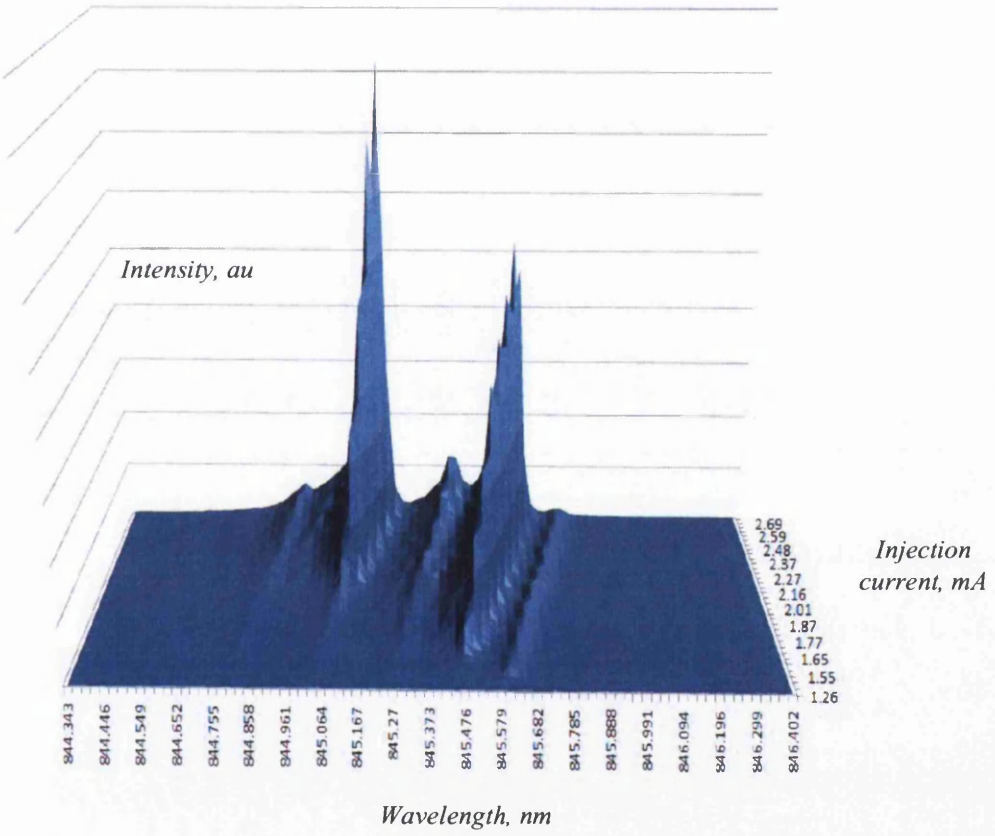

Fig. 6.13 Far-field collection of a range of injection currents from below threshold to above illustrating the red-shift of the transverse modes.

It is known that multiple modes limit the single mode power and also the distance a signal might travel before de-coherence due to dispersion of the individual modes. This in turn causes a severe degradation of the signal. These are important considerations for the use of VCSELs in fibre optic communications.

6.5.2 Near-field studies of an 845 nm commercial VCSEL

The injection current was set to 1.47 mA, just above the lasing threshold as shown in Figure 6.10. The output wavelength of the monochromator was then centred on the spontaneous emission wavelength of 840.49 nm, and the VCSEL aperture scanned with the SNOM. As shown in Figure 6.14, emissions were detected with the aid of a PMT for intensity, and a low noise APD for the monochromatic light. Figure 6.14 below shows (a) topographic, (b) total intensity and (c) spectrally filtered intensity at 840.49 nm.

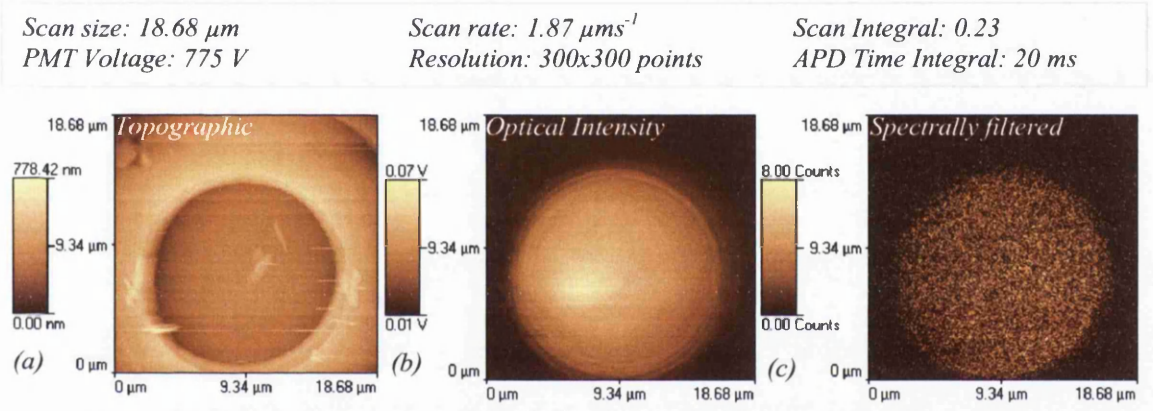

Fig. 6.14 Topographic (a), total intensity (b), and spectrally filtered in the spontaneous emission region (c), of the VCSEL having a lasing threshold of 1.40mA, driven at 1.47 mA.

The intensity in Figure 6.14(b) is dominated by the fundamental transverse mode intensity, slightly off the central axis, while Figure 6.14(c) shows a small percentage of the spontaneous emission, ~ 840.49 ± 0.10 nm as the slit width at the exit of the spectrometer was not widened. The relatively flat and uniform nature of this optical image illustrates the general lack of structure for non-coherent light within such a device.

A second scan was immediately carried out without switching off the device, with the same scanning parameters used to obtain the data in Figure 6.14. Figure 6.15 shows (a)

topographic, (b) total intensity and (c) spectrally filtered intensity at the lasing wavelength.

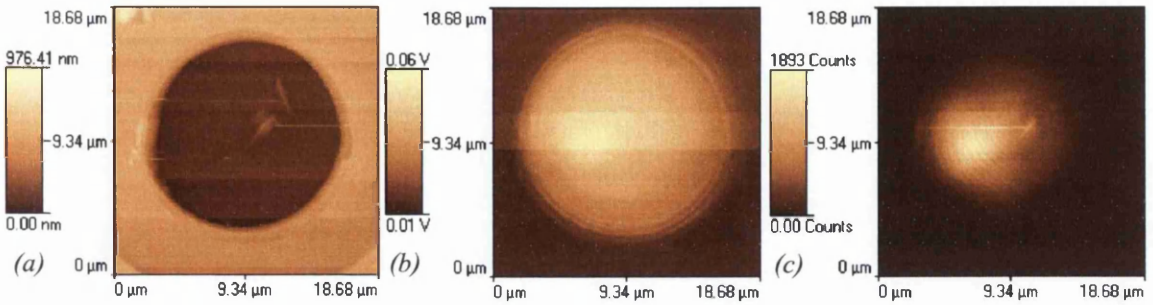

Fig. 6.15 Topographic (a), total intensity (b) and spectrally filtered at the lasing wavelength of the VCSEL, having a lasing threshold of 1.40 mA and driven at 1.47 mA (c).

The aperture of the device can thus be measured directly from the topographic images shown in Figure 6.14 and Figure 6.15, as shown in Figure 6.16, revealing a near circular structure. In one direction it measures 12.86 µm and perpendicular to this it measures 12.82 µm. The eccentricity here, valued at ~ 0.003, can be accounted for within the error of the scan resolution of the topographic image, thus the average of these two values is taken to be the true diameter of the aperture, at 12.84 µm.

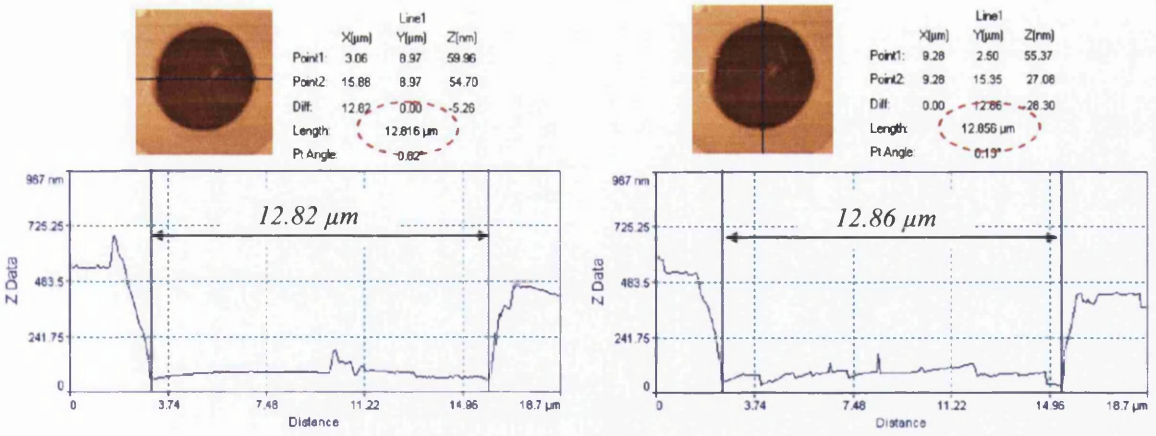

Fig. 6.16 Measurement of the aperture dimensions of the ~ 845 nm emitting VCSEL. This slight elliptical shape is within error of the scan parameters and the aperture is therefore considered to be circular.

The spectrally filtered peak in Figure 6.15(c) appears Gaussian in nature, as per the line scan shown in Figure 6.17(c) below. The Gaussian beam's maximum occurs off to one side of the central axis of the physical aperture. This is likely attributable to an offset

buried oxide-confining region within the device, steering the recombination centre away from the aperture's central axis. The off-set nature of the laser will be considered an important reason in later discussions in this chapter as a reason for the presence of circular, regularly spaced modulations of the output of the device, as can be seen in Figure 6.17(a). This figure is an addition of the optical and topographic data showing the intensity off-centre within the physical cavity. Figure 6.17(b) is a software-enhanced image of Figure 6.15(c) that exaggerates the modulations. Figure 6.17(c) shows a cross-section through the enhanced optical image revealing the regularity of these peaks.

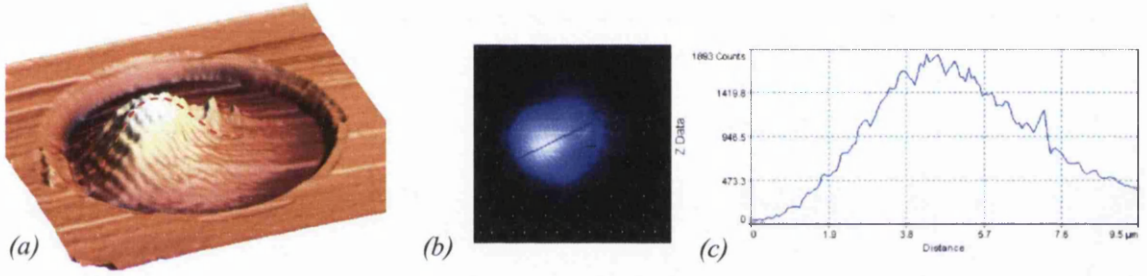

Fig. 6.17 Cross-section of the spectrally filtered image at threshold operation, showing the Gaussian nature of the fundamental mode (TEM_{00}). (a) shows a software representation of the optical superimposed onto the topographic data to show the spatial position of the fundamental TEM_{00} mode relative to the aperture, while (b) shows the optical, spectrally filtered intensity of the TEM_{00} mode, and (c) the line scan indicated in (a) and (b).

6.5.3 Detection of multiple transverse modes in the near-field

To study the development of transverse modes and the presence of concentric rings, higher injection currents were considered just above threshold current. Due to the fact that no cooling mechanism was present for temperature control of the device, and considering the duration that SNOM scans take, an injection current just above threshold which exhibited the presence of multiple transverse modes was selected. A far-field collection at an injection current of 2.34 mA is shown in Figure 6.18.

From this spectrum the wavelengths selected for single wavelength scanning were 844.95 nm, 845.19 nm, 845.56 nm and a combination of the remaining two dominant peaks at 845.37 nm.

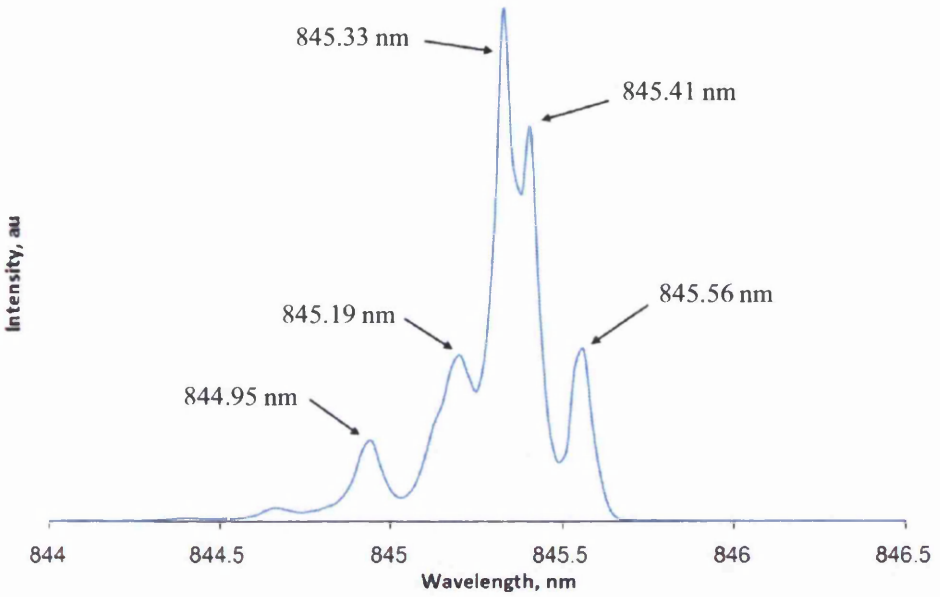

Fig. 6.18 Far-field collection of the VCSEL at 2.34 mA showing 5 transverse modes, the dominant present at approximately 845.33 nm.

The output power of the device was not measured with a power meter so its power had to be estimated from information on the specification sheet, bearing in mind that such values can vary by up to 30%. The output of the device was rated at 1.85 mW, at an injection current of 8 mA.

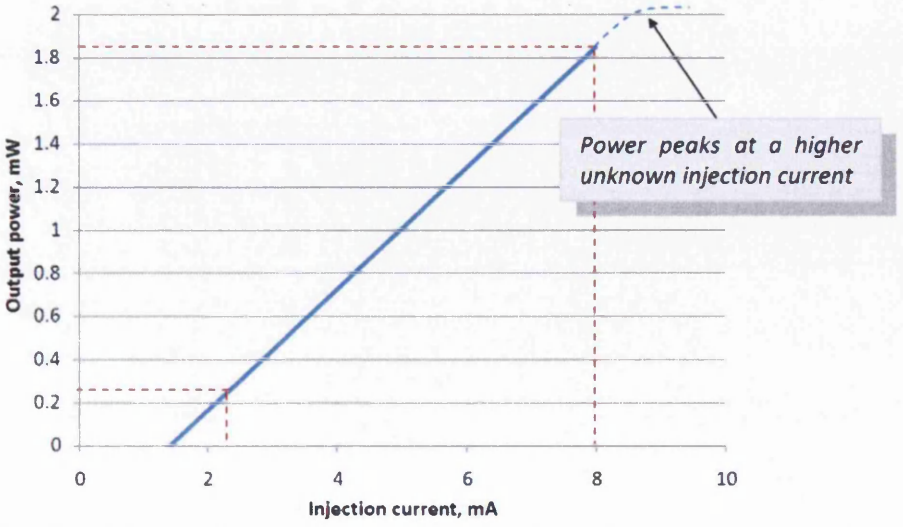

Fig. 6.19 Assuming a relatively linear response, allows us to determine the output power of the device at an intermediate injection current of 2.34 mA.

With the lasing threshold is at 1.40 mA and that the response before levelling off as shown in Figure 6.19 is likely to be fairly linear, we can deduce that at an injection current of 2.34 mA, the power is approximately 0.26 mW.

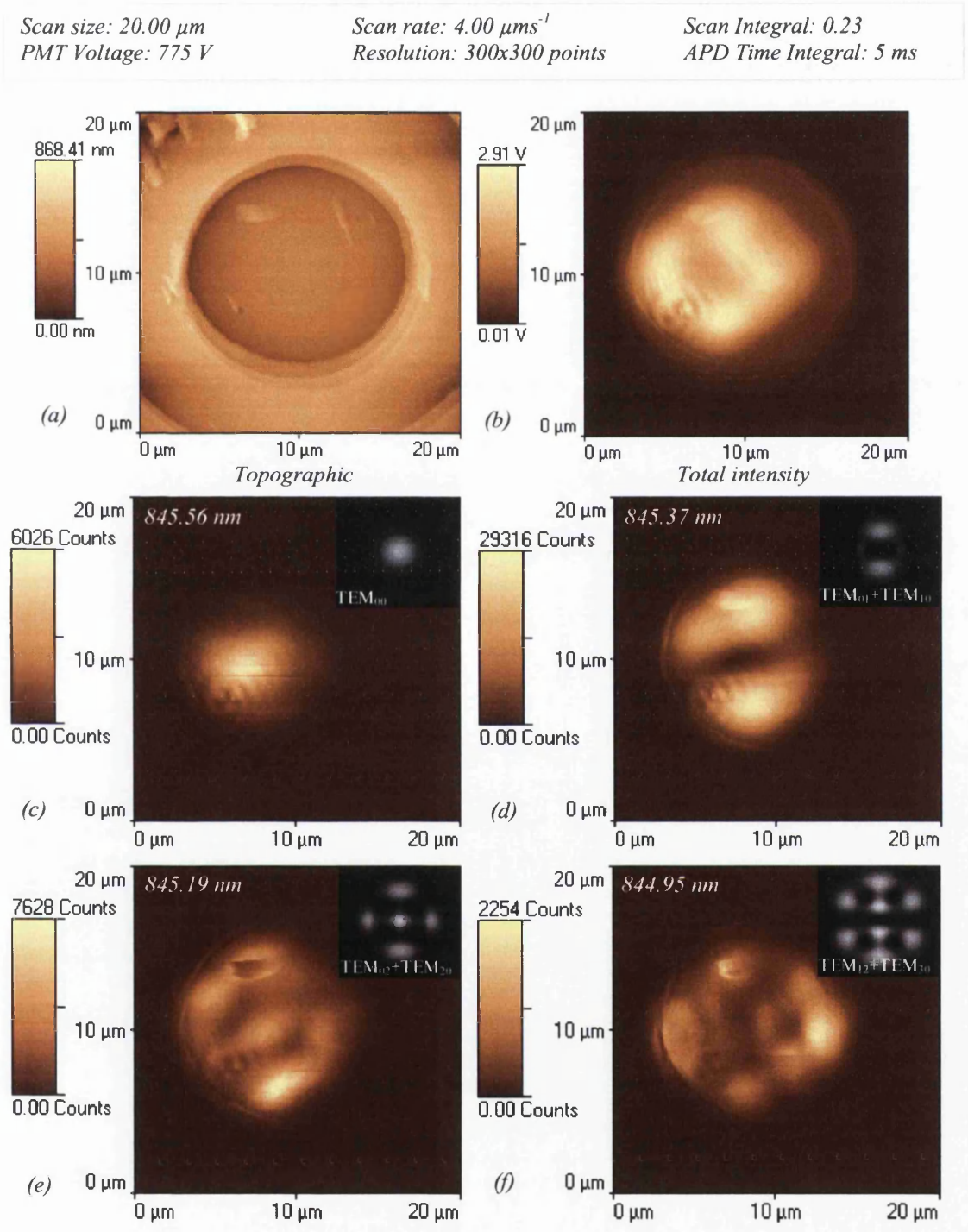

Fig. 6.20 Topographic (a), total intensity (b) and four spectrally filtered images at each of 4 wavelengths at 845.56 nm (c) 845.37 nm (d) 845.19 nm (e) and 844.95 nm (f). Each of the filtered images has its simulated Hermite-Gaussian TEM mode combinations shown as an inset ((a) TEM_{00}, (b) TEM_{01} and low intensity TEM_{10}, (c) TEM_{02} and low intensity TEM_{20}, and (d) TEM_{12} and TEM_{30}).

Before any spectrally filtered transverse modes were obtained, topographical and optical images were obtained to determine the spatial extent of the new multi-transverse mode output, as displayed in Figure 6.20(a-b). The intensity distribution at 2.34 mA is significantly different due to the 5 transverse modes now present, compared to the previous image in which only the fundamental is seen. Also, as before, the optical axis is off-set from the physical central axis of the aperture. Using the values obtained from the far-field collection in Figure 6.18, topographical, total-intensity and spectrally filtered images were obtained for each of the selected wavelengths, shown in Figure 6.20.

Neglecting spontaneous emissions, the combined intensity from the four filtered images contribute approximately to the total intensity observed in Figure 6.20(b). Individually Figures 6.20(c-f) show a range of Hermite-Gaussian TEM modes emitted simultaneously from the cavity. Figure 6.20(c) represents a TEM_{00} mode, Figure 6.20(d) predominantly TEM_{01} with a very low intense TEM_{10}, Figure 6.20(e) TEM_{02} and lower intense TEM_{20} and Figure 6.20(f) TEM_{12} and TEM_{30} modes. These spectrally filtered images and the transverse mode interpretations are all in full agreement with that discussed by Degen *et al.* [4]. The appropriate theoretical TEM modes have been combined and shown as grey-scale insets for each of the filtered images in Figure 6.20 (c-f). It should also be noted that the work published by Degen *et al.* [4] was studying that of the emission as a function of injection current. Different transverse modes become dominant dependent on the injection current. The time taken to generate the images of Figure 6.20, and their subsequent reproducibility, highlights the stability of the individual transverse modes within the gain medium at this injection current. In contrast to the studies performed by Degen *et al.* [4] and Knopp *et al.* [2],

the modes shown in Figure 6.20(c-f) were all produced at a single fixed injection current of 2.34 mA showing their simultaneous presence within the gain medium of the device.

The relative near-field intensities of Figure 6.20(c-f), were 6026, 29316, 7628, and 2254 respectively, and show good agreement with the far-field intensity spectrum of Figure 6.13. Figure 6.20(d) shows clearly the dominance at 845.37 nm. This wavelength is actually midway between the two closely spaced spectral transverse modes at 845.33 nm and 845.41 nm shown in the far-field of Figure 6.13.

Lu *et al.* [3] studied the spectral properties of VCSELs in the near-field using a tapping mode tuning fork SNOM arrangement. In their method, the collected light was directed to a monochromator allowing only a narrow bandwidth of light to pass through to a light sensitive detector, similar to the setup shown in Figure 5.9. The results were spatially defined intensity images of spectrally filtered transverse modes. Lu *et al.* [3] were studying a similar sized apertured device to that used for the work presented, albeit at a high injection current, which resulted in several more higher-order transverse modes. Hörsch *et al.* [5] used an alternative method to generate spectrally filtered near-field images of different transverse modes emitted from a VCSEL. Their equipment setup allowed the collection of spectra at each point within a 64 x 64 image, which was then software filtered to extract the spectrally filtered images representing the different transverse modes.

6.6 Detection limitations at the nano-scale

It is worth noting the operational emitted power of the device to determine what the minimum detectable output power density one might expect to detect using the equipment setup used throughout these experiments. According to the manufacturer's specification sheet in Appendix 6, the device emits approximately 1.85 mW at an injection current of 8 mA. This can vary appreciably by up to 30% depending on operating conditions and on the quality of the final product; however, using these values we can deduce from the fact that lasing threshold is at 1.40 mA, the output power is of the order of 0.26 mW at an injection current of 2.34 mA, as discussed in Section 6.5.3. The power density across the VCSEL aperture can be calculated as an average of the total power emitted. Using the SNOM measurement of the ring aperture having a measured diameter of 12.84 μm, the power density can be approximated as,

$$\frac{P}{\pi\left(\frac{d}{2}\right)^2} = \frac{0.26x10^{-3}}{\pi\left(\frac{12.84x10^{-6}}{2}\right)^2} \approx 2\,\mathrm{MWm}^{-2}.$$

Of the spectrally filtered transverse modes shown in Figure 6.24, Figure 6.24(d) showed a count rate of approximately 30,000 per 5 ms. Therefore, if the power density dropped by 3 orders to 2 kWm^{-2}, this would likely give a detected count rate of 30 counts per 5 ms. Obviously, the power could be reduced further with an extended integration time of 10 or 15 ms, but then the image scan-times take far longer and introduce the possibility of either scan instability or perhaps more importantly, the device output characteristics changing due to heating effects etc.

With regards to efficiency, at an output power of 0.26 mW at a wavelength of λ = 850 nm, the energy per photon emitted is,

$$E = \frac{hc}{\lambda} = 2.339x10^{-19}\,\mathrm{J}.$$

Thus, the number of photons emitted per second at an injection current of 2.34 mA is,

$$\frac{0.26x10^{-3}}{2.339x10^{-19}} \approx 10^{15}\ \text{photons s}^{-1}.$$

Of the 4 transverse modes detected, the total count rate is ~ 50,000 per 5 ms, approximately $10^7\ \mathrm{s}^{-1}$. The circular tip aperture of the SNOM is estimated to be 100 nm in diameter, covering an area of $\pi\left(\frac{100x10^{-9}}{2}\right)^2\ \mathrm{m}^2$. The fractional area relative to the total VCSEL aperture is,

$$\frac{\pi\left(\frac{100x10^{-9}}{2}\right)^2}{\pi\left(\frac{12.84x10^{-6}}{2}\right)^2} \approx 6x10^{-5}.$$

Taking into account the APD efficiency of photon detection at 500nm of 45%, we can deduce the efficiency of the SNOM and other associated optical equipment as,

$$\frac{\text{Detected photons by the SNOM tip}}{\text{Number of photons from whole aperture}} \cdot \frac{\text{SNOM tip aperture area}}{\text{VCSEL aperture area}} \cdot \frac{1}{0.45},$$

giving

$$\frac{10^7}{10^{15}} \cdot \frac{1}{6x10^{-5}} \cdot \frac{1}{0.45} \approx 3.71x10^{-4}.$$

This is actually a very high efficiency considering that the efficiency of a SNOM probe is supposed to be of the order of 10^{-4} to 10^{-7} as discussed in Chapter 3. Thus a number of inaccuracies are likely such as underestimating the SNOM aperture size, or more likely the estimate of the VCSEL output power being too low. But this value of 10^{-4} is a reasonable estimate.

6.7 Localised spectroscopy of a VCSEL

To further illustrate the strength of the spectroscopic setup used, multiple spectra were obtained from several, highly localised, locations across the VCSEL's aperture.

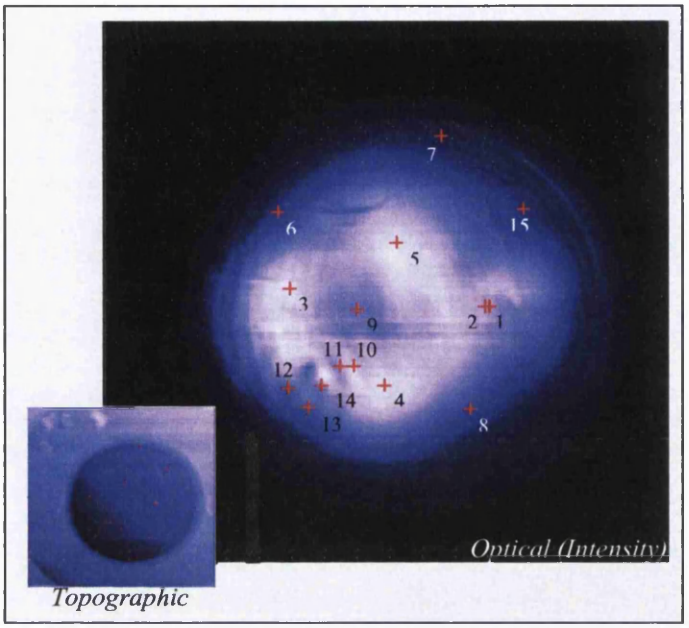

Fig. 6.21 Topographic (inset) and optical intensity images illustrating the locations of the point spectroscopy.

An injection current of 2.34 mA was used for this, identical to that used to obtain the spectrally filtered images in Figure 6.21, although the VCSEL had been powered off for a period of time. The transverse mode structure was therefore expected to possess differences to that obtained for the spectrally filtered image in Figure 6.20(b).

Collection times were a maximum of 4 ms per spectrum due to a slightly opened fibre tip. This minimised any chance of CCD saturation, limited to 64 k counts per pixel. The spectra collected are shown in Figure 6.22. These have also been separated into pairs and are shown in Figure 6.23 allowing the variation in peak height for different transverse modes to be seen more clearly.

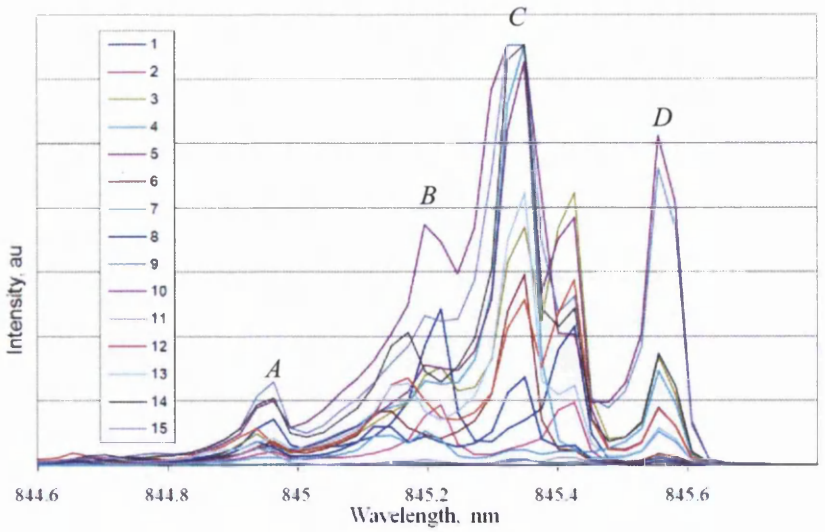

Fig. 6.22 Spectra collected at points 1 to 15, as indicated in Figure 6.21.

Key spectral characteristics are highlighted in Figure 6.22, where *A* represents a TEM_{00} mode, *B* is predominantly TEM_{01} with possibly a very low intense TEM_{10}, *C* is likely to be TEM_{02} and lower intense TEM_{20}, and *D* a mixture of TEM_{12} and TEM_{30} modes as discussed in section 6.5.3. The peak wavelengths of Figure 6.22 do appear to be at approximately the same wavelengths as for the imaging in Figure 6.13 even though the device had been through several power cycles. Spectrum 9 shown in Figure 6.23, located in the centre of the optical axis, has 2 spectral peaks, the most intense being at 845.56 nm with a second at 845.19 nm. This spectrum was collected at a location which only has a detectable intensity as a result of the TEM_{00} fundamental transverse mode in Figure 6.20(c) and a combination of TEM_{02} with a contribution from a lower intense TEM_{20}, shown in Figure 6.20(e). Spectral pairs (3, 9) and (4, 5) in Figure 6.23 highlight the single and simultaneous multimode spatial presence across the aperture. It also shows the reproducibility of the transverse mode spectrum intensity profile for a given injection current after the device had been powered for several days. As discussed previously, this localised collection of spectra is similar to that carried out by Hőrsch *et al.* [5] who constructed spectrally filtered images through post-processing, of spectra collected in a 64 x 64 grid.

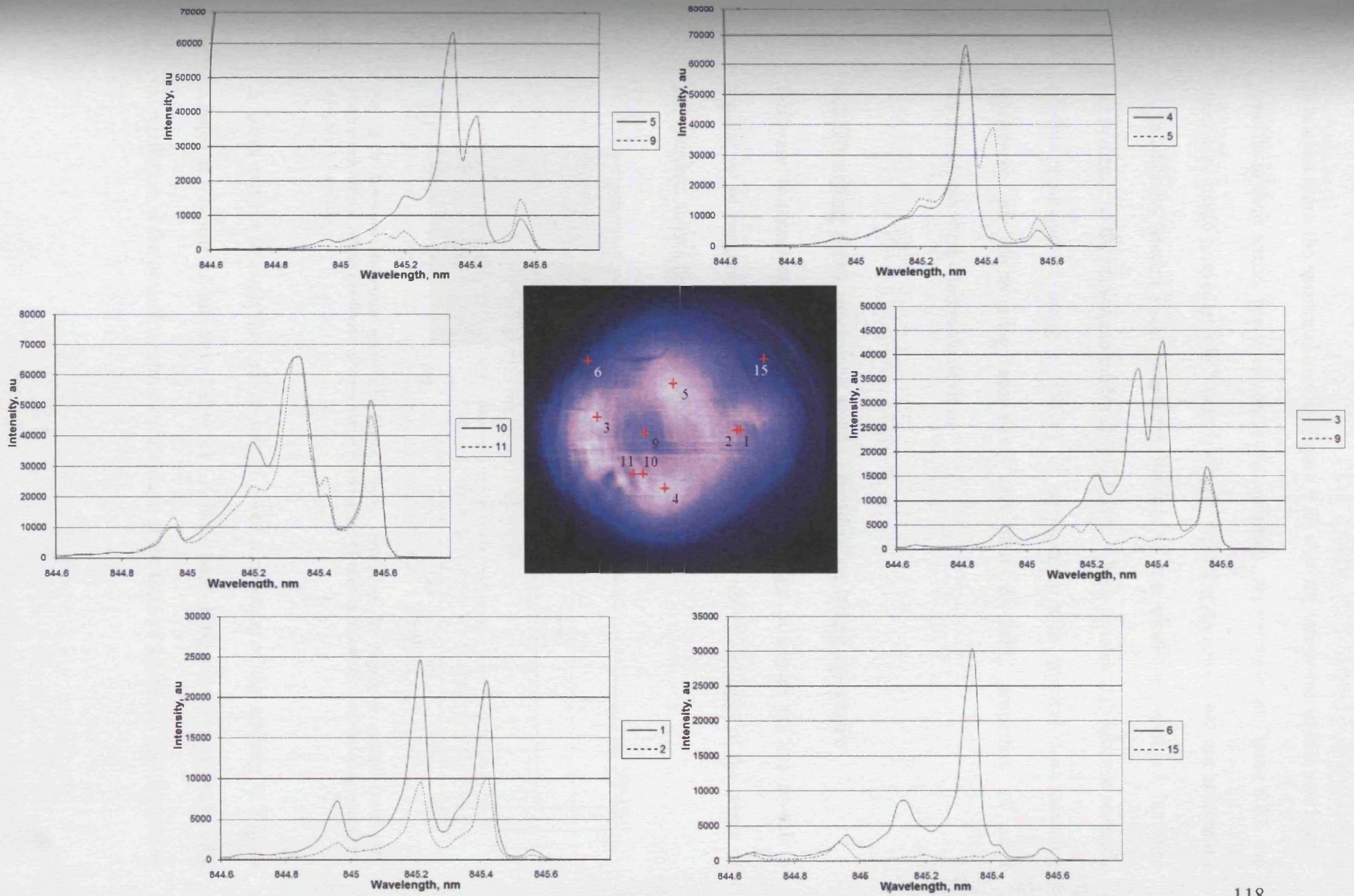

Fig. 6.23 Multiple point spectra highlighting the ability to spectrally determine the optical properties at the nano-scale.

It is clear from the spectra shown in Figure 6.23 that the transverse modes are highly specific in their spatial presence across the aperture. For example, in Figure 6.23, the transverse mode centred at 845.37 nm is clearly visible at location 5 but not at location 4. In addition, spectra 3 and 9 show the presence of most modes at position 3, but only the presence of the transverse modes at 845.56nm. These spectra highlight the strength of the technique of using a SNOM in conjunction with spectral discriminating equipment for determining near-field, and thus far-field, properties of such semiconductor opto-electronic devices.

6.8 Standing wave presence at the circular emitting aperture

Software enhancement of the spectrally filtered image in Figure 6.15(c) reveals a regular set of concentric rings that appear to originate above and right of the centre of the aperture, shown here in Figure 6.24(a).

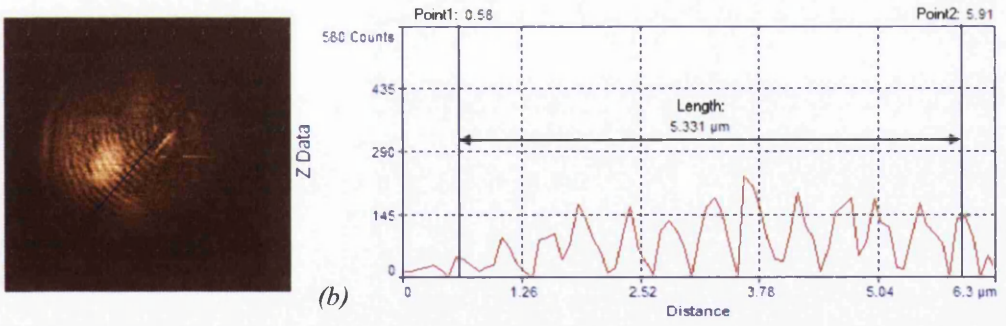

Fig. 6.24 Software enhanced spectrally filtered image revealing the regularly spaced concentric rings/modulations of the fundamental transverse mode of the Gaussian beam (a), peak spacing measures 424 nm ± 5 nm (b).

A cross section through the optical image gives a measure of the spacing in Figure 6.24(b) as 424 nm ± 5 nm from Table 6.1. A large part of the error here is due to lack of resolution in the optical information obtained at the time of the scan. The image size

if 18.68 μm with a resolution of 300 x 300 points, thus each point accounts for a minimum of 62 nm.

Spacing, nm		
425	*441*	*442*
425	*425*	*450*
425	*425*	*433*
425	*477*	*424*

Mean, nm	*424*
Variance	*348.75*
S.D.	*18.67*
S.E.	*5.39*

Table 6.1 Spacing of fringes in Figure 6.28 having a mean value of 424 nm with a standard error of 5.

This modulation is also visible in each of the spectrally filtered images in Figure 6.20(c-f). Knopp *et al.* [2] found standing waves to be present within their optical images while studying VCSEL in the near-field using a SNOM. The standing waves were however Cartesian and not circular in their presence within the aperture, as is the case described here. It was noted that they could not be artefacts of the scanning process as they are not aligned to the horizontal or vertical directions of the scanned image. Knopp *et al.* [2] state the fringe patterns were possibly due to Fresnel patterns. These were said to result from the diffraction of light at a discontinuity in the phase as it exits the top distributed Bragg reflector under the ring contact, compared to the open aperture to air. The peak-peak spacing of the standing wave of 424 ± 5 nm, is effectively half the VCSEL operational wavelength, i.e. $\lambda/2$ = 422.5 nm. It is also clear that the concentric modulation is not centred on the aperture and this follows from both Figures 6.15(c) and 6.20(b) showing the optical modes to be positioned off the physical aperture's central axis.

In this study, the concentric standing waves are clearly visible when the current is just above threshold, as shown in Figure 6.15(c). The fringes however become less clearly concentric as the current is increased to 2.34 mA, as shown in the near-field wavelength

filtered images of Figure 6.20(c-f). It appears as though the complexity of the TEM modes affects the generation of the standing wave.

Standing wave pattern formation has previously been reported by Hegarty *et al.* [6] for VCSELS when operating at a single frequency close to lasing threshold and in negatively detuned lasers above threshold. Extended non-linear patterns resembling transverse plane waves with Cartesian symmetry have also been observed by Ackerman *et al.* [7], despite the circular nature of the aperture. Their origin is predicted to occur as a result of tilted plane waves in the laser cavity. The effect on multimode emission is not predicted, and the circular nature of the concentric standing waves shown in Figure 6.15(c) and 6.20(b) is not accounted for. Ackermann *et al.* [7] indicated the formation of high-order Laguerre modes as well as the Cartesian symmetry structures but these appear as a function of aperture size, with many of these effects occurring in wide aperture VCSELs.

The concentric nature shown in Figure 6.24(a) can be explained by the effect of Gaussian beam clipping and truncation as discussed by Uray [8] and Siegman [9]. Figure 6.24(a) represents the clearest evidence of the concentricity, and the main TEM_{00} mode is apparent in the output optical intensity. The general Huygens integral for the field amplitude $\tilde{u}(r)$ at a plane z, above a circular aperture of diameter $2a$, located at z_0 and illuminated by a cylindrically symmetric source function $\tilde{u}_0(r_0)$ is given by [9],

$$\tilde{u}(r) = i2\pi N e^{-i\pi N(r/a)^2} \int_0^1 \frac{r_0 \tilde{u}_0(r_0) e^{-i\pi N(r/a)^2}}{a} J_0\left(\frac{2\pi N r r_0}{a^2}\right) d\left(\frac{r_0}{a}\right). \qquad 6.1$$

The Fresnel number N in this case is given by

$$N \equiv \frac{a^2}{(z - z_0)\lambda} . \qquad 6.2$$

Equation 6.2 allows for the origin of the diffraction to be determined to a limited accuracy. Note that the mechanism for force-feedback with the SNOM ensures the tip-aperture being no more than several nanometres from the surface of the device, thus the ~ 422 ± 5 nm periodicity is suggestive of the Fresnel diffraction pattern arising from within the device, rather than at the air discontinuity; if the latter were the case, then many more orders of diffraction would be visible.

Knopp *et al.* [2] suggested that the patterns observed appeared to originate from within the device, possibly at a distributed Bragg reflector. The evidence indicates something very similar is occurring in this device, related to the buried structure of the cavity and its ring contact.

Using equation 6.2, with an aperture a = 6.42 μm, wavelength of λ = 845 nm, and a Fresnel number $N \approx 20$, together give a diffraction plane depth $z - z_0 \approx 2.5$ μm. This is the point of origin of these standing waves deep below the surface of the aperture.

As other modes start to dominate, the concentricity becomes more difficult to analyse and the intensity of the modulation is directly related to the spatial position of the lasing mode. However, cross-sectional line profiles for each mode show that the periodicity is still effectively ~ 424 nm and any observed difference is within the limits of our measurement. This could be explained by considering that the higher order transverse modes are no longer Gaussian in nature and hence the Gaussian clipping effect due to a sub-surface discontinuity results in a more complex Fresnel pattern, seemingly

originating from particular positions around the aperture as the emitted light is no longer circularly symmetric.

It should be noted that it would not be expected to observe these modulation features when using a focussing lens system, as used in the work by Degen *et al.* [4] and Hegarty *et al.* [6]. This is due to the dependence of Fresnel number N on z (equation 6.2), and is where a near-field probe based imaging system has an advantage.

6.9 Consequence of surface modification to the near-field

During the scanning process, surface damage occurred at the aperture surface due to a SNOM tip crash, visible in the bottom left of the topographical image, shown in Figure 6.25(a). Also, note the subsequent distortion of the intensity in the optical image in Figure 6.25(b). The consequences of such damage are not clear without further investigation but it is clear that a small defect such as that in Figure 6.25(a) causes optical effects far across the aperture.

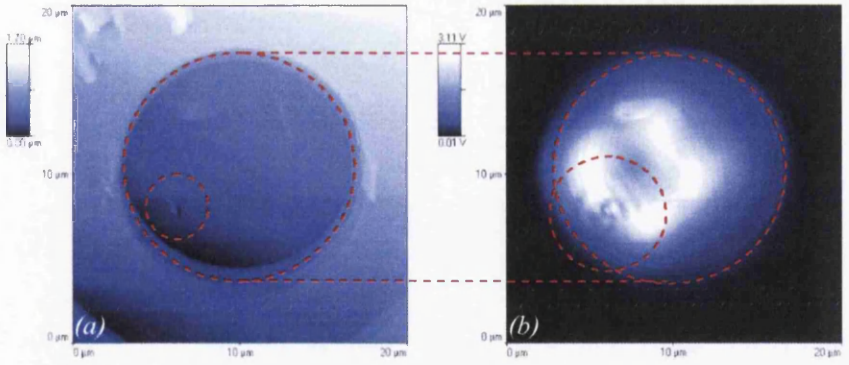

Fig. 6.25 Topographical (a) and intensity (b) images at an injection current of 2.34 mA. Note the offset of light emitted from the circular aperture and the damage to the surface on the bottom left of (a) within the aperture.

Zooming in on an enhanced portion of the damaged area in the optical image of Figure 6.25(b) periodic spacing of the fringes of ~850 nm are clearly visible, i.e. that of the wavelength of the emitted radiation from the device shown in Figure 6.26.

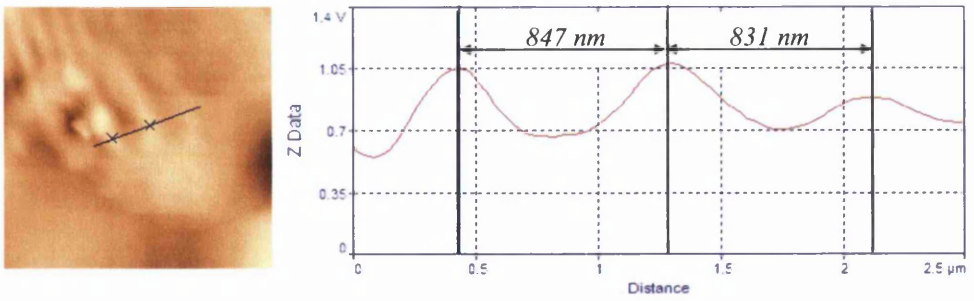

Fig. 6.26 Software enhanced region of Figure 6.30(b) above showing the inter-peak spacing to be approximately 850 nm, i.e. that of the wavelength of the emitted radiation.

The effect this has on the near-field structure can be better illustrated by comparing the fundamental mode before and after surface damage has occurred, as shown in Figure 6.27.

The ~ 424 nm spaced standing wave visible in Figure 6.27(a) is still present in Figure 6.27(b) but at a much reduced level in comparison to the standing wave spaced ~ 850 nm apart as a result of the surface damage.

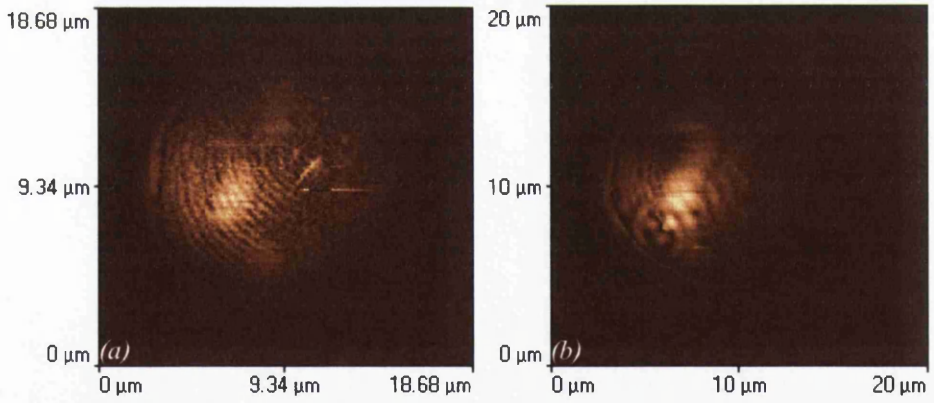

Fig. 6.27 Software enhanced collection images of the fundamental Gaussian before (a) and after (b) a tip has crashed causing damage to the surface.

The origin of these modulations is possibly due to this defect extending below the surface of the VCSEL aperture, even lower than the previously described aperture ring. This could cause a further diffraction of the Gaussian beam with a smaller Fresnel number when detected at the surface. Further studies would be required to fully understand their presence, spacing and the effect they may have on the modal output of

the device. It has been shown that controlled modification of the aperture has a suppressing effect on certain modes; in a similar fashion to reducing aperture size as discussed by Hashizume and Koyama [10], or by applying surface gratings to control the polarisation as discussed by Haglund *et al.* [11] and Ostermann *et al.* [12].

6.10 Conclusion

Scanning near-field optical microscopy is a powerful tool that can be used to aid in investigation of a variety of materials including semiconductor lasers. Such an instrument provides information far beyond the diffraction limit that inhibits standard optical microscopes. This has the added benefit that optical information is filtered spatially by using a localised probe at the material surface so that point spectroscopy can be obtained, a function very difficult to achieve with conventional optics.

It has been shown that at higher injection currents than the lasing threshold, VCSELs possess multi-transverse mode structures in the far-field. This is as a result of highly structured, yet complex, transverse modes, whose presence depends upon the injection current of the device. Several transverse modes were detected in the near-field and spectrally filtered to produce high resolution images illustrating their simultaneous presence at a single injection current.

The successful near-field, high resolution imaging using the SNOM, at two different injection currents revealed the presence of concentric modulations, which were determined to be ~ 422 nm spaced standing waves. Calculations revealed these to originate as a result of Gaussian beam clipping ~ 10 μm below the surface of the aperture. Standing waves have been observed in the past at the surface of such devices

but never reported as having a highly regular concentric nature. It was also noted that structural changes at the surface of the device had a modulating effect on the intensity across the surface of the aperture, of approximately one wavelength spacing. Surface modification is an important topic with regards to controlling the far-field polarisation and transverse mode emissions as discussed by Hagland *et al.* [11] and Ostermann *et al.* [12].

References

[1] Sharma A., Yarrison-Rice J.M., Jackson H.E., Choquette K.D.. J. Appl. Phys. **92** (11), 6837, (2002)

[2] Knopp K.J., Christensen D.H., Rhodes G.V., Pomeroy J.M., Goldberg B.B., Ünlü M.S., J. of Lightwave Tech. **17**, 1429, (1999)

[3] Lu N.H., Chen C.Y., Lin C.S., Liu W.C., Tsai D.P., Scanning **26**, I-43, (2004)

[4] Degen C., Fischer I., Elsäßer W., Optics Express **5**, 38, (1999)

[5] Hörsch I., Kusche R., Marti O., Weigl B., Ebeling K.J., J. Appl. Phys. **79**, 3831, (1996)

[6] Hegarty S.P., Huyet G., McInerney J.G., Choquette K.D., Phys. Rev. Lett. **82**, 1434, (1999)

[7] Ackemann T., Barland S., Cara M., Balle S., Tredicce J.R., Jäger R., Grabherr M., Miller M., Ebeling K.J., J. Opt. B: Quantum Semiclass. Opt. **2**, 406, (2000)

[8] Uray H., Appl. Opt. **43**, 620 (2004)

[9] Siegman A.E., Lasers, University Science Books, 727-736, (1986)

[10] Hashizume J., Koyama F., Appl. Phys. Lett. **84**, 3226 (2004)

[11] Haglund A., Gustavsson J.S., Bengtsson J., Jedrasik P., Larsson A., IEEE J. Quantum Electron. **42**, 231 (2006)

[12] Ostermann J.M., Debernardi P., Michalzik R., IEEE J. Quantum Electron. **42** (7), 690-698, (2006)

7 Scanning near-field optical microscopy of quantum dots

7.1 Introduction

Crystalline quantum dots are generally of the order of a few nanometres in size and have been studied intensively for the past few decades. Researchers have found a number of uses for quantum dots to take advantage of their well defined spectral emissions. Two such applications include improving the output efficiency of light emitting devices, and a source of robust fluorescence for tagging within biological structures. In this latter case, cadmium selenide (CdSe) core quantum dots are one of the most common varieties currently in use, partly due to their inherent high quantum yield. As Chapter 3 indicated, the response of quantum dots is complex and these near-field investigations are conducted to give greater insight into their optical response.

This chapter presents the results of numerous experiments to detect single quantum dots while immobilised in a spin coated polymethyl-methacrylate (PMMA) polymer matrix. PMMA was used to help produce a uniform spread of quantum dots on the surface of a mica substrate. Without this polymer being present, it was difficult to achieve a consistent density of quantum dots on the mica surface without clustering. There was also the problem that if they were not immobilised, there was the probability that quantum dots would attach to the scanning near-field optical microscope (SNOM) probe, thus leading to further experimental complications.

7.2 Fluorescent measurements of low concentrations of quantum dots in solution

Two types of quantum dots were used throughout this work. The first was comprised of a CdSe core coated with hexadecylamine (HDA – CH_3-$(CH_2)_{15}$-NH_2) which gives a slightly lower quantum yield compared to a crystalline shell such as zinc sulphide (ZnS), as reported by Talapin *et al.* [1] and Cumberlan *et al.* [2]. The samples available were in powder form, so precise quantities were mixed in toluene to generate a solution of known concentration. Later experiments used cadmium selenide/zinc sulphide (CdSe/ZnS) core/shell quantum dots from Evident Technologies. These were pre-dissolved in toluene at a concentration of 5-8 mg (dependent on the quantum dot core size) of quantum dots to 10 ml of toluene.

Two CdSe core quantum dot sizes were available of the HDA coated variety. Their absorptions were centred at 545 nm and 465 nm with their emissions at ~ 565 nm and ~ 498 nm respectively. Due to size dispersion, a number of these dots had an absorption peak at the Ar^+ lasing wavelength of 488 nm. The larger sized dots however would still absorb at shorter wavelengths than that of the peak at 545 nm.

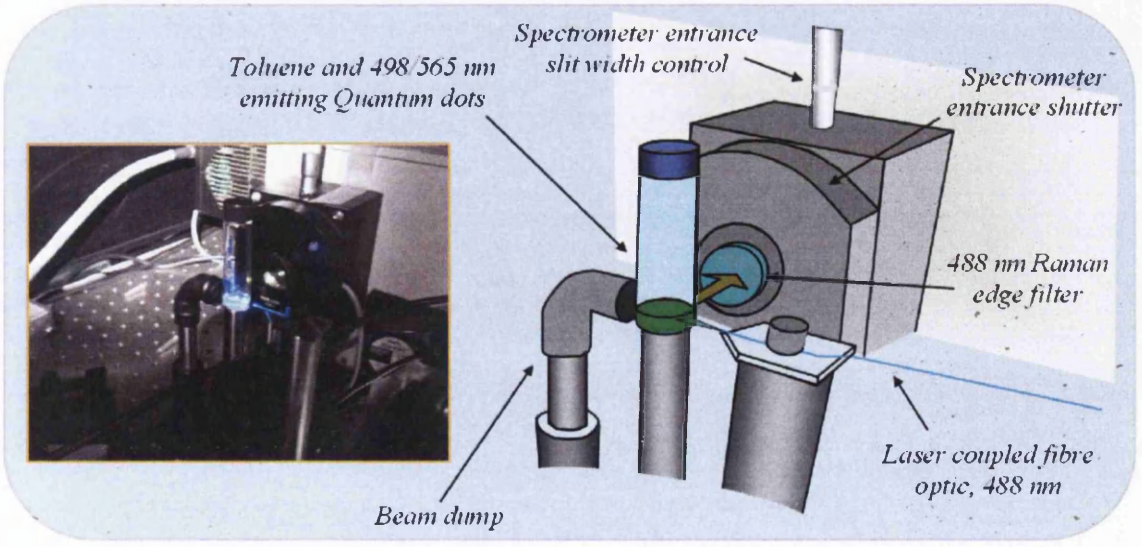

Fig. 7.1 Illumination of quantum dot samples to determine the spectral peak for later near-field use.

A fibre coupled Ar^+ laser with an output of less than 1 mW at 488 nm was positioned to illuminate a sample bottle shown in Figure 7.1. No focussing was required due to the high intensity of the fluorescence.

Solutions of 498 nm and 565 nm emitting quantum dots, and a combination of both were prepared and their fluorescent emissions recorded as shown in Figure 7.2.

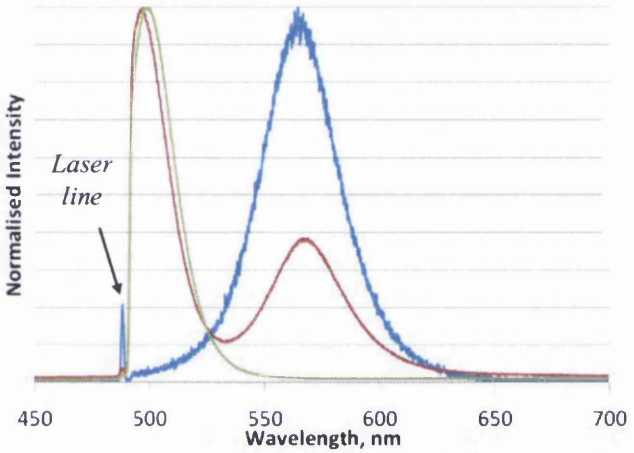

Fig. 7.2 Far-field illumination of 3 solutions of single (green – 498 nm, blue – 565 nm) and mixed (red) CdSe/HDA quantum dots.

The quantum dots emitting around a wavelength of 498 nm show a strong asymmetric emission due to the presence of a long pass filter at ~ 490 nm just above the laser-line wavelength. The full-width at half-maximum (FWHM) for the 565 nm fluorescent peak in Figure 7.2 measured ~ 37 nm. This broad spectral response is primarily a result of the 5% size distribution of the quantum dots due to the limitations of the post-manufacturing filtration process, and as shown by Murray *et al.* [3], is a typical variation resulting from such preparation methods that will be discussed later in this chapter.

7.3 Far-field illumination of quantum dots

Similar to experiments by Chevalier *et al.* [4], a confocal microscope was used to carry out some initial fluorescence measurements on small numbers of CdSe/ZnS core/shell quantum dots. A pipette was used to place a small quantity of these quantum dots, dissolved in toluene, onto a glass slide as illustrated in Figure 7.3. A cover-slip was placed over the top to cause the droplet to spread over a larger area before drying.

The sample was illuminated with a standard mercury lamp and the optics focused to the surface plane containing the quantum dots by eye using the bifocal lenses. There were many regions where fluorescence was intense but in between were darker contrasting areas where there were very few quantum dots present. In these darker regions, single or small clusters of fluorescing quantum dots could be seen rapidly fluctuating in fluorescent intensity (blinking). Such blinking has been reported in numerous publications from such authors as Nirmal *et al.* [5], Gómez *et al.* [6] and Shimizu *et al.* [7]. A 25 mW 405 nm emitting laser, operating at 46% power, was then used to excite a quantum dot sample. When used in conjunction with a 420 nm long pass filter, only fluorescence was allowed to pass to the photomultiplier tube (PMT) for detection.

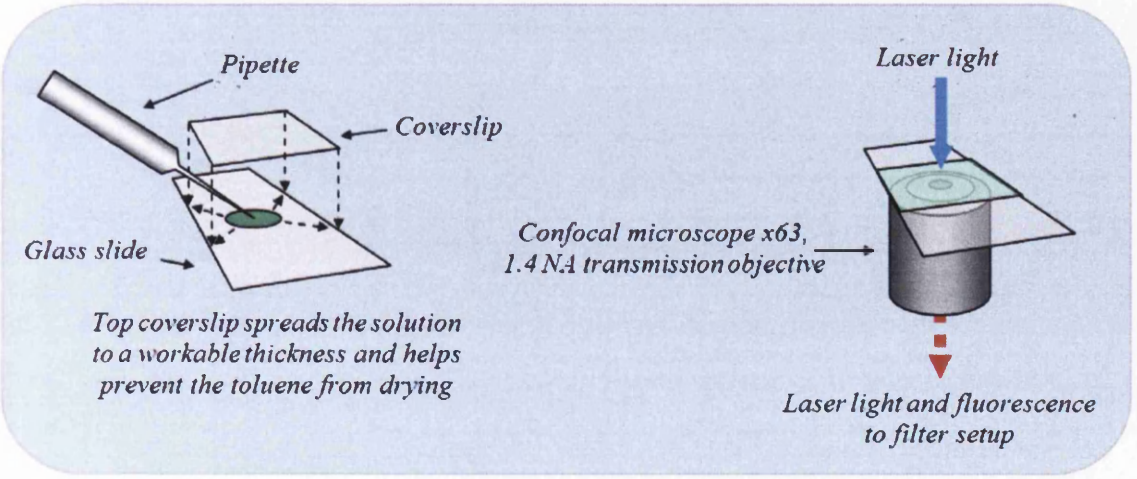

Fig. 7.3 Slide preparation for confocal microscopic studies.

Images 146.2 μm^2 in size were obtained of an area devoid of almost any fluorescence. Subsequent images at 22.3 μm^2, each consisting of 512 x 512 pixels with a dwell time of 3.2 μs and 8-bit colour depth per pixel, revealed the quantum dots. Repeated scans were collected at this dimension to optimise the focus of the optics. Three independent scans were then performed within different areas of this 22.3 μm^2, as shown in Figure 7.4(a). Two of 4.6 μm^2 are shown in Figure 7.4(b) and 7.4(c), and one of 4.4 μm^2 shown in Figure 7.4(d), all having scan parameters 3.2 μs/512x512/8-bit. After each zoomed scan, the 22.3 μm^2 area was re-imaged resulting in these ~4.5 μm^2 areas showing little or no fluorescence. One scan of 2.3 μm^2, Figure 7.4(e), was also carried out within Figure 7.4(a), but the overall effect was a photo-bleaching of the surrounding 4.6 μm^2 area. Each of these small zoomed scans initially produced a strong fluorescent image, but repeated imaging at this scale, resulted in the dots reducing in intensity after just one or two repeated frames.

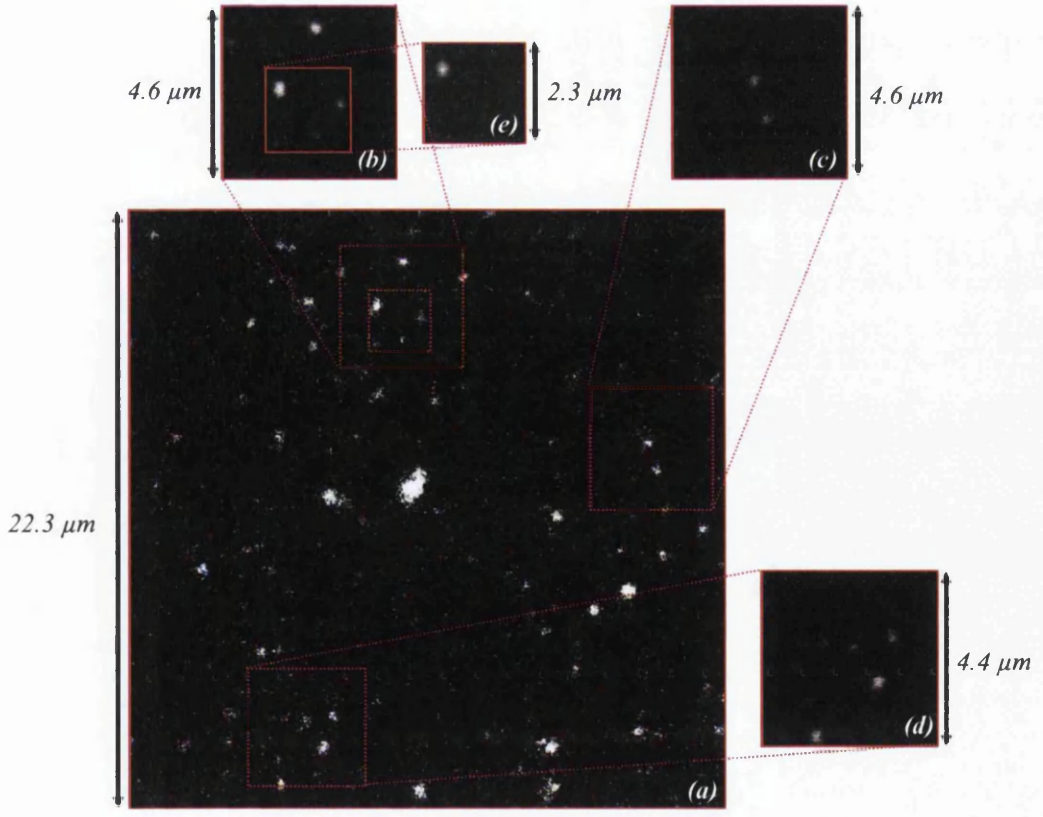

Fig. 7.4 Scan of 22.3 μm^2 area using a confocal microscope with successive zoomed scans as small as 2.3 μm^2.

What these results reveal is that the confocal microscope, which in this instance uses only a PMT and not the more sensitive avalanche photodiode (APD), is able to detect at least small clusters of quantum dots. This instrument can therefore be used to detect structures which will later be imaged with higher resolution at the nano-scale using the SNOM.

7.4 Sample preparation of quantum dots and PMMA in toluene

Two types of quantum dots were studied for the work in this thesis. Initial experiments studied CdSe cores coated with HDA as with experiments by Talapin *et al.* [1] and Pientka *et al.* [8]. These, however, were in powder form which were diluted in toluene to a specific initial concentration and placed in a water bath at approximately 40 °C, occasionally shaken to aid the dissolving process, until no solid could be seen. The CdSe/ZnS quantum dots purchased from Evident Technologies were already dissolved in toluene, thus reducing sample preparation time.

Specific concentrations of PMMA having a molecular weight of 112300 were prepared using a microbalance. 12 μg of PMMA was placed into a sterile glass vial. 12 mg of toluene was added and the bottle sealed and warmed to 60 °C and occasionally shaken to aid the dissolving process until no PMMA white solid could be seen. This resulted in a quantity of PMMA in toluene of concentration 0.1% by weight, as with work by Empedocles and Bawendi [9].

To prepare the samples, 2 μl of the quantum dot in toluene solution was combined with, 200 μl of 0.1% PMMA/toluene. In this way, the density of the quantum dots in toluene was reduced by 100, while the concentration of the PMMA in toluene remained

virtually constant at 0.1%. This step was repeated with 2 μl of this new solution together with another 200 μl of 0.1% PMMA/toluene resulting in a 1:10,000 concentration reduction of the original quantum dot solution, as illustrated in Figure 7.5. 2 μl of this solution was then dropped onto freshly cleaved mica, and immediately spin coated at 2 krpm (or higher, depending on the experiment). This gave a thin and even film of PMMA, with a low concentration of quantum dots embedded within the polymer matrix.

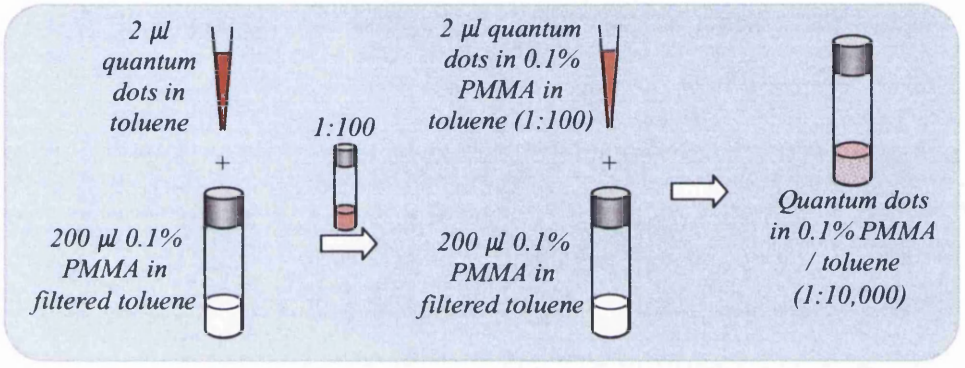

Fig. 7.5 Sample preparation through simple dilution for repetitive results.

It was found experimentally that the higher the spin speed, the thinner the PMMA layer on the mica. This was shown by the fact that at 2 krpm there were far more sub-surface quantum dots compared with those at 3 krpm. This was determined by the optical presence of quantum dot fluorescence having a better match with the number of topographic features at higher spin-speeds, as shown in section 7.6.

The resulting samples consisted of a small piece of mica with a 2-3 nm layer of PMMA with a few quantum dots per μm^2 as shown in Figure 7.6.

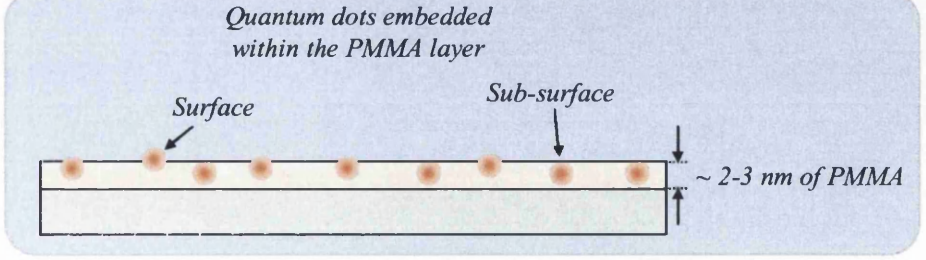

Fig. 7.6 A few nm thick layer of PMMA, embedded with a low concentration of either CdSe/HDA or CdSe/ZnS core/shell quantum dots, spin coated on the atomically flat surface of freshly cleaved mica.

The quantum dots having a diameter approximately the same as the PMMA film thickness resulted in some being virtually sub-surface while the majority was topographically visible.

7.5 Determination of thin film thickness

Mica was the choice substrate due to its transparent nature and near atomic flatness. It was not easy to determine the thickness of a spin coated polymer film on mica. A knife cannot be drawn across the surface to cut the PMMA without also damaging the delicate structure of mica. Instead, a piece of silicon wafer was used to determine film thickness due to its rigid surface structure. A 2 µl drop of this 0.1% PMMA in toluene was dropped onto the silicon wafer and immediately spin coated at 2 krpm before any toluene could evaporate. The thickness of the PMMA was then measured by scratching through the thin polymer layer with a sterile, sharp razor edge, and the scratch imaged with a desktop atomic force microscope (AFM) as shown in Figure 7.7.

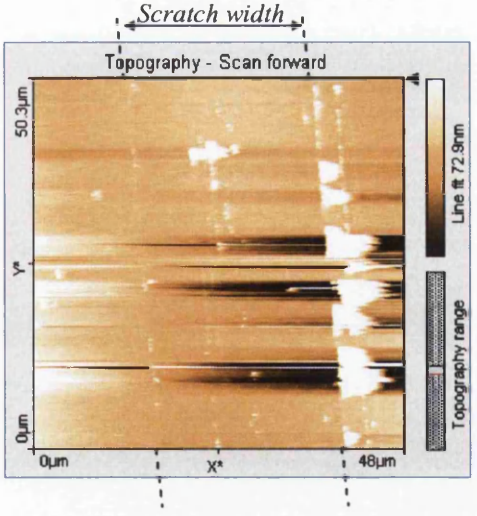

Fig. 7.7 Topographic scan of a scratch drawn through a nanometre thin film of PMMA, spin-coated onto the surface of silicon, revealing a PMMA thickness of ~ 2.4 nm.

The actual scratch is difficult to see and so dashed lines are present to highlight the scratch edges. It was however difficult to measure the height difference between inside

the scratch and outside due to the debris from the PMMA that had been swept to the sides. An average height on the outside to the lowest within revealed a depth of ~ 2.4 nm. This thickness was deemed ideal as it was similar to the diameter of the CdSe quantum dot cores. This enabled direct comparisons between optical and topographic images to isolate and identify the presence of the quantum dots at the PMMA surface.

7.6 Near-field studies of quantum dots in a PMMA matrix

Near-field studies of monolayers of quantum dots were carried out by immobilising them in a polymer matrix of polymethyl-methacrylate (PMMA) to reduce quantum dot movement at the surface once the toluene solvent had evaporated. Moreover, as stated in the introduction, it reduces the probability of quantum dots attaching themselves to the SNOM probe during a scan.

Figure 7.8 shows the equipment setup utilised for the study of quantum dots. The SNOM is used to optically excite the quantum dots in the near-field and the resulting fluorescence is collected with a transmission lens and directed towards an avalanche photodiode (APD) detector. APDs having an approximate 45% photon detection efficiency at wavelengths in the range 500-600 nm were used due to the extremely low intensity of emitted fluorescence. The 50/50 mirror was used to allow imaging of topographic and total fluorescent intensity with subsequent point spectroscopy, without the need to open the dark-enclosure which would disturb the precise probe location at the surface. It also allowed the opportunity of monochromatic imaging using the second APD through the spectrometer. The presence of this partial mirror did however result in 50% of the signal being lost in each of the two parts of the experiment.

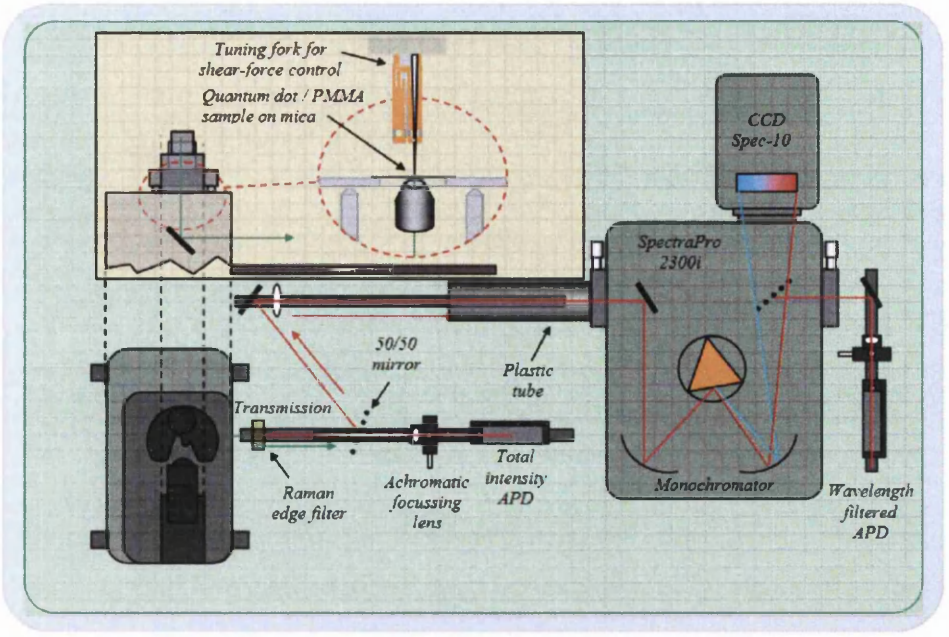

Fig. 7.8 Spectroscopic setup used to detect single quantum dots. APD's were used to detect total intensity and single wavelength emissions.

The achromatic lens allowed precise focussing to a small spot onto the APD sensor regardless of the wavelength of light, else refocusing would have been required upon a change of laser.

Initial SNOM images of spin coated CdSe/HDA quantum dots embedded in a few nanometre-thick layer of PMMA are shown in Figure 7.9. Quantum dots emitting at 565 nm and 498 nm were used in equal quantities and mixed before combining with the PMMA solution.

7.6.1 Polymer surface roughness and uniformity

Both the topographical Figure 7.9(a) and optical images Figure 7.9(b) show the presence of the quantum dots. In order to detect the quantum dots effectively, it was necessary to use a SNOM probe with an aperture of the order of 150 nm. As a result, the resolution of the optical image is reduced and estimated to be approximately 150 nm, the size of the probe aperture. The topographic image in Figure 7.9(a) has had

background subtraction and levelling processes carried out to enhance the presence of the 2-3 nm quantum dots. The optical image in Figure 7.9(b) has had its blue to white ratio optimised to remove background noise allowing the signatures of potentially single quantum dots to be visible. The sizes of the circles are larger than the optical and physical dimensions in order to not obstruct the area being highlighted. These positions were determined by comparing the physical presence of a raised topographic point with the simultaneous rise in optical response in Figure 7.9(a) and 7.9(b) respectively.

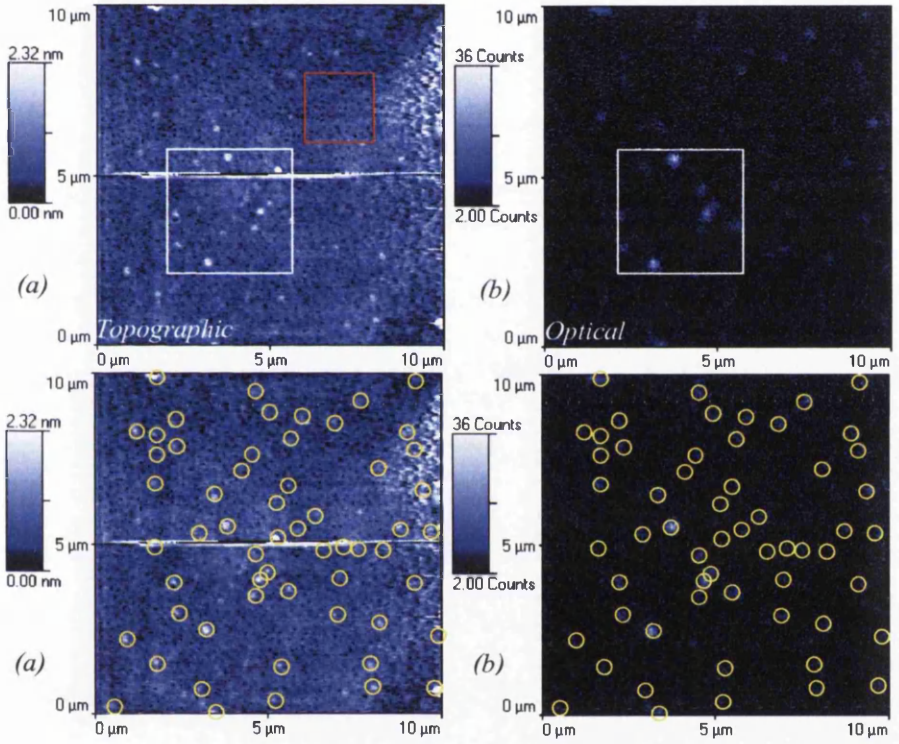

Fig. 7.9 CdSe/HDA quantum dots in 0.1% PMMA/toluene, spin coated at 2 krpm onto mica images with a 488 nm Ar^+ laser operating at <1mW. For the 10 µm^2 image, the left side (a) represents the topographic response and the right side (b) the optical response, detected with an APD.

The red box indicates the area used to measure the surface roughness of the PMMA layer in Figure 7.10, and the white box highlights an area topographically and optically scanned with the SNOM for the next set of data shown later in Figure 7.12.

For this 2 μm^2 region shown in Figure 7.10 with a maximum height range of 1.44 nm, the RMS roughness measured ~ 0.20 nm. This was automatically calculated with the in-built software function and so is a statistic of multiple points from the image.

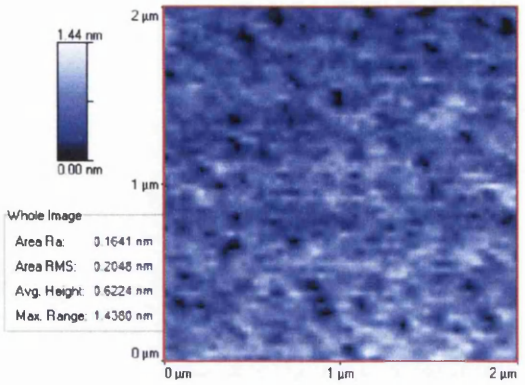

Fig. 7.10 Surface roughness measurement of PMMA spin coated onto mica at 2 krpm revealing an overall height variation of 1.44 nm.

This could be considered large compared to the near atomically flat mica beneath it. The roughness is primarily due to pitting. This is believed to be the result of tiny droplets of water and/or toluene trapped within the PMMA that dry leaving the pitted structure at the surface. Such effects are difficult to eliminate. Figure 7.11 effectively illustrates the tiny pits due to the drying of water/toluene at the surface.

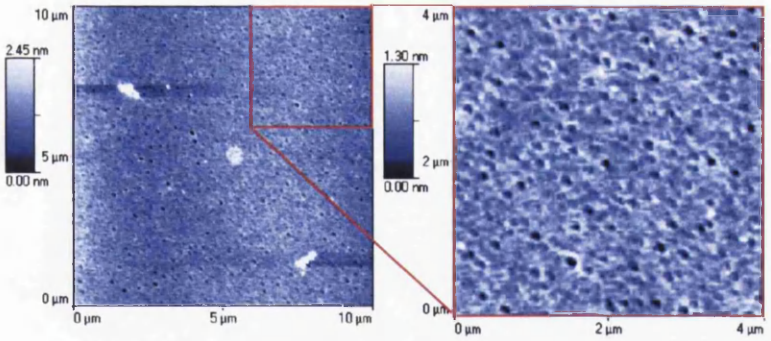

Fig.7.11 Pitted topographic structure due to surface water and the drying effect of toluene.

To scan with more detail, a zoom of Figure 7.9 was performed, resulting in Figure 7.12. Figures 7.12(c,d) are duplicates of Figures 7.12(a,b) so that the presence of quantum dots can be highlighted without obscuring their presence. The lower half of the topographic image suffered from some scanning artefacts making it a little noisy but the

circled *x-y* coordinates of points of interest remained situated in the same positions compared with subsequent scans. At this higher resolution it is possible to obtain more interesting features both topographically and optically. More accurate measurements of the surface RMS roughness reveal a smoother surface than previously measured. Optical effects such as quantum dot fluorescent intermittency can also be observed more readily and are discussed later in this chapter. The optical resolution in Figure 7.12(b) is measurable as approximately 150 nm for the less bright regions. For the brighter points, the topography in Figure 7.12(a) suggests aggregation of multiple quantum dots, making it more difficult to determine resolution. The vertical line on the right hand side of the topographic images in Figure 7.12(a) and 7.12(c) are the result of the SNOM tip, pushing a thin region of the PMMA to one side with each line scan.

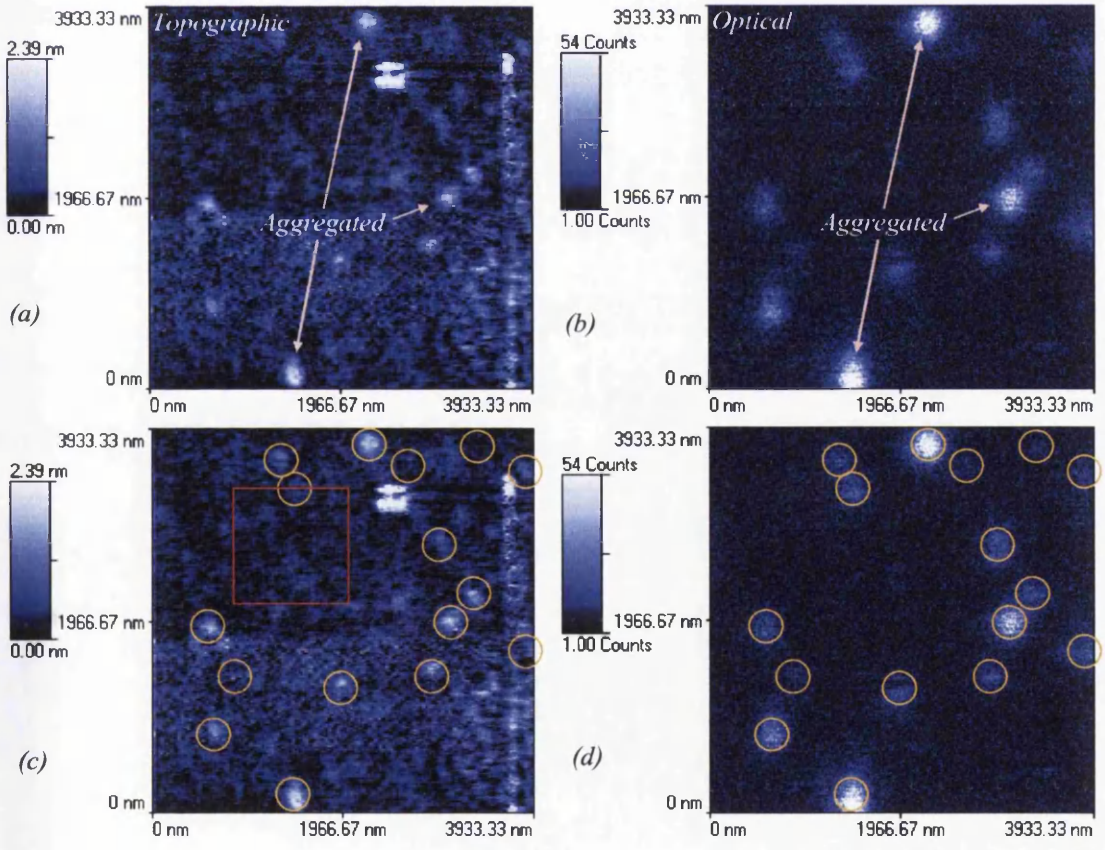

Fig. 7.12 CdSe/HDA quantum dots in 0.1% PMMA in toluene, spin coated at 2 krpm onto mica images with a 488 nm Ar^+ 20 mW laser [<1 mW from fibre optic feed to SNOM]. Again, the red box indicates the position where the surface RMS roughness measurement was taken.

Surface roughness is partly a function of the full height range of the topography. The height range in Figure 7.10 is 1.44 nm compared to 1.23 nm in Figure 7.13 which could account for the change in the area RMS roughness value from 0.20 nm to 0.15 nm. This roughness value of 0.15 nm is considered more accurate as it was obtained using data with a higher topographical resolution.

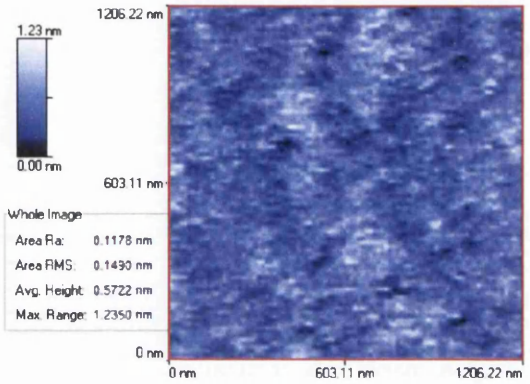

Fig. 7.13 PMMA and quantum dots spin coated onto mica at 2 krpm having a height variation of 1.23 nm revealing an overall RMS surface roughness measurement of 0.15 nm.

The pitting of the surface varied in size from one sample to the next. In most of the samples they were almost immeasurable yet Figure 7.14 shows an extreme example. This sample was prepared in the same way as other samples but with CdSe/ZnS quantum dots pre-prepared in toluene at manufacture, consisting of 0.1% PMMA, spin coated on mica at 2 krpm for 30 seconds. The pits in the PMMA appear to be ~ 800 nm across.

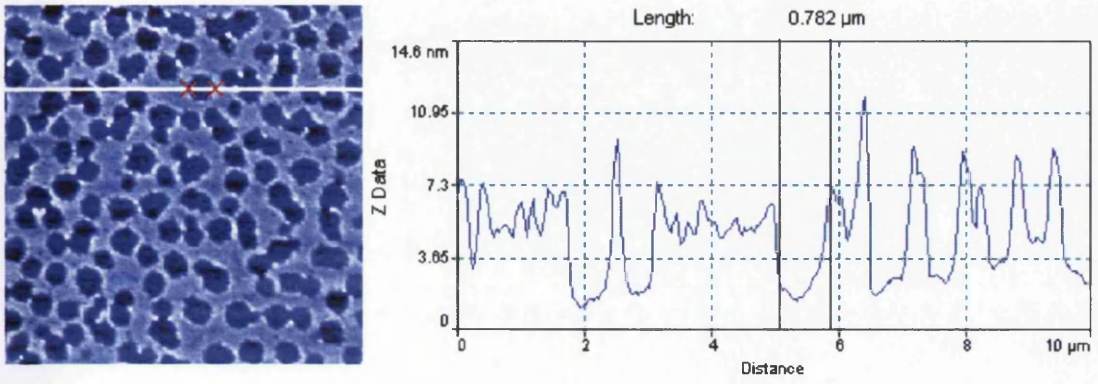

Fig. 7.14 Measurement of the 'pitting' of the PMMA spin coated on mica in some samples showing holes as large as 800 nm or more across – CdSe/ZnS quantum dots in 0.1% PMMA.

There are several papers discussing such observations when using nano-particles with 2 different polymers such as PMMA and polystyrene to generate a regular topographic structure, which can then be used in further experiments, as shown by Minelli *et al.* [10,11] and Santer *et al.* [12]. The domains in such cases form due to de-mixing of the polymers. The sizes of the domains in Figure 7.14 are comparable to some domain dimensions contained in a publication by Minelli *et al.* [11], who spin-coated small concentrations of quantum dots intermixed with two different polymers. However, only one polymer is present here, and so the effect is most likely the result of de-wetting. The polymer layer is too thin and has no overall attraction to the charged surface of the mica, resulting in aggregation. Minelli *et al.* [11] also noted, in some cases, that there was a higher concentration of nano-particles at the boundary between the two polymer phases, especially where the domains within the PMMA were larger than normal. Smaller topographic and optical sized images in Figure 7.15 were obtained from subsequent scans within the area shown in Figure 7.14. It was noted that the majority of the quantum dots appeared to be at the boundary of the domains where the PMMA was at its highest topographical extent, a height of ~ 8.32 nm. This is probably a result of de-wetting. The quantum dot concentration within the PMMA and toluene solution at the edges of the de-wetting regions increases. A few quantum dots appear to reside in the lower regions of PMMA between boundaries where the PMMA is ~ 3 nm thick, thus no clear topographical evidence of the quantum dots (Ø ≈2.6 nm) is noticeable.

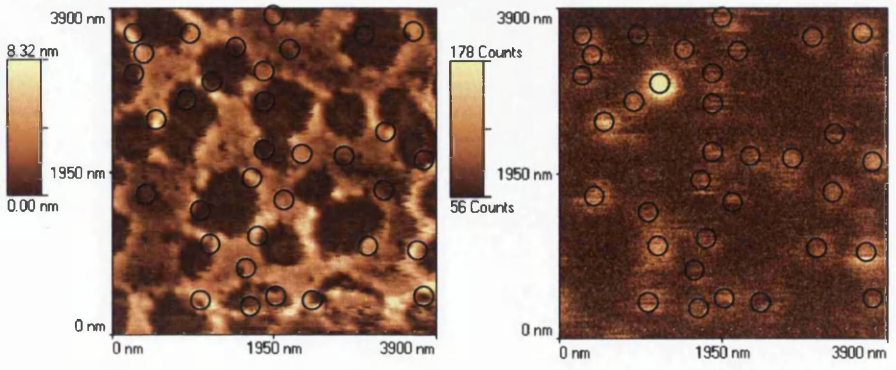

Fig. 7.15 CdSe/ZnS quantum dots embedded within an 8.32 nm thick PMMA layer resulting in a highly pitted structure with the majority of the quantum dots present within the highest PMMA regions.

The thickness of the PMMA in Figure 7.15 is slightly thicker than that in Figure 7.12 as a result of the presence of the nano-particles. The likelihood is that a similar, or possibly smaller, volume of PMMA per unit area of substrate is present, but redistributed.

Optically, it must be noted that the fluorescent intensity, as a result of multiple excitations and emissions of these Cd$e/ZnS core/shell quantum dots, is significantly higher than that obtained for the CdSe/HDA variety. This was observable in the optical imaging as the increased signal to noise ratio of the ZnS coated dots, hence showing the improved confinement and heightened quantum yield as a result. This was found with various probes and determined not to be a function of aperture size, laser power or probe deterioration.

To resolve this issue of the PMMA separating into domains, many solutions were prepared to the same specifications, and topographical scans were carried out. The resulting pitting structure was found to vary with each sample. There appeared to be no mechanism that could guarantee the dimension, or even the presence of the pitting effect within the PMMA. Eventually, it was discovered that the toluene used to dilute the solutions was not as pure as was first believed. The initial solutions prepared were contaminated with particles which were preventing the creation of a flat homogeneous PMMA layer on the substrate surface. Instead the PMMA separated into regions of polymer bound by particles, including quantum dots.

Final quantum dot solutions were prepared using toluene passed through a 200 nm-pored filter to reduce the presence of larger particulates. This filtered toluene was then

stored in a sterile glass vial and sealed with a cap lined with polytetrafluoroethylene (PTFE), a hard polymer that is non-reactive with toluene. The overall change in the topography was subtle as not all samples to this point had suffered from contamination. However, the large holes in the PMMA as shown in Figure 7.15(a) were not seen again, only the very small drying holes were apparent due to humidity/toluene drying.

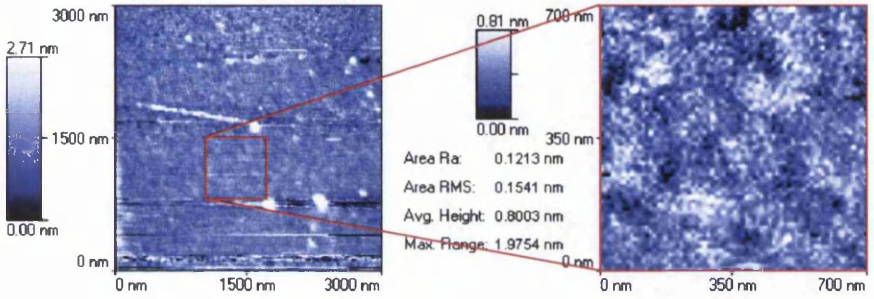

Fig. 7.16 Topography of 0.1% PMMA on mica using 200 nm-pored filter to reduce particulates in toluene.

A final topographical image in Figure 7.16 shows little change in the surface roughness where the toluene was filtered removing the larger particulates when compared to the roughness in Figure 7.10. This is an indication of an inherent roughness due to the random structure of the PMMA on the surface of the mica. A smaller area of 700x700 nm had to be chosen in order to avoid larger topographical features. The area RMS roughness remained at the minimum of approximately 0.15 nm.

7.6.2 Polymer layer thickness measured by quantum dot topography

The supplier of the CdSe/HDA quantum dots gave no information as to the dimensions of the CdSe core, but using the information for CdSe/ZnS nanocrystals supplied by Evident Technologies, an upper size limit of the dots can be estimated as having a diameter of ~2.6 nm for quantum dots that emit at a wavelength of ~560 nm. A small fraction of this value can be attributed to the HDA covering, and typically 4 Å for a ZnS shell as measured by Kortan *et al.* [13]. Hines and Guyot-Sionnest [14] also

manufactured colloidal CdSe/ZnS quantum dots and confirmed the presence of the cores and shells using x-ray photoemission spectroscopy (XPS). Transmission electron microscopy (TEM) was then used to measure the thickness of the ZnS capping layer as 6 ± 3 Å in close agreement with Kortan *et al.* [13].

The quantum dot indicated with the red arrow marked 'buried' in Figure 7.17(a) is only 0.3 nm above the average height of the surrounding polymer, the PMMA can therefore be estimated to be at least 2.3 nm thick. It has a fluorescent emission as intense as that labelled as '*comparison*' in Figure 7.17(b) which is topographically 1.79 nm proud of the mean PMMA level, as shown in Figure 7.17(c). It can therefore be said that the surrounding polymer matrix has little effect on the intensity of this particular quantum dots due to its high transparency. It is possible however, that there may be more than one quantum dot at the location marked 'buried'.

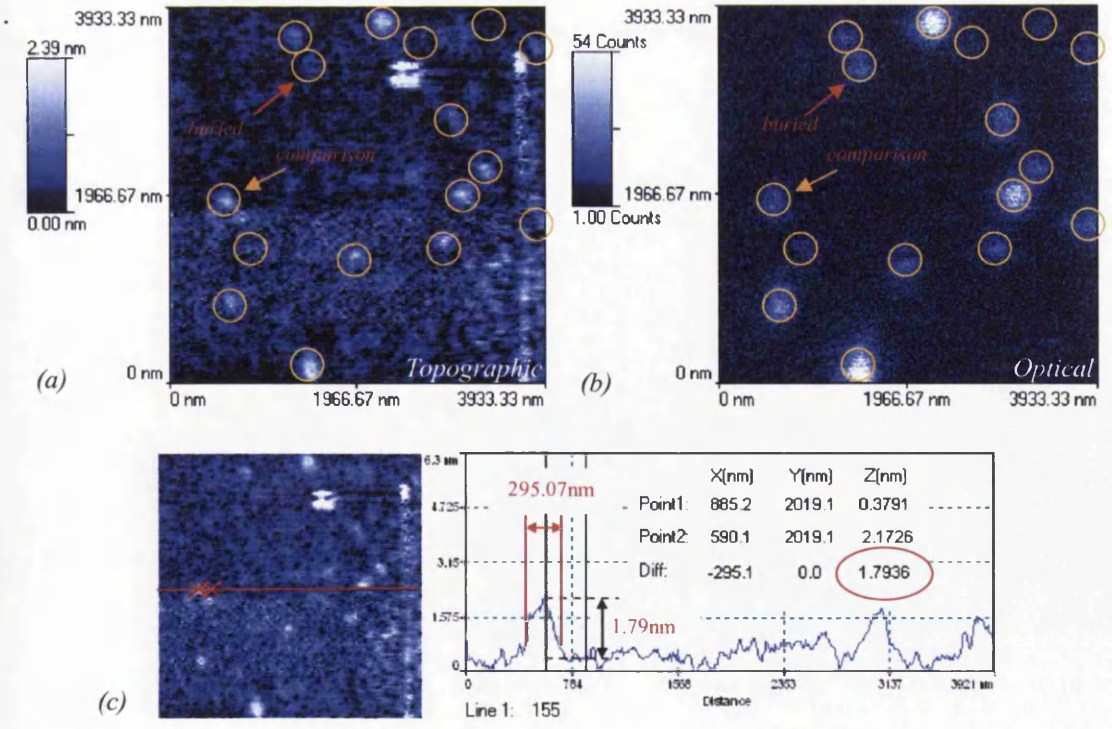

Fig. 7.17 CdSe/HDA quantum dots in 0.1% PMMA in toluene, spin coated at 2 krpm onto mica. Quantum dots excited with a 488 nm Ar^+ laser operating at <1 mW, shows that the burying depth in PMMA matrix has no detectable effect on the fluorescence emission intensity. Image (a) represents the topography, image (b) is the simultaneously acquired optical image and (c) is a single line scan showing the topographic height of the quantum dot labelled as 'comparison'.

From the point of view of optical resolution, Figure 7.18 shows the best obtained for CdSe/ZnS quantum dots in a PMMA polymer matrix at ~ 88 nm. This is just over an order of magnitude larger than the size of the quantum dots, yet significantly beyond the diffraction limit that hinders conventional imaging techniques.

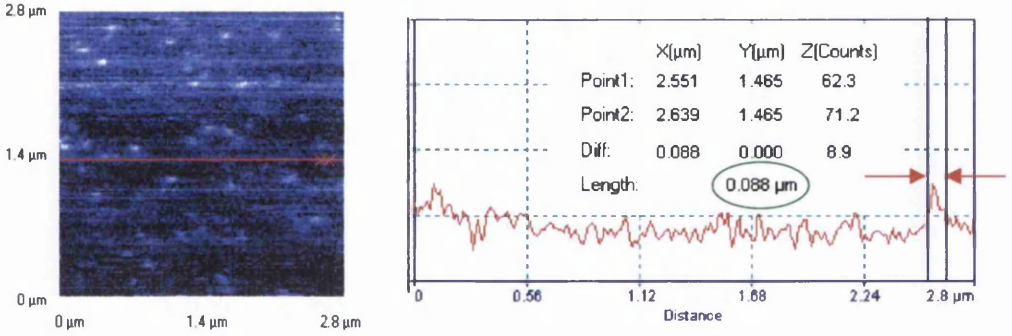

Fig. 7.18 CdSe/ZnS quantum dots / 0.1% PMMA in toluene, spin coated at 2 krpm onto mica. Quantum dots excited with a 488 nm Ar^+ laser operating at <1 mW, with a spatial optical resolution of < 90 nm.

7.7 Quantum dot fluorescence intermittency (Blinking)

Figure 7.19(a,b,c) show three successive ~ 4 μm scans of the same area. 3 fluorescent points marked as '*Active*' in Figure 7.19 are assumed to be the result of single quantum dots. In Figure 7.19(a) fluorescence is detected at all 3 locations, in Figure 7.19(b), no fluorescence is detected at any of the 3, and in Figure 7.19(c) 2 of them again fluoresce while the 3rd remains inactive. This could be due to either the quantum dot having deteriorated through oxidation, resulting in a permanent structural change to its surface, or the core of the quantum dot itself. As discussed by Javier and Strousse [15], the quantum dot could also be in a temporary dark state whereby the excited electron has been trapped at a surface state leaving the core positively charged, unable to recombine within its normal 10's of nanosecond lifetime, as discussed by Achermann *et al.* [16] and Wang *et al.* [17]. Further absorptions lead to picosecond lifetime Auger processes involving non-radiative recombination, reducing the overall detected level of fluorescence activity.

The fluorescence emitted from single quantum dots has been recorded by other groups using a range of different experimental setups such as total internal reflection fluorescence-image correlation spectroscopy (TIRF-ICS), Bachir *et al.* [18], and epifluorescence / laser-scanning confocal microscopy by groups such as Chevalier *et al.* [4], Nirmal *et al.* [5] and Shimizu *et al.* [7].

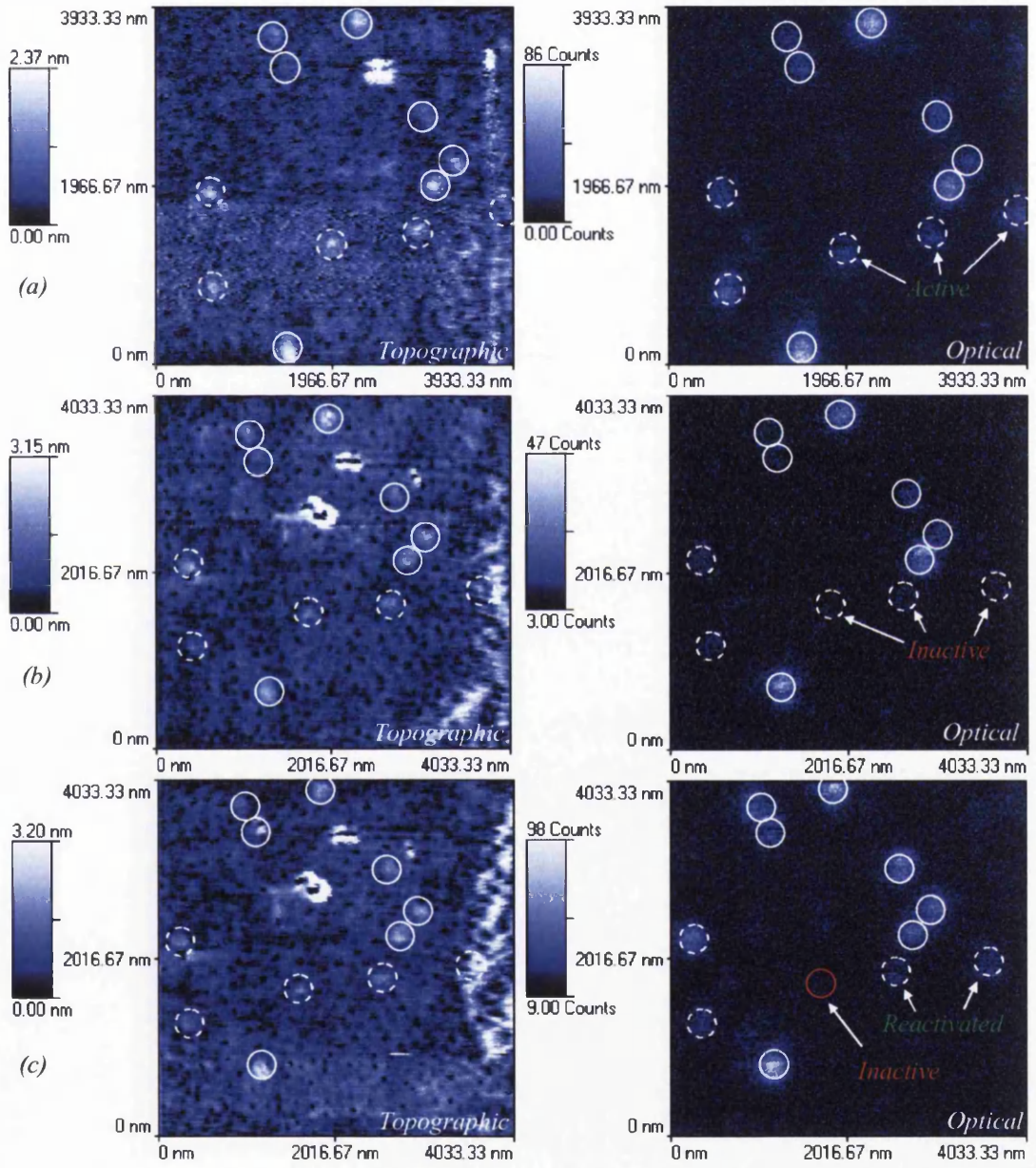

Fig. 7.19 Three successive topographic and optical images showing the blinking effect of quantum dots. Topographic image pair (a) represent the first scan showing 3 active quantum dots, (b) show all 3 dots to be inactive while (c) show two have reactivated, while the 3 remains in a dark-state.

In this work after topographic and optical images were obtained, the SNOM probe was positioned and held steady such that its aperture was only a few nano-meters over what was believed to be a single quantum dot. The fluorescence was recorded with the APD set to 10 ms integration, for a time of 600 s, shown in Figure 7.20. It is believed however, that there is a degree of variation in the laser power that is modulating the signal.

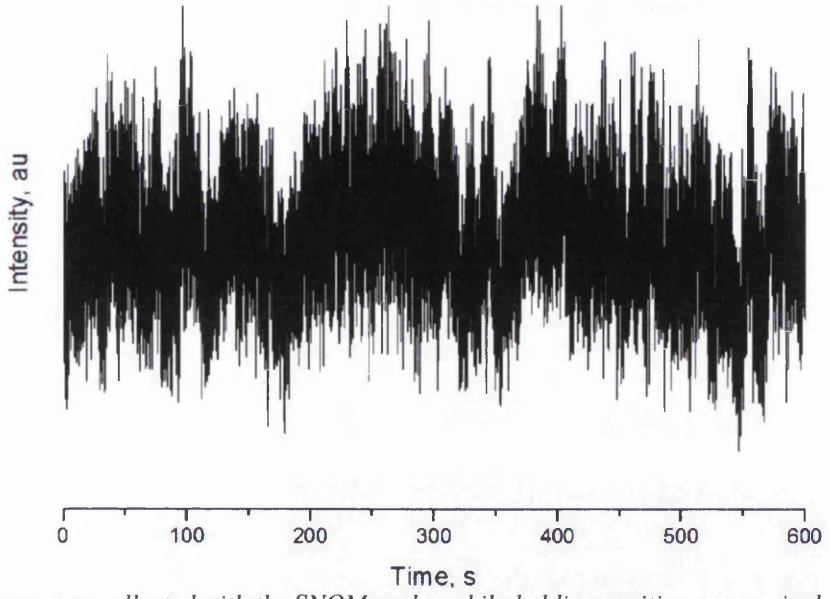

Fig. 7.20 Fluorescence collected with the SNOM probe, while holding position over a single quantum dot. Integration time is 10 ms per point, for a total duration of 600 s.

Due to the low intensity fluorescent response from the quantum dot, relative to the background, and the modulating effect of the excitation laser, it is difficult to observe the full switching on / off of the fluorescence from the single dot. Expanding a 40 s section of the data, shown in Figure 7.21, reveals sudden changes in fluorescent intensity riding on a varying level of intensity. To test for laser power fluctuations within the fluorescence data, a higher sampling period of significantly less than 10 ms would be required.

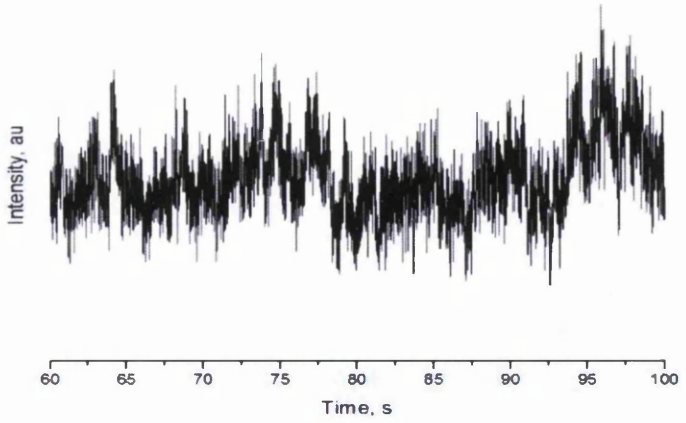

Fig. 7.21 40 second expansion of the fluorescence collected with the SNOM probe holding position over a single quantum dot. This graph shows a little more clearly the sudden changes in intensity due to the varying numbers of dark states of the quantum dot within the integration time of 10 ms, relative to the varying level of excitation intensity from the Ar^+ laser source.

Note, this 600 s trace does not show it actually switch off and might well represent the fluorescent emission of 2 or more quantum dots within the optical field, as discussed by Chevalier *et al.* [4].

The lack of a completely off state of the quantum dot for any significant time could be for one of several reasons:

- If the quantum dot is well formed such that it contains little or no surface states or deep traps within the energy gap then the formation of an exciton is most likely to lead to radiative recombination without any trapping processes, either internally at an impurity, or at the core surface in a deep trap.
- The laser power being relatively low, at less than 1 mW injected into the SNOM fibre, results in nanowatts at the aperture due to a theoretical transmission of between 10^{-4} and 10^{-7}. Therefore, a relatively constant level of fluorescence is expected as there is a low probability that the quantum dot will be re-excited once it is already in an excited state. This is due to its nano-second recombinative lifetime. Any photons absorbed before the first exciton has

radiatively recombined, resulting in a non-radiative Auger process. This will cause the net fluorescence to be reduced. The recorded fluorescent level over any interval significantly longer than the recombination lifetime will oscillate around a mean level due to these dark states. It can therefore be stated that blinking is occurring, at least for this quantum dot, only on a timescale shorter than the 10 ms integration time used in the experiment. Thus, for a relatively steady state system, any significant changes in the level of intensity over a long duration is likely to be due to laser power level fluctuations or coupling inefficiencies at fibre-splices.

7.8 Point spectroscopy of CdSe/HDA quantum dots

Two colours of CdSe/HDA quantum dots mixed in PMMA were spun on mica and a 10 µm SNOM image, shown in Figure 7.22, revealed the topographic and optical presence of quantum dots. Regions of high intensity can be seen within the red boxed area.

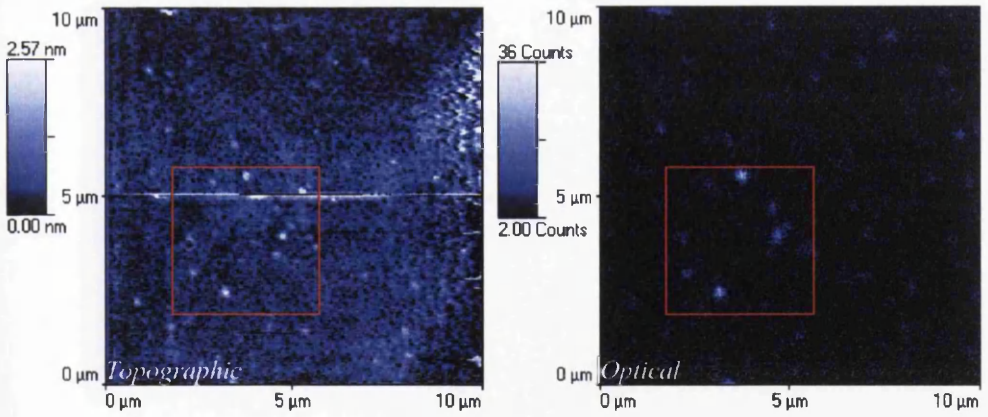

Fig. 7.22 Multiple point spectroscopy was carried out at locations within the marked red region to ascertain the number of quantum dots present at each bright area.

A subsequent smaller scan shown in Figure 7.23, from within the red box defined in Figure 7.22, showed clustering of the quantum dots. This was known to be a lateral

feature as opposed to them gathering on top of each other due to the low height of 2.80 nm from the mean PMMA background.

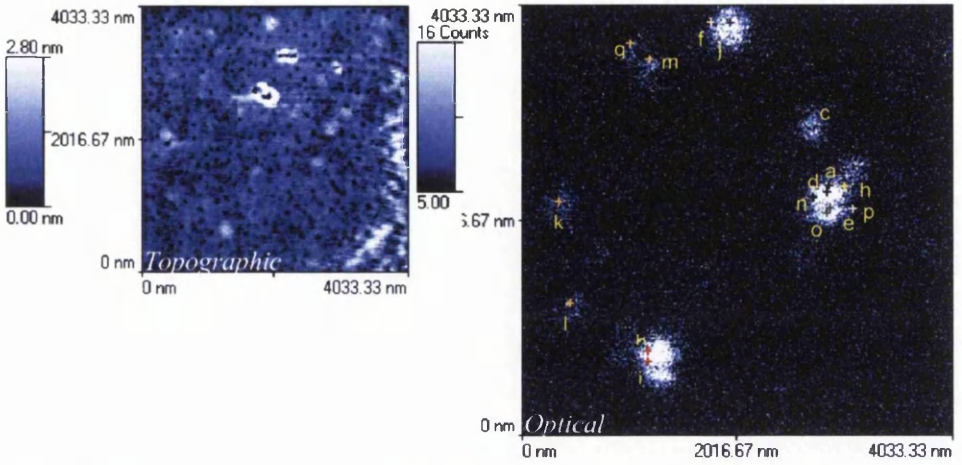

Fig. 7.23 Multiple point spectroscopy, used to ascertain the number of quantum dots present at each bright area.

Another indication is that of the large difference in optical fluorescent intensity between the different dots. For instance, points (g,k,l,m) are all relatively low in intensity, whereas the rest are within regions of not only slightly larger intensity, but also higher density of fluorescence. A higher fluorescent intensity, being the opposite of intermittency (blinking), will be more likely to occur where more than one quantum dot is fluorescing, or at least in an active state.

Following the scan shown in Figure 7.23, point spectroscopy was carried out at 16 locations on and around the more intensely fluorescent regions, as these were more likely to be the result of quantum dot aggregation. These spectra are shown in Figure 7.24, the majority of which were collected with an integration time of 5 minutes, while 4 of them were collected over a period of 10 minutes, shown in Figure 7.24(d-g).

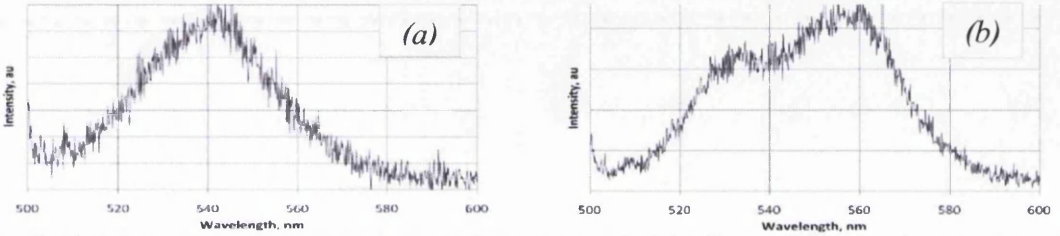

Fig. 7.24 Point spectroscopy carried out at locations marked in Figure 7.23, showing mostly multiple quantum dot fluorescence, evident due to the asymmetry in the spectral peak.

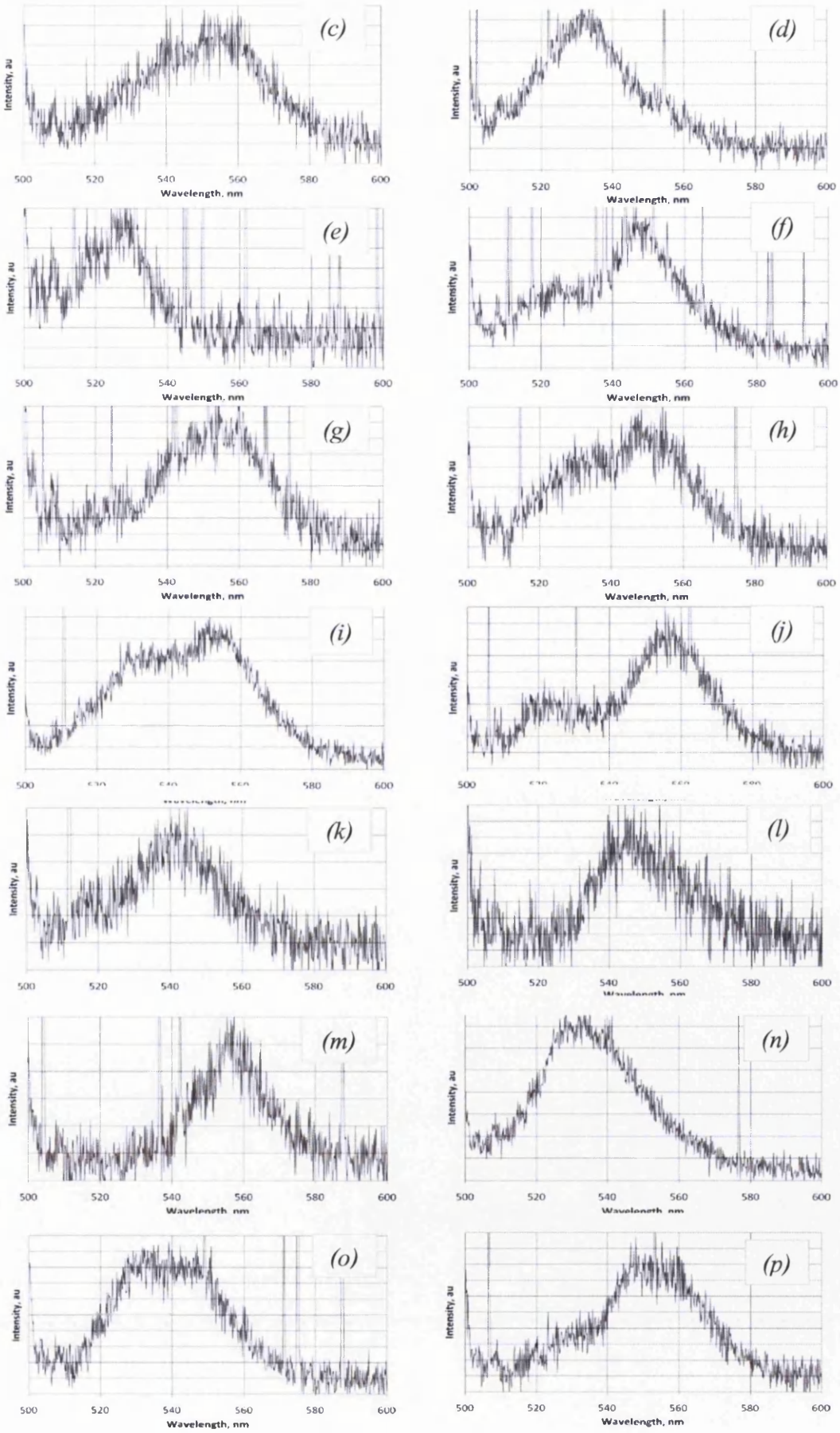

Fig. 7.24 (continued) Point spectroscopy carried out at locations marked in Figure 7.23, showing mostly multiple quantum dot fluorescence, evident due to the asymmetry in the spectral peaks.

It is difficult to determine a precise measurement of FWHM from the spectra in Figure 7.24 partly due to excessive noise, and partly due to their asymmetry as a result of multiple fluorescent emissions from multiple quantum dots.

All spectra within Figure 7.24 are non-Gaussian apart from Figure 7.24(m) which is also noisy due to the low detected fluorescent intensity, but the most likely candidate of a single quantum dot emission.

Considering that the sample consists of two different quantum dot colours having peaks centred at 498 nm and 560 nm for concentrated solutions, the majority of the spectra are the result of those of the longer wavelength colour. The spectral peaks in Figures 7.24(b,d,f,i,j) indicate the likelihood of the presence of both quantum dot colours due to the separation between the two peaks. These are however an assumption, but it must be noted that the ensemble spectra of these two quantum dot samples are broad, and as can be seen in Figure 7.2, spectrally overlap to some degree. Figure 7.24(e) is almost certainly the result of a single emission from the shorter wavelength quantum dot sample.

As the sample consists of equal concentrations of both colours, there should be equal emissions at both ends of this spectral range. Most are at 540-560 nm and in the case of a double emission from both colours, the 540-560 nm is always the dominant compared to those at 520-530 nm. This is a good indication of Förster resonant energy transfer (FRET) whereby fluorescently absorbing and emitting donor and acceptor molecules and quantum dots, within a certain distance of each other, can pass energy, without

fluorescent emission from the donor taking place, providing a number of conditions are met.

From experiments carried out by Gómez *et al.* [6], an expected spectral emission for a single CdSe/CdS/ZnS quantum dot embedded in PMMA at room temperature would be symmetrical in shape with a FWHM of 15-18 nm. This can be attributed partly due to light-driven spectral diffusion as a result of Stark shifting, but mainly due to thermal broadening at room temperature as discussed by Empedocles *et al.* [9]. A Stark shift occurs when there is a change of the electric field in and around the quantum dot as a result of an alteration of the electronic configuration after excitation. This is also discussed in-depth in Chapter 3, section 3.8.1

7.9 Single quantum dot optical measurements

Due to the fluorescent blinking nature of quantum dots, it was relatively easy to identify single or small clusters of quantum dots. Figure 7.25 represents a spectrum obtained from a small cluster of CdSe/ZnS quantum dots from Evident Technologies.

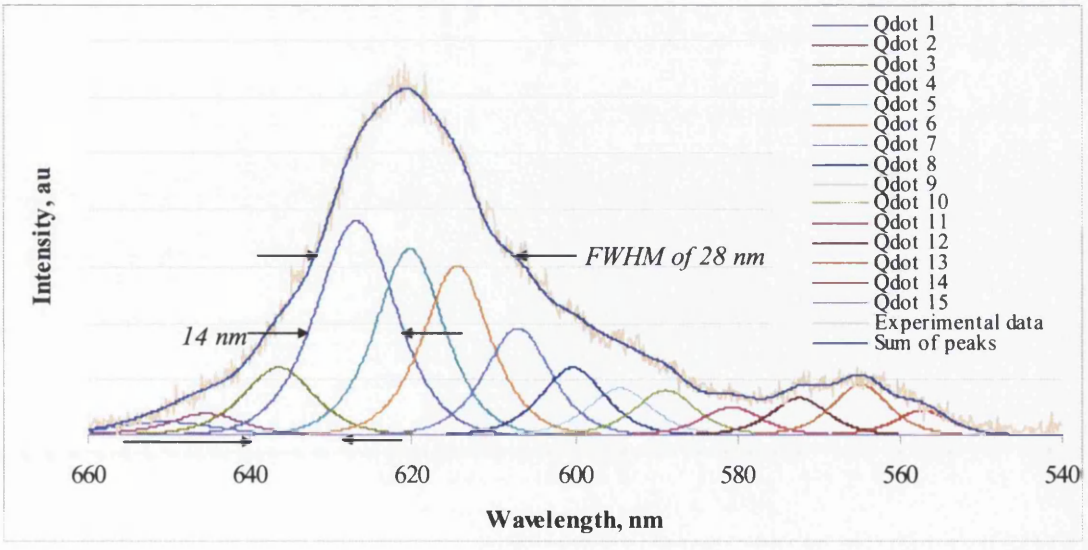

Fig. 7.25 Small cluster of quantum dots giving a spectral FWHM of ~ 28 nm, de-convolved to several ~ 14 nm Voigt functions consisting of both Gaussian and Lorentz distributions.

The spectrum was de-convolved using Microsoft Excel to span the ~28 nm FWHM of the main peak with Voigt functions,

$$V(x;\sigma,\gamma) = \int_{\infty}^{\infty} G(x-x';\sigma)L(x-x';\gamma)dx'.$$

This allowed the fit to account for broadening due to both thermal and spectral diffusion effects, with G the Gaussian, and L the Lorentzian functions, using the parameters variance, σ, of 0.025 nm, and Gamma, γ of ~ 0.02 nm respectively, with x the energy and x' the mean energy. This is only an estimated fit but clearly shows the presence of multiple quantum dots at a single location, while taking into account single dot broadening effects due to spectral diffusion and thermal effects.

A fluorescent spectrum collected from what was believed to be a single, fluorescently blinking, CdSe/ZnS quantum dot is shown in Figure 7.26, with a small contribution from a second localised dot. A Voigt function fit, using similar parameters used for the cluster fit shown in Figure 7.25, with a FWHM estimated to be 14 nm, in addition to a small fluorescent contribution from a second dot. This was the minimum FWHM spectral collection from the optical studies of quantum dots and is in close agreement with the minimum of 15 nm from far-field measurements of single CdSe/CdS/ZnS quantum dots in PMMA by Gómez *et al.* [6].

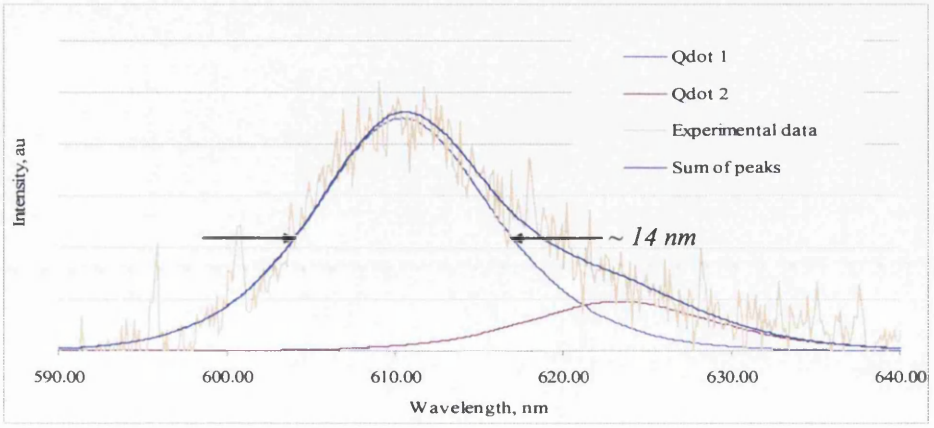

Fig. 7.26 Fluorescence emitted from a single CdSe/ZnS quantum dot having a spectral FWHM of ~ 14 nm with a small contribution from a second, lower intense dot.

The experimental results presented here ensured the confinement of the excitation area using a highly localised near-field source. This FWHM for a single quantum dot is considerably narrower than the ensemble far-field illuminated measurement of 37 nm from Figure 7.2.

7.10 Measurements of a single q-dot attached to the scanning probe

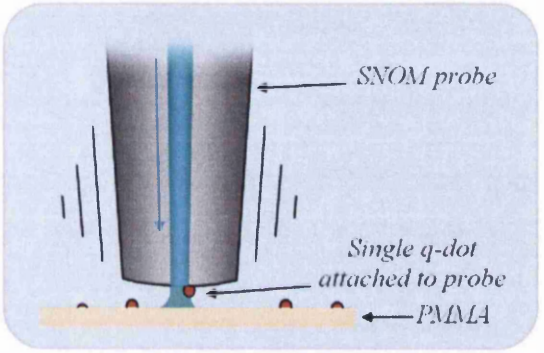

Fig. 7.27 Single CdSe/ZnS quantum dot attached to the underside of the SNOM probe within sight of the emitting aperture.

For a number of scans, a quantum dot attached itself to the underside of the SNOM probe within sight of the aperture as illustrated in Figure 7.27.

Background fluorescence was present throughout several scans for a period of a few hours, one of which is shown in Figure 7.28. The topographic image in Figure 7.28(a) shows regions of topographic height indicative of both single quantum dots and aggregation that match the bright fluorescent points within the optical image of Figure 7.28(b). The majority of the optical image, however, is masked by a fluorescent background level emitted from a single quantum dot attached to the underside of the probe. However, it must be noted, that it is possibly not the same quantum dot emitting throughout the whole optical image.

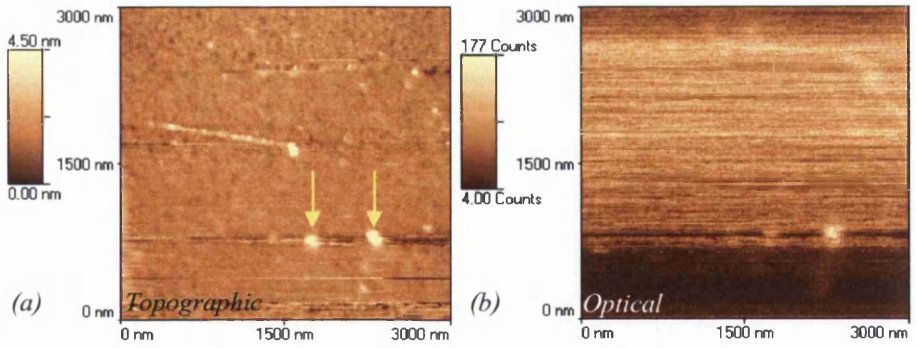

Fig. 7.28 Single CdSe/ZnS quantum dot attached to the underside of the SNOM probe within close proximity of the emitting aperture.

The question of whether or not it is the same quantum dot throughout that is attached to the underside of the tip arises from the sudden switch off of this background fluorescent level as it passes over the two large topographical regions, marked with yellow arrows in Figure 7.28. It is known that the probe does physically interact with the PMMA / quantum dots due to the occasional sweeping to one side of the polymer, as seen in Figure 7.19(a,b,c). Therefore, at the bottom of Figure 7.28(b), where the optical intensity begins to rise again for the last few scan-lines, this could be the result of an entirely different quantum dot.

To prove the presence of a single attached quantum dot, the probe was located at several positions within Figure 7.28 where both the topographic and optical images showed no features indicating the presence of a quantum dot. At each location a spectrum was obtained, two of which are shown in Figure 7.29.

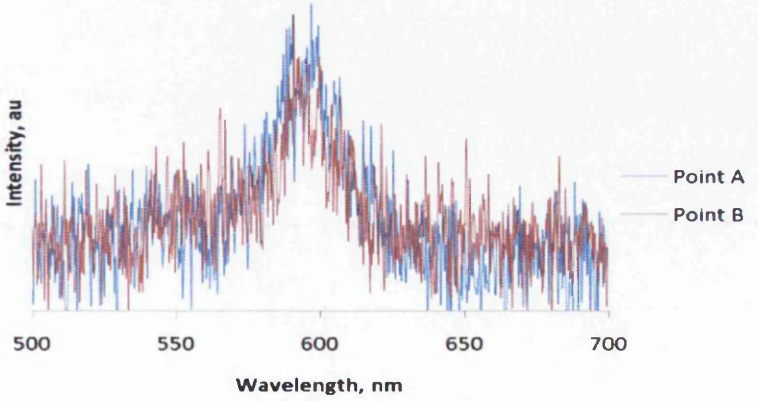

Fig. 7.29 Two spectra collected in the near-field at random locations at the surface of the image in Figure 7.28 where no quantum dots appeared to be present. The similarity in the spectra indicates that a quantum dot has attached to the emitting aperture of the SNOM probe.

The peak wavelength for both spectra in Figure 7.29 is at 595 ± 2 nm, the similarity a good indication that there is a quantum dot attached to the underside of the SNOM probe. The FWHM of the two spectra is 16 ± 1 nm, again a good indication of single quantum dot fluorescence.

The fluorescence level throughout most of Figure 7.28(b) however is not at a constant intensity and is better observed from a rotated view, shown in Figure 7.30. In the optical image, this masking fluorescence begins at a low level, and within a few scan lines quickly builds up to a maximum level, maintains a relatively constant level for 2/3 of the scan and then drops to virtually nothing for the remainder of the scan.

Fig. 7.30 Optical image illustrating the rapid rise and fall of the fluorescent intensity from a single quantum dot at the aperture of the SNOM probe. On the last line of this optical image, the quantum dot leaves the dark state and again begins to fluoresce.

The time evolution of the fluorescence rises from ~ 50 counts/15 ms/pixel in approximately 10 minutes to ~160 counts/15 ms/pixel, and then slowly returns down to 10 counts/15 ms/pixel, the background level.

Taking a closer look at a single line scan in Figure 7.31 from the optical image in Figure 7.28, an increase in blinking events results in a reduction of intensity measured over a distance of <50 nm, equivalent to 5 pixels. At 15 ms per pixel, while including operational overheads within the equipment, this is approaching 0.1 s for the 5 pixels.

This spatial width of <50 nm is far beyond the optical resolution of the probe, i.e. the SNOM probe has an aperture of approximately 100 nm and so the evanescent field present would be at least this wide, and thus the drop in intensity over this width can only be due to quantum dot blinking.

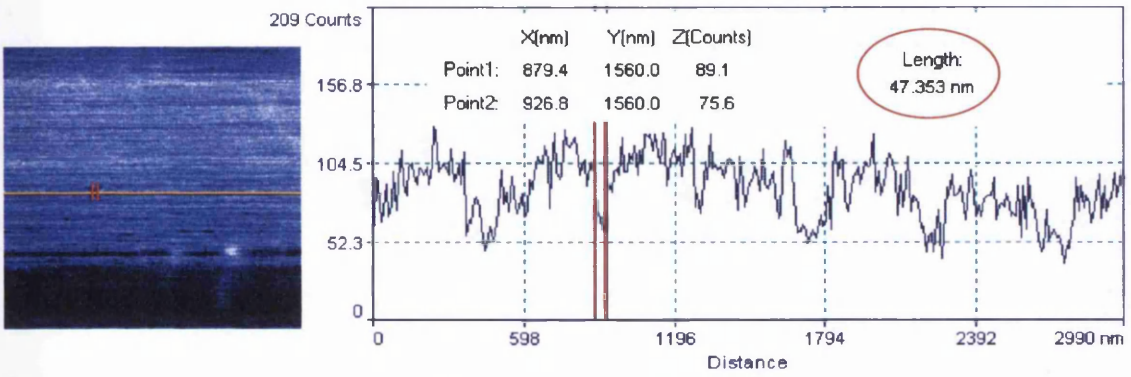

Fig. 7.31 Single CdSe/ZnS quantum dot attached to the underside of the SNOM probe within sight of the emitting aperture.

There is clear evidence of quantum dot photobrightening, as discussed by Javier and Strousse [15], Ebenstein *et al.* [19] and Pelton *et al.* [20], whereby repeated excitation with a laser source can cause the net fluorescence from individual quantum dots to increase. The reactivation of quantum dots from a dark state occurs when trapped electrons return to the core of the quantum dot making them fluorescently active. It must be noted, however, that with increased excitation intensity, the greater the probability of the dot entering a dark state and risk of permanent structural damage. Returning to optical images in Figures 7.19(a,b,c), Figure 7.32 compares the brightness of 3 quantum dots in a line.

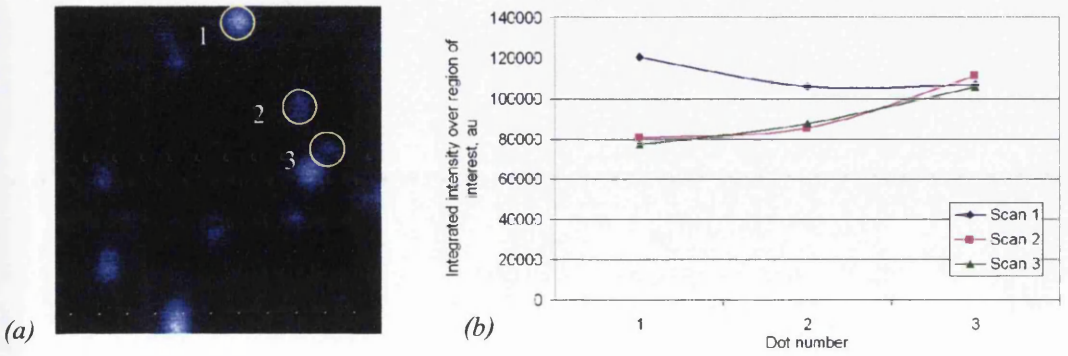

Fig. 7.32 Intensity comparison (a) of 3 quantum dots circled in (b) from successive scans shown in Figure 7.19(a-c), highlighting the photo-brightening effect.

Figure 7.32(a) indicates the regions of comparison, while Figure 7.32(b) represents the integrated intensity in the area of each dot for 3 successive optical scans. Two of the dots, marked '2' and '3' show a significant increase in detected intensity from $80x10^3$ units to over $100x10^3$ units. This is an increase of 20% due to photo-activation. The 3rd position marked as '1' is believed to be comprised of several quantum dots due to its significant brightness and low level of blinking events through the scanning process. Within this small cluster, one or more dots are experiencing photobleaching, evident from its successive decrease in intensity.

7.11 Far-field FRET measurements of quantum dots

Fŏrster resonant energy transfer (FRET), now commonly referred to as fluorescent resonant energy transfer, is a term given to the mechanism whereby energy is transferred between two fluorescent molecules. The more common name is a bit of a misnomer as there is no actual fluorescence exchange, only energy directly. A fluorescent donor enters an excited state by some means, and instead of recombining radiatively, the energy is transferred to an acceptor molecule via a long range dipole-dipole coupling mechanism, at which point the donor molecule returns to its ground state. Typical values of Fŏrster radius are between 5 and 10 nm dependent on the particle system, defined where the efficiency of energy transfer, E, is 50%, as discussed by Lakowicz [21]. Here E is given by,

$$E = \frac{1}{1+\left(r/R_0\right)^6}, \qquad 7.1$$

where r is the acceptor-donor separation distance, and R_o the Fŏrster distance for the two quantum dots. R_o however depends on a number of factors such as the donor

emission and acceptor absorption spectra and their relative molecular orientation, and is expressed as,

$$R_0^{\ 6} = 8.8 \times 10^{23} \kappa^2 n^{-4} Q_0 J, \qquad 7.2$$

with κ^2 the dipole orientation factor for the two molecules, n the refractive index, Q_o the fluorescence quantum yield of the donor molecule with no acceptor molecule present, while J is the factor that describes the spectral overlap of the donor emission and the acceptor absorption spectra.

During an experiment discussed in section 7.8, with a sample of two different quantum dots sizes spin-coated on mica, spectroscopy found a lower level of fluorescence intensity from the higher energy emitting quantum dots at <540 nm, compared to those emitting at ~565 nm. To investigate the reason for this, solutions of the two quantum dot sizes were tested for overall fluorescence as shown in Figure 7.33.

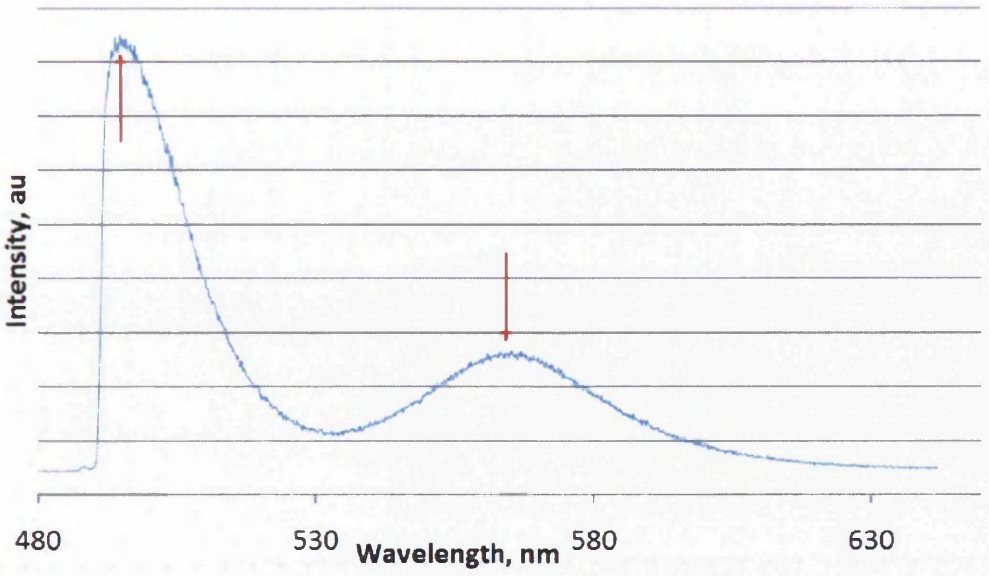

Fig. 7.33 Far-field excitation/collection of two colours of quantum dots in solution. The two red arrows indicate the peaks monitored during drying of the solution.

This was achieved by simply firing the laser through the side of the glass vial directly outside of the entrance slit of the spectrometer, as shown in Figure 7.1. The fluorescence from the bottle indicated that both quantum dots were fluorescing as a result of the 488 nm laser excitation, detected by the spectrometer's CCD detector.

The samples studied in the near-field are spin coated, with the toluene evaporating in the process, so it was decided to investigate not only what happens when a drop of this solution had dried, but also during the transition to drying.

Cover-slips were placed on the SNOM sample stage with the SNOM head-unit removed. The laser was fired from the far field, non-focussed, down onto the cover-slip and the transmission optics aligned to collect from the surface of the cover-slip to the spectrometer as shown in Figure 7.34. The Raman edge filter was used to remove the laser line, thus allowing only fluorescence to pass.

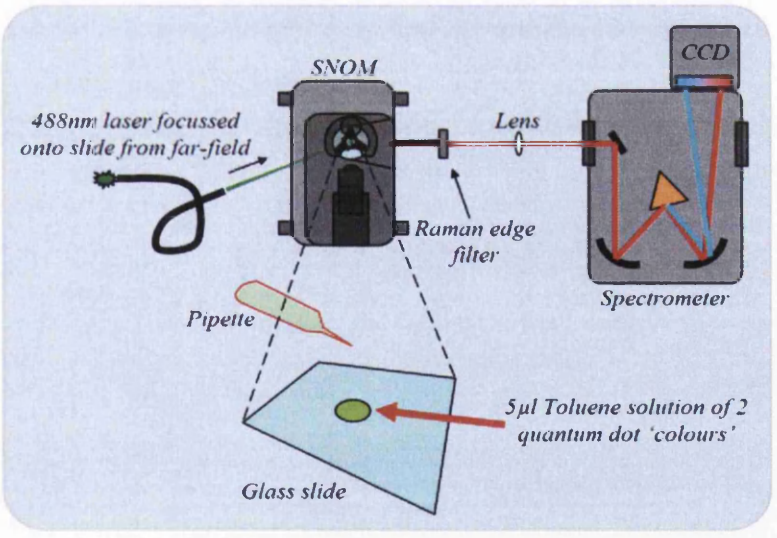

Fig. 7.34 Far-field illumination of droplets of quantum dot dispersed in toluene to help determine the spectral changes that occur during drying.

Using a pipette, 5 µl of the quantum dot in toluene solution was dropped onto the glass slide. The laser firing from the far-field caused the quantum dots to fluoresce. The

CCD was used to collect several hundred successive spectra, each of < 1 second integration as the toluene evaporated and the droplet dried. The data was then manipulated to extract the 498 nm and 565 nm intensity peak values with respect to time and plotted as shown in Figure 7.35.

The graph in Figure 7.35 can be explained by the drying mechanism of the droplet. As illustrated in Figure 7.36(a-e), the droplet is initially large and emits fluorescence from the area that is illuminated, including any subsequent internal reflections.

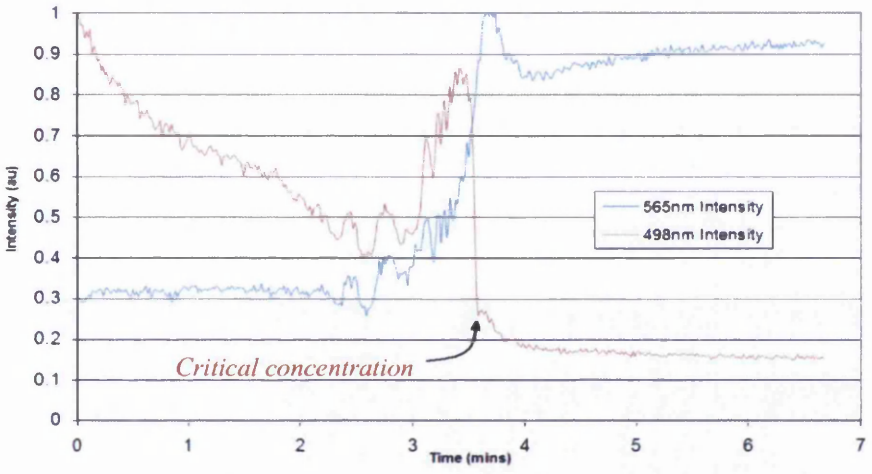

Fig. 7.35 Fluorescent response of two different sized quantum dots as their solvent dried, their increasing proximity resulting in fluorescence or direct energy exchange, at a critical concentration (marked).

During drying, Figure 7.36(b-d), the surface tension in the toluene pulls the quantum dots that have not attached themselves to the cover-slip glass surface, into the centre region increasing the quantum dot density. The 488 nm laser is only exciting a fraction of the solution present on the glass slide. The number of quantum dots being excited by the laser from the far-field thus increases resulting in an increase in fluorescence detected from both quantum dot colours.

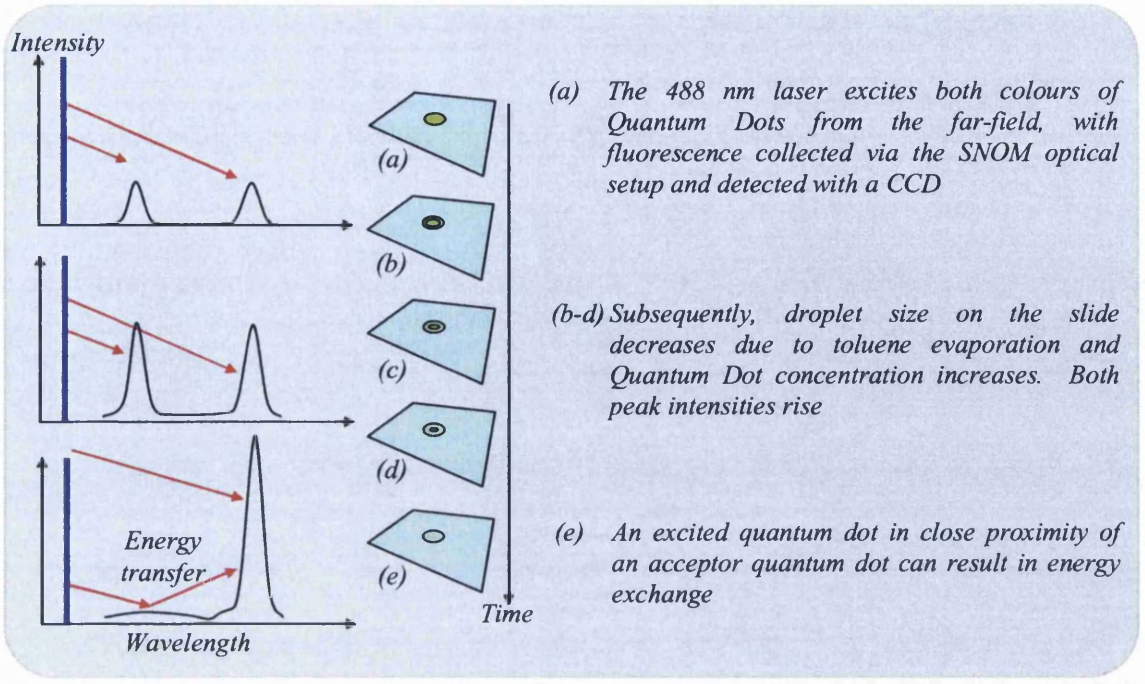

Fig. 7.36 The action of a drying quantum dot containing two quantum dot colours, illustrating the energy transfer.

The two graphs in Figure 7.35 are individually normalised to emphasize the various critical points in time. The level of fluorescence from the 498 nm emitting quantum dots begins to reduce to 50% of its initial level. This effect did not occur with every sample tested in this way, but varied between samples. At around 3 minutes, the detected fluorescent intensity began to increase as the reduced size droplet pulled the quantum dots into the laser illuminated area. At just over 3.5 minutes, the detected fluorescent intensity of the 565 nm quantum dots rose sharply, while at the same time that of the 498 nm sharply dropped. This was the critical concentration of the droplet, shown in Figure 7.36(e). At this point FRET occurred between the smaller quantum dots and the larger quantum dots due to their close proximity. This energy was then emitted as fluorescence of lower energy at 565 nm and the relative intensity of the two quantum dot colours separated dramatically.

A similar test was carried out by Kagan *et al.* [22] who compared two quantum dot coloured, spin coated samples. In their experiments, the intensity of the lower energy quantum dots was found to initially be lower than those of higher energy. Upon spin-coating a small quantity of this solution, and illuminating with the same light source, it was found that the intensity of the lower energy was greater due to FRET.

Such mechanisms are used in the field of biology to quantify for instance, molecular dynamics of protein-protein interactions, protein-DNA interactions and protein structure changes. Experiments in recent years by Sekatskii [23] and Műller *et al.* [24] among several groups have shown how FRET experiments can be carried out in the near-field. This is achieved through the attachment of quantum dots to the SNOM probe that act as the donor for the FRET mechanism to acceptor molecules at the surface. Because of the small Főrster radius of most molecules, acceptor molecular fluorescence can only occur when the SNOM probe is in close proximity; i.e. within a few nanometres. Thus the optical resolution of a 50 nm aperture SNOM probe is significantly improved from being aperture size limited, to approximately twice that of the Főrster radius.

7.12 Conclusion

Far-field measurements of concentrated solutions of quantum dots revealed spectral widths in excess of 36 nm, in agreement with manufacturer's specifications.

The sample preparations showed the successful and repeatable ability to generate 2-3 nm thick layers of the PMMA polymer, embedded with a monolayer of either CdSe/HDA or CdSe/ZnS core/shell quantum dots. This process appeared to cause no noticeable interference of the spectral emissions when studied in the near-field. The

minimum surface RMS roughness of the PMMA was measured at 0.15 nm, determined to be as a result of the disordered spread of the polymer during spin coating. Topographic and optical imaging in the near-field revealed a density of quantum dots, in some cases, less than 10 quantum dots per μm^2, although such low concentrations were not necessary due to the SNOM being capable of achieving optical resolutions of <150 nm.

Near-field optical imaging revealed single quantum dot blinking events over a wide range of times, from less than 10 ms up to several hours showing the complexity of the mechanics of nano-sized materials.

Near-field spectroscopy measurements of single quantum dots revealed spectral widths as low as 14 nm for both CdSe/HDA and CdSe/Zns core/shell variants. CdSe/ZnS had a noticeably greater quantum yield compared to CdSe/HDA, manifesting itself in a greater signal to background contrast during imaging, in good agreement with current literature [6].

Spatial resolution measurements of single quantum dots were in good comparison with the dimensions of the scanning probe aperture, achieving optical resolutions of at best, ~90 nm. This highlights the strength of near-field imaging, with its ability to detect differing spectral signatures at optical resolutions of a significant fraction of the diffraction limit.

A CdSe/ZnS quantum dot that had attached itself within the aperture of the scanning probe revealed a near-field spectral measurement with a FWHM of approximately 16

nm. This quantum dot, or one that changed places with it also showed a changing rate of blinking events over time, evident from a gradual varying level of brightness over 2 hours, during image acquisition. It is important to understand blinking events that cause this brightening effect that occurs as a result of a net increase of fluorescence. Blinking events create complications in experiments where an emission would be expected but none were detected, resulting in a null result.

Final experiments involved measurements in the far-field on samples of mixed size quantum dots. Results indicated the possibility of a FRET mechanism due to the drop in higher energy fluorescence, for a high concentration of quantum dots dried on a substrate. Further investigations need to be carried out in the near-field to progress this work.

References

[1] Talapin D.V., Rogach A.L., Kornowski A., Haase M., Weller H., Nano Letters **1** (4), 207-211, (2001)

[2] Cumberland S.L., Hanif K.M., Javier A., Khitrov G.A., Strouse G.F., Woessner S.M., Yun C.S., Chem. Mater. **214**, 1576-1584, (2002)

[3] Murray C.B., Norris D.J., Bawendi M.G., J. Am. Chem. Soc. **115**, 8706-8715, (1993)

[4] Chevalier N., Nasse M.J., Stark M., Motte J.F., Woehl J.C., Huant S., J. Korean Phys. Soc. **47**, S126-S129, (2005)

[5] Nirmal M., Dabbousi B.O., Bawendi M.G., Macklin J.J., Trautman J.K., Harris T.D., Brus L.E., Nature **383**, 802-804, (1996)

[6] Gómez D.E., van Embden J., Mulvaney P., Appl. Phys. Lett. **88**, 154106, (2006)

[7] Shimizu K.T., Neuhauser R.G., Leatherdale C.A., Empedocles S.A., Woo W.K., Bawendi M.G., Phys. Rev. B **63**, 205316, (2001)

[8] Pientka M., Dyakonov V., Meissner D., Rogach A., Talapin D., Weller H., Lutsen L., Vanderzande D., Nanotechnology **15**, 163-170, (2004)

[9] Empedocles S.A., Bawendi M.G., J. Phys. Chem. B **103**, 1826-1830, (1999)

[10] Minelli C., Geissbuehler I., Eckert R., Vogel H., Heinzelmann H., Liley M., Colloid Polym. Sci. **282**, 1274-1278, (2004)

[11] Minelli C., Frommen C., Hinderling C., Pugin R., Heinzelmann H., Liley M., Colloid Polym. Sci. **284**, 482-488, (2006)

[12] Santer S., Kopyshev A., Yang H.K., Ruehe J., Macromolecules **39**, 3056-3064, (2006)

[13] Kortan A.R., Hull R., Opila R.L., Bawendi M.G., Steigerwald M.L., Carroll P.J., Brus L.E., J. Am. Chem. Soc. **112**, 1327-1332, (1990)

[14] Hines M.A., Guyot-Sionnest P.J., J. Phys. Chem. **100**, 468-471, (1996)

[15] Javier A., Strouse F., Chem. Phys. Lett. **391**, 60-63, (2004)

[16] Achermann M., Hollingsworth J.A., Klimov V.I., Phys. Rev. B **68**, 245302, (2003)

[17] Wang L.W., Califano M., Zunger A., Franceschetti A., Phys. Rev. Lett. **91**, 056404, (2003)

[18] Bachir A.I., Durisic N., Hebert B., Grűtter P., Wiseman P., J. Appl. Phys. **99**, 064503, (2006)

[19] Ebenstein Y., Mokari T., Banin U., Appl. Phys. Lett. **80** (21), 4033-4035, (2002)

[20] Pelton M., Grier D.G., Guyot-Sionnest P.J., Appl. Phys. Lett. **85** (5), 819-821, (2004)

[21] Lakowicz J.R., Principles of Fluorescence Spectroscopy, 3rd Edition, Kluwer Academic, New York, (2006)

[22] Kagan C.R., Murray C.B., Nirmal M., Bawendi M.G., Phys. Rev. Lett. **76**, 1517-1520, (1996)

[23] Sekatskii S.K., Phil. Trans. R. Soc. Lond. A **362**, 901-919, (2004)

[24] Műller F., Gőtzinger S., Gaponik N., Weller H., Mlynek J., Benson O., J. Phys. Chem. B **108**, 14527-14534, (2004)

8 Final conclusions

Developments to a scanning near-field microscopy (SNOM) have been successfully implemented to carry out spectroscopic analysis of both vertical cavity surface emitting lasers (VCSEL) and cadmium selenide quantum dots.

The modifications and expansions to the standard SNOM have included the addition of a spectrometer with a cooled CCD detector. These arrangements, together with a range of focussing apparatus and optical channelling techniques, have allowed the careful, progressive development and optimisation of the often complex task of detection of extremely low levels of light.

Integration of specialised partial mirrors enabled the possibility of bi-directional optical paths to allow maximisation of coupling efficiencies at fibre-optic terminations. This was achieved with the aid of a second laser that was aligned and carefully focussed along the back-path, through a fibre-optic coupling unit into the 5μm core of a single-mode fibre to the SNOM probe via a fibre-splice. Optimisation of the fibre-splice was of paramount importance for the collection-mode configuration of the SNOM to detect light emissions within the optical aperture of the VCSEL. Without such a set-up, optical alignment procedures would have been difficult and significantly time consuming to complete.

Such complex optical set-ups have allowed the SNOM to be operated in near-field stimulation and collection modes, involving both reflection and transmission optics, thus maximising its versatility. By using such configurations, it has been possible to obtain simultaneous topographic and spectroscopically filtered images of transverse

modes within the near-field of a VCSEL. The successes of these experiments led to changes to the experimental set-up, which allowed both the detection and spectroscopic characterisation of mixed samples of quantum dots in the near-field.

The summary of results discussed herein show the success of the experimental set-ups used that can be applied to a range of different configurations for low light level detection, as is generally necessary at the nano-scale. They also show a vast potential for future experiments that can be carried out in the near-field that could be extended into the biological field, thus enhancing the resolution and contrast of imaging techniques.

This chapter summarises these findings and discusses future developments in context to the progress made by this research.

8.1 Vertical cavity surface emitting lasers

A number of VCSELs were studied in the near-field using a number of experimental detection configurations to compliment the high resolution imaging capabilities of the SNOM.

Far-field spectra for a range of injection currents allowed the determination of the exact point of lasing of several different VCSELs. It was found that the total intensity of spontaneous emission reached a maximum at this lasing threshold for the two measured devices as expected.

Topographic and optical imaging in the near-field of the aperture of an ~ 845 nm lasing VCSEL having an ~13 μm optical aperture with a power density of ~ 2 MWm^{-2} showed a highly ordered, yet complex transverse mode structure. The optical aperture was re-imaged while filtering at various wavelengths as dictated by a far-field spectrum with the aid of a monochromator, to show the simultaneous presence of these individual modes and their relative intensities for a fixed injection current. These were successfully compared with the theoretical structural patterns of various combinations of TEM modes. Point spectroscopy in the near-field illustrated the presence and absence of different transverse modes at several different locations within the aperture as well as the highly localised collection capability of the experimental setup [1].

At low lasing level injection currents, further analysis showed concentric modulations indicating evidence of clipping of the fundamental TEM_{00} Gaussian beam several microns below the surface of the aperture [2]. At increased injection currents, the presence of higher order TEM modes resulted in this concentric modulation becoming a more complicated structure across the aperture. Structural changes at the surface of the device also showed a modulating effect on the intensity across the surface of the aperture, of approximately one wavelength spacing. The idea of modifying the surface of VCSELs has been a topic of investigation for many years with the aim of controlling the transverse mode structure and the polarisation of such devices [3,4]. Such modulations have been discussed in literature [5,6,7], but never fully revealed in near-field measurements to be concentric as those measured here.

Analysis and discussions of these spectrally filtered images and concentric modulations of the fundamental and higher order TEM modes have since been published by Holton *et al* [8].

8.2 Semiconductor CdSe quantum dots

Successful preparations were difficult to achieve due to clustering problems with quantum dots, and impurities within the toluene that generated holes within the thin polymethyl-methacrylate (PMMA) layer. Different colours of cadmium selenide/zinc sulphide (CdSe/ZnS) and cadmium selenide/hexadecylamine (CdSe/HDA) core/shell quantum dots were individually mixed at different concentrations with PMMA in toluene. Drops of the resulting solution were spin coated on silicon and cleaved mica. The resulting thickness of the PMMA was measured with an atomic force microscope at ~2.4 nm for concentrations of PMMA of 0.1% to toluene by weight, spun at 2 krpm.

SNOM was used to simultaneously image the topographical and optical response of the mica spun samples. Concentrations were optimised to produce several small clusters with a few single quantum dots spread across the mica. Topographic measurements, coupled with the optical imaging to confirm the presence of a quantum dot, confirmed the thickness of PMMA to be approximately, or less than, the diameter of the quantum dots, roughly ~ 2.6 nm.

Initial samples from spin-coating a variety of mixtures of quantum dots in low concentrations of PMMA in toluene showed the PMMA separating into domains where the mica coverage was ~50% or less due to a combination of dewetting and contamination from particulates in the toluene. After filtering the toluene, these

domains were minimised and a minimum surface roughness of 0.15 nm was achieved, at which point the topographical presence of the quantum dots was clearly visible.

The CdSe/ZnS quantum dots were found to have a greater quantum yield than that for CdSe/HDA. This has been indicated in literature to be due to the presence of the wider band-gap material enhancing the electron confinement within the core, while the only effect of HDA was to remove surface states [9,10,11,12].

Optical resolution was limited by the size of the aperture of the SNOM tapered/coated optical fibre probe. With smaller apertured probes and an optimised experimental setup however, imaging of single/small clusters of quantum dots with <100 nm optical resolution was successfully achieved.

Optical response of single or small clusters of quantum dots showed a significant blinking effect. It was noted that repeated imaging of a single quantum dot would sometimes result in it becoming completely inactive, and returning for subsequent images. This highlights an important characteristic of quantum dots [13,14,15]. A time trace of the fluorescence from a single quantum dot showed the net effect of blinking events, albeit modulated by fluctuations in the laser intensity, affecting its overall brightness. This was better illustrated in an image where a single quantum dot, attached within the emitting aperture of the SNOM probe, fluoresced with initially increasing brightness, finally decreasing until it completely entered a dark state.

The fluorescent emission of a single quantum dot was expected to be spectrally Gaussian as a result of spectral diffusion over long collection times. Point spectroscopy

of 2 different coloured quantum dots in PMMA spin coated on mica, showed the different wavelength emissions at single locations. The spectral shape of fluorescence was used to determine the presence of one or more quantum dots, spectrally close in colour. The minimum spectral width measured for a single CdSe/ZnS quantum dot was ~14 nm and compared favourably with very dilute quantum dot mixtures measured in the far-field [13,16]. Where 2 or more quantum dots were present within a single spectrum, the emission at longer wavelength was always found to have a greater intensity. This was taken as an indication of some quenching activity for different sized quantum dots in close proximity.

As a result of this reduced intensity of the higher energy fluorescent emissions, far-field measurements of solutions of 2 colours of quantum dots dissolved in toluene were carried out which showed a strong quenching effect. Due to the lateral optical resolution of the SNOM being aperture limited to 50 nm or more, this exceeds the ~10 nm or less Fŏrster distance for quantum dots [17] and would therefore not be straightforward to distinguish between two adjacent, different sized quantum dots at the surface. Fŏrster resonant energy transfer experiments have been carried out by other groups in the near-field [18,19], utilising a quantum dot functionalised SNOM probe, to measure the change in spectral properties as a function of distance relative to quantum dots on a sample. Another method to determine the presence of different coloured quantum dots would be with fluorescence lifetime imaging, a technique increasingly being used in the imaging process of multiple fluorophores within biology [17].

8.3 Future opportunities and direction of this work

The work contained within this thesis has shown the spectroscopic development and optimisation of a generic SNOM imaging system. Future possibilities might include studies on a wide variety of electroluminescent and fluorescently active devices and materials. One very active area is that of Főrster resonant energy transfer mechanisms between quantum dots and organic fluorophores in the field of biology [20]. Complex studies of fluorescence lifetime measurements in the near-field, such as those of Cadby *et al.* [21] help to determine the mechanisms of energy transfer between donor and acceptor molecules. Other areas currently being investigated that are utilising the spectroscopic capabilities are that of Raman and apertureless SNOM (ASNOM). ASNOM utilises a sharp gold tip that can enhance the Raman signal produced from far-field illumination at the sample surface. This produces a detectable contrasting signal that can be used to generate high resolution imaging and a wealth of information on chemical properties of the material.

It can be seen that there is much work and many techniques that can utilise the near-field spectral capabilities of the SNOM. The developments that have been instigated during this work can be furthered and expanded to reveal ever more optical and structural information about materials and devices beyond the diffraction limit.

References

[1] Hörsch I., Kusche R., Marti O., Weigl B., Ebeling K.J., J. Appl. Phys. **79**, 3831, (1996)

[2] Siegman AE., Lasers, University Science Books, 727-736, (1986)

[3] Haglund A., Gustavsson J.S., Bengtsson J., Jedrasik P., Larsson A, IEEE J. Quantum Electron. **42**, 231 (2006)

[4] Ostermann J.M., Debernardi P., Michalzik R., IEEE J. Quantum Electron. **42** (7), 690-698, (2006)

[5] Knopp K.J., Christensen D.H., Rhodes G.V., Pomeroy J.M., Goldberg B.B., Ünlü M.S., J. of Lightwave Tech. **17**, 1429, (1999)

[6] Hegarty S.P., Huyet G., McInerney J.G., Choquette K.D., Phys. Rev. Lett. **82**, 1434, (1999)

[7] Ackemann T., Barland S., Cara M., Balle S., Tredicce J.R., Jäger R., Grabherr M., Miller M., Ebeling K.J., J. Opt. B: Quantum Semiclass. Opt. **2**, 406, (2000)

[8] Holton M.D., Rees P., Dunstan P.R., J. Appl. Phys. **101**, 023103 (2007)

[9]Peng X., Schlamp M.C., Kadavanich A.V., Alivisatos A.P., J. Am. Chem. Soc. **119**, 7019-7029, (1997)

[10] Bowen-Katara J.E., Colvin V.L., Alivistos A.P., J. Phys. Chem. **98**, 4109-4117, (1994)

[11] Hines M.A., Guyot-Sionnest P.J., Phys. Chem. **100**, 468-471, (1996)

[12] Empedocles S.A., Norris D.J., Bawendi M.G., Phys. Rev. Lett. **77**, (18), 3873-3876, (1996)

[13] Neuhauser R.G., Shimizu K.T., Woo W.K., Empedocles S.A., Bawendi M.G., Phys. Rev. Lett. **85** (15), 3301-3304, (2000)

[14] Javier A., Strouse G.F., Chem. Phys. Lett. **391**, 60-63, (2004)

[15] Empedocles S.A., Bawendi M.G., J. Phys. Chem. B. **103**, 1826-1830, (1999)

[16] Gómez D.E., van Embden J., Mulvaney P., Appl. Phys. Lett. **88**, 154106, (2006)

[17] Lakowicz J.R., Principles of Fluorescence Spectroscopy, 3rd Edition, Kluwer Academic, New York, (2006)

[18] Sekatskii S.K., Phil. Trans. R. Soc. Lond. A **362**, 901-919, (2004)

[19] Műller F., Gőtzinger S., Gaponik N., Weller H., Mlynek J., Benson O., J. Phys. Chem. B **108**, 14527-14534, (2004)

[20] Zhang C.Y., Yeh H.C., Kuroki M.T., Wang T.H., Nature Lett. **4**, 826-831, (2005)

[21] Cadby A.J., Dean R., Elliott C., Jones R.A.L., Fox A.M., Lidzey D.G., Adv. Mat. **19** (1), 107, (2007)

Appendix 1 – Estimation of number of quantum dots in a solution

From the information supplied by the Evident Technologies, it was possible to estimate the quantity of actual CdSe/ZnS quantum dots present within the 10 ml of toluene. CdSe quantum dots can form two different crystal structures namely Wurzite and Zinc-Blende. The quantum dots studied were of the Zinc-Blende crystal lattice structure, with a lattice constant of 0.605 nm, as confirmed by Kortan *et al.* [1] and shown in Figure A3.1 [2]. ZnS has a lattice constant of 0.54093 nm as given in the Handbook of Chemistry and Physics [3].

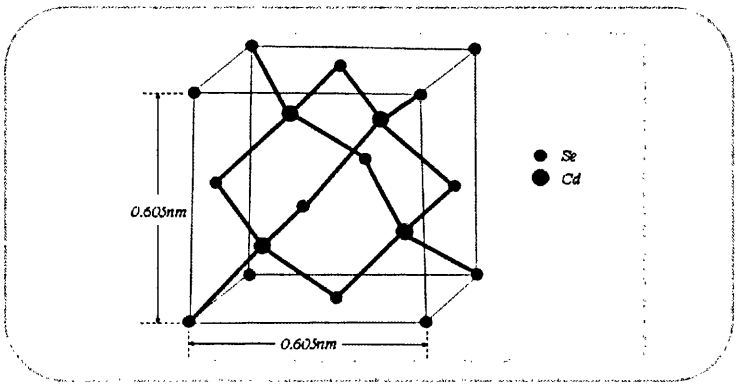

Fig. A3.1 Zinc-Blende crystal lattice structure for CdSe core quantum dots.

For the CdSe/ZnS quantum dots, the following calculation gives approximately the number of quantum dots contained in a 10 ml toluene sample as supplied by Evident Technologies.

CdSe lattice spacing 0.605 nm Cd = 112.41 amu, Se=78.96 amu
ZnS lattice spacing 0.54093 nm Zn = 85.39 amu, S=32.07 amu

There are 8 atoms per unit volume lattice, an average of 4 atoms of Cd (Zn) and 4 atoms of Se (S) per unit lattice.

0.605 nm^3 cell of CdSe there are 4 x 112.41 (Cd) + 4 x 78.96 (Se) = 765.48 amu
0.54093 nm^3 cell of ZnS there are 4 x 85.39 (Zn) + 4 x 32.07 (S) = 469.84 amu

For a CdSe dot 2.6 nm in diameter, a shell thickness 0.4 nm of ZnS would give optimum passivation and enhanced confinement effects as determined by Kortan *et al.* [1]. The number of dots present in 5 mg of CdSe/ZnS material can thus be estimated from:

$$4/3*pi*1.3\ nm^3 / 0.605\ nm^3 = 41.56 \times 765.48\ amu\ of\ CdSe\ in\ 2\ nm\ radius\ sphere$$

$$4/3*pi*(1.7^3 - 1.3^3)\ nm^3 / 0.54093\ nm^3 = 71.88 \times 469.84\ amu\ of\ ZnS\ in\ 0.4\ nm\ thick\ shell$$

$$Mass = (41.56 \times 765.48 + 71.88 \times 469.84) \times 1.66 \times 10^{-27} = 1/089 \times 10^{-22}\ kg / dot$$

$$[1\ amu = 1.66 \times 10^{-27}\ kg]$$

Therefore, in 5 mg of quantum dots there are $5 \times 10^{-6} / 8.433 \times 10^{-23} \approx 4.59 \times 10^{16}$ dots.

Constants obtained from the Handbook of Chemistry and Physics [3]

Appendix 2 - Gratings

As discussed by Demtrőder [4], parallel rays of light incident on the grooves of a grating will refract as a function of wavelength, as indicated in Figure A2.1.

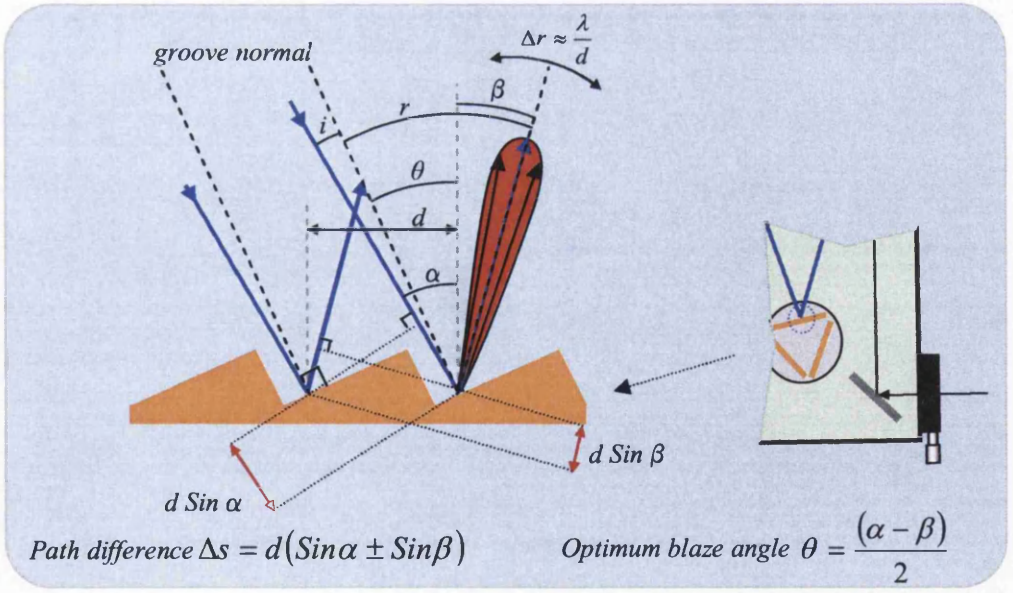

Fig. A2.1 Light incident on the spectrometer grating is diffracted at an angle as a function of wavelength.

It can be seen that the path difference for 2 coherent light rays of equal wavelength interfere constructively when the path difference Δs is an integer multiple m of the incident wavelength λ, as given by,

$$\Delta s = m\lambda = d\left(Sin\alpha \pm Sin\beta\right). \qquad A2.1$$

Reflectivity, R, of such ruled gratings is a function of blaze angle, θ, and the diffraction angle, r. When R reaches its maximum value, the incidence angle, i, and refraction angle, r, relative to the groove normal are equal, giving specular reflection. The reflectivity function has a broad distribution as opposed to a sharp response. Incidence angle α is a function of spectrometer construction, while the angle of constructive interference, β, is wavelength dependent. The blaze angle needs to be specified for a spectral range for optimisation of the spectrometer. In order to determine the spectral resolving power of such a spectrometer with a particular grating, it is necessary to look at the distribution of the light refracted from the multiple grooves. The phase difference, ϕ, can be expressed as a function of path difference, given by equation A2.1, as,

$$\phi = 2\pi \frac{\Delta s}{\lambda}. \qquad A2.2$$

The sum of the amplitude of light across N grooves, all diffracted in direction β, can be expressed as,

$$A_R = \sqrt{R}\sum_{m=1}^{N-1} A_g e^{im\phi} = \sqrt{R}A_g \frac{1-e^{iN\phi}}{1-e^{-i\phi}}, \qquad A2.3$$

where A_g is the amplitude of the partial wave incident on a single groove, and $R(\beta)$, a function of β, is the reflectivity of the grating. Intensity, I_R, can be determined from the amplitude of the reflected waves,

$$I_R = \varepsilon_0 c A_R A_R^*. \qquad A2.4$$

Using the identities,

$$\left.\begin{aligned} Cos^2x - Sin^2x &= Cos2x, \\ 1 - Cos2x &= 2Sin^2x, \\ Sin2x &= 2SinxCosx, \\ \text{and } Sinx = \frac{e^{ix} - e^{-ix}}{2i}\ Cosx &= \frac{e^{ix} + e^{-ix}}{2}, \end{aligned}\right\} \quad A2.5$$

we can say,

$$\left|1 - e^{iN\phi}\right| = \left|1 - CosN\phi + iSinN\phi\right|,$$

$$= \left|2Sin^2\frac{N\phi}{2} + iSin\frac{N\phi}{2}Cos\frac{N\phi}{2}\right|$$

$$= \left|2Sin\frac{N\phi}{2}\right|\left|Sin\frac{N\phi}{2} + iCos\frac{N\phi}{2}\right|$$

$$= 2Sin\frac{N\phi}{2}. \quad A2.6$$

A similar treatment, when applied to the second exponential in equation A2.3 results in,

$$A_R = \sqrt{R}A_g\frac{1 - e^{iN\phi}}{1 - e^{-i\phi}},$$

$$= \sqrt{R}A_g\frac{Sin\dfrac{N\phi}{2}}{Sin\dfrac{\phi}{2}}. \quad A2.7$$

Thus the intensity, I_R, can be expressed as,

$$I_R = RI_0\frac{Sin^2\dfrac{N\phi}{2}}{Sin^2\dfrac{\phi}{2}}, \quad A2.8$$

with $I_0 = \varepsilon_0 cA_g A_g^*$ and having N-1 minima at values of

$$\frac{N\phi}{2} = n\pi, \qquad n = 1,2,...N-1,$$

with principle maxima at integer multiples of 2π, where phase ϕ is given by,

$$\phi = 2m\pi = 2m\frac{\Delta s}{\lambda}. \qquad A2.9$$

This is for a fixed angle α, and path difference between beams from adjacent grooves for some angles of β_m at an integer multiple of λ. The higher the value of N, the sharper the principle maxima, i.e. the more defined the angle β_m.

Not only is the intensity of the diffracted light a function of the number of grooves per millimetre, but more importantly, the resolution is a function of the number of grooves illuminated, as illustrated in Figure A2.2,

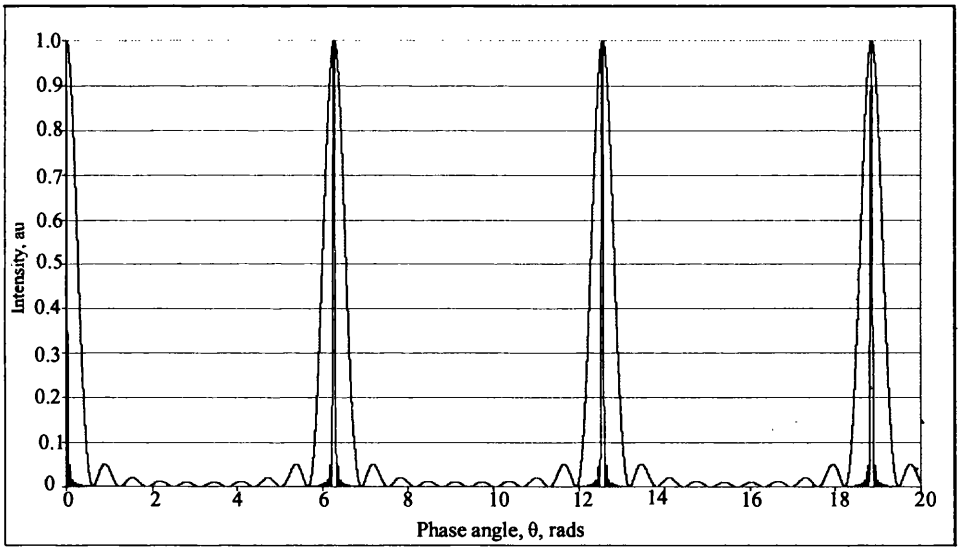

Fig. A2.2 Detected resolution is improved with increased number of illuminated grooves. This figure shows the improvement in resolution when the number of grooves is increased from 10 to 100.

Looking closely at the intensity either side of β_m, $\beta_m + \epsilon$, with $\epsilon << \beta_m$, one can say,

$$Sin(\beta_m + \varepsilon) = Sin\beta_m Cos\varepsilon + Cos\beta_m Sin\varepsilon \approx Sin\beta_m + \varepsilon Cos\beta_m,$$

$$\text{and } \phi = 2m\pi = 2m\pi + 2\pi\frac{d}{\lambda}\varepsilon Cos\beta_m = 2m\pi + \delta_1. \qquad A2.10$$

Thus, the intensity becomes $I_R = RI_0 \dfrac{Sin^2\left(\frac{N\delta_1}{2}\right)}{Sin^2\left(\frac{\delta_1}{2}\right)}$ where $\delta_1 << 1$. Therefore,

$$I_R \approx RI_0N^2 \frac{Sin^2\left(\frac{N\delta_1}{2}\right)}{\left(\frac{N\delta_1}{2}\right)^2}, \qquad A2.11$$

having minima at $N\delta_1 = \pm 2\pi$, and central maxima, a width of

$$\frac{2\lambda}{NdCos\beta_m}. \qquad A2.12$$

Differentiating the grating equation,

$$Sin\beta = \frac{m\lambda}{d} - Sin\alpha, \qquad A2.13$$

with respect to λ, we find the angular dispersion for a given angle α,

$$Cos\beta.\frac{d\beta}{d\lambda} = \frac{m}{d},$$

$$\frac{d\beta}{d\lambda} = \frac{m}{dCos\beta}. \qquad A2.14$$

Rearranging equation A2.13 for *m/d* and substituting back into equation A2.14 gives,

$$\frac{d\beta}{d\lambda} = \frac{Sin\alpha \pm Sin\beta}{\lambda Cos\beta}, \qquad A2.15$$

i.e. dispersion is not a function of the number of grooves, *N*.

Resolving power can be determined from equation A2.14 by using base half-width, equation A2.12, and applying the Rayleigh criterion that two lines at λ and $\lambda+\Delta\lambda$ are only just resolvable when the maximum intensity $I(\lambda)$ falls on the minimum for $I(\lambda+\Delta\lambda)$,

$$\frac{d\beta}{d\lambda}\Delta\lambda = \frac{\lambda}{NdCos\beta},$$

or

$$\frac{\lambda}{\Delta\lambda} = \frac{Nd(Sin\alpha \pm Sin\beta)}{\lambda}. \qquad A2.16$$

Using $m\lambda = d(Sin\alpha \pm Sin\beta)$ leads to $R = \frac{\lambda}{\Delta\lambda} = mN$ i.e. resolving power is a function of the diffraction order and more importantly, the number of illuminated grooves, *N*.

Appendix 3 - Etalons

Plane-parallel etalons can be used to filter out particular frequencies by the superposition of multiple reflections from their partially reflecting inner surfaces as shown in Figure A3.1.

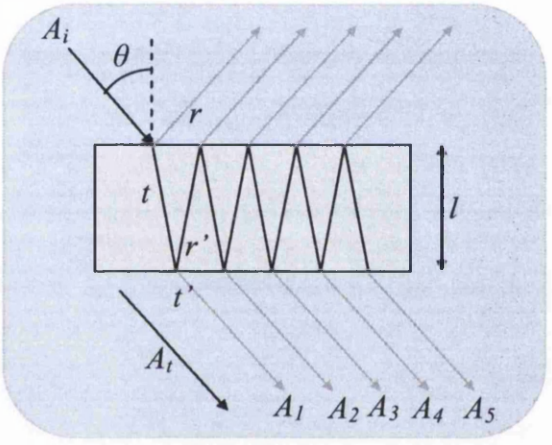

Fig. A3.1 An etalon with single incident beam results in multiple, evenly spaced transmitted beams, above and below the device.

The optical phase gained by one round trip within the cavity, for a given wavelength is given by

$$\delta = \frac{4\pi n l Cos\theta}{\lambda}. \qquad A3.1$$

Amplitudes of successive transmitted waves are dependent on the amplitudes of previously reflected waves within the etalon planes,

$$A_1 = tt', \qquad A_2 = tt'r'^2 e^{i\delta} A_i, \qquad A_3 = tt'r'^4 e^{2i\delta} A_i,$$

with $$A_t = A_i tt'\left(1 + r'^2 e^{i\delta} + r'^4 e^{2i\delta}\right),$$

and $$A_t = \frac{tt'}{1 - rr'e^{i\delta}} A_i, \qquad A3.2$$

with t and r the transmission and reflection coefficients at the etalon surfaces respectively, and l the separation between the two reflecting surfaces, as shown in Figure A3.1. The transmitted intensity,

$$T = \frac{A_t A_t^*}{A_i A_i^*} = \frac{(tt')^2}{(1 - rr')^2 4\sqrt{rr'} Sin^2\left(\delta/2\right)}, \qquad A3.3$$

which for identical etalon surfaces, $r = r'$, gives

$$T = \frac{1}{1 + F.Sin^2\left(\delta/2\right)}, \qquad A3.4$$

with

$$F = \frac{4R}{(1-R)^2} \text{ and } r^2 + t^2 = 1. \qquad A3.5$$

If l is of the order of 15 μm and $n \sim 4$, then the effective optical thickness is at least 60 μm, with a roundtrip ~ 120 μm.

Appendix 4 – Spectrometer spectral limitations

Simulations were carried out using the etalon equations A3.1-A3.5, with parameters l = 7 μm, and n = 4 for the average thickness and refractive index of silicon at -70°C respectively. Intensity values for blackbody spectra were calculated at a range of wavelengths, and the modulations due to etalon behaviour within the silicon layer resulted in peaks in the range of 650-700 nm. These peaks resembled those seen in the blackbody spectrum shown in Figure 5.16, making it possible to estimate the variation in the thickness of the silicon across the back of the CCD.

In order to simulate the modulation of the white light at the detector, it was necessary to estimate the blackbody spectrum, such that Wien's displacement law [5] was used to determine the temperature of the light source as ~ 4000 K,

$$\lambda_m T = 2.9 \times 10^{-3} mK \ , \qquad A4.1$$

where T is the temperature of the light source and λ_m is the wavelength of the peak intensity. A blackbody radiation curve was then generated using

$$B_\lambda(T) = \frac{2hc^2}{\lambda^5}\left[\exp\left(\frac{hc}{\lambda kT}\right) - 1\right]^{-1} . \qquad A4.2$$

Figure A4.1 illustrates basic etalon behaviour within the silicon layer at wavelengths beyond the visible spectrum where silicon becomes transparent using a fixed value of finesse, F, defined in equation A3.5. A series of regular peaks are seen to be transmitted through the silicon layer to the detecting points of the CCD.

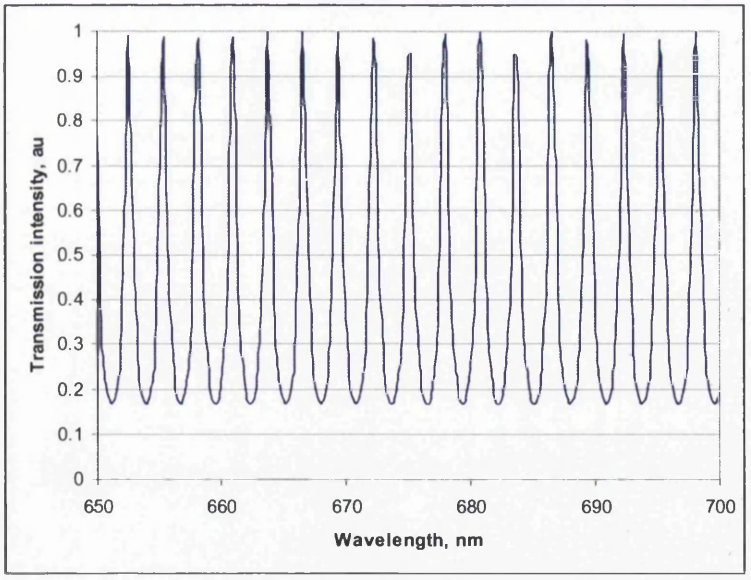

Fig. A4.1 A simplified example of spectral etalon behaviour as a function of wavelength, for a fixed spacing between two reflecting surfaces.

The graph for silicon absorption shown in Figure 5.21 was digitised and the normalised absorption efficiency for wavelength range 550 nm to 950 nm was calculated as shown

in Figure A4.2, with a linear Y-axis, better illustrating the poor absorption outside of the visible spectrum.

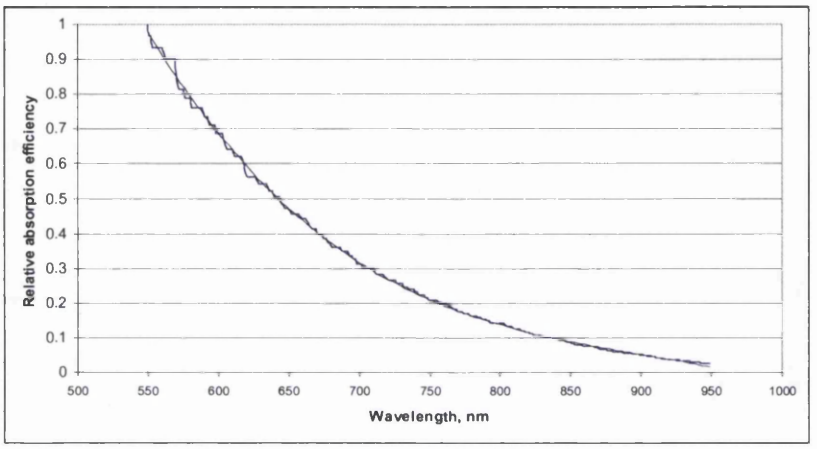

Fig. A4.2 A smaller range of the silicon absorption coefficient was extracted from Figure 5.14 and then normalised in this range. The curve fit was used to extract relative absorption of silicon in this spectral range.

Figure A4.3 shows how the relative silicon absorption efficiency affects this etalon behaviour in this narrow band. This was calculated in the wavelength range of 650 nm to 700 nm to modify the reflection factor of the Finesse function in equation A3.5. With increasing wavelength, the overall intensity reduces.

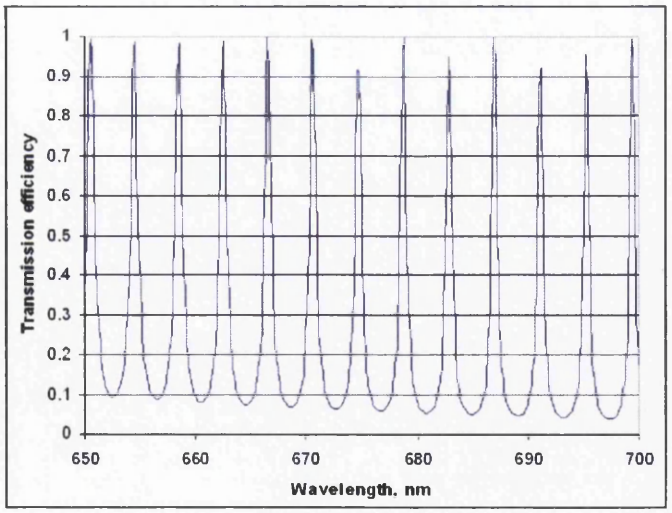

Fig. A4.3 Simple etaloning behaviour as a function of wavelength for a fixed spacing of two reflecting surfaces, while accounting for silicon absorption efficiency.

An algorithm, shown in Appendix 5, was written, to generate a digital bump-map to simulate a varying thickness of the silicon-layer detecting material of the CCD. One such map is shown in Figure A4.4. The thickness of the silicon layer was set at 7.00 ± 0.01μm.

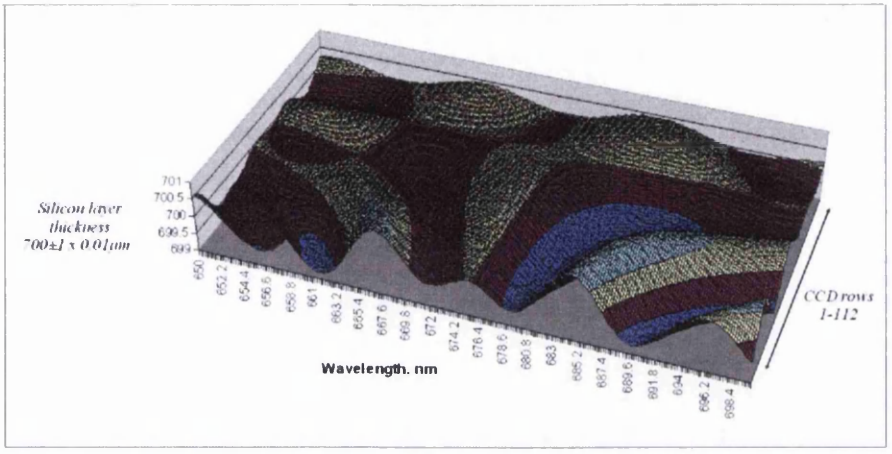

Fig. A4.4 Simulation of the variation of the thickness of silicon on the back of the CCD.

Combining the entire bump-map from Figure A4.3 for the variation of silicon thickness with the etalon behaviour in Figure A4.1 across a section of the CCD, results in Figure A4.5. Note the large variation of the etalon transmission peaks at 680 nm to 700 nm. This is a pseudo-random thickness but illustrates nicely its ability to vary the detection efficiency at a given wavelength, for a given CCD row.

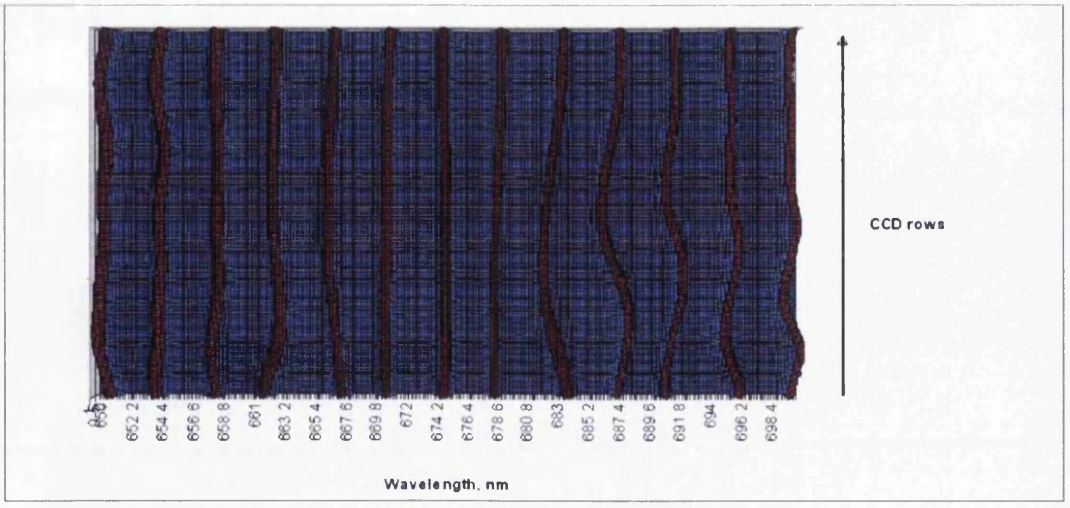

Fig. A4.5 The combined effects of variation of the thickness of the silicon layer, and the etaloning behaviour at longer wavelengths.

Figure A4.6 shows a small portion of the data taken from Figure 5.16 obtained from the spectrometer using the white light source, in the range 650 to 700 nm.

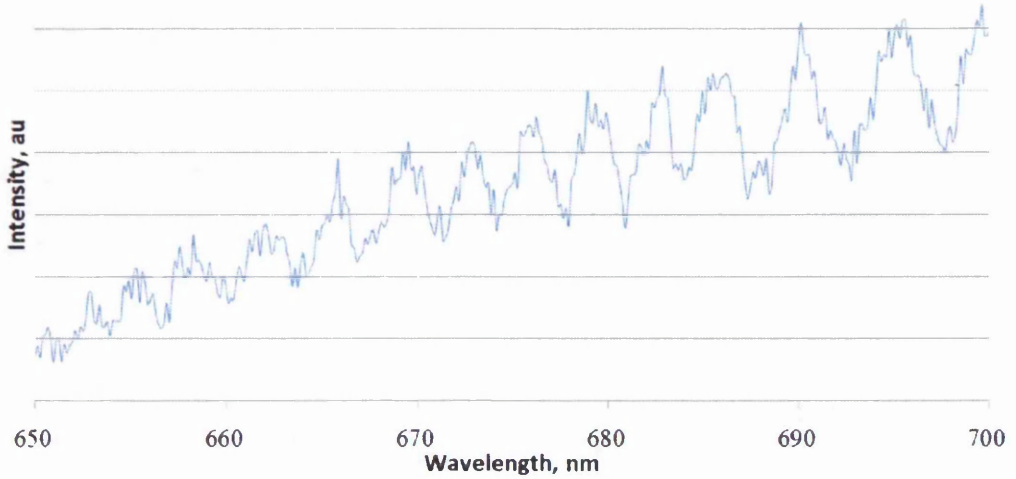

Fig. A4.6 The data obtained from the spectrometer (one CCD row only) using a white-light source in the range 650 nm to 700 nm to compare with simulated data.

The real peak spacing in Figure A4.6 varies between 3-5 nm, and compares well with that simulated, shown in Figure A4.3. The simulated data however has a different finesse value, F, from equation A3.5, resulting in sharper peaks to help emphasize the effects.

Figure A4.7 combines that in Figure A4.5 with a dropping silicon absorption coefficient thus heightening the modulation effect observed in Figure 5.16. Figure A4.7 best illustrates the overall effect for several rows of the CCD.

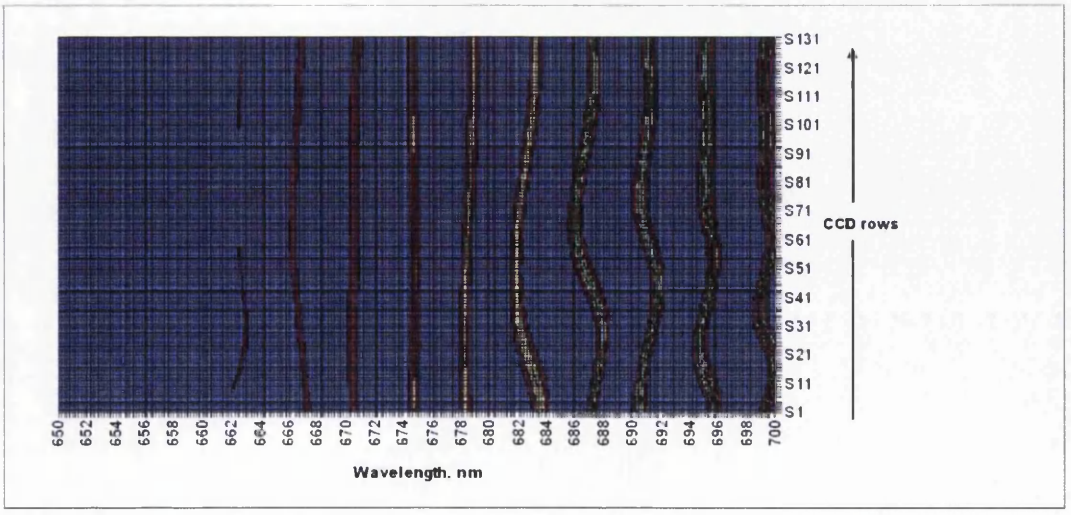

Fig. A4.7 Simulated CCD detection (132 rows) of a white-light source at T=4000 K in the spectral range of 650-700 nm, accounting for variation of silicon thickness and silicon absorption as a function of wavelength.

This highlights the similarities in the etalon behaviour with wavelength due to the varying silicon thickness, while accounting for silicon absorption, for a white-light source at T = 4000 K.

It was determined that it might well be possible to compensate for the varying thickness of the silicon layer, and also for the spectral etaloning effect. This would however require a much more detailed study to be carried out, making sure that all efficiencies at the grating and mirrors etc are accounted for. This would enable the variation in the thickness to be calculated and a 2048 x 512 matrix of compensation factors could be generated for the CCD. This would not however account for sub-pixel thickness variations. The spectral etaloning effect would need to be calculated for each grating as a function of angle, i.e. a variation in the centred wavelength falling on the grating would alter the modulation peaks due to a combination of spectral and spatial etaloning. Compensating for etalon behaviour would not be suitable for low intensity measurements due to the 30-50% modulations observed above 800-850 nm, as a result of the reduced absorption, as the error introduced would be too significant.

Appendix 5 – Algorithm to generate a pseudo-random thick silicon layer

The following algorithm was developed on a BBC Micro (6502) emulator to produce a data-file that contained points defining a varying height bitmap in a format that was comprehensible enough by MS EXCEL to allow it to be imported as an ASCII file.

```
10 XSIZE=8:          REM stepping factor
20 YSIZE=2 :         REM stepping factor
30 XSTART=-1000 :    REM initial co-ordinate
40 XSTOP=1000:       REM final co-ordinate
50 NL=132 :          REM number of CCD rows
60 MDF=0.8 :         REM modifier coefficient
```

```
70Y=OPENOUT"HEIGHT" :       REM open output file
80 BPUT #Y,ASC(",") :       REM place Excel column separator
90 P1=0.45:P2=0.85:P3=0.67 :  REM 3 sine-wave relative phase
100 B1=8.5:B2=11.5:B3=9.5 :  REM 3 sine-wave relative amplitude
110 F1=0.3: F2=0.07: F3=0.012 :  REM 3 sine-wave frequencies
120 FOR B=1 TO NL*YSIZE STEP YSIZE : REM LOOP through NL CCD rows
130     FOR A=XSTART TO XSTOP STEP XSIZE : REM loop through CCD pixels
140             X=640+A :       REM centre coord
150             MD=SIN(SQR(X^2+B^2)*MDF*0.0175) : REM 4th sine-wave factor
160             YVAR=((SIN((A*F1+SIN((P1*B)*0.175))*0.0175))*B1+SIN(( A*F2+
                SIN((P2*B)*0.175))*0.0175)*B2+SIN((A*F2+P3*B )*0.0175)*B3)*MD :
                REM calculate bump-map height at this co-ordinate
170             IF INT(YVAR*4)<0 THEN BPUT #Y,ASC("-") :
                REM put a '-' to the file if value is negative
180             S$=STR$(ABS(INT(YVAR))) :
                REM store magnitude of value as a string of characters
190             FOR S=1 TO LEN(S$):BPUT #Y,ASC(MID$(S$,S,1)):NEXT S :
                REM output each character in the string to file
200             BPUT #Y,ASC(",") : REM place Excel column separator
210             NEXT A : REM return to calculate next bump-map value
220     BPUT #Y,ASC(CHR$(13)) : REM put newline character to file
230     NEXT B :REM return for next CCD row
240 CLOSE #Y : REM close output file
250 END :       REM end program
```

An example of a 'bump-map' as shown below in Figure A5.1 was typical of the type of data generated with the above algorithm. The various parameters would alter the number of oscillations in x and y, the depth of modulation and the randomness of the final bump-map.

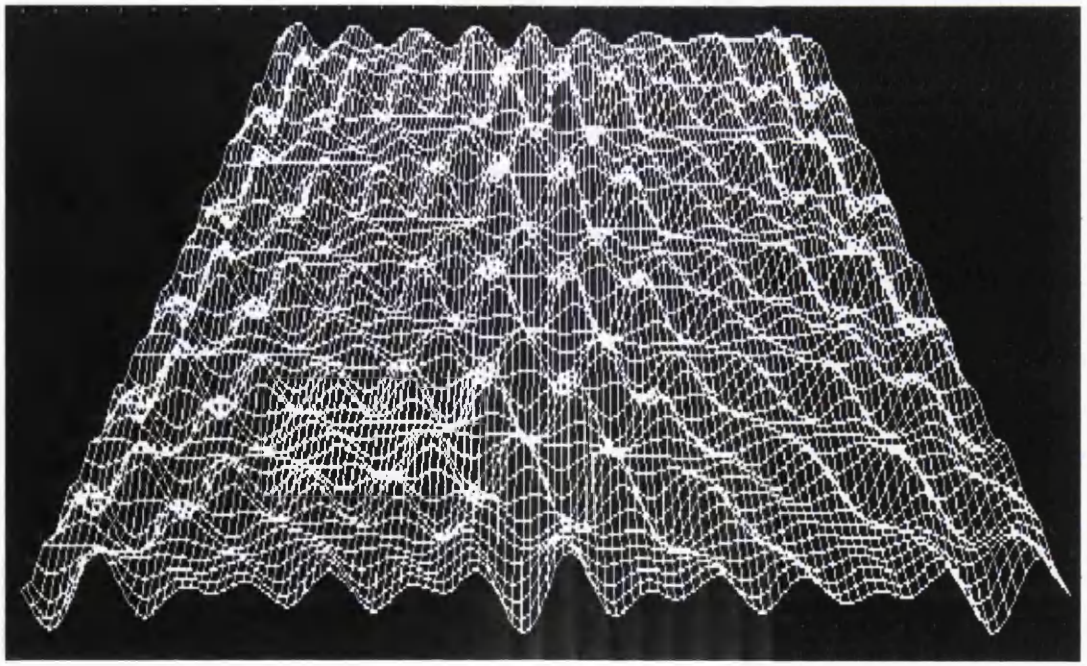

Fig. A5.1 Graphical representation of the data output to an Excel file, for use as a bump-map. It represents the pseudo-random varying thickness across a piece of silicon for use as the back of the CCD detector.

Appendix 6 Manufacturers specification sheet for the 850 nm VCSEL discussed in section 6.5

THORLABS INC
435 Route 206 • P. O. Box 366
Newton, NJ 07860-0366
www.thorlabs.com
SALES (973) 579-7227
FAX (973) 300-3600

VCSEL-850

850nm VCSEL Laser Diode in TO-46 Package

1. Feature

a. Oxidation process
b. Flat window
c. Monitor Photodiode
d. High speed 2.5Gbps

2. Application:

a. High-speed data communications and telecommunications applications
b. Gigabit Ethernet
c. Fiber Channel
d. ATM transceiver modules and system

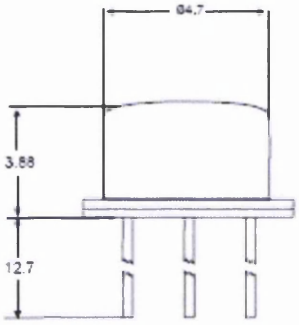

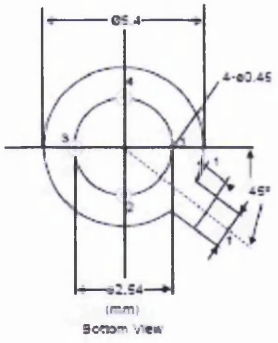

1. Case
2. VCSEL Anode
3. VCSEL Cathode/Photodiode Anode
4. Photodiode Cathode

3. Optical and Electrical Characteristics

Parameter	Symbol	Min.	TYP.	Max.	Unit	Test Condition
Peak Wavelength	λ_p	830	845	860	nm	I_f = 8mA@RT
Spectral Width (RMS)	$\Delta\lambda$	-	-	0.85	nm	I_f = 8mA@RT
Beam Divergence	Θ	-	25	30	Deg	Full width at $1/e^2$; I_f = 8mA@RT
Forward Voltage	V_f	1.7	1.9	2.2	V	I_f = 8mA@RT
Threshold Current	I_{th}	-	2.2	3	mA	-
Slope Efficiency	dP/dI	0.12	0.32	0.4	W/A	I_f = 8mA@RT
Optical Ouptut Power	P_{out}	-	1.85	-	mW	I_f = 8mA@RT
Dynamic Resistance	dV/dI	20	40	65	Ω	I_f = 8mA@RT
Rise / Fall Time	t_r / t_f	-	50	100	ps	20%-80%
Jitter p-p	t_j	-	35	-	ps	-
e_p Temperature Coefficient	$\delta e_p/\delta T$	-	0.06	-	nm/°C	T_A=0~70°C, I_f= 8mA
Operating Temperature Range	T_{op}	-5	25	80	°C	-
Monitor Current	I_m	100	-	-	µA	I_f = 8mA@RT

2. Maximum Ratings

Parameter	min.	Max.	Unit	Condition
Storage Temperature	-40	100	°C	-
Operating Temperature	0	85	°C	-
Continuous Forward Current	-	10	mA	-
Continuous Reverse Voltage	-	5	V	@10µA

3. Monitoring PIN Specs

Parameter	Symbol	Min.	TYP.	Max.	Unit	Test Condition
Dark Current	I_r	-	0.2	1	nA	V_r = 10V
Shunt Resistance	P_D	100	200	-	GΩ	–
Breakdown Voltage	V_{br}	-	50	-	V	-
Junction Capacitance	C_D	-	40	-	pF	@V_r = 10V, 10KHz

References

[1] Kortan A.R., Hull R., Opila R.L., Bawendi M.G., Steigerwald M.L., Carroll P.J., Brus L.E., J. Am. Chem. Soc. **112**, 1327-1332, (1990)

[2] Cartmell E., Principles of Crystal Chemistry, Royal Inst. of Chem. No. **18**, (1971)

[3] Handbook of Chemistry and Physics, 64th Ed., CRC Press, (1983-1984)

[4] Demtrőder, Laser Spectroscopy – Basic Concepts and Instrumentation, 3rd Ed., Springer, (2003)

[5] Woan G., The Cambridge Handbook of Physics Formulae, (2000)